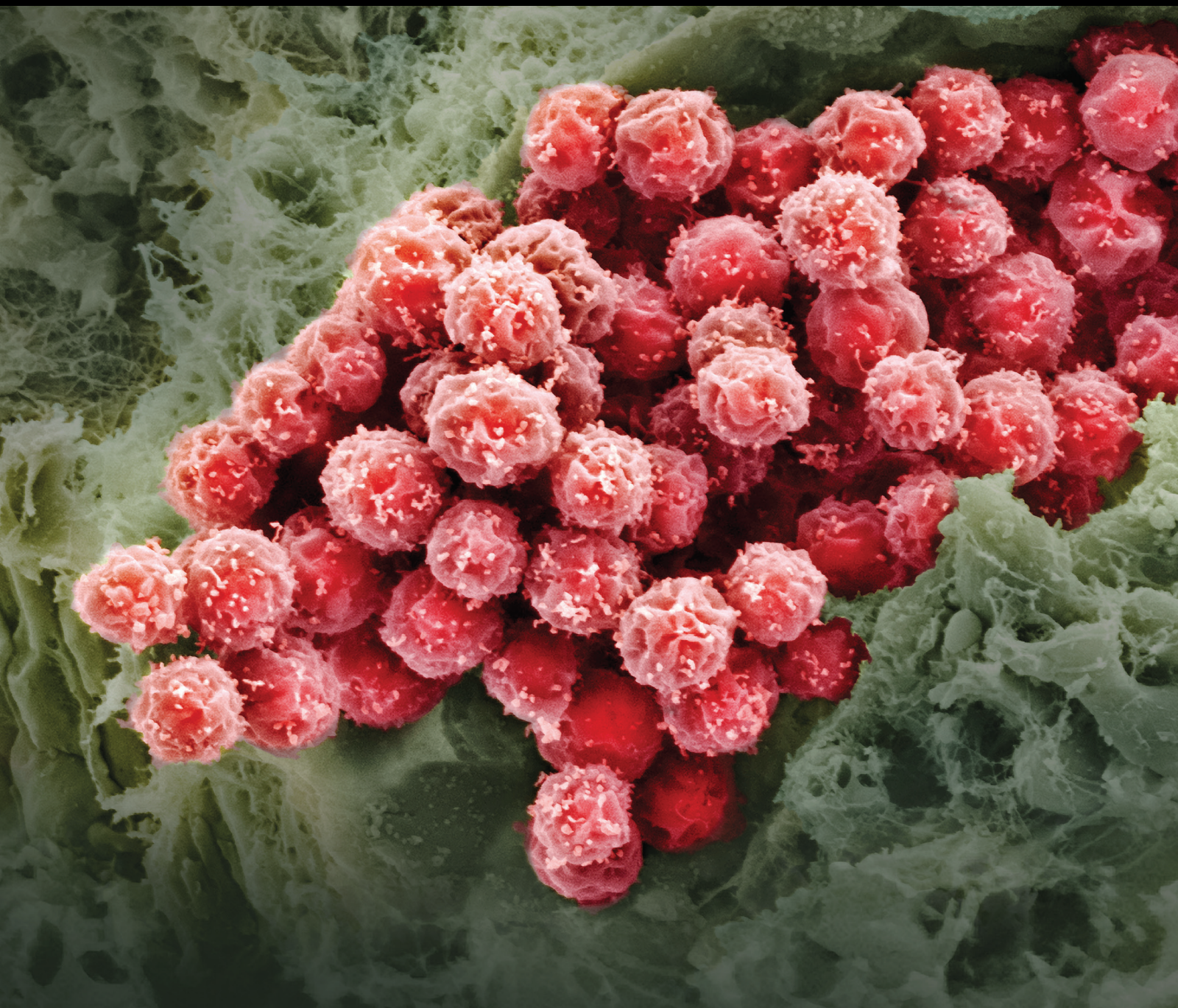# Smart Materials for Stem Cell Therapy

Lead Guest Editor: Jingan Li
Guest Editors: Juan Wang and Kun Zhang

Smart Materials for Stem Cell Therapy

Smart Materials for Stem Cell Therapy

Lead Guest Editor: Jingan Li
Guest Editors: Juan Wang and Kun Zhang

Shuiqiao Yuan ![ID], China
Dunfang Zhang ![ID], China
Ludovic Zimmerlin, USA
Ewa K. Zuba-Surma ![ID], Poland

Contents

Retraction

Retracted: Loading Gentamicin and Zn^{2+} on TiO$_2$ Nanotubes to Improve Anticoagulation, Endothelial Cell Growth, and Antibacterial Activities

Stem Cells International

This article has been retracted by Hindawi following an investigation undertaken by the publisher [1]. This investigation has uncovered evidence of one or more of the following indicators of systematic manipulation of the publication process:

(1) Discrepancies in scope

(2) Discrepancies in the description of the research reported

(3) Discrepancies between the availability of data and the research described

(4) Inappropriate citations

(5) Incoherent, meaningless and/or irrelevant content included in the article

(6) Manipulated or compromised peer review

The presence of these indicators undermines our confidence in the integrity of the article's content and we cannot, therefore, vouch for its reliability. Please note that this notice is intended solely to alert readers that the content of this article is unreliable. We have not investigated whether authors were aware of or involved in the systematic manipulation of the publication process.

In addition, our investigation has also shown that one or more of the following human-subject reporting requirements has not been met in this article: ethical approval by an Institutional Review Board (IRB) committee or equivalent, patient/participant consent to participate, and/or agreement to publish patient/participant details (where relevant).

Wiley and Hindawi regrets that the usual quality checks did not identify these issues before publication and have since put additional measures in place to safeguard research integrity.

We wish to credit our own Research Integrity and Research Publishing teams and anonymous and named external researchers and research integrity experts for contributing to this investigation.

The corresponding author, as the representative of all authors, has been given the opportunity to register their agreement or disagreement to this retraction. We have kept a record of any response received.

References

[1] Y. Lin, L. Zhang, Y. Yang et al., "Loading Gentamicin and Zn^{2+} on TiO$_2$ Nanotubes to Improve Anticoagulation, Endothelial Cell Growth, and Antibacterial Activities," *Stem Cells International*, vol. 2021, Article ID 9993247, 13 pages, 2021.

Hindawi

Retraction

Retracted: High-Resolution Microscopy to Learn the Nuclear Organization of the Living Yeast Cells

Stem Cells International

This article has been retracted by Hindawi following an investigation undertaken by the publisher [1]. This investigation has uncovered evidence of one or more of the following indicators of systematic manipulation of the publication process:

(1) Discrepancies in scope

(2) Discrepancies in the description of the research reported

(3) Discrepancies between the availability of data and the research described

(4) Inappropriate citations

(5) Incoherent, meaningless and/or irrelevant content included in the article

(6) Manipulated or compromised peer review

The presence of these indicators undermines our confidence in the integrity of the article's content and we cannot, therefore, vouch for its reliability. Please note that this notice is intended solely to alert readers that the content of this article is unreliable. We have not investigated whether authors were aware of or involved in the systematic manipulation of the publication process.

Wiley and Hindawi regrets that the usual quality checks did not identify these issues before publication and have since put additional measures in place to safeguard research integrity.

We wish to credit our own Research Integrity and Research Publishing teams and anonymous and named external researchers and research integrity experts for contributing to this investigation.

The corresponding author, as the representative of all authors, has been given the opportunity to register their agreement or disagreement to this retraction. We have kept a record of any response received.

References

[1] R. Wang, A. Huang, Y. Wang et al., "High-Resolution Microscopy to Learn the Nuclear Organization of the Living Yeast Cells," *Stem Cells International*, vol. 2021, Article ID 9951114, 7 pages, 2021.

Hindawi

Retraction

Retracted: Study of the Structure and Properties of ZnS Utilized in a Fluorescence Biosensor

Stem Cells International

This article has been retracted by Hindawi following an investigation undertaken by the publisher [1]. This investigation has uncovered evidence of one or more of the following indicators of systematic manipulation of the publication process:

(1) Discrepancies in scope

(2) Discrepancies in the description of the research reported

(3) Discrepancies between the availability of data and the research described

(4) Inappropriate citations

(5) Incoherent, meaningless and/or irrelevant content included in the article

(6) Manipulated or compromised peer review

The presence of these indicators undermines our confidence in the integrity of the article's content and we cannot, therefore, vouch for its reliability. Please note that this notice is intended solely to alert readers that the content of this article is unreliable. We have not investigated whether authors were aware of or involved in the systematic manipulation of the publication process.

Wiley and Hindawi regrets that the usual quality checks did not identify these issues before publication and have since put additional measures in place to safeguard research integrity.

We wish to credit our own Research Integrity and Research Publishing teams and anonymous and named external researchers and research integrity experts for contributing to this investigation.

The corresponding author, as the representative of all authors, has been given the opportunity to register their agreement or disagreement to this retraction. We have kept a record of any response received.

References

[1] Y. Ren, H. Zhou, X. Wang, Q. W. Liu, X. D. Hou, and G. F. Zhang, "Study of the Structure and Properties of ZnS Utilized in a Fluorescence Biosensor," *Stem Cells International*, vol. 2021, Article ID 7067146, 6 pages, 2021.

Retraction

Retracted: Severity Assessment of COVID-19 Using a CT-Based Radiomics Model

Stem Cells International

This article has been retracted by Hindawi following an investigation undertaken by the publisher [1]. This investigation has uncovered evidence of one or more of the following indicators of systematic manipulation of the publication process:

(1) Discrepancies in scope

(2) Discrepancies in the description of the research reported

(3) Discrepancies between the availability of data and the research described

(4) Inappropriate citations

(5) Incoherent, meaningless and/or irrelevant content included in the article

(6) Peer-review manipulation

The presence of these indicators undermines our confidence in the integrity of the article's content and we cannot, therefore, vouch for its reliability. Please note that this notice is intended solely to alert readers that the content of this article is unreliable. We have not investigated whether authors were aware of or involved in the systematic manipulation of the publication process.

Wiley and Hindawi regrets that the usual quality checks did not identify these issues before publication and have since put additional measures in place to safeguard research integrity.

We wish to credit our own Research Integrity and Research Publishing teams and anonymous and named external researchers and research integrity experts for contributing to this investigation.

The corresponding author, as the representative of all authors, has been given the opportunity to register their agreement or disagreement to this retraction. We have kept a record of any response received.

References

[1] Z. Xu, L. Zhao, G. Yang et al., "Severity Assessment of COVID-19 Using a CT-Based Radiomics Model," *Stem Cells International*, vol. 2021, Article ID 2263469, 10 pages, 2021.

Retraction

Retracted: Severity Assessment of COVID-19 Using a CT-Based Radiomics Model

Stem Cells International

This article has been retracted by Hindawi following an investigation undertaken by the publisher [1]. This investigation has uncovered evidence of one or more of the following indicators of systematic manipulation of the publication process:

(1) Discrepancies in scope

(2) Discrepancies in the description of the research reported

(3) Discrepancies between the availability of data and the research described

(4) Inappropriate citations

(5) Incoherent, meaningless and/or irrelevant content included in the article

(6) Peer-review manipulation

The presence of these indicators undermines our confidence in the integrity of the article's content and we cannot, therefore, vouch for its reliability. Please note that this notice is intended solely to alert readers that the content of this article is unreliable. We have not investigated whether authors were aware of or involved in the systematic manipulation of the publication process.

Wiley and Hindawi regrets that the usual quality checks did not identify these issues before publication and have since put additional measures in place to safeguard research integrity.

We wish to credit our own Research Integrity and Research Publishing teams and anonymous and named external researchers and research integrity experts for contributing to this investigation.

The corresponding author, as the representative of all authors, has been given the opportunity to register their agreement or disagreement to this retraction. We have kept a record of any response received.

References

[1] Z. Xu, L. Zhao, G. Yang et al., "Severity Assessment of COVID-19 Using a CT-Based Radiomics Model," *Stem Cells International*, vol. 2021, Article ID 2263469, 10 pages, 2021.

Research Article

Severity Assessment of COVID-19 Using a CT-Based Radiomics Model

Zhigao Xu [ID],[1,2] **Lili Zhao,**[2] **Guoqiang Yang** [ID],[1,3] **Ying Ren** [ID],[4] **Jinlong Wu,**[2] **Yuwei Xia,**[5] **Xuhong Yang,**[5] **Milan Cao,**[6] **Guojiang Zhang,**[6] **Taisong Peng,**[7] **Jiafeng Zhao,**[8] **Hui Yang,**[2] **Jinfeng Hu,**[7] **and Jiangfeng Du** [ID][1,3]

[1]*College of Medical Imaging, Shanxi Medical University, Taiyuan, 030001 Shanxi Province, China*

[2]*Department of Radiology, The Third People's Hospital of Datong, Datong, 037008 Shanxi Province, China*

[3]*Department of Radiology, First Hospital of Shanxi Medical University, Taiyuan, 030001 Shanxi Province, China*

[4]*Department of Materials Science and Engineering, Henan University of Technology, Zhengzhou, 450001 Henan Province, China*

[5]*Huiying Medical Technology Co., Ltd, Room A206, B2, Dongsheng Science and Technology Park, Haidian District, Beijing City, 100192, China*

[6]*Department of Science and Education, The Third People's Hospital of Datong, Datong, 037008 Shanxi Province, China*

[7]*Department of Radiology, The Second People's Hospital of Datong, Datong, 037005 Shanxi Province, China*

[8]*Department of Rehabilitation Medicine, Xiantao First People's Hospital, Xiantao, 433000 Hubei Province, China*

Correspondence should be addressed to Guoqiang Yang; doctor_ygq@163.com and Jiangfeng Du; dujf@sxmu.edu.cn

The coronavirus disease of 2019 (COVID-19) has evolved into a worldwide pandemic. Although CT is sensitive in detecting lesions and assessing their severity, these works mainly depend on radiologists' subjective judgment, which is inefficient in case of a large-scale outbreak. This work focuses on developing a CT-based radiomics model to assess whether COVID-19 patients are in the early, progressive, severe, or absorption stages of the disease. We retrospectively analyzed the CT images of 284 COVID-19 patients. All of the patients were divided into four groups (0-3): early ($n = 75$), progressive ($n = 58$), severe ($n = 75$), and absorption ($n = 76$) groups, according to the progression of the disease and the CT features. Meanwhile, they were split randomly to training and test datasets with the fixed ratio of 7 : 3 in each category. Thirty-eight radiomic features were nominated from 1688 radiomic features after using select K-best method and the ElasticNet algorithm. On this basis, a support vector machine (SVM) classifier was trained to build this model. Receiver operating characteristic (ROC) curves were generated to determine the diagnostic performance of various models. The precision, recall, and f_1-score of the classification model of macro- and microaverage were 0.82, 0.82, 0.81, 0.81, 0.81, and 0.81 for the training dataset and 0.75, 0.73, 0.73, 0.72, 0.72, and 0.72 for the test dataset. The AUCs for groups 0, 1, 2, and 3 on the training dataset were 0.99, 0.97, 0.96, and 0.93, and the microaverage AUC was 0.97 with a macroaverage AUC of 0.97. On the test dataset, AUCs for each group were 0.97, 0.86, 0.83, and 0.89 and the microaverage AUC was 0.89 with a macroaverage AUC of 0.90. The CT-based radiomics model proved efficacious in assessing the severity of COVID-19.

1. Introduction

The outbreak of coronavirus disease 2019 (COVID-19), which began in December 2019, is a severe acute respiratory syndrome coronavirus 2 (SARS-CoV-2) infection. The World Health Organization (WHO) has declared COVID-19 a global pandemic, and by 6 August 2021, there have been 200,840,180 confirmed cases of COVID-19, including 4,265,903 deaths, reported to the WHO [1]. Nucleic acid testing (NAT) of the reverse transcription polymerase chain reaction (RT-PCR) is currently the most reliable diagnostic method for COVID-19, but chest computed tomography (CT) is recognized as an important tool for severity assessment, as well as an important complementary diagnostic

technique. Therefore, chest CT has become an indispensable tool in the screening and severity assessment of COVID-19.

When the number of infected people is small and the number of doctors is sufficient, it is feasible to assess the severity of such patients manually; however, in case of a large-scale outbreak, there may be too few radiologists. Therefore, the development of automated and reproducible analysis methods to extract more information from image-based features is a requirement. Radiomics—the high-throughput extraction of large amounts of image features from radiographic images—addresses this problem and is one of the approaches that hold great promise [2]. Researchers have proposed the use of radiomic features to quantify various tumor phenotypes on medical images, to describe this heterogeneity and furthermore, and utilize these features as predictors of genetics and clinical outcomes [3]. For the diagnosis of COVID-19 based on GGO lesions, a CT-based radiomics model could be a promising supplementary tool for improving specificity for COVID-19 in a population confounded by ground glass opacity changes from other etiologies. Furthermore, the assistance afforded by application of artificial intelligence has improved radiologists' performance in distinguishing coronavirus disease 2019 pneumonia from noncoronavirus disease 2019 pneumonia at chest CT.

Therefore, to relieve pressure on radiologists when evaluating the severity of COVID-19 and to avoid mistakes under fatigue, the present research establishes a radiomics model by evaluating the relationship between CT staging and CT-based radiomics characteristics of COVID-19.

2. Materials and Methods

2.1. Patient Population and Ethical Approval.
Our institutional review board (IRB) waived written informed consent for this retrospective study, which evaluated deidentified data and brought no potential risk to patients. To avert any potential breach of confidentiality, no link between the patients and the researchers was available.

Patient data were collected from the First People's Hospital of Xiantao of China, during the period between February 2020 and June 2020. The inclusion criterion of COVID-19 was conformity to the Diagnosis and Treatment of COVID-19 (revised edition of the provisional 7th edition) which forms the guidelines for the National Health Commission of the People's Republic of China [4]. We included patients having a history of contact in epidemic areas or with known patients: these patients had been confirmed as COVID-19 cases by polymerase chain reaction (PCR). Meanwhile, the inclusion criteria also included the following: (1) patients have received CT examination, and the CT images can be obtained; (2) there were no other chest diseases or history of chest surgery in these patients before CT examination; and (3) their clinical data are complete and comprehensive. The exclusion criteria include the following: (1) the quality of CT images is so poor that they cannot be used for analysis, and (2) chest CT shows other chest diseases, such as tuberculosis and lung cancer. Clinical infor-

mation and chest CT data of 303 consecutive COVID-19 patients with COVID-19 were collected.

For this study, 284 COVID-19 patients were enrolled. There were 123 males and 161 females, aged from 1 to 91 years old, with a mean average age of 55.50 ± 14.97 y. In the training set, there were 89 males and 108 females, with a mean average age of 54.56 ± 15.47 y (ranging from ages of 1 to 91 y); in the test set, there were 34 males and 53 females, with a mean average age of 57.61 ± 13.61 y (ranging from ages of 29 to 89 y).

2.2. CT Examination.
The GE Optima 660 and GE Optima 540 spiral CT scanners were used. Patients adopted a supine position, and scanning was performed at the end of inspiration using the conventional dose. For each patient, the scanning range was from the apex of the lung to the costophrenic angle, the slice thickness was 5 mm, the tube voltage was 120 kV, and the tube current was 100 mA. All imaging data were reconstructed by using a medium-sharp reconstruction algorithm with a thickness of 1.25 mm.

2.3. Marking of CT Images.
Original CT images, which were exported in DICOM format from CT scanners, were uploaded to Radcloud (Huiying Medical Technology Co., Ltd, Beijing, China). Subsequently, CT features of COVID-19 patients were investigated. The location, morphology, distribution, extent, density, and internal structure of the lesions were observed to identify features such as thickened lobular septum and central nodules of the lung lobules. The relationships between lesions and bronchial blood vessels, the condition of stripe signs, and the presence of solid component signs were determined. Morphological changes and imaging signs were observed in patients with dynamic follow-up.

For each patient, the severity of COVID-19 was determined following both the guidelines in 2019-nCoV (Trial Version 7) issued by the China National Health Commission and the guidelines for medical imaging in auxiliary diagnosis of coronavirus disease 2019 issued by the Chinese Research Hospital Association Radiology Committee on Infectious and Inflammatory Disease, et al. [4, 5]. COVID-19 is classified into four stages: mild, moderate, severe, and resorption stages, based on the severity thereof: (1) early stage: focal ground-glass opacity (GGO) was not distributed across segments, but multiple lesions may occur; (2) advanced stage: the lesions were distributed across segments and had a large range of GGO, including the paving-stone sign and mixed GGO and solid component signs. There were also solid component signs, regardless of the size of the range; (3) severe stage: it developed from the advanced stage, and the lesion area had increased significantly based on previous examination. The CT manifestation was evinced by the presence of "butterfly sign" and even "white lung"; and (4) resorption stage (or recovery stage): the main manifestation was the narrowed lesion range and the lightened density based on data from the previous stage, and the characteristic stripe sign appeared.

The segmented images marked by experts were used as the standard to evaluate the collected thin-layer CT images.

Two radiologists, each with at least five years of chest-imaging experience, manually outlined the ROI using the labelling tool in the Radcloud platform. They considered the distribution and image features of disease foci in COVID-19 (Figures 1–4). In the event of disagreement between the two primary radiological interpretations, a third experienced thoracic radiologist with 16 years of experience adjudicated in reaching a final decision.

2.4. Radiomic Feature Extraction. After image preprocessing, 1688 radiomic features were extracted for each subject using the PyRadiomics v3.0 (open source software), including original features and features (original features except shape features) as transformed by logarithm, wavelet (LLL, LLH, LHL, LHH, HLL, HLH, HHH, and HHL), exponent, gradient, square, square root, and local binary pattern applied in 2D and 3D. Among 107 original features, 14 were related to shape features, 18 first-order, and 24 GLCM (grey-level cooccurrence matrix), 14 GLDM (grey-level dependence matrix), 16 GLRLM (grey-level run length matrix), 16 GLSZM (grey-level size zone matrix), and five NGTDM (neighboring grey-tone difference matrix) features. First-order statistics describe the distribution of voxel intensities within the image region defined by the mask through commonly used basic metrics. GLCM describes the second-order joint probability function of an image region constrained by the mask. GLDM quantifies grey-level dependencies in an image. GLRLM quantifies grey-level runs, which are defined as the length in number of pixels, of consecutive pixels that have the same grey-level value. GLSZM quantifies grey-level zones in an image. A grey-level zone is defined as the number of connected voxels that share the same grey-level intensity. NGTDM quantifies the difference between a grey-value and the mean average grey value of its neighbors within a preset distance. Detailed information about these features is available in the documentation supplied with the PyRadiomics software.

2.5. Feature Selection and Model Building. To verify the credibility of the manual segmentation between the two radiologists, the CT scans of 10 patients were randomly selected and segmented by the two radiologists for double-blind interpretation. Interclass correlation coefficients (ICC), which can be used to assess the interobserver reproducibility of ROIs delineated, can be obtained from the following equation:

$$ICC = \frac{(MS_R - MS_E)}{MS_R + ((MS_C - MS_E)/n)}, \qquad (1)$$

where MS_R represents mean square for rows; MS_C is mean square for columns; MS_E denotes mean square for error; and n is the number of subjects. The value of ICC was greater than 0.75.

After feature extraction, 70% of the dataset was randomly assigned to the training set and for all cases, features were normalized to the normal distribution by mean and variance scaling. The trained SVM classifier was evaluated on the test dataset while the training and feature selection was conducted only on the training data. K-best was applied to select the most significantly relevant feature set with threshold of 0.05. To avoid overfitting caused by the radiomic features being larger than the sample size, ElasticNet, a regularized, generalized model, linearly combines the L_1 and L_2 penalties of the least absolute shrinkage and selection operator and ridge methods to realize a built-in feature weighting mechanism, making an appropriate balance between model generalization and diagnostic performance. The model was trained with 10-fold cross-validation to attain the optimal α-value. Following the optimal α-value, an optimal simplified feature set was determined. An SVM classifier was built to distinguish among the four COVID-19 groups based on final reduced imaging radiomic features. The receiver operating characteristic (ROC) curve was plotted as a classifier of each group, and the area under the curve (AUC) measure was applied to evaluate model performance. The 95% confidence level was assessed on the variation of the AUC. Micro- and macroaverage AUC, precision, recall, and f_1-score were also calculated to assess model performance for multiclass classification.

3. Results

3.1. The Radiomics Workflow. The radiomics workflow is illustrated in Figure 5. In this study, 284 patients were retrospectively included to investigate the validity of radiomics-based classification with 75, 58, 75, and 76 cases, respectively, for groups 0, 1, 2, and 3 (early stage, progressive stage, severe stage, and absorptive stage). The dataset was split at random to form training and test datasets with a fixed ratio of 7 : 3 in each category, resulting in 197 (52 cases in group 0, 40 in group 1, 52 in group 2, and 53 in group 3) for the training dataset and 87 cases for the test dataset.

3.2. Radiomic Features. Of all the radiomic features extracted, the median ICC was 0.885; 1011 of 1688 features (59.9%) were robust, with ICC > 0.75. Then, 38 radiomic features were nominated from 1688 radiomic features after using select K-best method and the ElasticNet algorithm (Figure 6 and Table 1). The 38 features contain four first-order features, two shape features, nine grey-level cooccurrence matrix (GLCM) features, 10 grey-level dependence matrix (GLDM) features, five grey-level run length matrix (GLRLM) features, six neighboring grey-tone difference matrix (NGTDM) features, and two grey-level size zone matrix (GLSZM) features.

3.3. Model Classification Performance. An SVM classifier was trained based on optimal feature set on training dataset. The precision, recall, and f_1-score of the classification model for the macroaverage and microaverage were 0.82, 0.82, 0.81, 0.81, 0.81, and 0.81 for the training dataset and 0.75, 0.73, 0.73, 0.72, 0.72, and 0.72 for the test dataset. The AUCs for groups 0, 1, 2, and 3 on the training dataset were 0.99, 0.97, 0.96, and 0.93, and the microaverage AUC was 0.97 with a macroaverage AUC of 0.97 (Figure 7(a)). On the test dataset, AUCs for each group were 0.97, 0.86, 0.83, and 0.89 and the microaverage AUC was 0.89 with a macroaverage AUC of 0.90 (Figure 7(b)).
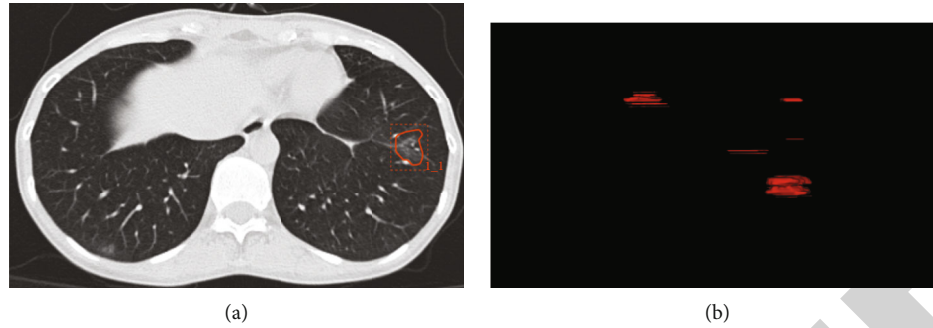
Figure 1: A case of confirmed mild COVID-19. A 33-year-old female presented with a 2-day history of fever and cough. (a) CT imaging revealed diffuse pure GGO with distribution in the left lower lobe. The area of the lesions was delineated on the axial. (b) The reconstructed images.
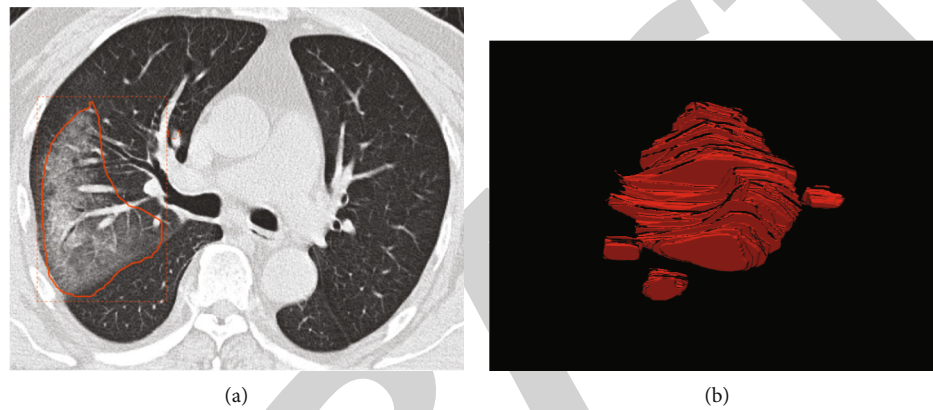
Figure 2: A case of confirmed mild COVID-19. A 63-year-old male presented with a 5-day history of fever, cough, and mild dyspnea. (a) CT imaging revealed pure GGO with distribution in the left lower lobe. The area of the lesions was delineated on the axial. (b) The reconstructed images.
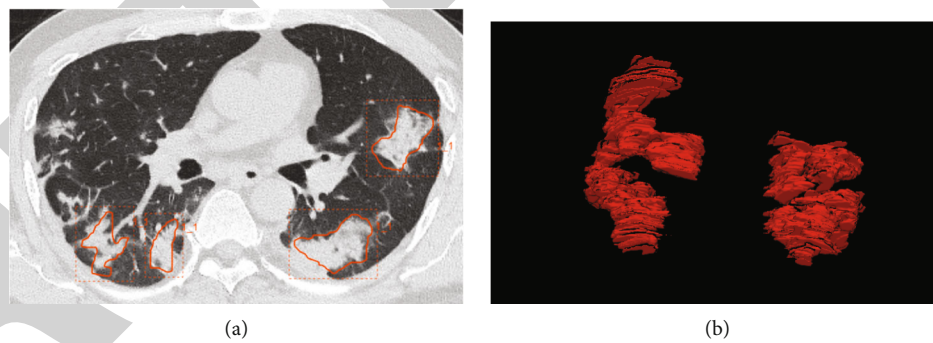
Figure 3: A case of confirmed severe COVID-19. A 45-year-old male presented with a 12-day history of fever, cough with expectoration, and mild dyspnea. (a). CT imaging revealed multiple consolidation with symmetric distribution in both lungs. The area of the lesions was delineated on the axial. (b) The reconstructed images.

4. Discussion

Assessing pulmonary lesions using computed tomography (CT) images is of significance to the severity diagnosis and treatment of coronavirus disease 2019- (COVID-19-) infected patients. Such assessment mainly depends on the subjective judgment of radiologists, which is inefficient and presents difficulties for those with low levels of experience, especially in primary or community hospitals [6–8]. In this study, we uncover some of the radiomic features that contribute to evaluation of the severity of COVID-19 patients. A radiomics model aiming at assessing automatically the severity of COVID-19 was demonstrated, with favorable predictive accuracy, achieving an average AUC performance of 0.97 on a training dataset and 0.90 on a test dataset. Prediction outputs generated from our radiomics model further augmented human expert performance. More importantly, the model is expected to relieve the workload of radiologists

(a)

(b)
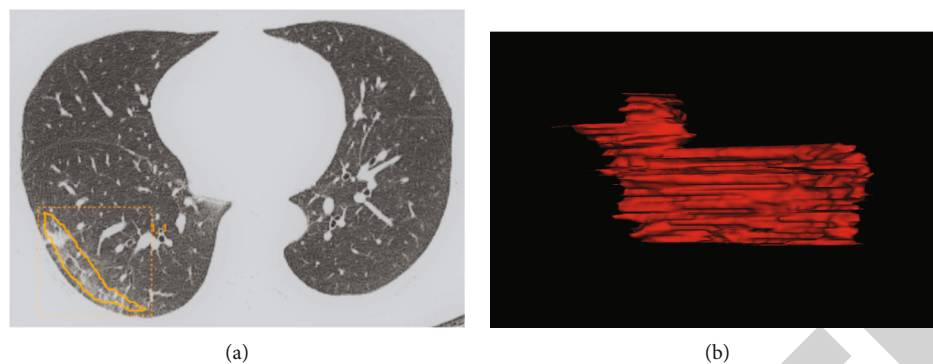
FIGURE 4: A case of confirmed COVID-19 of the resorption stage. A 63-year-old male presented with a 15-day history of fever and cough. (a). CT imaging revealed pure GGO with reticular distributed in the right lower lobe. The area of the lesions was delineated on the axial. (b) The reconstructed images.
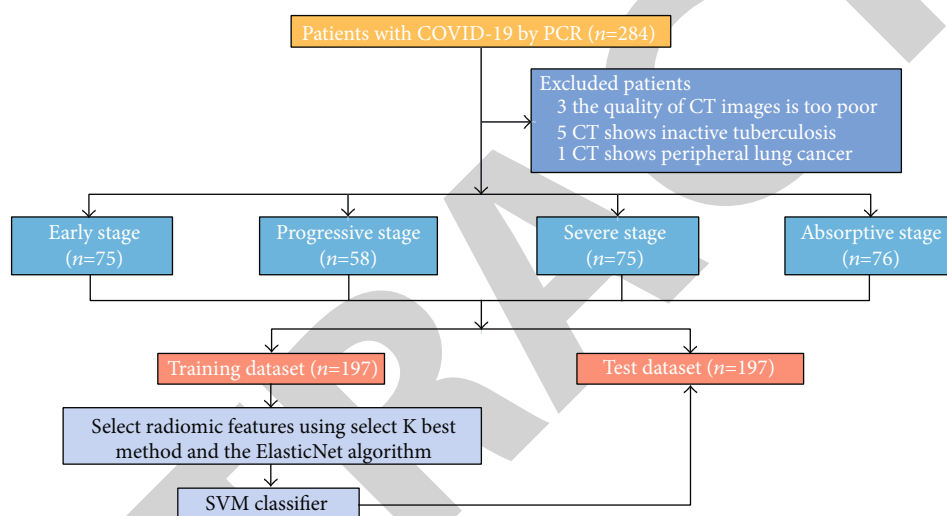
FIGURE 5: Flowchart through the study.

and provide rapid, accurate severity assessments for COVID-19 patients.

Studies have found that the development of COVID-19 pneumonia is usually related to the increase in the number and size of GGO lesions [9]. In the early stage, there will be multiple small plaque shadows and interstitial changes in the lungs. CT in the middle stage of the disease shows an increase in the number and size of GGO, and GGO gradually transforms into multifocal consolidation; about 10 days after the onset of symptoms, the consolidation range often reaches its maximum, and it is transformed into fibrosis in the late stage [10–12]. Therefore, chest CT findings tend to be used as one of clinical manifestations in the confirmation of the diagnosis of COVID-19 infection [4]. Many clinical studies have investigated the CT imaging signs related to COVID-19 infection such as GGO, GGO with lung consolidation, interlobular septal thickening, and pulmonary fibrosis for patients at different stages and severity [13–15].

According to the time of onset, clinical manifestations, lesion range, and CT manifestations, COVID-19 can be roughly divided into four stages: early stage, advanced stage, severe stage, and resorption stage (recovery stage) [4, 5]. In

this study, 284 patients were retrospectively graded as early stage with 75 cases, progressive stage with 58 cases, severe stage with 75 cases, and absorptive stage with 76 cases. Early-stage COVID-19 manifested as single or multiple nodules with mixed GGO as the main part, and the boundaries were blurred with a "halo sign," and some showed a "thickened blood vessel" sign. Compared with the early-stage CT findings, the lesion range of progressive-stage COVID-19 was further expanded, the density increased, and fusion or mass-like consolidation appeared. In severe cases, diffuse lesions of both lungs are often present. The CT image showed a large patchy or fusion-like consolidation with symmetrical distribution across both lungs, showing a "butterfly sign" or "upside-down butterfly sign" and even presenting with "white lung." The COVID-19 resorption stage (recovery stage) was manifested as the density of lesions decreased, and it is gradually completely absorbed, or GGO is completely resorbed, leaving a few stripes or small patchy consolidation signs, or consolidations are gradually replaced by GGO with stripes. Although chest CT has high sensitivity when identifying COVID-19 infection and evaluating its severity, the result mainly depends on the subjective

(a)

(b)

Coefficients in ElasticNet model

(c)
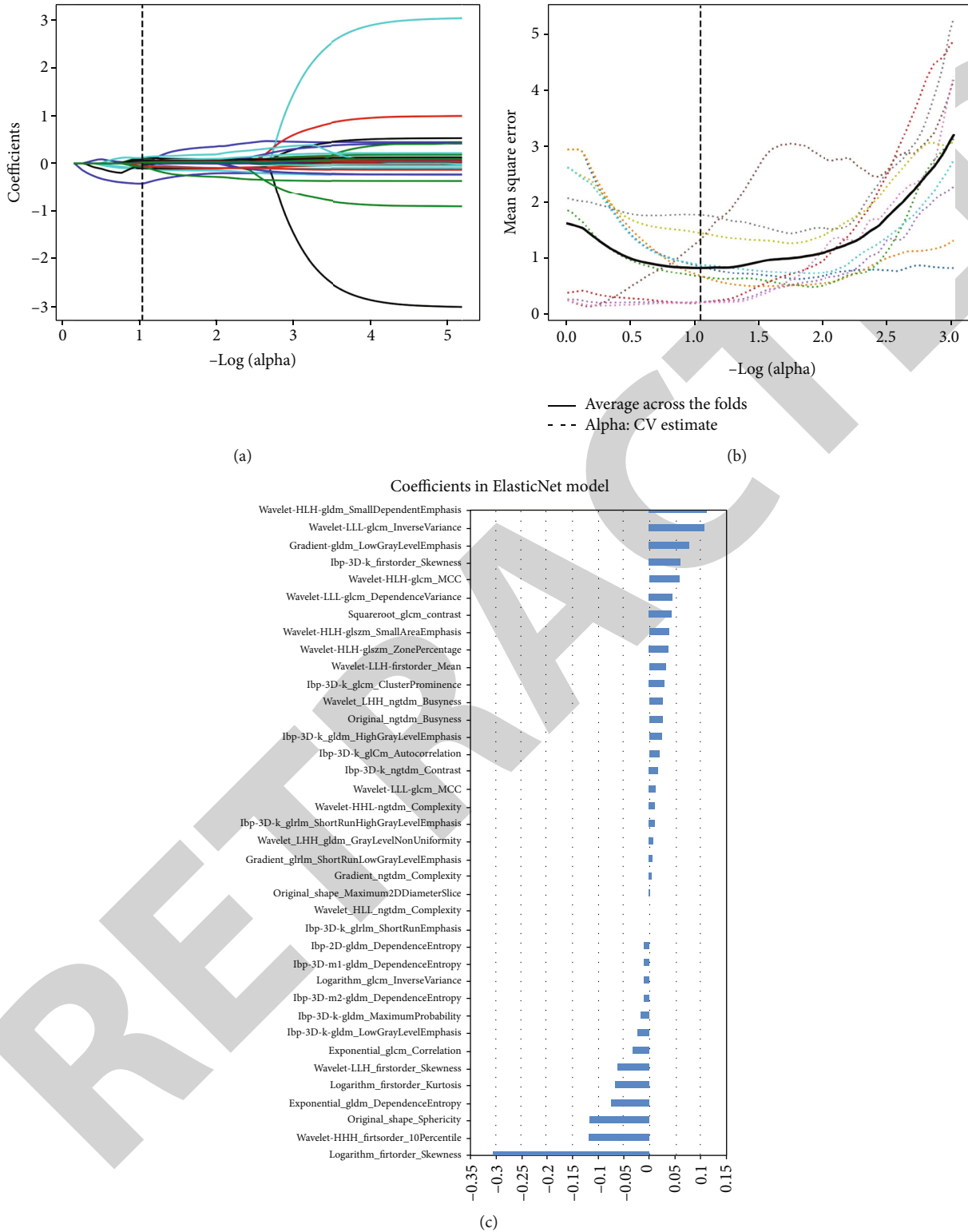
Figure 6: ElasticNet algorithm for feature selection. The first (a) shows coefficient profiles along the full path of possible values for radiomic features. The MSE path (b) indicates that the dotted vertical line was plotted at the value selected using 10-fold cross-validation in (a). The coefficients in the ElasticNet model (c) resulted in 38 features based on selected optimal values.

judgment of the radiologist(s) and the work is time-consuming [16, 17].

In this article, an ElasticNet radiomics model was exploited and investigated to evaluate the severity of COVID-19 patients. Ground-glass opacities and consolidation are the most relevant imaging features in COVID-19 pneumonia [17], which were identified by chest CT with high sensitivity. A radiomics model based on machine

Table 1: Description of the selected radiomic features and their associated feature types and filters.

Radiomic features	Associated_filters	Types
Logarithm_firstorder_Skewness	Logarithm	First order
Logarithm_firstorder_Kurtosis	Logarithm	First order
Llogarithm_glcm_InverseVariance	Logarithm	GLCM
Original_shape_Sphericity	Original	SHAPE
Exponential_gldm_DependenceEntropy	Exponential	GLDM
Gradient_gldm_LowGrayLevelEmphasis	Gradient	GLDM
Gradient_glrlm_ShortRunLowGrayLevelEmphasis	Gradient	GLRLM
Original_shape_Maximum2DDiameterSlice	Original	SHAPE
Exponential_glcm_Correlation	Exponential	GLCM
Wavelet-HLL_ngtdm_Complexity	Wavelet-HLL	NGTDM
Gradient_ngtdm_Complexity	Gradient	NGTDM
Wavelet-LHH_gldm_GrayLevelNonUniformity	Wavelet-LHH	GLDM
Squareroot_glcm_Contrast	Squareroot	GLCM
lbp-2D_gldm_DependenceEntropy	lbp-2D	GLDM
lbp-3D-m1_gldm_DependenceEntropy	lbp-3D-m1	GLDM
Original_ngtdm_Busyness	Original	NGTDM
lbp-3D-m2_gldm_DependenceEntropy	lbp-3D-m2	GLDM
lbp-3D-k_gldm_HighGrayLevelEmphasis	lbp-3D-k	GLDM
lbp-3D-k_gldm_LowGrayLevelEmphasis	lbp-3D-k	GLDM
lbp-3D-k_glcm_MaximumProbability	lbp-3D-k	GLCM
lbp-3D-k_glrlm_ShortRunEmphasis	lbp-3D-k	GLRLM
lbp-3D-k_glcm_Autocorrelation	lbp-3D-k	GLCM
lbp-3D-k_ngtdm_Contrast	lbp-3D-k	NGTDM
lbp-3D-k_glcm_ClusterProminence	lbp-3D-k	GLCM
Wavelet-LLL_glcm_InverseVariance	Wavelet-LLL	GLCM
lbp-3D-k_glrlm_ShortRunHighGrayLevelEmphasis	lbp-3D-k	GLRLM
Wavelet-LLL_glcm_MCC	Wavelet-LLL	GLCM
Wavelet-HLH_glszm_ZonePercentage	Wavelet-HLH	GLSZM
Wavelet-HLH_gldm_SmallDependenceEmphasis	Wavelet-HLH	GLDM
Wavelet-HLH_glcm_MCC	Wavelet-HLH	GLCM
Wavelet-HLH_glszm_SmallAreaEmphasis	Wavelet-HLH	GLSZM
Wavelet-LLH_firstorder_Skewness	Wavelet-LLH	First order
Wavelet-HHH_firstorder_10Percentile	Wavelet-HHH	First order
Wavelet-LLL_gldm_DependenceVariance	Wavelet-LLL	GLDM
lbp-3D-k_firstorder_Skewness	lbp-3D-k	First order
Wavelet-HHL_ngtdm_Complexity	Wavelet-HHL	NGTDM
Wavelet-LLH_firstorder_Mean	Wavelet-LLH	First order
Wavelet-LHH_ngtdm_Busyness	Wavelet-LHH	NGTDM

GLCM: grey-level cooccurrence matrix; GLRLM: grey-level run length matrix; GLSZM: grey-level size zone matrix; NGTDM: neighboring grey-tone difference matrix; GLDM: grey-level dependence matrix.

learning can detect minute changes in the VOIs which are difficult to see with the naked eye, let alone estimate the size thereof; thus, the radiological features hidden in GGO lesions are extracted and quantified: CT-based radiomics characteristics such as the degree and density of GGO can divide patients with COVID-19 pneumonia into different development stages [18, 19].

The radiomics model of COVID-19 studies based on CT images involves predominantly of diagnostic and prognostic value; a majority of the recently published studies focus on the diagnosis and differentiation of COVID-19 such as those using UNet for automated detection of GGO areas [20, 21] and differentiation of COVID-19 pneumonia from other viral pneumonia using radiomics or deep-learning methods [22–24]. However, to the best of our knowledge, there have been few studies on the validity of CT for assisting decision-making in the management of COVID-19 with regard to stratification of disease severity and prediction of
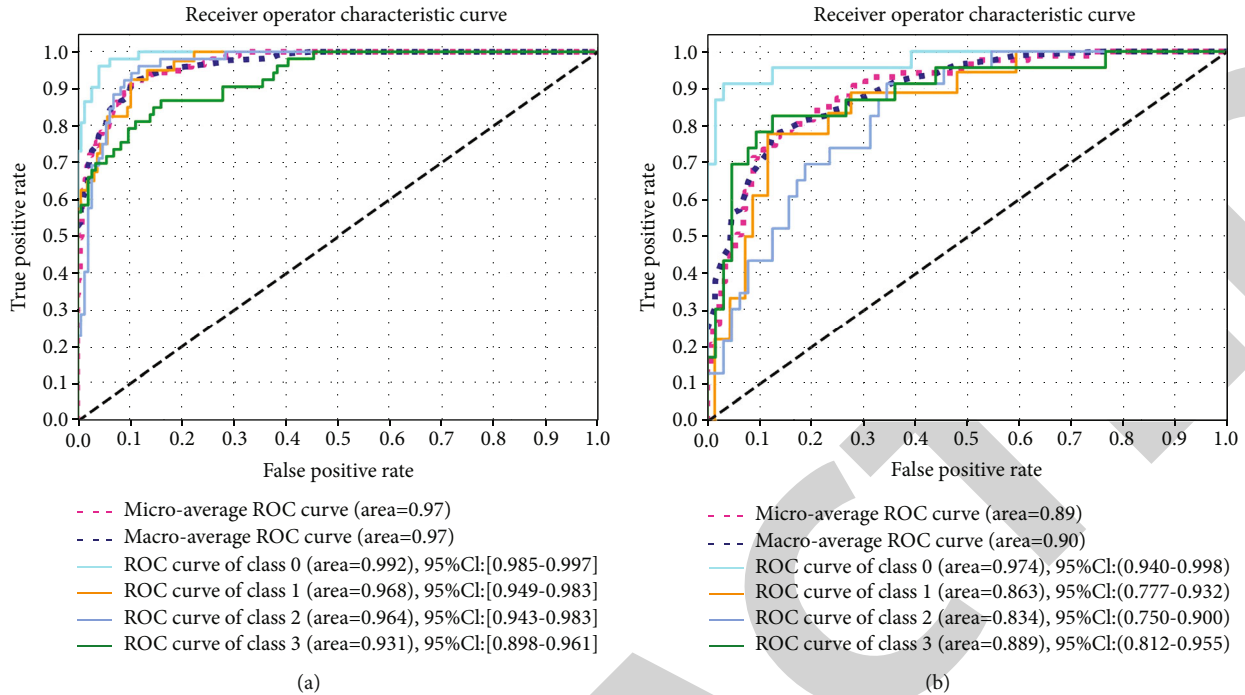
Figure 7: ROC curves of the SVM classifier on the training set (a) and test set (b).

clinical outcomes [18, 25]. Additionally, few studies have focused on the use of a radiomics model to assess the severity of COVID-19: one study classifying two types of COVID-19 severity (nonsevere and severe) instead of four types was undertaken to assess the relevance of CT image features [26]. Research by Cai et al. stratifies the severity into moderate, severe, and critical groups with AUCs greater than 0.925 [20]. In the present study, we collected more CT image data from COVID-19 patients; all patients were divided into four developmental stages: early stage, advanced stage, severe stage, and prognosis stage according to the essence of lung GGO lesions; then, we stratified the severity of the disease by CT quantification.

Using a select K-best method, 38 radiological characteristics were nominated from 1688 radiomic features in our study, which reflected intrinsic information such as lesion intensity and textural features that cannot otherwise be detected by radiologists [27]. For example, first-order features mainly reflect the internal texture of lesions; wavelet features mainly reflect the change of time domain and frequency domain information within the lesion [28]. Among the 38 features, six first-order features, 30 texture features, and two shape features comprised the optimal feature set, indicating different feature dimensions to be considered during the staging of COVID-19. The five most relevant features are logarithm_first-order_Skewness, wavelet-HHH_first-order_10Percentile, original_shape_Sphericity, wavelet-HLH_gldm_SmallDependenceEmphasis, and wavelet-LLL_glcm_Inverse Variance, four of which are high-order features transformed by different filters. Logarithm_first-order_Skewness measured the asymmetry of the distribution of values about the mean value, wavelet-HHH_first-order_10Percentile denoted the 10th percentile of the image, origi-

nal_shape_Sphericity equated the roundness of the shape of the VOI to a sphere, and wavelet-HLH_gldm_SmallDependenceEmphasis assessed the distribution of small dependencies. In our research, four types of severity groups of COVID-19 were distinguished by SVM classifier; then, the ROC curve of each group was plotted. Finally, the ElasticNet radiomics model shows favorable predictive accuracy, achieving an average AUC performance of 0.97 on the training dataset and one of 0.90 on the test dataset, indicating the strong efficacy of the proposed CT-based radiomics model in assessing the severity of COVID-19 disease.

5. Conclusions

A CT-based radiomics model was provided that can be used to assess the severity of COVID-19, which can help radiologists undertake rapid diagnosis, especially useful when the medical system is overloaded.

6. Limitations

Our research has several limitations. First of all, this was a retrospective study; we divided COVID-19 patients into four severity levels based on the CT imaging manifestations of COVID-19 patients, such as the degree of GGO lesions, without combining specific clinical symptoms and other factors: some studies have shown that the CT manifestations of COVID-19 may vary with age; elderly patients predominantly present with combined features such as opacity, while young patients present predominantly GGO [9], which may lead to inaccurate demarcation and introduce selection bias. Besides, our research lacks multicenter verification: use of

only a single device and model may limit the popularization and application of the results.

Data Availability

Conflicts of Interest

The authors declare that there are no conflicts of interest regarding the publication of this paper.

Acknowledgments

References

[1] https://www.who.int/emergencies/diseases/novel-coronavirus-2019.

[2] P. Lambin, E. Rios-Velazquez, R. Leijenaar et al., "Radiomics: extracting more information from medical images using advanced feature analysis," *European Journal of Cancer*, vol. 48, no. 4, pp. 441–446, 2012.

[3] S. S. Yip and H. J. Aerts, "Applications and limitations of radiomics," *Physics in Medicine and Biology*, vol. 61, no. 13, pp. R150–R166, 2016.

[4] http://www.nhc.gov.cn/xcs/zhengcwj/202003/46c9294a7dfe4cef80dc7f5912eb1989.shtml.

[5] H. J. L. S. Li, S. Y. Liu, H. B. Xu, and J. L. Cheng, "Guideline for medical imaging in auxiliary diagnosis of coronavirus disease 2019," *Chinese Journal of Medical Imaging Technology*, vol. 36, no. 3, pp. 321–331, 2020.

[6] G. Herpe, M. Lederlin, M. Naudin et al., "Efficacy of chest CT for COVID-19 pneumonia diagnosis in France," *Radiology*, vol. 298, no. 2, pp. E81–81E87, 2021.

[7] Y. Xiong, D. Sun, Y. Liu et al., "Clinical and high-resolution CT features of the COVID-19 Infection," *Investigative Radiology*, vol. 55, no. 6, pp. 332–339, 2020.

[8] K. C. Liu, P. Xu, W. F. Lv et al., "Differential diagnosis of coronavirus disease 2019 from community-acquired-pneumonia by computed tomography scan and follow-up," *Infectious diseases of poverty*, vol. 9, no. 1, 2020.

[9] S. Salehi, A. Abedi, S. Balakrishnan, and A. Gholamrezanezhad, "Coronavirus disease 2019 (COVID-19): a systematic review of imaging findings in 919 patients," *AJR. American Journal of Roentgenology*, vol. 215, no. 1, pp. 87–93, 2020.

[10] S. Zhou, Y. Wang, T. Zhu, and L. Xia, "CT features of coronavirus disease 2019 (COVID-19) pneumonia in 62 patients in Wuhan, China," *AJR. American Journal of Roentgenology*, vol. 214, no. 6, pp. 1287–1294, 2020.

[11] X. Ding, J. Xu, J. Zhou, and Q. Long, "Chest CT findings of COVID-19 pneumonia by duration of symptoms," *European Journal of Radiology*, vol. 127, p. 109009, 2020.

[12] S. Bhandari, G. Rankawat, M. Bagarhatta et al., "Clinico-radiological evaluation and correlation of CT chest images with Progress of disease in COVID-19 patients," *The Journal of the Association of Physicians of India*, vol. 68, no. 7, pp. 34–42, 2020.

[13] M. Chung, A. Bernheim, X. Mei et al., "CT imaging features of 2019 novel coronavirus (2019-nCoV)," *Radiology*, vol. 295, no. 1, pp. 202–207, 2020.

[14] H. Shi, X. Han, N. Jiang et al., "Radiological findings from 81 patients with COVID-19 pneumonia in Wuhan, China: a descriptive study," *The Lancet. Infectious diseases*, vol. 20, no. 4, pp. 425–434, 2020.

[15] Y. Zhu, Z. H. Gao, Y. L. Liu et al., "Clinical and CT imaging features of 2019 novel coronavirus disease (COVID-19)," *The Journal of Infection*, vol. 81, no. 1, pp. 147–178, 2020.

[16] T. Ai, Z. Yang, H. Hou et al., "Correlation of chest CT and RT-PCR testing for coronavirus disease 2019 (COVID-19) in China: a report of 1014 cases," *Radiology*, vol. 296, no. 2, pp. E32–32E40, 2020.

[17] Z. Cheng, L. Qin, Q. Cao et al., "Quantitative computed tomography of the coronavirus disease 2019 (COVID-19) pneumonia," *Radiology of Infectious Diseases*, vol. 7, no. 2, pp. 55–61, 2020.

[18] Z. Xie, H. Sun, J. Wang et al., "A novel CT-based radiomics in the distinction of severity of coronavirus disease 2019 (COVID-19) pneumonia," *BMC infectious diseases*, vol. 21, no. 1, 2021.

[19] J. Qiu, S. Peng, J. Yin et al., "A radiomics signature to quantitatively analyze COVID-19-infected pulmonary lesions," *Interdisciplinary sciences, computational life sciences*, vol. 13, no. 1, pp. 61–72, 2021.

[20] W. Cai, T. Liu, X. Xue et al., "CT quantification and machine-learning models for assessment of disease severity and prognosis of COVID-19 patients," *Academic Radiology*, vol. 27, no. 12, pp. 1665–1678, 2020.

[21] J. Chen, L. Wu, J. Zhang et al., "Deep learning-based model for detecting 2019 novel coronavirus pneumonia on high-resolution computed tomography," *Scientific reports*, vol. 10, no. 1, 2020.

[22] P. Silva, E. Luz, G. Silva et al., "COVID-19 detection in CT images with deep learning: a voting-based scheme and cross-datasets analysis," *Informatics in medicine unlocked*, vol. 20, p. 100427, 2020.

[23] H. Panwar, P. K. Gupta, M. K. Siddiqui, R. Morales-Menendez, P. Bhardwaj, and V. Singh, "A deep learning and grad-CAM based color visualization approach for fast detection of COVID-19 cases using chest X-ray and CT-scan images," *Chaos, Solitons & Fractals*, vol. 140, p. 110190, 2020.

[24] M. Turkoglu, "COVID-19 detection system using chest CT images and multiple kernels-extreme learning machine based on deep neural network," *IRBM*, vol. 42, no. 4, pp. 207–214, 2021.

[25] G. Wu, P. Yang, Y. Xie et al., "Development of a clinical decision support system for severity risk prediction and triage of COVID-19 patients at hospital admission: an international Multicenter study," *The European respiratory journal*, vol. 56, no. 2, p. 2001104, 2020.

[26] Z. Tang, W. Zhao, X. Xie et al., "Severity assessment of COVID-19 using CT image features and laboratory indices," *Physics in medicine and biology*, vol. 66, no. 3, article 035015, 2021.

Review Article

Design and Optimization of the Circulatory Cell-Driven Drug Delivery Platform

Pengyu Gao ᴵᴰ, **Dan Zou** ᴵᴰ, **Ansha Zhao** ᴵᴰ, **and Ping Yang** ᴵᴰ

*Key Laboratory for Advanced Technologies of Materials, Ministry of Education, School of Material Science and Engineering,
Southwest Jiaotong University, Chengdu 610031, China*

Correspondence should be addressed to Ping Yang; yangping@swjtu.edu.cn

Achievement of high targeting efficiency for a drug delivery system remains a challenge of tumor diagnoses and nonsurgery therapies. Although nanoparticle-based drug delivery systems have made great progress in extending circulation time, improving durability, and controlling drug release, the targeting efficiency remains low. And the development is limited to reducing side effects since overall survival rates are mostly unchanged. Therefore, great efforts have been made to explore cell-driven drug delivery systems in the tumor area. Cells, particularly those in the blood circulatory system, meet most of the demands that the nanoparticle-based delivery systems do not. These cells possess extended circulation times and innate chemomigration ability and can activate an immune response that exerts therapeutic effects. However, new challenges have emerged, such as payloads, cell function change, cargo leakage, and in situ release. Generally, employing cells from the blood circulatory system as cargo carriers has achieved great benefits and paved the way for tumor diagnosis and therapy. This review specifically covers (a) the properties of red blood cells, monocytes, macrophages, neutrophils, natural killer cells, T lymphocytes, and mesenchymal stem cells; (b) the loading strategies to balance cargo amounts and cell function balance; (c) the cascade strategies to improve cell-driven targeting delivery efficiency; and (d) the features and applications of cell membranes, artificial cells, and extracellular vesicles in cancer treatment.

1. Introduction

According to the World Health Organization (WHO) report in 2018, cancer remains one of the top 10 global causes of death [1]. Because tumor cells lead to immortality, migration, and loss of contact inhibition, most patients only benefit from combined treatments, such as surgery, chemotherapy, radiotherapy, and immune therapy. In terms of prevention of the recurrence and metastasis of unresectable tumors, cancer treatment still faces many challenges, especially with respect to nonsurgery therapies and diagnoses. Currently, ensuring the delivery of sufficient cargos to lesions precisely and effectively is an important issue for nonsurgery therapies and diagnoses [2, 3].

Earlier, a nanoparticle-based drug delivery system (DDS) was developed, which improved the solubility of chemotherapeutics and lessened their toxicity to normal tissues. From intravenous injection to tumor sites, cargo-loaded nanopar-

ticles (NPs) go through a CAPIR cascade: Circulation, Accumulation, Penetration, Internalization, and Drug Release [4]. In the blood circulatory system, naked NPs are vulnerable to the reticuloendothelial system (RES). Recently, they have also been found to be hitchhiked by circulating cells before being phagocytosed by RES tissues [5]. Modifying NPs with stealth molecules, such as polyethylene glycol (PEG) [6] and polyglycerol (PG) [7], has been reported to reduce the clearance risk and overcome some pharmacokinetic-related issues. During the accumulation and penetration to stages, it has been recognized that 10–1000 nm NPs can make full use of enhanced permeability and retention (EPR) effects via intercellular extravasation to accumulate at and penetrate tumor tissues [3]. When NPs are coupled with targeting molecules (e.g., Fe_3O_4, short peptides, and antibodies), then the passive delivery system can be transformed into an active system [3, 8]. However, a recent study revealed that approximately 97% of NPs themselves accumulate in an active

transcellular manner through endothelial cells (ECs) [9], which advances our understanding of the NP accumulation mechanism in tumors to a new level. When NPs arrive at the lesion, their neutral surface charge, particle size below 100 nm, and nonspherical shape can further increase the penetration and internalization rates [10]. Additionally, NPs have made it possible to maintain the drug at a certain concentration in the tumor tissues, via self-diffusion, degradation, or a stimulus response, such as a response to pH, an enzyme, light, radiation, a magnetic field, or ultrasound [11]. Compared to free cargos, an NP-based DDS protects them from the phagocyte system; has an enhanced *in situ* cargo concentration, especially for hydrophobic systems; has facilitated specific delivery for one/multiple cargos; and has release control. The NP-based DDS has improved the evolution of nonsurgery therapies and diagnosis strategies.

NPs exhibit the substantial potential to deliver drugs, yet outstanding performance is limited to reducing side effects of anticancer drugs and not enhancing therapeutic efficacies [4]. The basic reason for this is that the NP-based DDS has long suffered from rapid clearance from the RES and a low targeting delivery efficiency of 1% [10]. Low targetability partially results from interstitial fluid pressure, which is 10–40 times higher in tumor cells than in normal cells [10], and from heterogeneous EPR, wherein the EPR mechanism has failed in tumors, such as lymphoma subtypes [12]. NPs smaller than 20 nm penetrate deeper, but this size is in a perfect clearance range for the RES [4]. The blood-brain barrier (BBB) is another obstacle for brain tumors because NPs scarcely cross it [13]. Furthermore, in the BBB, shear stress also impedes the distribution of NPs. NPs are taken up in a flow speed-dependent manner; i.e., the faster the flow, the lower the uptake. Various shear stresses in tumor vasculature may result in a heterogeneous NP distribution [14]. Because controlled release and biocompatibility are also required, an NP-based DDS faces a crucial challenge to be multifunctional [8] simultaneously.

In the past twenty years, the cell-driven DDS has gained much attention as an alternative approach. Additionally, an increasing number of studies have shown that a cell-driven DDS can address the major concerns of NP-based systems [15, 16]. Endogenous cells have a long circulation time with low toxicity risk and are not removed by the RES or kidneys [17]. Immune and stem cells can chemomigrate and transverse blood barriers, including the BBB; thus, they can penetrate the deep tumor matrix [18] instead of EPR-dependent intracellular extravasation [12]. These results have provided a new DDS and shed light on improving circulating and targeting delivery efficiency *in vivo* for cancer diagnosis and therapy. This article will focus on (a) the properties of circulatory cells, mainly red blood cells (RBCs), leukocytes, and mesenchymal stem cells (MSCs); (b) the loading strategies for balancing payload amounts and cell functions; (c) the cascade strategies for improving cell-driven targeting delivery efficiency; and (d) the cell membrane and small extracellular vesicles (EVs) as drug carriers for targeting delivery.

2. Utilizable Properties of Circulatory Cells

A tumor is a neotissue, which obtains nutrients and oxygen via RBC-involved angiogenesis. Tumors are also an inflammatory microenvironment, which is flooded with diverse cells, including MSCs [19] and different leukocytes (monocytes (MOs) [20], macrophages (MAs), neutrophils (NEs), natural killer cells (NKs), and T and B lymphocytes [21]). A large number of RBCs, leukocytes, and MSCs exist in the blood; it is a good source for drug delivery carriers, as listed in Table 1 [15, 16, 19]. Moreover, these cells circulate through the body without any immune or clearance risk that the NPs suffer, and they can easily infiltrate blood vessel barriers. Because of the innate features and their involvement in tumorigenesis, they are regarded as an ideal vehicle for drug delivery to realize the CAPIR cascade, as is shown in Figure 1(a).

2.1. Red Blood Cells (RBCs). RBCs, also called erythrocytes, are the richest blood cell group. There are approximately 3.5–5 million RBCs per μL, which have the longest lifespan of approximately 120 d. They also possess a high surface-to-volume ratio, and CD47 is expressed on the surface to protect cells from being taken up by immune cells. RBCs contain a large internal cavity without nuclei or organelles; thus, there are no normal endocytosis or exocytosis functions [22, 23]. RBCs contain approximately 270 million oxyhemoglobin molecules per cell, supporting their fundamental oxygen transportation function [24]. These features suggest that RBCs could be helpful as a carrier for drug delivery because they are easy to obtain, have a long circulation time with good biocompatibility and low clearance risk, are convenient for necessary modification, and have no possibility of tumorigenicity and a low drug leakage risk. Additionally, RBCs are oxygen-rich and can increase the productivity of toxic reactive oxygen species (ROS) for photodynamic therapy (PDT). This process enhances the PDT effect under a hypoxic tumor microenvironment and reduces PDT-caused O_2 deficiency that boosts tumor growth [24].

2.2. Leukocytes. Leukocytes, formally known as immune cells, fight against diseases. Approximately 4000–10000 cells exist per μL of blood, with at least a 24 h lifespan. When foreign substances, such as bacteria, enter the body, leukocytes respond to inflammatory signals and intrinsically chemomigrate back and forth through the blood vessel barriers to the diseased tissues. Leukocytes are part of the RES and can mobilize additional leukocytes to phagocytize particles or cross blood barriers. The ability of MAs to engulf aurum (Au) was increased 2.4-fold relative to that of nonphagocytes [25]. The unique engulfment, chemomigration, and immune activation features made them the perfect candidate as a drug carrier for target delivery.

2.2.1. Monocytes (MOs)/Macrophages (MAs). MOs are the largest blood cells and account for 2–8% of the leukocyte group. As a precursor, MOs are transformed into MAs once they are in tissues. They have versatile receptors on the cell membrane and react to foreign substances through nonspecific antigen recognition. Compared with other leukocytes,

TABLE 1: Properties of red blood cells, mesenchymal stem cells, and leukocytes.

	RBC	MSC	Leukocyte					
					0.0004-0.001			
			Neutrophil	Eosinophil	Basophil	Monocyte	Lymphocyte	
							25-35%	
Amount (million/μL)	3.5-5	To be determined						
			50-70%	1-3%	0.4-1%	2-8%	T cell	B cell
							75%	10-15%
Diameter (μm)	7-8.5	30-40	10-12	12-15	12-15	20-30	6-12	6-12
Lifespan (days)	120	1-2	3-4	8-12	12-15	1-5	4-35	>30

Circulum

Accumulation

Internalization

Drug release

Penetration

To be there
To be free

5-step *CAPIR* cascade $Q = Q_c \times Q_A Q_P \times Q_I \times Q_R$

(a)

Monocyte recruitment

Monocytes

Tumor cells

CCL2
M-CSF
VEGF

IL-3
M-CSF

Differentiation

CSFs
IL-4
IL-10
TGFβ

M2-polarization

Tumor promotion

M-CSF
VEGF
PDGF
FGF
MMPs
TGFβ
ECM proteins

Vessel

TAM

TNFα
Il-1β
MMPs
Proteases

Down-regulation of adaptive immunity

Naive T cell anergy

CCL18

Treg stimulation and recruitment

IL-10, CCL17
TGFβ, CCL-22

Th1 inhibition

CCL17
CCL22 *Th2 recruitment*

Metastasis

(b)

FIGURE 1: (a) Scheme of the CAPIR cascade of a nanomedicine to deliver a free drug into cancer cells. The overall efficiency, Q, is the product of the efficiencies of five steps. Reproduced with permission [4]. Copyright 2017. John Wiley and Sons. (b) Overview of molecules that can recruit monocytes/macrophages to tumor sites and turn into tumor-associated macrophages. Reproduced with permission [26]. Copyright 2009. John Wiley and Sons.

MOs/MAs responded to inflamed tissues rapidly and have the strongest ability for phagocytosis. They can be recruited to sites via several tumor-related factors: (a) cancer-related cytokines (e.g., CSF-1, VEGF, and PDGF); (b) chemokines (e.g., CCL-2/5/7/8/12); (c) fibrinogen; and (d) fibronectin and other factors produced during extracellular matrix (ECM) cleavage (in Figure 1(b)) [26]. After intravenous injection, it took MOs/MAs 6–12 h to arrive at inflamed

tissues [27, 28] and in the brain [18]. Owing to chemohoming properties, MOs/MAs can penetrate the deep tumor matrix. Up to 70–80% of MAs were found in the tumor mass, part in the antitumor phenotype M1 and part in the protumor phenotype M2 [29, 30]. Having the largest size, a strong phagocytosis function, homing and penetration ability, and the possibility of the M1 antitumor phenotype make MOs/MAs beneficial for targeted drug delivery.

2.2.2. Lymphocytes.

Lymphocytes make up 25–35% of the leukocytes and are the smallest cells. They play an essential role in the immune response. Lymphocytes mainly include B, NK, dendritic cells, and T cells, in which T cells account for 75% of the total and work in the lymphatic fluid. Differing from the MOs/MAs, those lymphocytes activate an immune response via specific antigen recognition. Then, the activated cells present antibodies on the surface to specifically track and kill tumor cells through a ligand-receptor interaction [31]. EPR almost failed to function in some tumors, such as lymphomas, wherein the detected dose of either free drugs or NPs was 10 times lower than that in the blood, spleen, and liver. However, the activated polyclonal T cells can be successfully trafficked by tumor receptors, such as CD62L and CCR7, to the lymph node [12]. T cells were also recruited by CXCR4 and integrins $\alpha 4$, $\beta 1$, and $\beta 2$ to bone marrow and the spleen, respectively [12].

Similarly, NK cells can be chemoattracted by CXCL9 [17] and specifically recognize IL-2 on tumor cells [32]. Similar to MAs, T cells are another common cell type in tumor tissues [21], and it has been reported that T cells take 20–40 h to migrate to lymphoid organs in mice [12]. Based on specific recognition of tumor antigens, lymphocytes are normally used to activate the immune response of the patients to reduce the tumor burden. Moreover, because they patrol lymph nodes, lymphocytes carrying chemotherapeutics can simultaneously serve in both immunotherapy and chemotherapy to exert a cytotoxic effect on tumor cells.

2.2.3. Neutrophils (NEs).

NEs are the largest leukocyte cell group, consisting of approximately 50–70%, and feature many internal NPs ($0.2–0.4\,\mu m$). Most particles are enzyme-rich lysosomes that are correlated with phagocytosis and digestive functions. NEs fight against foreign substances either through phagocytosis or neutrophil extracellular traps (NETs) [33]. Along with MOs/MAs, NEs possess strong innate chemotaxis with two kinds of chemokines: (a) collagen, fibrin fragments, products of activated complement, and cytokine and (b) microbial polypeptide with N-formylmethionine residue [34]. After interacting with chemokines, receptors, such as PSGL-1, CD44, and L-selectin, are highly expressed on the NE membranes [35]. Under inflammatory stimuli (IL-8, TNF-α, IL-1, and IL-17), the activated ECs overexpress E-selectin and P-selectin ligands to slow the NE rolling speed. The integrin superfamily (ICAM and VCAM) on the EC membrane further enhances the adhesion by binding with LFA-1 ($\alpha L\beta 2$) and Mac-1 ($\alpha M\beta 2$) on the NE surface [35, 36]. Additionally, Dietmar V is a shared and unique adhesion receptor related to transendothelial migration among different leukocytes [37]. A study showed that it took NEs 1 h to migrate to the stomach [38], and approximately 1.2–4.4% of NEs were in the tumor mass [39]. Moreover, an *in vitro* study showed that NP-loaded NEs could penetrate 80% of tumor tissues (Φ $300\,\mu m$), yet NPs were only observed on the periphery [36]. The features, including a rich source, strong inherent phagocytosis, homing and penetration ability, and unique NETs formed under inflammatory conditions, make NEs a powerful carrier for targeting drug delivery [34].

2.3. Mesenchymal Stem Cells (MSCs).

MSCs are larger than the largest leukocytes and have a lifespan of approximately 1–2 d [19]. As adult stem cells, MSCs exhibit self-reproduction and multidifferentiation capabilities. They possess low immune rejection because of the nonspecific antigens on the cell membrane. MSCs also have a rich source, including blood, bone marrow, umbilical cord tissue, placenta, adipose tissue, and skin tissue. Identical to leukocytes, MSCs also have innate homing and migration ability to inflamed and tumor tissues. Tumor growth factors (e.g., EGF, PDGF-α, PDGF-β, HGF, and GDF-15), chemotactic factors (e.g., CXCL9 and CCL-25), matrix metalloproteinases (MMP1, MMP3, and MMP9), and inflammatory cytokines (IL-1β, IL-2, and IL-7) were discovered in liver tumors to chemoattract MSCs [19]. Additionally, the time MSCs circulate in the blood was reduced under diseased conditions, being 30 h in healthy mice, 24 h in mice with subcutaneous tumors, 18 h for orthotopically transplanted liver tumors, and 12 h in those with metastatic lung tumors [19]. However, an *in vitro* study confirmed that the migration ability of MSCs to breast cancer cells was 9 times higher than that of noncancerous cells [40]. Therefore, MSCs can actively and effectively track tumor tissues. In addition to the largest size, differentiation ability, low immunogenicity, rich sources, and chemomigration, MSCs additionally recruit and activate immune cells to tumor tissues [41]. Generally, MSCs show great potential as a carrier for targeting drug delivery.

3. Loading Strategies for Cargo Amounts and Cell Function Balance

Circulatory cells have been deployed to load varied cargos, including chemo/immunotherapeutic medicine (paclitaxel (PTX) [36], doxorubicin (Dox) [38], TRAIL [42], and siRNA [43]), radiotherapeutic agents (AuNRs [44], carbon nanotubes [45], ZnF16Pc [24], and Ce6 [46]), and diagnosis agents (fluorescent probe [47], ICG [48], and quantum dots [40]). The most commonly used loading methods are backpack and encapsulation. MOs were even reported to take an agent with a diameter of $7\,\mu m$ on the surface [49] and particles of $1\,\mu m$ inside [44] to cross the blood barrier that cargos alone cannot achieve. However, unlike inanimate NPs, cells respond to internal and external environments. Inappropriate loading approaches and cargo amounts may alter anticipated behaviors. Therefore, it is critical to balance the pros and cons on the premise of maintaining necessary cell functions.

Electrostatic interaction

(a)

Ligand-receptor interaction

Silica nanorattle · Doxorubicin CD90/CD73 Antibody

(b)

Covalent conjugation

Biotin-avidin interaction

Biotin Neutravidin

(c)

(d)
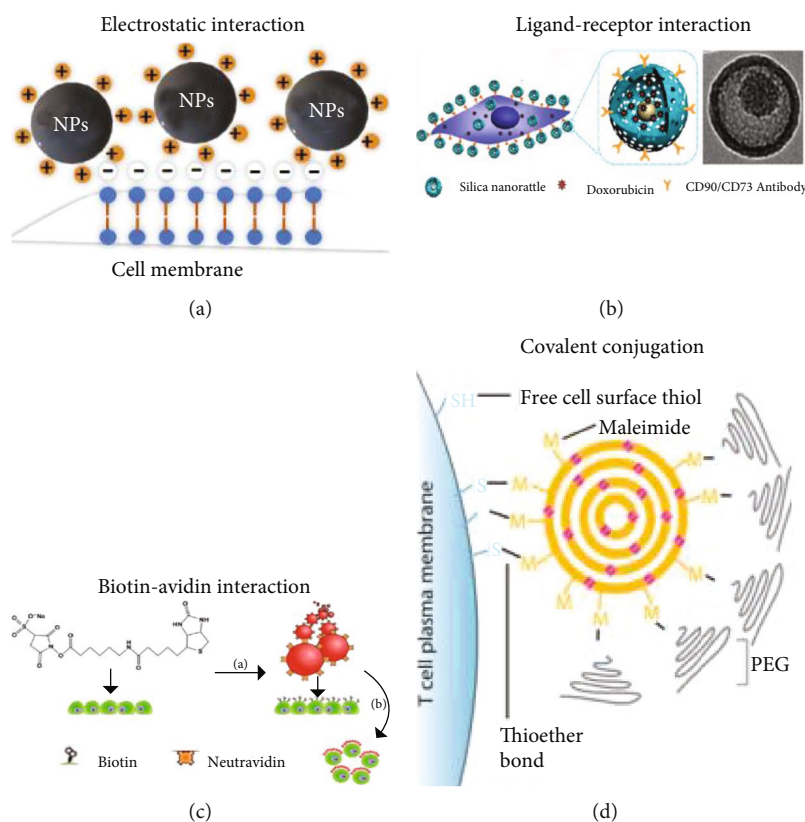
FIGURE 2: (a) Scheme of NPs conjugated with cell membranes via electrostatic interaction. (b) Dox was bound on the MSC membranes via the CD90/CD73 antibody-ligand interaction. Reproduced with permission [52]. Copyright 2011. American Chemical Society. (c) FluoSpheres (red) modified by NeutrAvidin (orange) to bind to biotinylated MSC membranes. Reproduced with permission [58]. Copyright 2010. American Chemical Society. (d) SN-38 NPs were anchored on T cells via a thiol group expressed on the cell membrane. Reproduced with permission [12]. Copyright 2015. American Association for the Advancement of Science.

3.1. Backpack Approach.

The cell membrane, 7–8 nm thick, consists of a phospholipid bilayer as the basic skeleton, interweaved with proteins and glycolipids. The protein residues and oligo/polysaccharide chains on the membrane surface provide multiple possibilities to backpack cargos [50].

The backpack approach is simple, and cell preparation is not required. It is suitable for cells having special surface properties, such as releasing cargos via redox change [43, 51]; potential for *in vivo* cell binding; and easy regulation of the manner of cargo release. However, this approach has risks of detachment from the membrane, an alteration of membrane-related functions, or internalization by host cells.

3.1.1. How to Conjugate Cargos on Membranes with Low Cell Function Impacts?

There are four cargo backpack methods. As shown in Figure 2, these include electrostatic/hydrophobic interactions [51], ligand-receptor binding via receptors on cell membranes [52], biotin-avidin binding via biotinylated cell membranes [53], and covalent conjugation via chemical groups, such as thiols or amines, on the cell membrane [54], wherein the biotin-avidin and covalent conjugation are considered the strongest binding and have specific ligand-receptor recognition that has the potential for *in vivo* hitchhiking use [55–57].

The cell membrane is essential for normal function, especially for the receptor-mediated signal pathways. Cargos

attached to the cell membrane may influence cell behaviors, such as cell adhesion, migration, and even internal signal transduction [18]. Backpack place, cargo size, and loading amounts are important in this process. NPs attached to the main body exhibit a weaker impact on cell migration and reorganization than protrusion [58]. Additionally, NPs of 300 nm less than 100 ± 20 per cell did not substantially affect T cell function [54]. Likewise, using 5% of the cell membrane for Dox packing was acceptable; however, this means loaded drugs are $1.0 \mu g$ per million cells [18]. Current free drug amounts of Dox [18], PTX [38], SN-38 [12], curcumin, and aPD1 [56] had a range of 1–3 mg per kg in animal tests and still showed limited therapeutic effects. Shp1 was demanded less, at approximately $76.5 \mu g$ per mouse [59]. However, the cell amount used for clinical therapy was only approximately 1–10 million, although the recommended effective clinical dose is 4.58–11.92 mg per kg (Abraxane dose, calculated based on 60 kg, 175 cm patients) [60]. Rather than a burden, the cargo can therefore also be exploited to enhance rheotaxis. Gao et al. attempted to improve photosensitizer Ce6 backpack concentration and attain higher than $6 \mu g \, mL^{-1}$, which caused RBC hemolysis within 48 h [46]. However, Tang et al. adopted another method to increase the amount without impacting cell functions. A negative charge surface was modified into a positive one and conjugated with anti-CD45 and IL-15Sa. The

surface binding amounts were increased approximately 4-fold to 7.68 μg per million cells [51].

Considering the necessary expected cell functions, the cargo density on the surface is a potentially involved factor, limiting the backpack amounts as were the NP properties [61]. Extra cargo modifications could weaken the impact on cargo conjugation and achieve an expected dose, such as receptors for recognition and cytokine loading for biological stimulation.

3.1.2. How to Avoid Internalization?

Except for RBCs, both leukocytes and MSCs exhibit phagocytosis, which may threaten the backpack methods because cargos could be engulfed by carriers themselves [51]. To retain them on the cell membranes, factors related to the internalization process must be taken into account.

An early work by Jiang et al. indicated that internalization could be initiated by cell surface receptor-cytokine interactions [62], which Park et al. found was consistent on polystyrene sphere (PS). Compared with fibronectin-uncoated PS, the biocoated group increased internalization amounts by 3–5-fold [44]. Additionally, Li et al. modified NPs with the anti-CD73/90 antibody and found the loading amounts associated with MSCs increased 22% more than those of naked NPs [52]. Instead of a saturation-caused surface backpack, this may result from anti-CD73/90-enhanced internalization. However, receptor-mediated internalization does not necessarily mean initiation. Several receptors on T cell surfaces were reported to trigger the internalization process, yet the CD45a leukocyte common antigen on the cell membrane slowed the process. NPs modified with the anti-CD45 antibody could anchor on the T cell membrane for 6 h to several days to avoid internalization [51]. However, this differed for MAs because CD45 was internalized along with NPs [63].

Putting the receptor effect aside, the internalization process was also regulated by particle size. NPs of approximately 2–10 nm and 70–100 nm had a weaker initiation effect than those of approximately 25–50 nm on the process of receptor-mediated internalization of cancer cells [62]. Similarly, compared to 100–200 nm NPs, 50–100 and 200–300 nm NPs, respectively, had 1.56- and 2-fold lower uptake rates by MAs [64]. Both results exhibited a parabola tendency with a peak in the middle. This might be the optimal internalization size range, but it varies with cell lines because when the internalization process is slower than NP clustering on the cell surface, NPs would eventually not be engulfed [58]. This may further explain why internalized amounts of AuNPs were 1.5-fold lower with an increasing diameter from 7 to 14 nm [25]. A study by Park et al. on uncoated PS microbeads also indicated approximately a 2-fold decline of internalized amounts when size was increased from 100–200 to 1000 nm [44]. Although biocoating greatly enhances internalized numbers, the PS microbeads of 1000 nm internalized by MOs have strong phagocytosis ability and were only 1/800 of uncoated NPs of 45 nm engulfed by T cells [65]. Therefore, appropriately increasing NP size decreases the possibility of being internalized.

Other factors also influence the internalization process. Jiang et al. realized that this process could be greatly weakened at low temperatures [62]. Consistent with this finding, NP uptake amounts were decreased by 80% at 4°C compared to 37°C [18]. Based on this, Chandrasekaran et al. backpacked anti-CD57-modified NPs at 4°C to protect them from NK cell engulfment [42]. Huang et al. attached NPs at 4°C without antibody modification, and NPs were retained on the T cell surface for 3 d [12]. Moreover, some photothermal-therapeutic agents were cell-selective. Ly-6C^{high} MOs could internalize single-walled nanotubes (SWNT) to nearly 100%; however, for NEs, this was only 3%, and both Ly-6C^{low} MOs and lymphocytes were lower than 1% [45]. Another factor that influences the internalization process is NP shape. Nonspherical shape can decrease phagocytosis risk to some extent [49].

Generally, it appears that avoiding internalization-initiating receptor modification, increasing the NP diameter, lowering incubation temperature, and using a nonspherical shape may reduce the internalization risk. However, to what extent these factors influence and compromise cell functions in internalization progress still needs to be determined. An additional issue to be considered for the backpack approach is that NPs on cell membranes may cause protein corona formation, which could affect biological interactions because of the change in protein orientation and conformation [66].

3.2. Encapsulation Approach.

Another cargo loading method, similar to the "Trojan horse," was to encapsulate them into the inner cellular space, as shown in Figure 3. Normally, innate endocytosis was one way to engulf items, which can be realized simply by incubating cells and cargos together. However, it did not work for RBCs. Because of the lack of cellular organelles, RBCs lack the endocytosis function that leukocytes and MSCs have, such that hypotonic dialysis is always deployed in this condition.

The encapsulation approach provides possibilities for a high loading rate without altering the normal functions of cell membranes and for taking cargos through the blood vessel barrier without unnecessary interactions. However, it is also challenging because high loading rates increase the risk of cell cytotoxicity and unnecessary early leakage.

3.2.1. How to Enhance Encapsulating Amounts without Cytotoxicity?

A high loading rate is one strong advantage of the encapsulation approach, but achieving this is quite complicated. Tumor chemotherapeutics/agents, such as PTX and Dox, are extremely toxic compared with the backpack approach, which was finished within 1 h. The encapsulation method always takes several hours to incubate the drug-loaded NPs or other agents with cells, as shown in Table 2. Consequently, there is the expectation that sufficient drug encapsulation will induce sudden cell death and therefore a low loading rate [18].

It was reported that 1–12.5 μg mL^{-1} Dox was toxic to MAs [30, 67]. However, the Dox amounts that Fu et al. adopted were more than 4-fold, and no cell function effects were observed [68]. Except for MAs, Dox at such high concentrations also exhibited a small toxic effect on MSCs [52].
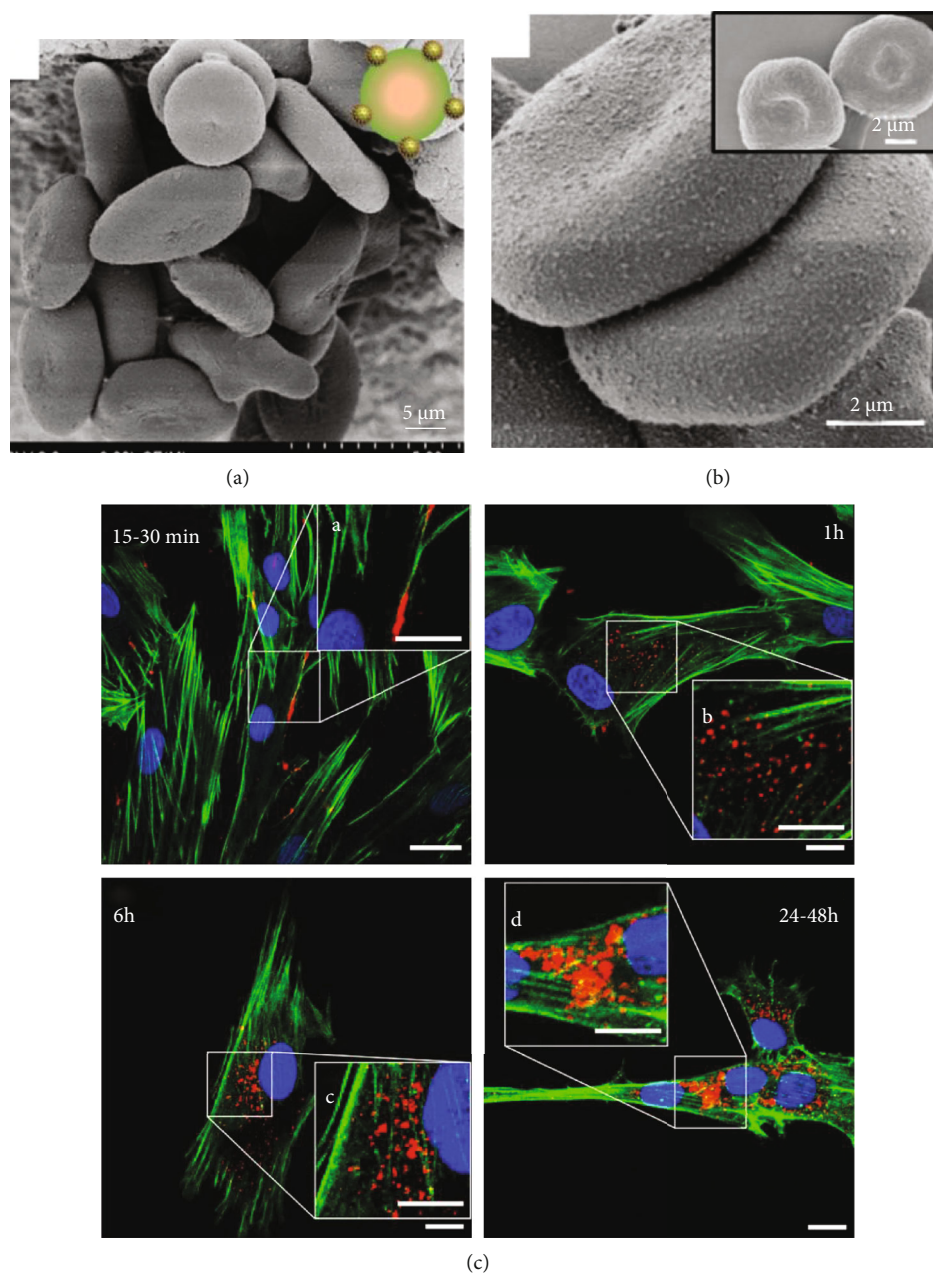
FIGURE 3: Backpack and encapsulation approaches. (a) Scanning electron microscope (SEM) images of RBCs which were backpacked with multitheranostic probes for cancer surgery guidance and therapy. (b) SEM images of higher magnification of cargo-loading RBCs, and the insert shows naked RBC images. Reproduced with permission [48]. Copyright 2019. Ivyspring International Publisher. (c) Confocal micrographs of quantum dot distribution in MSCs after 15–30 min, 1 h, 6 h, and 24–48 h incubation. Nuclei, Hoechst blue; actin, Phalloidin green; quantum dots, red. Scale bar for main images, 15 μm; scale bar for insert images, 10 μm. Reproduced with permission [40]. Copyright 2017. Dove Medical Press.

The two studies verified that most Dox-treated MAs and MSCs were in the G0/G1 phase; thus, they successfully escaped from the G2/M phase-dependent cytotoxicity of Dox. Additionally, drug-resistant protein P-glycoprotein was indicated on MAs [68] and MSCs [52] to facilitate Dox efflux and keep cells viable. The overexpressed ATP-binding cassette transporters on MSCs further maintained the stem cell state. Yet MSCs seemed more sensitive to PTX than Dox because 0.1 μg mL^{-1} PTX was reported to be toxic to MSCs [69]. The discrepancy in Dox toxicity on MAs is still unclear because they have the same cell sources of RAW264.7. One deduction could be made: most of the MAs in the toxic groups were in the G2/M phase. One other finding was that placing Dox on NP surfaces instead of encapsulation resulted in 20% T cell death after 5 h and 60% after 15 h [70]. Thus, free drugs were not expected to be directly internalized by cells.

Strategies to solve this were to associate free drugs with NPs first and then encapsulate the drug-loaded NPs into cells to avoid direct exposure-caused cell toxicity. Several

TABLE 2: Cargo loading conditions of encapsulation and backpack approaches.

Refs.	Loading method	Culture time	Incubation temperature	Drugs/NPs	Drug/NP size (nm)	Drug concentration for loading	Cell carrier type	Final loading amounts (μg drug per million cells)	Cancer type	In vitro/in vivo
[70]	Encaps	5 min	Unknown	Dox/TargetMAG NPs	50	2 μg/mL	T cell	Dox 0.192	N/A	In vitro
[18]	Encaps.	2 h	37°C	Dox/silica NPs	28.4	20 μg/mL	MA	Dox 16.6	Glioma	In vivo
[72]	Encaps.	4 h	37°C	Dox/poly(AAc-co-DSA) NPs	260	13.6 μg/mL	MO	Dox 1.44	Prostate cancer	In vivo
[67]	Encaps.	6 h	Unknown	Dox/liposome NPs	145	25 μg/mL	MA	Dox 4.4	Breast cancer	In vivo
[69]	Encaps.	8 h	37°C	PTX/PLGA NPs	135	8 ng/mL	MSC	PTX 1	Glioma	In vivo
[38]	Encaps.	12 h	Unknown	PTX/albumin NPs	100-130	200 μL PTX	NE	PTX 18	Gastric cancer	In vivo
[53]	BP	20 min	Unknown	Curcumin/chitosan NP-biotin	377	50 μg/mL	MSC	Curcumin 54.73	Lung cancer	In vivo
[59]	BP	30 min	37°C	NSC-87877/liposome NP-PEG	200	T cell : NP ratio = 1 : 1000	T cell	100 NPs/cell	Prostate tumor	In vivo
[12]	BP	30 min	4°C	SN-38/liposome NPs	340	Unknown	T cell	SN-38 0.4	Lymphoma	In vivo
[46]	BP	30 min	RT	Chlorin e6	Molecule	3 μg/mL	RBC	$\sim 6 \times 10^6$ Ce6 molecules on the surface	Breast cancer	In vitro
[51]	BP	1 h	37°C	IL-15Sa/nanogel-PEG	121	0.67 μg/mL	T cell	IL-15Sa 7.68	Melanoma	In vivo
[52]	BP	1 h	37°C	Dox/SN-anti-CD90/CD73	152.9	100 μg/mL	MSC	1500 NPs/cell	Glioma	In vivo
[24]	BP	1 h	4°C	ZnF16Pc/biotin-ferritin	15-18	Unknown	RBC	2×10^7 ZnF16Pc molecules on the surface	Glioma	In vivo

Encaps. = encapsulation; BP = backpack; RT = room temperature. For other abbreviations, please refer to the abbreviation list.

types of NPs that exhibited good biocompatibility, biodegradability, and capability to load hydrophilic/hydrophobic drugs were widely studied for drug carrying. Liposomes (including unilamellar and multilamellar) enhanced the maximum tolerated dose (MTD) 20-fold in MAs of PTX [71] and 50–200-fold for Dox [30, 67]. It was also reported that poly(lactic-co-glycolic acid) (PLGA) NPs were able to enhance 5-fold higher for Dox MTD for MAs [64], yet no obvious change was observed for PTX MTD on MSCs [69]. Huang et al. also deployed poly(-AAc-co-DSA) and raised Dox MTD for MOs more than 3-fold [72]. One more drug-covering material is albumin. Albumin-bound NPs translated PTX into the commercial cancer drug Abraxane, for which the phase III data indicated that albumin allowed a 1.5-fold increase in MTD of Abraxane than that of free PTX; however, when the dose was beyond MTD, 25% of patients notably suffered from neutropenia [57]. Based on these findings, it is not difficult to conclude that encapsulating NP-protected drugs into cells prevents cytotoxicity and increases the loading rate.

3.2.2. How to Ensure Retaining Sufficient Drugs Inside without Early Leakage? Drugs are supposed to have a long retention period in cells. It took as long as 6–12 h for MAs to arrive at brain lesions [18], approximately 20–40 h for T cells to arrive at a lymphoid organ [12], and at least 4–6 h for MSCs to arrive at lung and liver tumors [19]. During circulation, drugs must stay with NPs to ensure the cell carrier function remains unchanged and there is sufficient drug for delivery to tumor sites. For example, 40% of Dox in NPs was released from MAs after 8 h [64], and 50–90% of SN-38 in NPs was released within 6–12 h [73]. It was also reported that approximately 60% of PTX in NPs was released from MSCs within 30 min [74]. These facts indicate that most drugs were unloaded before arriving at tumor lesions and further cause systematic toxicity.

One leakage threat was from lysosomes. This organelle has a low pH of 5 and is flooded with approximately 60 types of hydrolases, which may degrade NPs inside the organelle. Acid-responsive NPs were found to begin intracellular release within 15 min [75]. Therefore, the backpack approach is suggested to carry unprotected, acid-responsive drugs/NPs for cancer therapy. Another threat was from exocytosis. Cells engulfed drugs/NPs inside via endocytosis, but exocytosis correspondingly placed encapsulated NPs in danger of leakage. Interestingly, the two threats are not related to RBCs because they do not have lysosomes or an exocytosis function. RBC membranes are impermeable, and normally, no more than 5% of free drugs leak within 2 h [46]. Besides lysosomes and exocytosis, drug-resistant protein P-gp is one more threat for cells that expressed the protein because it was found that 65% of free Dox was extruded from MAs within 2 h [68].

One option is choosing proper NPs that are themselves beneficial for drug retention to reduce leakage risk. For example, poly(AAc-co-DSA)-coated Dox has a restricted release lower than 20% within 24 h from MOs [72]. Another solution is modulating NP structure. Instead of polymers or liposomes, Zhang et al. adopted silica as a nanocapsule to load Dox and then encapsulated the complex into MAs [18]. To realize minimal liberation during migration and controlled release *in situ*, the drug-loaded MAs achieved a two-phase drug release by modulating silica coating thickness from 12 to 52 nm and keeping two times the amount of the drugs inside NPs. One more possibility is to enhance the internalization process, which was discussed in detail in Section 3.1.2. Based on this strategy, Moku et al. attached one cell-penetrating peptide-transactivator of transcription (TAT) peptide on the cell membrane. Compared with naked NPs, the uptake of TAT NPs was enhanced 3-fold, and retention amounts of drugs/NPs were accordingly increased 2-fold in MSCs, as expected [74].

4. Cascade Strategies for Improving Cell-Driven Targeting Delivery Efficiency

The delivery efficiency of NPs varied with tumor types, targeting methods (active or passive), material properties (inorganic/organic, particle size, surface charge, and particle shape), and transplantation approaches (orthotopic allo/xe-nografts). The factors mentioned above strongly affect the delivery efficiency and have been well studied for NPs. However, according to the analysis of over 10 years (2006–2016), the delivery efficiency of NPs to tumors was still less than 1%, with only 0.7% reaching the lesion on average, and the majority was in a nonspecific interaction manner [10]. This low delivery efficiency in tumors resulted from the following facts: NPs were cleared by RES and kidneys [8]; NPs rely on EPR effects to accumulate in tumor lesions, which failed in the clinic [76]; and a 10-40-fold fluid interstitial pressure hampered NP penetration and distribution [10]. Recently, circulatory cells from the blood were widely studied, as listed in Table 3, which shows great potential to facilitate the CAPIR process to improve diagnosis and therapeutic efficacy.

4.1. Circulation Ability. Regarding clearance threats on NP-based DDS, the long circulation time of circulatory cells in the whole body, as discussed in Section 2, reduces the risk to an extremely low level. In the study of Huang et al., 60% of Dox/NP-encapsulated MOs arrived in prostate tumors after 48 h postintravenous injection, but 80% of free NPs were found trapped in the liver [72].

4.2. Accumulation Strategies. The concern about the EPR-dependent accumulation of NPs would not hinder circulatory cells because they are chemoattracted by tumor-related signals and actively transmigrated into tumors with their payloads. However, a recent study found that, instead of long-term recognized intercellular extravasation, NPs deployed an active transportation manner via transcellular mechanisms to accumulate into tumor tissues [9]. The work revealed that gap frequency was as low as 8% in all studied tumor types, in which more than half the gaps were transcellular channels. Would it be controversial that NPs were difficult to accumulate in tumors without obvious EPR effects? If not, did it result from low retention, despite being transported inside? Regardless of whether NPs depend on EPR or not, they must face the same issue of the low accumulation rate that circulatory cells can enhance. Based on the following three strategies, accumulation of the cell vehicle was achieved, and the efficiency was enhanced.

4.2.1. Innate Homing Ability. The basic approach to target the lesion was based on the innate chemotaxis response of cells to tumor-related signals, as depicted in Section 2. Compared with the average mentioned above that reached a rate of 1%, approximately $44.4 \pm 5.4\%$ of PTX/NP-encapsulated MSCs arrived in mouse gliomas through natural homing ability [69]. Dox/NP-encapsulated MA-treated mice also appeared to have a higher density in glioma tissue than Dox/NP alone [64]. The accumulation amounts of SN-38/NP-backpacked T cells were 63 times higher than that of free SN-38/NPs at 20 h in lymphomas and remained high for 4 d [12]. It was confirmed that several ligand-receptors bound to blood vessels could slow the rolling pace of cells and facilitate the transmigration process [35]. Similarly, Chen et al. revealed that ECs in tumor vasculature had different phenotypic profiles with various shear stresses, and

TABLE 3: Different cells loaded with varied cargos for cancer diagnosis and therapy.

Refs.	Cell type	Loading method	Drugs/NPs	Drug/NP size (nm)	Cancer type	In vivo/ in vitro
[36]	NE	Encaps.	PTX/liposome NPs	100	Glioblastoma	In vitro
[38]	NE	Encaps.	BSA/PTX NPs	130	Gastric cancer	In vivo
[55]	NE	Injecting and engulfed by NE in vivo	BSA/PLGA NPs	450	Prostate cancer	In vivo
[12]	T cell	BP	SN-38/liposome NPs	340	Lymphoma	In vivo
[43]	T cell	BP	siRNA/liposome NPs	150	N/A	In vitro
[59]	T cell	BP	NSC-87877/liposome NPs	200	Prostate cancer	In vivo
[51]	T cell	BP	IL-15Sa/nanogel	121	Melanoma	In vivo
[54]	T cell	BP	Liposome NPs	100/200/300	Lymphoma/lung cancer	In vivo
[56]	T cell	Injecting and hitchhiking T cell in vivo	Curcumin/aPD1/PEG NPs	43-50	Melanoma	In vivo
[65]	T cell	Encaps.	AuNPs	45	Lymphoma	In vivo
[70]	T cell	Encaps.	Dox/TargetMAG NPs	50	N/A	In vitro
[17]	NK	BP	PTX/liposome NPs	220	Ovarian cancer	In vivo
[42]	NK	BP	TRAIL/anti-CD57/liposome NPs	161	Prostate/breast/colon cancer	In vitro
[57]	NK	Injecting and hitchhiking NK in vivo	Trail/anti-NK1.1/liposome NPs	138	Melanoma, colon cancer	In vivo
[18]	MA	Encaps.	Dox/SiO_2 NPs	28.4	Glioblastoma	In vivo
[25]	MA	Encaps.	Au/BSA nanorods	7	Liver cancer	In vivo
[30]	MA	Encaps.	Dox/liposome NPs	150	Lung cancer	In vivo
[47]	MA	BP	Fluorophores	N/A	Breast cancer	In vivo
[64]	MA	Encaps.	Dox/PLGA NPs	141.6	Glioblastoma	In vivo
[67]	MA	Encaps.	AuNRs & Dox/liposome NPs	145	Breast cancer	In vivo
[68]	MA	Encaps.	Dox only	N/A	Breast cancer	In vivo
[71]	MA	Encaps.	PTX/Fe_3O_4/liposome NPs	110.36	Breast/colon cancer	In vitro
[73]	MA	Encaps.	SN-38 NPs	119.13	Lung/breast cancer	In vivo
[44]	MO	Encaps.	Polystyrene microbeads	100/300/1000	N/A	In vitro
[45]	MO	Encaps.	RGD/cy5.5/PEG-SWNT	0.8-1.2	Glioblastoma	In vivo
[49]	MO	BP	LbL disk (500 nm thick)	7000	Inflamed lung	In vivo
[72]	MO	Encaps.	Dox/poly(AAc-co-DSA) NPs	200-260	Prostate cancer	In vivo
[6]	NSC	BP	Docetaxel/PEG-PDPAEMA NPs	400	Breast cancer	In vivo
[19]	MSC	Bioengineered	Fluorescence	N/A	Liver/lung cancer	In vivo
[40]	MSC	Encaps.	Quantum dots/PEG NPs	14.5	Breast cancer	In vivo
[41]	MSC	Bioengineered	IFN-α	N/A	Melanoma	In vivo
[52]	MSC	BP	Dox/silica nanorattle	152.9	Glioblastoma	In vitro
[53]	MSC	BP	Curcumin/chitosan NPs	377	Lung cancer	In vivo
[58]	MSC	BP	FluoSpheres	40	Liver cancer	In vitro
[69]	MSC	Encaps.	PTX/PLGA NPs	135.3	Glioblastoma	In vivo
[74]	MSC	Encaps.	PTX/PLGA/TAT NPs	225	Lung cancer	In vivo
[23]	RBC	Encaps.	ICG-BSA NPs & free Dox	N/A	Glioblastoma	In vitro
[24]	RBC	BP	Ferritin/ZnF16Pc NPs	15-18	Glioblastoma	In vivo
[46]	RBC	Both	Free Dox (in), Ce6 (on membrane)	N/A	Breast cancer	In vitro
[48]	RBC	Both	ICG/BSA (in), upconversion NPs (on membrane)	40	Liver cancer	In vivo
[61]	RBC	BP	PS or LDNG NPs	171/268	N/A	In vitro

Encaps. = encapsulation; BP = backpack. For other abbreviations, please refer to the abbreviation list.

ligand-receptor interaction can resist the flow stress and extend residence time on EC surfaces, thereby increasing the accumulation rate [14].

4.2.2. Amplifying Tumor-Related Signals In Situ.

One method to improve accumulation rate is to amplify the inflammatory tumor signal for chemoattraction based on innate homing ability:

(i) Under a postsurgical inflammatory condition, Xue et al. increased the targetability of PTX/NP-encapsulated NEs 86-fold and 1162-fold compared to that of PTX/NPs and single Taxol, respectively [36]

(ii) Radiation is also employed to enlarge local inflammatory conditions. Using enhancing radiation intensity, inflammatory factors such as IL-8, IL-10, and TNF-α in tumors were amplified approximately 1.3–1.56-fold. Accordingly, NEs exhibited a radiation dose-dependent tumor accumulation, showing obvious cell clusters in tumors at 1 h postinjection, which lasted for 2 d [38]. After γ-ray pretreatment, a hypoxia core featured by a decreased vascular density and increased hypoxia microenvironment was augmented in tumors to recruit tumor-associated MAs. In this context, Dox/NP-encapsulated MOs presented a higher aggregation in tumors than did Dox/NPs [72]

4.2.3. Targeting Modification on Cell Carriers.

Modifying cells themselves is another method to support high accumulation rates:

(i) Lymphocytes can recognize tumors via specific antigens; therefore, they retain tumor-related antigen receptors and facilitate this process. For example, NP-backpacked CD8+ T cells retained receptors that specifically recognized OVA-1 in tumors, which amplified accumulation 176-fold more at the tumor site than free NPs after 2 h [54]. Engineered NK cells that expressed CD19 and Her2 receptors showed higher accumulation rates than nonengineered cells against CD19/Her2-positive tumors [17]. Recently, cytotoxic T lymphocytes were reported to release supramolecular attack particles (SMAPs) with TSP1 surface proteins to target tumor cells and then performed independent killing [77]

(ii) Conjugating targeting molecules on the cell surface. RGD is a short peptide that targets $\alpha v \beta_3$ integrin-positive tumors, and modifying RBCs with RGD allowed an obvious attachment in tumors that native RBCs could not achieve [23, 48]

(iii) For magnetizing modification, cell carriers have internalized magnetic particles, such as Fe_3O_4, to follow guidance from electromagnetic fields. This method was widely studied as external assistance to control the cell path, and MA motion and speed were found to be enhanced 29 times that of normal

cells [71]. Along with this, it may improve SMAP capability and make a concession to the premise of reducing early leakage risk

Enhancing accumulation can reduce drug demands. SN-38/NP-backpacked T cells had density 90 times higher in lymphomas than that in free drugs of 10-fold injection doses. Moreover, T cells with a 1/40 drug dose of free SN-38 eased the tumor burden that free SN-38 could not [12]. It was also found that TNF-α-transduced MSCs secreted TNF-α for 2 weeks and showed equal effects at a low dose to free TNF-α at a high dose [41].

4.3. Penetration Ability.

NPs normally are distributed around the periphery of tumor tissues. For example, Dox was reported to diffuse only 8–16 μm from the tumor vessel, and Dox/NPs were limited to 10–20 μm [72]. By modulating NP size, infiltrating long distances could be feasible. NPs can penetrate into deep tumor tissue only if the diameter is smaller than 20 nm, and this size range will be difficult to escape from RES clearance [4].

Unlike NPs, circulatory cell-driven drug delivery was able to chemomigrate without obstacles even under the condition of a high-pressure tumor matrix. As discussed in Section 2, leukocytes and MSCs are components of tumor tissues. Furthermore, leukocytes can perform compartmentalized and mixed distribution in tumors [78]. In animal tests, it has been confirmed that, regardless of high pressure, the hypoxic microenvironment in the tumor tissues had a stronger ability to recruit leukocytes into deep regions [72]. In glioma, spheroids at the depth that Dox/NP-MAs migrated were 1.56-fold that of NPs alone (56.42 μm vs. 36.07 μm) [64]. Furthermore, Dox/NP-MOs penetrated farther than 100 μm from the nearest vessel [72]. Therefore, once drug-carrying circulatory cells accumulated in the tumor sites, the penetration process was in a clear pattern.

4.4. Drug Release Profiles and Internalization.

Concerning the CAPIR cascade, the final two steps of NPs were internalization for drug release, but the order for circulatory cells was reversed. Cargos were released first via transcellular mechanisms, then were internalized by tumor cells. As illustrated in Figure 4, there are three kinds of drug release patterns for cell-driven drug delivery systems, as discussed below.

4.4.1. Exocytosis.

Exocytosis was the fundamental function that drug-encapsulated cells employed. By optimizing the drug leakage profile during circulation, drugs/NPs released via exocytosis could be slowed in the early phase and quickened in the late phase for tumor cell internalization [18]. Drug efflux also occurred after the drugs and NPs were dissociated inside cells [69]. This meant that drugs/NPs were internalized by tumor cells in two patterns: intact drugs/NPs and free drugs.

The internal tumor microenvironment was also reported to accelerate exocytosis speed. Under inflammatory signals of the IFN-γ condition, Dox/NP-MAs were activated to release the drug two times faster within 4 h than the group without IFN-γ [64]. The same tendency happened to
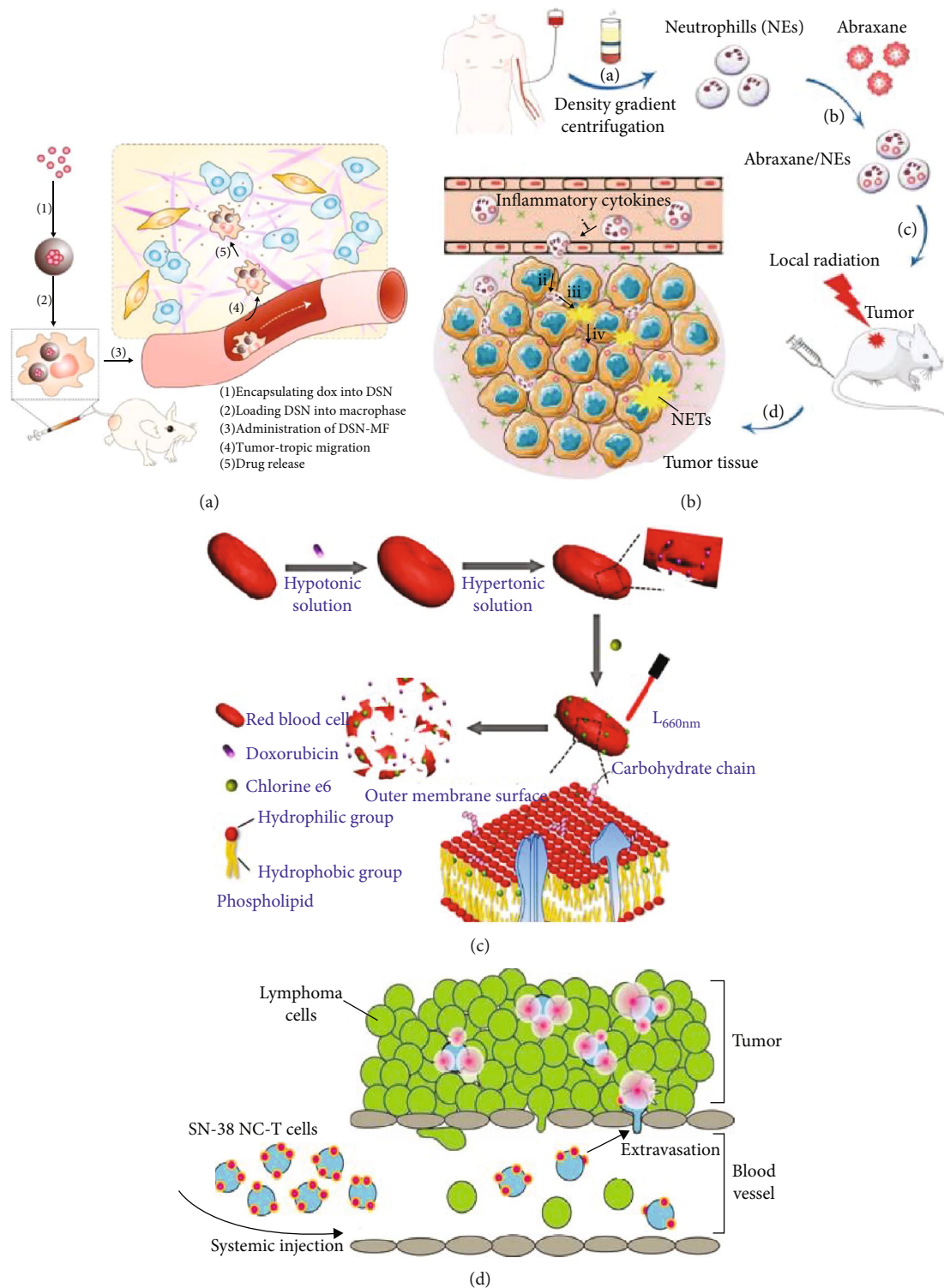
FIGURE 4: Three drug release patterns. (a) Exocytosis: either free Dox or Dox/SiO$_2$ NPs were secreted by MAs for glioblastoma treatment. Reproduced with permission [18]. Copyright 2018. John Wiley and Sons. (b) Cell disintegration I: Abraxane-encapsulated NEs disintegrated and formed the neutrophil extracellular traps to kill gastric cancer. Reproduced with permission [38]. Copyright 2018. John Wiley and Sons. (c) Cell disintegration II: Dox-encapsulated and Ce6-backpacked RBCs were disintegrated by photoradiation for breast cancer. Reproduced with permission [46]. Copyright 2017. American Chemical Society. (d) Cell-drug dissociation: SN-38 was dissociated from the T cell membrane into lymphoma cells. Reproduced with permission [12]. Copyright 2015. American Association for the Advancement of Science.

Dox/NP-MOs in acidic tumor environments [72]. However, exocytosis did not work for RBCs because there are no organelles to function in efflux, and they rely on diffusion or disintegration only.

4.4.2. Cell Disintegration.

Cell disintegration was one pattern to trigger drug release in lesions, used for both the drug-encapsulated and backpacked cells. As mentioned in Section 3.2.2, chemotherapeutics threatened the normal function of cells. When they arrived at the tumor sites, free drugs reached a high concentration inside carriers as designed, and cells started to disintegrate to release all tumor-toxic freights [30]. Additionally, NEs had a unique feature that could amplify this toxic process. Under a condition of high postsurgical inflammation environment of TNF-α, CXCL1/KC, and IL-8, NEs could destroy themselves into NETs to release both original toxic proteins and loaded toxic drugs [36].

External interventions like ultrasound, radiation, heat, and NIR were also deployed to destruct cells for drug release *in situ*. Those interventions were initially involved in radiotherapy. With ultrasound aid, MOs encapsulated with echogenic particles and drugs disintegrated and showed substantial cancer cell killing ability *in vitro*. RBCs released 80–100% of Dox under radiation conditions within 10 min, and the speed was 16 times faster [23, 46]. RBC disintegration is an important premise for PDT, which can simultaneously damage tumor vasculatures and generate abundant ROS toxic to cancer cells [24]. However, additional approaches are united for chemo/radiotherapies and diagnoses to amplify treatment efficacy. Suppose both imaging agents and photosensors are carried via RBCs and can simultaneously realize bioimaging-directing tumor resection via NIR-II fluorescence and killing tumor cells under the PDT condition [48]. Given the disintegration-responsive feature under acidic environments and NIR laser conditions, MAs released $29.3 \pm 1.69\%$ of the drugs in 1 h, which took approximately 24 h under a pH of 7.4 with no laser conditions [67].

4.4.3. Cell-Drug Dissociation.

Cell-drug dissociation is another pattern to unload cargos into the tumor sites. For these drugs that cannot interact with tumor cells well if retained on the host cell membrane, cell dissociation must be considered. Li et al. backpacked MSCs with Dox/silica nanorattles that were responsive to pH change. Compared with pH 7, pH 4 led to an alteration of interaction force strength between nanorattles and drugs and stimulated a 3-fold greater dissociation [52]. Similarly, Tang et al. backpacked T cells with a protein nanogel interlinked by a reduction-responsive reversible cross-linker. Once in tumor tissue, the raised tumor antigen concentration activated T cells. The surface reduction was correspondingly increased on the cell membrane, which initiated cell dissociation with drugs [51].

4.4.4. Internalization and Survival Extension.

Regardless of adopting any release approach, drugs/NPs were internalized in a mixed manner for free drugs and drugs/NPs, except for those products, such as ROS, performing killing tasks completely without internalization. The internalization efficiency of drugs/NPs in tumor cells was determined by NP design, and carrier cells hardly played a role in this process.

The cell-driven drug delivery system at least extended the survival rate. After tumor surgery, the number of survival days of SN-38/NP-T cell-treated mice was extended by 10 d relative to both free SN-38 and SN-38/NPs [12]; that of Shp1/NP-T cell groups showed a 14 d increase compared to that of the untreated group [59], and that of PTX/NP-NE-treated mice was, respectively, increased by approximately 32 and 23 d longer than free Taxol and PTX/NPs [36]. In general, these targeting strategies with circulating cells pragmatically overcame the problems NP-based systems faced. Regardless of some issues to be solved, such as balancing loading amounts and function, it created new strategies and insights for targeted cancer therapy.

5. Cell Derivatives as Drug Carriers for Targeting Delivery

As biological entities, native cells are complex and fragile. Augmenting while balancing the functionality remains a topic of study. Two other candidates derived from cells provided extra clues for targeting drug delivery: the cell membrane and small extracellular vesicles (EVs), as listed in Table 4.

5.1. Cell Membrane

5.1.1. Native Cell Membrane.

The efficiency of circulatory cell delivery of drugs is attributed to the following features: reducing RES clearance risk, targeting and accumulating in tumor sites, and exerting a cytotoxic effect. These topics have been partly related to cell membrane proteins that provide a "do not eat me" signal [22], tumor-targeting proteins [46], and death-initiating proteins [77]. Therefore, the cell membrane plays a key role in drug/NP delivery.

Cell membranes of circulatory cells are biological materials. As expected, they present good biocompatibility, long circulation time, and tumor-targeting and accumulation abilities. Blood leukocyte membranes express signature protein CD45 or CD3Z and adhesion protein LFA-1 or CD11a for vascular extravasation [79]. NK membranes express the signature protein CD56 and tumor-targeting/toxic receptors NKG-2D and NKp30 [32]. After being used to decorate NPs, leukocyte membrane- and NK membrane-coated NPs were stable in both PBS and 90% fetal bovine serum within 24 h, and no early degradation or drug leakage was observed. However, the membrane-coated NPs presented a donor membrane-dependent clearance where particles exhibited the same membrane as phagocytic cells, and the internalization chance decreased by approximately 75%. When this does not occur, it is low to 10% [79]. Both kinds of membranes facilitated a 2-fold higher accumulation in tumors relative to that in free NPs. Consistent with this, MA membrane-coated NPs reached a mean retention time and half-life in the plasma 2 times more than that in uncoated NPs [80]. MA membranes were additionally found to have

TABLE 4: Different cell derivatives loaded with varied cargos for cancer diagnosis and therapy.

Refs.	Cell type	Loading method	Drugs/NPs	Drug/NP size (nm)	Cancer type	*In vivo/ in vitro*
[32]	NK membrane	Coating	Gadolinium/PLGA NPs	109	Breast cancer	*In vivo*
[79]	MO membrane	Coating	Silicon particles	3200	Melanoma	*In vivo*
[80]	MA membrane	Coating	Dox/IND/Ce6/PEG/bilirubin complex	107	Breast cancer/ melanoma	*In vivo*
[81]	MA membrane	Coating	PTX-albumin NPs	138.7	Melanoma	*In vivo*
[82]	MA membrane	Coating	Dexamethasone	N/A	Inflamed ear	*In vivo*
[83]	RBC membrane	Coating	Dox/Kirenol/phosphorous quantum dots	10	Cervical cancer	*In vivo*
[86]	Tumor cell membrane	Coating	AuNPs	40	N/A	*In vitro*
[22]	RBC sEVs	Encaps.	Free clodronate	N/A	CD47$^{-/-}$model	*In vivo*
[95]	Blood sEVs	Between lipid layers	Free Dox	N/A	Liver cancer	*In vivo*
[96]	T cell sEVs	N/A	Chimeric antigen receptor	N/A	Breast cancer	*In vivo*
[101]	Tumor cell sEVs	Encaps.	ZnO nanocrystals	91	KB cancer	*In vitro*
[102]	Blood sEVs	Both	Dox/miRNA21 inhibitor (in), MTf/L17E (on EVs)	106	Glioblastoma	*In vivo*
[103]	RBC sEVs	Encaps.	RNA	N/A	Breast cancer	*In vivo*
[104]	Cancer sEVs	Encaps.	Free methotrexate	N/A	CCA	*In vivo*
[87]	Artificial RBC	Encaps.	Hemoglobin-dopamine complex	100	Breast cancer	*In vivo*

Encaps. = encapsulation; BP = backpack. For other abbreviations, please refer to the abbreviation list.

5.88-fold higher cellular uptake efficiency than that of uncoated NPs [81]. Unlike the top-down approach in the studies mentioned above, Parodi et al. functionalized particles with leukocyte lesion-targeting molecules to create a leukosome via the bottom-up method. Compared with naked particles, it also decreased clearance from RES and kidneys by 1.5–2.6-fold and increased accumulation 7-fold in the inflamed vessels [82]. In addition to leukocytes, membranes of RBCs [83], platelets [84], and stem cells [85] were also widely used for particle camouflage. Cancer cell membranes were also studied as NP coating to target cancer cells in return. Compared with naked NPs, liposome-coated NPs, RBC membrane-coated NPs, and trypsinized HeLa membrane-coated NPs, HeLa membrane-coated NPs achieved enhanced cellular uptake efficiency [86]. This did not necessarily mean the cancer cell membrane itself surpassed other membranes to target tumor cells, because one cancer-specific membrane protein on the HeLa cell-integrin $\alpha v\beta 3$ was found to function in HeLa targeting. Therefore, the tumor-targeting design should be based on distinct cancer cell types.

5.1.2. Synthetic Membrane/Cell.

By mimicking the natural function of cell carriers, synthetic membranes and cells were constructed. Because hemoglobin itself is susceptible to autooxidation, to overcome large oxygen loss for PDT, Liu et al. assembled artificial RBCs with basic features of size, shape, and deformability. Amazingly, the artificial RBC capacity was augmented to achieve 10-fold payloads of a hemoglobin-dopamine complex [87]. Similarly, Guo et al. deployed a silica cell bioreplication method to rebuild RBCs

successfully, and these cells expanded possible carrying contents from hemoglobin to drugs, ATP biosensors, and magnetic NPs [88]. Hindley et al. deployed a bottom-up synthetic strategy to behave biologically to construct an artificial cell with a communication pathway [89]. Strictly speaking, a synthetic cell/cell membrane is not a cell derivative, especially for synthetic cells similar to a robot, which is a simplification and augmentation process that screens unnecessary functions and amplifies/adds expected ones. However, they provide a new perspective on the DDS beneficial elements from cells.

5.2. Small Extracellular Vesicles (Small EVs)

5.2.1. A Real Drug Delivery Medium In Vivo.

Extracellular vesicles are lipid bilayer-coated and are released from parent cells, consisting of small extracellular vesicles of exosomes (30–150 nm), ectosomes (100–1000 nm) [90], large vesicles of apoptosis bodies (1–5 μm) [91], and oncosomes (1–10 μm) [92]. These vesicles have versatile contents, including proteins and genetic materials, secreted for short-/long-distance communication by all types of cells under physiological and pathological conditions. EVs have rich sources in body fluids, such as blood, saliva, urine, cerebrospinal fluid, and milk.

Small EVs are involved in drug delivery *in vivo*. Smith et al. found that carbon nanotubes were taken up by 8 μm circulating cells once injected into the blood [45]. Recently, Chaudagar et al. observed a similar phenomenon wherein NEs were *in vivo* activated to internalize NPs (BSA-NP-cabozantinib) to assist drug delivery to lesions [55]. Kim

et al. further realized that, instead of being internalized directly by tumor cells, NPs could be first engulfed by local MAs [93]. Importantly, approximately 16.5% of released drugs were entrapped within MAs-exosomes by calculation [18]. More recently, it was revealed that cytotoxic T lymphocytes killed cancer cells by releasing both ectosomes and supramolecular attack particles, wherein supramolecular attack particles were found to work independently [77]. Because NPs are taken into mediating cells and entrapped in vesicles, studies have paid much attention to small EVs as carrier candidates.

5.2.2. Carrier Features of Small EVs for Drug Delivery. Besides a nanoscale size similar to that of NPs and blood circulation properties similar to those of circulatory cells, small EVs also provide targeting efficiency and have the potential to reduce cell carrier side effects. Similar to cell carriers, the loading method is a critical link for small EVs, and it has been detailed elsewhere by Yang et al. [94]:

(i) Small EVs have an inherent escape capability from clearance. Ectosomes of RBCs were reported to maintain the parent "don't eat me" protein CD47 [22]. Yang et al. then utilized blood exosomes for delivering Dox, which reduced drug accumulation in the liver and heart [95]

(ii) Small EVs were able to target and accumulate in tumor tissues as cells did. EVs contained transmembrane signature proteins and versatile receptors for membrane anchoring. For example, except for T cell signature proteins of CD8 and CD3, exosomes and ectosomes were shown to retain tumor-targeting proteins of T cell receptors (TCRs) [96] and FasL, respectively [77]. Both proteins can initiate tumor death. Moreover, the amounts of surface chimeric antigen receptors (CAR-engineered tumor-targeting proteins) on purified exosomes were similar to those on cells [96]

(iii) Inflammation and low pH are two hallmarks of the tumor microenvironment. As discussed in Section 2, inflammatory signals chemoattract related cells to sites and enhance the EV internalization process. TNF-α loosened the tight conjunction between cells, and the activated cells had 3 times higher internalization ability with a time extension [97]. A low pH value also increased the timing of exosome uptake by tumor cells. Under acidic conditions (pH 6), the uptake emerged 15 min earlier than that under a pH 7.4 condition, and the uptake amounts were 1.5-fold higher during the first 5 min [98]. An acidic environment further increased cargo release efficiency. Instead of being engulfed into lysosomes, exosomes under acidic conditions tended to directly fuse with the tumor cell membranes to release the cargo. It was also shown that the fusion process was cell-dependent. The fusion activity of tumor exosomes was 19–23% for metastatic tumor cells and 9–12% for primary tumor cells, whereas it was

barely detectable in normal cells, which provided another perspective on exosome targetability

(iv) Small EVs can reduce cell carrier side effects while efficiently killing tumor cells. An important feature of CARs-exosomes inherited from cytotoxic T cells is that they can exert a cytotoxic effect against tumor cells. Additionally, CARs-exosomes perfectly rid themselves of PD-1 on the vesicle membrane (PD-1 is normally expressed on parent cells and interacts with PD-L1 on the tumor surface to weaken the cell antitumor effect). No cytokine release syndrome was observed in CAR-exosome therapy, common toxicity in CAR-T therapy [96]

5.2.3. Application of Small EVs in Tumor-Targeting Delivery. Small EVs secreted from donor cells retained the mother cell signature and function protein, and the selectivity was maintained, to some extent, to ensure targetability and therapeutic effects.

Exosomes from engineered leukocytes expressed tumor-targeting Lamp2b, which reached an encapsulation efficiency of 20% with Dox. Dox/EVs appeared in tumor sites within 30 min after injection, peaked at 2 h, and disappeared at 8 h, although no signal was detected in the tumor area at any time for nontargeting protein exosomes [99]. The off-target case in the control group may be caused by losing some of the tumor-targeting proteins of donor cells. CAR-T-derived exosomes retained the necessary targeting proteins and inhibited 67–70% of tumor growth for both the breast and lung cancer therapies in animals [96]. Another study showed the same tendency [100]. Instead of bioengineering, Wang et al. fed donor cells with PTX and biotinylated these cells, then obtained expected PTX-loading exosomes with dual ligands of biotin and avidin on the membrane to target tumor cells. These biotinylated exosomes extended the accumulation signal to 48 h after injection, but blank exosomes were almost lost in circulation. This loss may result from cell line discrepancy because circulatory cells (usually leukocytes) were the ones with rich tumor-related targeting proteins. Dumontel et al. interestingly used tumor cell-derived exosomes to encapsulate ZnO nanocrystals and effectively kill tumor cells without any membrane modification [101]. Magnetic molecules were also applied to small EVs for targeting. Zhan et al. linked Fe_3O_4 nanoparticles on blood exosomes via a ligand-receptor interaction to simultaneously achieve both exosome separation and tumor targeting. The magnetic exosome group enhanced vesicle accumulation at the tumor site within 1 h to a level that the normal group took 24 h to achieve (Figure 5) [102].

Besides chemotherapeutic drugs, genes are another type of cargo that have been widely studied with small EVs. One advantage, as discussed previously, is that small EVs can fuse with cell membranes directly to prevent genes from degradation in lysosomes. Additionally, because of the lack of nuclei and organelles in RBCs, RBC-derived microvesicles are a great carrier for gene delivery. Usman et al. deployed RBC microvesicles to load antisense oligonucleotides to

(a)

(b)

(c)
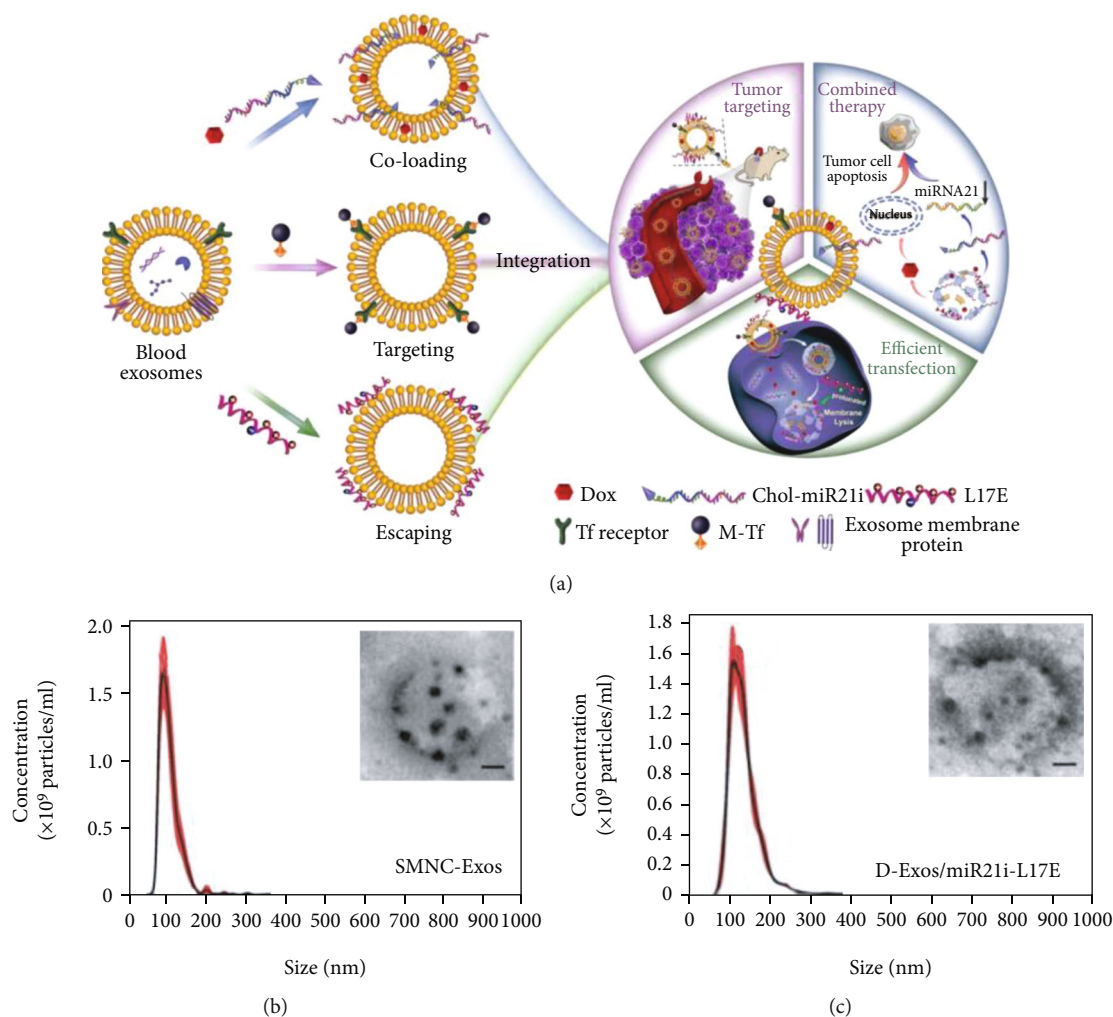
FIGURE 5: (a) Scheme of gene/chemotherapy on a blood exosome basis. Chemotherapeutic drugs and the cholesterol-modified miRNA21 inhibitor were embedded between the vesicle lipid bilayers for tumor killing; both magnetic molecules and L17E peptides were bound onto the vesicle membrane, respectively, for targeting and lysosome escape. (b) According to nanoparticle tracking analysis (NTA), the original exosome size was 93 nm. (c) The size was increased to 106 nm on average, after cargo loading and membrane modification, and transmission electron microscope (TEM) images showed modified exosomes that retained a clustered structure. Reproduced with permission [90]. Copyright 2020. Ivyspring International Publisher.

successfully treat leukemia [103]. To cross the endosome membrane, endosomolytic peptide L17E was tethered on EVs to accelerate the escape of cargo from endosomes to the cytosol. Compared with nonmodified exosomes, RNA in modified exosomes that was entrapped in endosomes was less than one-third [102].

These EVs displayed a prolonged circulation time, high targeting efficiency, and therapeutic effects by modulating membrane protein expression and cell line discrepancy between donors and target cells. A clinical finding regarding methotrexate-containing microvesicles for treating cholangiocarcinoma reported that approximately 30% of patients were partially relieved upon biliary obstruction. After the first treatment, approximately 50% of the liver function of the patients was improved, and symptoms of jaundice were reduced [104]. This suggested the feasibility of small EVs as a competent drug delivery carrier for tumor therapy.

6. Challenges

6.1. Restricted CAPIR Process. There are two concerns regarding RBC accumulation and penetration ability. A high surface-to-volume ratio causes high deformability, yet it matters to what extent cells of 7–8.5 μm can transmigrate the 2 μm interendothelial gaps. Moreover, these cells are passively driven by blood flow, so they may have a problem penetrating the deep tumor matrix alone.

Similar to RBCs and cell membranes, crossing the blood barrier and accumulating well is a persisting issue for EVs because they cannot migrate as leukocytes/MSCs do. One in vitro Transwell study reported that exosomes migrated from a low chamber to an upper one via a transcellular mechanism [97] instead of gap diffusion. Sindhwani et al. recently also revealed that only seven EPR gaps were found in 313 vessels [9]. When taking the transcellular way, both the uptake-to-efflux ratio and the integrity of EVs need to

be determined, because an inflamed endothelium with highly expressed adhesion molecules and inflammation factors facilitate EV internalization, similar to ICAM-1 and TNF-α [105]. Additionally, the penetration ability of nano-EVs such as NPs may be weaker than that of cells under high fluid interstitial pressure, which impacts the distribution of EVs in lesions and the drug delivery efficiency afterward.

One addition that should be taken into consideration is that, to some extent, drugs loaded by cells increased survival rates, but attention has to be paid that it cannot completely prevent the regrowth of tumors, although it efficiently slows tumor recurrence [36].

6.2. Bringing New Issues. The demands of drug-loaded leukocytes were 10 times more than the normal level, which might evoke side effects in blood and obtain a great number of cells from patients themselves [106]. Additionally, the therapeutic effects of leukocytes were dependent on the *in situ* inflammatory level—no inflammation signal and no specificity [36]. Leukocyte-based therapies were further determined to cause two unique toxicities: cytokine release syndrome and immune activation syndrome [96], with a risk of secondary malignancies [68]. The clinical trial data of FDA-proved anti-CD19 CAR-T cell therapies indicated an association with B cell malignancies in 50–90% of patients [96]. Not only did leukocytes have secondary malignancy risks, but stem cell-based therapy also revealed a tumorigenicity possibility [107], which was immune-dependent [41]. Stem cells even partially contributed to the recruitment and activation of immune cells to tumor tissues and partially facilitated metastasis [19].

7. Conclusion

In recent decades, increasing efforts have focused on cell-driven drug delivery systems in the tumor area. Most of these were circulatory cells because they had special characteristics that the CAPIR cascade required, but NP-based DDS alone could not achieve to date, such as inherent biocompatibility, long circulation time, active accumulation, high penetration ability, and immune response activation. Despite emerging challenges, cell-driven drug delivery systems have performed well to date in enhancing targeting delivery efficiency. Clues for resolving the current limitations of the NP-DDS were encountered and provided the possibility for the development of precision medicine for cancer diagnosis and therapy.

Abbreviations

aPD1:	Anti-PD-1 monoclonal antibody
ATP:	Adenosine triphosphate
Au:	Aurum
AuNR:	Aurum nanorod
BBB:	Blood-brain barrier
BSA:	Bovine serum albumin
CARs:	Chimeric antigen receptors
CCA:	Cholangiocarcinoma
CCL-2:	C-C motif chemokine ligand 2
CCL-5:	C-C motif chemokine ligand 5
CCL-7:	C-C motif chemokine ligand 7
CCL-8:	C-C motif chemokine ligand 8
CCL-12:	C-C motif chemokine ligand 12
CCL-25:	C-C motif chemokine ligand 25
CCR7:	C-C motif chemokine receptor 7
CD62L:	L-selectin or lectin adhesion molecule 1
Ce6:	Chlorin e6
CSF-1:	Colony-stimulating factor 1
CXCL9:	C-X-C motif chemokine ligand 9
CXCR4:	C-X-C motif chemokine receptor 4
DDS:	Drug delivery system
Dox:	Doxorubicin
ECM:	Extracellular matrix
ECs:	Endothelial cells
EGF:	Epidermal growth factor
EPR:	Enhanced permeability and retention
EVs:	Extracellular vesicles
FasL:	Fas ligand
FDA:	Food and Drug Administration
GDF-15:	Growth differentiation factor
H:	Hour
Her2:	Human epidermal growth factor receptor 2
HGF:	Hepatocyte growth factor
ICAM:	Intercellular cell adhesion molecule
ICAM-1:	Intercellular cell adhesion molecule 1
ICG:	Indocyanine green
IFN-γ:	Interferon γ
IL-1:	Interleukin-1
IL-15Sa:	Interleukin-15 superagonist
IL-17:	Interleukin-17
IL-1β:	Interleukin-1β
IL-2:	Interleukin-2
IL-7:	Interleukin-7
IL-8:	Interleukin-8
IND:	Indoleamine 2,3-dioxygenase 1 inhibitor
LDNG:	Lysozyme-dextran nanogels
LFA-1:	Lymphocyte function-associated antigen 1
LFA-1 (αLβ2):	Lymphocyte function-associated antigen 1, αLβ2
M1:	Macrophage phenotype 1
M2:	Macrophage phenotype 2
Mac-1 (αMβ2):	Macrophage-1 antigen, αMβ2
MAs:	Macrophages
MOs:	Monocytes
MSCs:	Mesenchymal stem cells
MTD:	Maximum tolerated dose
NEs:	Neutrophils
NETs:	Neutrophil extracellular traps
NIR:	Near-infrared
NKG-2D:	Natural killer group protein 2 family member D
NKp30:	Natural killer cell p30-related protein
NKs:	Natural killer cells
NPs:	Nanoparticles
OVA-1:	Ovalbumin-1
PBS:	Phosphate-buffered saline
PD-1:	Programmed cell death protein 1
PDGF:	Platelet-derived growth factor

PDGF-α:	Platelet-derived growth factor α
PDGF-β:	Platelet-derived growth factor β
PD-L1:	Programmed cell death ligand 1
PDT:	Photodynamic therapy
PEG:	Polyethylene glycol
PG:	Polyglycerol
PLGA:	Poly(lactic-co-glycolic acid)
PS:	Polystyrene sphere
PSGL-1:	P-selectin ligand 1
PTX:	Paclitaxel
RBCs:	Red blood cells
RES:	Reticuloendothelial system
RGD:	Arginine-glycine-aspartic
ROS:	Reactive oxygen species
RT:	Room temperature
siRNA:	Small interfering RNA
SMAPs:	Supramolecular attack particles
SN-38:	7-Ethyl-10-hydroxycamptothecin
SWNT:	Single-walled nanotubes
TAT:	Transactivator of transcription
TCRs:	T cell receptors
TNF-α:	Tumor necrosis factor α
TRAIL:	Tumor necrosis factor-related apoptosis-inducing ligand
TSP1:	Thrombospondin-1
VCAM:	Vascular cell adhesion protein
VEGF:	Vascular endothelial growth factor
WHO:	World Health Organization.

Conflicts of Interest

The authors declare no conflict of interest, financial or otherwise.

Authors' Contributions

Pengyu Gao and Dan Zou contributed equally to this work.

Acknowledgments

References

[1] World Health Organization, "WHO - the top 10 causes of death," May 2018, http://www.who.int/en/news-room/fact-sheets/detail/the-top-10-causes-of-death.

[2] J. Shi, P. W. Kantoff, R. Wooster, and O. C. Farokhzad, "Cancer nanomedicine: progress, challenges and opportunities," *Nature Reviews Cancer*, vol. 17, no. 1, pp. 20–37, 2017.

[3] L. Jing, H. Hao, M. Peng, and W. Yuanquan, "Current status and prospect of cancer nanomedicine in clinical translation," *Science & Technology Review*, vol. 36, no. 22, pp. 118–126, 2018.

[4] Q. Sun, Z. Zhou, N. Qiu, and Y. Shen, "Rational design of cancer nanomedicine: nanoproperty integration and synchronization," *Advanced Materials*, vol. 29, no. 14, pp. 1–18, 2017.

[5] J. L. Betker, D. Jones, C. R. Childs et al., "Nanoparticle uptake by circulating leukocytes: a major barrier to tumor delivery," *Journal of Controlled Release*, vol. 286, pp. 85–93, 2018.

[6] R. Mooney, Y. Weng, E. Garcia et al., "Conjugation of PH-responsive nanoparticles to neural stem cells improves intratumoral therapy," *Journal of Controlled Release*, vol. 191, pp. 82–89, 2014.

[7] Y. Zou, S. Ito, F. Yoshino, Y. Suzuki, L. Zhao, and N. Komatsu, "Polyglycerol grafting shields nanoparticles from protein corona formation to avoid macrophage uptake," *ACS Nano*, vol. 14, no. 6, pp. 7216–7226, 2020.

[8] A. C. Anselmo and S. Mitragotri, "Cell-mediated delivery of nanoparticles: taking advantage of circulatory cells to target nanoparticles," *Journal of Controlled Release*, vol. 190, pp. 531–541, 2014.

[9] S. Sindhwani, A. M. Syed, J. Ngai et al., "The entry of nanoparticles into solid tumours," *Nature Materials*, vol. 19, no. 5, pp. 566–575, 2020.

[10] S. Wilhelm, A. J. Tavares, Q. Dai et al., "Analysis of nanoparticle delivery to tumours," *Nature Reviews Materials*, vol. 1, no. 5, 2016.

[11] G. Deng, X. Wang, and Z. Zhiguo, "Y. S. Nano-carriers and their drug release," *Journal of Shanghai Normal University (Natural Sciences)*, vol. 46, no. 6, pp. 780–788, 2017.

[12] B. Huang, W. D. Abraham, Y. Zheng, S. C. Bustamante López, S. S. Luo, and D. J. Irvine, "Active targeting of chemotherapy to disseminated tumors using nanoparticle-carrying T cells," *Science translational medicine*, vol. 7, no. 291, 2015.

[13] C. Zhan and W. Lu, "The blood-brain/tumor barriers: challenges and chances for malignant gliomas targeted drug delivery," *Current Pharmaceutical Biotechnology*, vol. 13, no. 12, pp. 2380–2387, 2012.

[14] Y. Y. Chen, A. M. Syed, P. MacMillan, J. V. Rocheleau, and W. C. W. Chan, "Flow rate affects nanoparticle uptake into endothelial cells," *Advanced Materials*, vol. 32, no. 24, p. 1906274, 2020.

[15] Y. Su, Z. Xie, G. B. Kim, C. Dong, and J. Yang, "Design strategies and applications of circulating cell-mediated drug delivery systems," *ACS Biomaterials Science & Engineering*, vol. 1, no. 4, pp. 201–217, 2015.

[16] X. Dong, D. Chu, and Z. Wang, "Leukocyte-mediated delivery of nanotherapeutics in inflammatory and tumor sites," *Theranostics*, vol. 7, no. 3, pp. 751–763, 2017.

[17] E. L. Siegler, Y. J. Kim, X. Chen et al., "Combination cancer therapy using chimeric antigen receptor-engineered natural killer cells as drug carriers," *Molecular Therapy*, vol. 25, no. 12, pp. 2607–2619, 2017.

[18] W. Zhang, M. Wang, W. Tang et al., "Nanoparticle-laden macrophages for tumor-tropic drug delivery," *Advanced Materials*, vol. 30, no. 50, 2018.

[19] C. Xie, Z. Yang, Y. Suo et al., "Systemically infused mesenchymal stem cells show different homing profiles in healthy and tumor mouse models," *Stem Cells Translational Medicine*, vol. 6, no. 4, pp. 1120–1131, 2017.

[20] M. K. Danquah, X. A. Zhang, and R. I. Mahato, "Extravasation of polymeric nanomedicines across tumor vasculature," *Advanced Drug Delivery Reviews*, vol. 63, no. 8, pp. 623–639, 2011.

[21] S. I. Grivennikov, F. R. Greten, and M. Karin, "Immunity, inflammation, and cancer," *Cell*, vol. 140, no. 6, pp. 883–899, 2010.

[22] X. Wan, S. Zhang, F. Wang et al., "Red blood cell-derived nanovesicles for safe and efficient macrophage-targeted drug deliveryin vivo," *Biomaterials Science*, vol. 7, no. 1, pp. 187–195, 2019.

[23] X. Sun, C. Wang, M. Gao, A. Hu, and Z. Liu, "Remotely controlled red blood cell carriers for cancer targeting and near-infrared light-triggered drug release in combined photothermal-chemotherapy," *Advanced Functional Materials*, vol. 25, no. 16, pp. 2386–2394, 2015.

[24] W. Tang, Z. Zhen, M. Wang et al., "Red blood cell-facilitated photodynamic therapy for cancer treatment," *Advanced Functional Materials*, vol. 26, no. 11, pp. 1757–1768, 2016.

[25] Z. Li, H. Huang, S. Tang et al., "Small gold nanorods laden macrophages for enhanced tumor coverage in photothermal therapy," *Biomaterials*, vol. 74, pp. 144–154, 2016.

[26] G. Solinas, G. Germano, A. Mantovani, and P. Allavena, "Tumor-associated macrophages (TAM) as major players of the cancer-related inflammation," *Journal of Leukocyte Biology*, vol. 86, no. 5, pp. 1065–1073, 2009.

[27] Y. Gu, S. Li, S. Feng et al., "Nanomedicine engulfed by macrophages for targeted tumor therapy," *International Journal of Nanomedicine*, vol. Volume 11, pp. 4107–4124, 2016.

[28] J. Xie, J. Wang, G. Niu et al., "Human serum albumin coated iron oxide nanoparticles for efficient cell labeling," *Chemical Communications*, vol. 46, no. 3, pp. 433–435, 2010.

[29] M. R. Choi, K. J. Stanton-Maxey, J. K. Stanley et al., "A cellular Trojan horse for delivery of therapeutic nanoparticles into tumors," *Nano Letters*, vol. 7, no. 12, pp. 3759–3765, 2007.

[30] J. Choi, H. Y. Kim, E. J. Ju et al., "Use of macrophages to deliver therapeutic and imaging contrast agents to tumors," *Biomaterials*, vol. 33, no. 16, pp. 4195–4203, 2012.

[31] S. A. Rosenberg, N. P. Restifo, J. C. Yang, R. A. Morgan, and M. E. Dudley, "Adoptive cell transfer: a clinical path to effective cancer immunotherapy," *Nature Reviews. Cancer*, vol. 8, no. 4, pp. 299–308, 2008.

[32] A. Pitchaimani, T. D. T. Nguyen, R. Marasini et al., "Biomimetic natural killer membrane camouflaged polymeric nanoparticle for targeted bioimaging," *Advanced Functional Materials*, vol. 29, no. 4, p. 1806817, 2019.

[33] V. Brinkmann and A. Zychlinsky, "Beneficial suicide: why neutrophils die to make NETs," *Nature Reviews. Microbiology*, vol. 5, no. 8, pp. 577–582, 2007.

[34] W. M. Nauseef and N. Borregaard, "Neutrophils at work," *Nature Immunology*, vol. 15, no. 7, pp. 602–611, 2014.

[35] N. Borregaard, "Neutrophils, from marrow to microbes," *Immunity*, vol. 33, no. 5, pp. 657–670, 2010.

[36] J. Xue, Z. Zhao, L. Zhang et al., "Neutrophil-mediated anticancer drug delivery for suppression of postoperative malignant glioma recurrence," *Nature Nanotechnology*, vol. 12, no. 7, pp. 692–700, 2017.

[37] D. Vestweber, "Adhesion and signaling molecules controlling the transmigration of leukocytes through endothelium," *Immunological Reviews*, vol. 218, no. 1, pp. 178–196, 2007.

[38] C. Ju, Y. Wen, L. Zhang et al., "Neoadjuvant chemotherapy based on Abraxane/human neutrophils cytopharmaceuticals with radiotherapy for gastric cancer," *Small*, vol. 15, no. 5, p. 1804191, 2019.

[39] I. Mishalian, R. Bayuh, L. Levy, L. Zolotarov, J. Michaeli, and Z. G. Fridlender, "Tumor-associated neutrophils (TAN) develop pro-tumorigenic properties during tumor progression," *Cancer Immunology, Immunotherapy*, vol. 62, no. 11, pp. 1745–1756, 2013.

[40] D. Dapkute, S. Steponkiene, D. Bulotiene, L. Saulite, U. Riekstina, and R. Rotomskis, "Skin-derived mesenchymal stem cells as quantum dot vehicles to tumors," *International Journal of Nanomedicine*, vol. Volume 12, pp. 8129–8142, 2017.

[41] C. Xu, L. Lin, G. Cao et al., "Interferon-α-secreting mesenchymal stem cells exert potent antitumor effect *in vivo*," *Oncogene*, vol. 33, no. 42, pp. 5047–5052, 2014.

[42] S. Chandrasekaran, M. J. McGuire, and M. R. King, "Sweeping lymph node micrometastases off their feet: an engineered model to evaluate natural killer cell mediated therapeutic intervention of circulating tumor cells that disseminate to the lymph nodes," *Lab on a Chip*, vol. 14, no. 1, pp. 118–127, 2014.

[43] L. Wayteck, H. Dewitte, L. De Backer et al., "Hitchhiking nanoparticles: reversible coupling of lipid-based nanoparticles to cytotoxic T lymphocytes," *Biomaterials*, vol. 77, no. -November, pp. 243–254, 2016.

[44] S. J. Park, Y. Lee, Y. J. Choi et al., "Monocyte-based microrobot with chemotactic motility for tumor theragnosis," *Biotechnology and Bioengineering*, vol. 111, no. 10, pp. 2132–2138, 2014.

[45] B. R. Smith, E. E. B. Ghosn, H. Rallapalli et al., "Selective uptake of single-walled carbon nanotubes by circulating monocytes for enhanced tumour delivery," *Nature Nanotechnology*, vol. 9, no. 6, pp. 481–487, 2014.

[46] M. Gao, A. Hu, X. Sun et al., "Photosensitizer decorated red blood cells as an ultrasensitive light-responsive drug delivery system," *ACS Applied Materials & Interfaces*, vol. 9, no. 7, pp. 5855–5863, 2017.

[47] B. P. Joshi, J. Hardie, M. A. Mingroni, and M. E. Farkas, "Surface-modified macrophages facilitate tracking of breast cancer-immune interactions," *ACS Chemical Biology*, vol. 13, no. 8, pp. 2339–2346, 2018.

[48] P. Wang, X. Wang, Q. Luo et al., "Fabrication of red blood cell-based multimodal theranostic probes for second near-infrared window fluorescence imaging-guided tumor surgery and photodynamic therapy," *Theranostics*, vol. 9, no. 2, pp. 369–380, 2019.

[49] A. C. Anselmo, J. B. Gilbert, S. Kumar et al., "Monocyte-mediated delivery of polymeric backpacks to inflamed tissues: a generalized strategy to deliver drugs to treat inflammation," *Journal of Controlled Release*, vol. 199, pp. 29–36, 2015.

[50] K. A. Davis, P.-J. Wu, C. F. Cahall, C. Li, A. Gottipati, and B. J. Berron, "Coatings on mammalian cells: interfacing cells with their environment," *Journal of Biological Engineering*, vol. 13, no. 1, 2019.

[51] L. Tang, Y. Zheng, M. B. Melo et al., "Enhancing T cell therapy through TCR-signaling-responsive nanoparticle drug delivery," *Nature Biotechnology*, vol. 36, no. 8, pp. 707–716, 2018.

[52] L. Li, Y. Guan, H. Liu et al., "Silica nanorattle-doxorubicin-anchored mesenchymal stem cells for tumor-tropic therapy," *ACS Nano*, vol. 5, no. 9, pp. 7462–7470, 2011.

[53] M. Xu, S. Asghar, S. Dai et al., "Mesenchymal stem cells-curcumin loaded chitosan nanoparticles hybrid vectors for

tumor-tropic therapy," *International Journal of Biological Macromolecules*, vol. 134, pp. 1002–1012, 2019.

[54] M. T. Stephan, J. J. Moon, S. H. Um, A. Bershteyn, and D. J. Irvine, "Therapeutic cell engineering with surface-conjugated synthetic nanoparticles," *Nature Medicine*, vol. 16, no. 9, pp. 1035–1041, 2010.

[55] K. Chaudagar, N. Landon-Brace, A. Solanki et al., *Cabozantinib unlocks efficient in vivo targeted delivery of neutrophil-loaded nanoparticles into murine prostate tumors*, bioRxiv, 2020.

[56] Z. Xiao, Z. Su, S. Han, J. Huang, L. Lin, and X. Shuai, "Dual PH-sensitive nanodrug blocks PD-1 immune checkpoint and uses T cells to deliver NF-*K*B inhibitor for antitumor immunotherapy," *Science Advances*, vol. 6, no. 6, 2020.

[57] S. Chandrasekaran, M. F. Chan, J. Li, and M. R. King, "Super natural killer cells that target metastases in the tumor draining lymph nodes," *Biomaterials*, vol. 77, pp. 66–76, 2016.

[58] H. Cheng, C. J. Kastrup, R. Ramanathan et al., "Nanoparticulate cellular patches for cell-mediated tumoritropic delivery," *ACS Nano*, vol. 4, no. 2, pp. 625–631, 2010.

[59] M. T. Stephan, S. B. Stephan, P. Bak, J. Chen, and D. J. Irvine, "Synapse-directed delivery of immunomodulators using T-cell-conjugated nanoparticles," *Biomaterials*, vol. 33, no. 23, pp. 5776–5787, 2012.

[60] D. Neil, "Nanoparticle albumin-bound paclitaxel (Abraxane®)," in *Albumin in Medicine*, M. Otagiri and V. T. G. Chuang, Eds., pp. 101–119, Springer, Singapore, 2016.

[61] D. C. Pan, J. W. Myerson, J. S. Brenner et al., "Nanoparticle properties modulate their attachment and effect on carrier red blood cells," *Scientific Reports*, vol. 8, no. 1, p. 1615, 2018.

[62] W. Jiang, B. Y. S. Kim, J. T. Rutka, and W. C. W. Chan, "Nanoparticle-mediated cellular response is size-dependent," *Nature Nanotechnology*, vol. 3, no. 3, pp. 145–150, 2008.

[63] S. K. Patel, Y. Zhang, J. A. Pollock, and J. M. Janjic, "Cyclooxgenase-2 inhibiting perfluoropoly (ethylene glycol) ether theranostic nanoemulsions—in vitro study," *PLoS One*, vol. 8, no. 2, article e55802, 2013.

[64] L. Pang, J. Qin, L. Han et al., "Exploiting macrophages as targeted carrier to guide nanoparticles into glioma," *Oncotarget*, vol. 7, no. 24, pp. 37081–37091, 2016.

[65] L. C. Kennedy, A. S. Bear, J. K. Young et al., "T cells enhance gold nanoparticle delivery to tumors in vivo," *Nanoscale Research Letters*, vol. 6, no. 1, p. 283, 2011.

[66] S. Qu, F. Sun, Z. Qiao, J. Li, and L. Shang, "In situ investigation on the protein corona formation of quantum dots by using fluorescence resonance energy transfer," *Small*, vol. 16, no. 21, 2020.

[67] V. NguyenDu, H. K. Min, D. H. Kim et al., "Macrophage-mediated delivery of multifunctional nanotherapeutics for synergistic chemo-photothermal therapy of solid tumors," *ACS Applied Materials & Interfaces*, vol. 12, no. 9, pp. 10130–10141, 2020.

[68] J. Fu, D. Wang, D. Mei et al., "Macrophage mediated biomimetic delivery system for the treatment of lung metastasis of breast cancer," *Journal of Controlled Release*, vol. 204, pp. 11–19, 2015.

[69] X. Wang, J.-Q. GAO, X. Ouyang, J. Wang, X. Sun, and Y. Lv, "Mesenchymal stem cells loaded with paclitaxel–poly(lactic-*co*-glycolic acid) nanoparticles for glioma-targeting therapy," *International Journal of Nanomedicine*, vol. Volume 13, pp. 5231–5248, 2018.

[70] U. Steinfeld, C. Pauli, N. Kaltz, C. Bergemann, and H.-H. Lee, "T lymphocytes as potential therapeutic drug carrier for cancer treatment," *International Journal of Pharmaceutics*, vol. 311, no. 1–2, pp. 229–236, 2006.

[71] V. NguyenDu, J. Han, G. Go et al., "Feasibility study of dual-targeting paclitaxel-loaded magnetic liposomes using electromagnetic actuation and macrophages," *Sensors and Actuators B: Chemical*, vol. 240, pp. 1226–1236, 2017.

[72] W.-C. Huang, W.-H. Chiang, Y.-H. Cheng et al., "Tumortropic monocyte-mediated delivery of echogenic polymer bubbles and therapeutic vesicles for chemotherapy of tumor hypoxia," *Biomaterials*, vol. 71, pp. 71–83, 2015.

[73] Z. Huang, X. Sun, X. Liu, Y. Shen, and K. Wang, "Macrophages as an active tumour-targeting carrier of SN38-nanoparticles for cancer therapy," *Journal of Drug Targeting*, vol. 26, no. 5–6, pp. 458–465, 2018.

[74] G. Moku, B. Layek, L. Trautman, S. Putnam, J. Panyam, and S. Prabha, "Improving payload capacity and anti-tumor efficacy of mesenchymal stem cells using TAT peptide functionalized polymeric nanoparticles," *Cancers (Basel).*, vol. 11, no. 4, p. 491, 2019.

[75] E. Scarpa, J. L. Bailey, A. A. Janeczek et al., "Quantification of intracellular payload release from polymersome nanoparticles," *Scientific Reports*, vol. 6, no. 1, 2016.

[76] F. Danhier, "To exploit the tumor microenvironment: since the EPR effect fails in the clinic, what is the future of nanomedicine?," *Journal of Controlled Release*, vol. 244, Part A, pp. 108–121, 2016.

[77] Š. Balint, S. Müller, R. Fischer et al., "Supramolecular attack particles are autonomous killing entities released from cytotoxic T cells," *Science*, vol. 368, no. 6493, pp. 897–901, 2020.

[78] L. Keren, M. Bosse, D. Marquez et al., "A structured tumor-immune microenvironment in triple negative breast cancer revealed by multiplexed ion beam imaging," *Cell*, vol. 174, no. 6, pp. 1373–1387.e19, 2018.

[79] A. Parodi, N. Quattrocchi, A. L. Van De Ven et al., "Synthetic nanoparticles functionalized with biomimetic leukocyte membranes possess cell-like functions," *Nature Nanotechnology*, vol. 8, no. 1, pp. 61–68, 2013.

[80] C. Hu, T. Lei, Y. Wang et al., "Phagocyte-membrane-coated and laser-responsive nanoparticles control primary and metastatic cancer by inducing anti-tumor immunity," *Biomaterials*, vol. 255, p. 120159, 2020.

[81] X. Cao, T. Tan, D. Zhu et al., "Paclitaxel-loaded macrophage membrane camouflaged albumin nanoparticles for targeted cancer therapy," *International Journal of Nanomedicine*, vol. Volume 15, pp. 1915–1928, 2020.

[82] R. Molinaro, C. Corbo, J. O. Martinez et al., "Biomimetic proteolipid vesicles for targeting inflamed tissues," *Nature Materials*, vol. 15, no. 9, pp. 1037–1046, 2016.

[83] X. Huang, B. Wu, J. Li et al., "Anti-tumour effects of red blood cell membrane-camouflaged black phosphorous quantum dots combined with chemotherapy and anti-inflammatory therapy," *Artificial Cells, Nanomedicine, and Biotechnology*, vol. 47, no. 1, pp. 968–979, 2019.

[84] C.-M. J. Hu, R. H. Fang, K. C. Wang et al., "Nanoparticle biointerfacing by platelet membrane cloaking," *Nature*, vol. 526, no. 7571, pp. 118–121, 2015.

[85] N. E. Toledano Furman, Y. Lupu-Haber, T. Bronshtein et al., "Reconstructed stem cell nanoghosts: a natural tumor

targeting platform," *Nano Letters*, vol. 13, no. 7, pp. 3248–3255, 2013.

[86] X. Xie, X. Hu, Q. Li et al., "Unraveling cell-type-specific targeted delivery of membrane-camouflaged nanoparticles with plasmonic imaging," *Nano Letters*, vol. 20, no. 7, pp. 5228–5235, 2020.

[87] W. L. Liu, T. Liu, M. Z. Zou et al., "Aggressive man-made red blood cells for hypoxia-resistant photodynamic therapy," *Advanced Materials*, vol. 30, no. 35, p. 1802006, 2018.

[88] J. Guo, J. O. Agola, R. Serda et al., "Biomimetic rebuilding of multifunctional red blood cells: modular design using functional components," *ACS Nano*, vol. 14, no. 7, pp. 7847–7859, 2020.

[89] J. W. Hindley, D. G. Zheleva, Y. Elani et al., "Building a synthetic mechanosensitive signaling pathway in compartmentalized artificial cells," *Proceedings of the National Academy of Sciences*, vol. 116, no. 34, pp. 16711–16716, 2019.

[90] H. Zhang, D. Freitas, H. S. Kim et al., "Identification of distinct nanoparticles and subsets of extracellular vesicles by asymmetric flow field-flow fractionation," *Nature Cell Biology*, vol. 20, no. 3, pp. 332–343, 2018.

[91] J. M. Gudbergsson, K. Jønsson, J. B. Simonsen, and K. B. Johnsen, "Systematic review of targeted extracellular vesicles for drug delivery - considerations on methodological and biological heterogeneity," *Journal of Controlled Release*, vol. 306, pp. 108–120, 2019.

[92] V. R. Minciacchi, S. You, C. Spinelli et al., "Large oncosomes contain distinct protein cargo and represent a separate functional class of tumor-derived extracellular vesicles," *Oncotarget*, vol. 6, no. 13, pp. 11327–11341, 2015.

[93] J. Kim, J. E. Lee, J. Lee et al., "Magnetic fluorescent delivery vehicle using uniform mesoporous silica spheres embedded with monodisperse magnetic and semiconductor nanocrystals," *Journal of the American Chemical Society*, vol. 128, no. 3, pp. 688-689, 2006.

[94] B. Yang, Y. Chen, and J. Shi, "Exosome biochemistry and advanced nanotechnology for next-generation theranostic platforms," *Advanced Materials*, vol. 31, no. 2, 2019.

[95] L. Yang, D. Han, Q. Zhan et al., "Blood TfR+ exosomes separated by a PH-responsive method deliver chemotherapeutics for tumor therapy," *Theranostics*, vol. 9, no. 25, pp. 7680–7696, 2019.

[96] W. Fu, C. Lei, S. Liu et al., "CAR exosomes derived from effector CAR-T cells have potent antitumour effects and low toxicity," *Nature Communications*, vol. 10, no. 1, p. 4355, 2019.

[97] C. C. Chen, L. Liu, F. Ma et al., "Elucidation of exosome migration across the blood–brain barrier model in vitro," *Cellular and Molecular Bioengineering*, vol. 9, no. 4, pp. 509–529, 2016.

[98] I. Parolini, C. Federici, C. Raggi et al., "Microenvironmental pH is a key factor for exosome traffic in tumor cells," *The Journal of Biological Chemistry*, vol. 284, no. 49, pp. 34211–34222, 2009.

[99] Y. Tian, S. Li, J. Song et al., "A doxorubicin delivery platform using engineered natural membrane vesicle exosomes for targeted tumor therapy," *Biomaterials*, vol. 35, no. 7, pp. 2383–2390, 2014.

[100] J. Wang, W. Li, L. Zhang et al., "Chemically edited exosomes with dual ligand purified by microfluidic device for active targeted drug delivery to tumor cells," *ACS Applied Materials & Interfaces*, vol. 9, no. 33, pp. 27441–27452, 2017.

[101] B. Dumontel, F. Susa, T. Limongi et al., "ZnO nanocrystals shuttled by extracellular vesicles as effective Trojan nanohorses against cancer cells," *Nanomedicine*, vol. 14, no. 21, pp. 2815–2833, 2019.

[102] Q. Zhan, K. Yi, H. Qi et al., "Engineering blood exosomes for tumor-targeting efficient gene/chemo combination therapy," *Theranostics*, vol. 10, no. 17, pp. 7889–7905, 2020.

[103] W. M. Usman, T. C. Pham, Y. Y. Kwok et al., "Efficient RNA drug delivery using red blood cell extracellular vesicles," *Nature Communications*, vol. 9, no. 1, p. 2359, 2018.

[104] Y. Gao, H. Zhang, N. Zhou et al., "Methotrexate-loaded tumour-cell-derived microvesicles can relieve biliary obstruction in patients with extrahepatic cholangiocarcinoma," *Nature Biomedical Engineering*, vol. 4, no. 7, pp. 743–753, 2020.

[105] A. Gonda, R. Moyron, J. Kabagwira, P. A. Vallejos, and R. N. Wall, "Cellular-defined microenvironmental internalization of exosomes," in *Extracellular Vesicles and Their Importance in Human Health*, G. D. B. Ana and A. R. C. Jose, Eds., pp. 1–30, IntechOpen, 2020.

[106] A. Gros, M. R. Parkhurst, E. Tran et al., "Prospective identification of neoantigen-specific lymphocytes in the peripheral blood of melanoma patients," *Nature Medicine*, vol. 22, no. 4, pp. 433–438, 2016.

[107] L. Gruen and L. Grabel, "Concise review: scientific and ethical roadblocks to human embryonic stem cell therapy," *Stem Cells*, vol. 24, no. 10, pp. 2162–2169, 2006.

Review Article

Stem Cell-Derived Nanovesicles: A Novel Cell-Free Therapy for Wound Healing

Jianghong Huang,[1,2] Jun Zhang,[2] Jianyi Xiong,[1] Shuqing Sun,[3] Jiang Xia [ID],[4] Lei Yang [ID],[1] and Yujie Liang [ID][5]

[1]*Department of Orthopedics, Shenzhen Second People's Hospital (First Affiliated Hospital of Shenzhen University, Health Science Center), Shenzhen 518035, China*
[2]*Tsinghua University Shenzhen International Graduate School, Class 9 of 2020 Engineering Ph.D., Shenzhen 518055, China*
[3]*Tsinghua University Shenzhen International Graduate School, Institute of Biomedicine and Health Engineering, Shenzhen 518055, China*
[4]*Department of Chemistry, The Chinese University of Hong Kong, Sha Tin, Hong Kong SAR, China*
[5]*Department of Child and Adolescent Psychiatry, Shenzhen Kangning Hospital, Shenzhen Mental Health Center, Shenzhen Key Laboratory for Psychological Healthcare & Shenzhen Institute of Mental Health, Shenzhen 518020, China*

Correspondence should be addressed to Jiang Xia; jiangxia@cuhk.edu.hk, Lei Yang; yiyuanbgs@126.com, and Yujie Liang; liangyjie@126.com

Wound healing and regeneration are a dynamic and complex process that requires a collaborative effort between growth factors, epidermal cells, dermal cells, extracellular matrix, and vessels local to the wound area. Mesenchymal stem cells participate in the recruitment site, mainly by releasing secretory factors and matrix proteins to promote wound healing. Stem cell-derived nanovesicles (CDNs), including microvesicles, exosomes, and exosome mimetics, contain most of the biologically active substances of their parent cells and have similar effects. CDNs can shuttle various proteins, messenger RNAs, and microRNAs to regulate the activity of receptor cells, and they play important roles in skin wound healing. This article reviews recent research progress on CDNs for wound repair. We summarize current knowledge on how CDNs regulate immunity, fibroblast activity, angiogenesis, and scar formation in the wound healing process. This review can help researchers explore new treatment strategies to enhance the therapeutic efficacy of CDNs, which have a promising future as naturally cell-free therapies.

1. Introduction

Approximately 100 million people suffer pain or discomfort from chronic wounds each year. Clinically, chronic wounds are common in large-area burns, late residual wounds, diabetic foot ulcers, venous leg ulcers, and pressure ulcers. The mildest wound is limited to the epidermis of the skin, while a more severe wound breaks the skin and subcutaneous tissue, and severe trauma can fracture the muscle, muscle bonds, and nerves. Wound healing refers to the healing process after the skin tissue is damaged by external forces and includes the complex, synergistic combination of tissue regeneration, granulation tissue hyperplasia, and scar tissue formation.

The development and application of tissue-engineered skin for wound healing has made significant progress. Some skin grafts and skin substitutes have been used clinically; however, they cannot meet the needs of patients with severe skin defects. In recent years, many researchers have applied mesenchymal stem cells (MSCs) as a type of pluripotent stem cell with self-renewal and multidirectional differentiation capabilities. Extracellular microvesicles (EVs) and exosomes (Exo) derived from MSCs are highly enriched in secreted bioactive factors. MSC-derived nanovesicles have

been proposed as a new "cell-free" treatment for skin wounds [1]. Compared with MSCs, cell-derived nanovesicles (CDNs) have shown not only higher therapeutic efficiency but also more convenient preparation, storage, transport, and administration. Moreover, they avoid the risk of immune rejection and tumorigenesis that come with stem cell transplantation. Therefore, MSC-derived nanovesicle-mediated therapy may be safer and more efficient than MSC-based therapy. Since 2015, many studies have explored CDNs for skin wound healing [2, 3] (Table 1 and Figure 1).

In this review, the roles of CDNs in skin wound healing are overviewed. In particular, the important roles of CDNs in each phase of the wound healing process are described. The mechanisms of action of CDNs are further discussed. The use of CDNs in combination with hydrogels for the treatment of skin wounds is also described.

2. Biological Characteristics of CDNs

Exos, EVs, and Exo mimetics are three types of nanoscale membrane vesicles that originate from native cells (Figure 2). Exos are secreted into the extracellular environment by a variety of cell types and tissues. The membrane surface markers of Exos mainly include CD9, CD63, CD81, and heat shock protein 70 (HSP70). Negative staining electron microscopy has shown that Exos isolated from different body fluids have a high degree of morphological diversity. Exos are cup-shaped under transmission electron microscopes, while they have a round morphology under cryoelectron microscopes. Immunogold labelling of Exos has been used to show the location of positive proteins (e.g., CD63) on Exos.

The biogenesis of Exos is a strict and refined regulation process that is divided into 3 stages: (1) deformation and invagination of the plasma membrane, (2) encapsulation of intracellular material to form vesicles and gradual fusion of the plasma membrane to support the formation of multivesicular bodies (MVBs), and (3) exocytosis of MVBs to form Exos. EVs (100–1000 nm in diameter) are secreted by shedding of the plasma membrane or outward budding. Exo mimetics are a type of nanovesicle with a similar size, morphology, and membrane protein labeling to native Exos. High-activity Exo analogs can be produced in large quantities by continuous extrusion.

Most cells and tissues can release CDNs, including MSCs, oligodendrocytes, B cells, T cells, endothelial cells, epithelial cells, tumor cells, adipose tissue, and cartilage tissue. CDNs carry DNA, microRNAs (miRNAs), proteins, cytokines, and membrane lipids from their parent cells, and they can release, transport, and transfer these molecules to recipient cells (such as endothelial cells, keratinocytes, and fibroblasts) to regulate a variety of biological processes, including inflammation, cellular immunity, cell proliferation, cell apoptosis, cell migration, and vascularization [4]. The surface of CDNs contains various lipids, including diglycerides, cholesterol, sphingolipids, and phospholipids, that maintain their nanostructure. The lipid bilayer membrane structure facilitates delivery of the vesicles to target cells and protects their protein, cytokine, and RNA cargo from degradation. In addition, the lipid component includes

signaling molecules that can participate in various cellular responses. CDNs contain a variety of proteins and genetic material that play important roles in their therapeutic effects. In terms of their protein component, CDNs contain proteins that are involved in angiogenesis and coagulation processes [5]. Exosomal matrix metalloproteinase (MMP) has been identified as an important mediator of angiogenesis [6, 7]. Fibroblast growth factor 2 (FGF2), vascular endothelial growth factor (VEGF), hepatocyte growth factor (HGF), and platelet-derived growth factor BB (PDGF-BB) have been identified in Exos and can stimulate angiogenesis [7]. In addition, tissue factor (TF) from platelets and monocytes has been detected in EVs, and TF is an important substance in the exogenous coagulation cascade [8]. Exos derived from dendritic cells contain major histocompatibility complex (MHC) class I molecules that can activate the response of CD8+ T cells, suggesting that EVs may serve as a source of extracellular antigens to activate immune intervention, enhance the antibacterial ability of wounds, and ultimately promote wound healing [9]. In terms of genetic biomolecules, a large number of messenger RNAs (mRNAs) and miRNAs carrying information from the parent cells have been found in EVs released in cell culture and body fluids. These genetic molecules are sorted and secreted by CDNs and then act on target cells to promote a variety of biological functions, such as angiogenesis and tissue repair. It has recently been discovered that MSC-derived EVs can mediate mRNA delivery to regulate the transcription of tissue-specific mRNAs, indicating that the mRNA present in stem cell-derived nanoparticles has a regulatory function [10]. Deregibus et al. found that EVs derived from endothelial progenitor cells activate endothelial cell angiogenesis through horizontal mRNA transfer [11]. In addition, there is evidence that EV mRNA can be translated into protein after being transferred to recipient endothelial cells, which was shown to activate the phosphoinositide 3 kinase (PI3K)/protein kinase B (AKT) signaling pathway and accelerate angiogenesis [11, 12]. The above studies provide evidence for the roles of EV mRNA and miRNA in the regulation of biological processes, but further research is still needed to fully understand the roles of EVs as gene carriers.

CDNs can act on recipient cells in a variety of ways. Through receptor-ligand interactions, binding of CDNs to cell surface receptors activates signaling pathways that mediate internalization by endocytosis [13]. CDNs can also be internalized through phagocytosis, pinocytosis, and micropinocytosis [14]. Their information-rich cargoes are then transmitted to the target cells to regulate the microenvironment and related protein functions [15].

3. MSC-Derived Nanovesicles in Wound Healing

MSCs have the potential for multidirectional differentiation, self-replication, and renewal, and they are often used as seed cells in the field of tissue regeneration [16]. MSCs can be obtained from many adult tissues. The most used sources of MSCs are bone marrow and adipose tissue [17, 18]. They can also be separated from a range of other tissues, including

TABLE 1: Overview of research on the use of CDNs for wound healing.

Cell source	Wound type	Function	Reference
LPS-pretreated hUC-MSCs	Diabetic cutaneous wound	Suppress inflammation and promote healing of diabetic wounds	[63]
H_2O_2-pretreated ADSCs	Skin flap model: ligation of blood vessels and blood perfusion	Improve the survival rate of animals with skin flaps; promote neovascularization and inhibit inflammation and cell apoptosis	[70]
Salidroside-pretreated mouse MSCs	Diabetic wound	Accelerate reepithelialization and wound closure	[71]
Pioglitazone-pretreated BMSCs	Diabetic wound	Promote angiogenesis and enhance wound repair	[72]
Neonatal serum-pretreated BMSCs	Skin wound healing model	Promote angiogenesis	[73]
Melatonin-pretreated hBMSCs	Rat diabetic wound healing model	Immunosuppressive effects	[38]
hUC-MSCs	Scratch assay and human skin permeation	Accelerate collagen synthesis and cell migration	[74]
hUC-MSCs	Rat burn injury model	Enhance wound closure and inhibit skin cell apoptosis	[2]
hUC-MSCs	Severe burn	Suppress inflammation and promote neovascularization	[75]
hUC-MSCs	Rat model of deep second-degree burn injury	Accelerate angiogenesis	[76]
hiPSCs	UV irradiation damage of human dermal fibroblasts	Ameliorate aging of skin fibroblasts	[77]
hiPSC-MSCs	Rat skin wound model	Promote collagen synthesis and enhance angiogenesis	[50]
Menstrual blood-derived MSCs	Diabetic foot ulcer	Suppress inflammation and accelerate wound healing	[78]
Human fibrocytes	Genetically diabetic ulcers	Enhance angiogenesis and augment keratinocyte proliferation and migration	[46]
Platelet-rich plasma	Rat diabetic wound model	Promote reepithelialization	[79]
Platelets	Ischemic wound healing	Regulate collagen synthesis and restore dermal architecture	[80]
Human dermal fibroblasts	UVB-induced skin photoaging	Reduce skin photoaging and inflammation	[81]
Human endothelial progenitor cells	Rat diabetic wound model	Regulate endothelial function	[82]
Human urine-derived stem cells	Mouse diabetic wound model	Promote the angiogenic activities of endothelial cells	[44]
Macrophage-derived Exos	Diabetic wound model	Promote endothelial cell proliferation, angiogenesis, and reepithelialization	[83]
Human amniotic epithelial cells	Rat full-thickness skin wound model	Stimulate fibroblast proliferation and migration; decrease scar formation	[55]
Oral mucosal epithelial cells	Rat full-thickness skin wound model	Proregenerative effects	[84]

Abbreviations: ADSC: adipose-derived MSC; BMSC: bone marrow-derived MSC; hiPSC: human-induced pluripotent stem cell; hUC-MSC: human umbilical cord-derived MSC; LPS: lipopolysaccharide.

Wharton's glue, cord blood [19], placenta [20], brain [21], and synovial fluid [22, 23]. Nearly a dozen studies have confirmed that MSCs play a positive role in wound repair. They participate in the entire process of wound repair and exert a variety of biological effects. Intradermal injection of MSCs is a common method that can promote skin damage repair, but the area and depth of the injection cannot be controlled and it may also cause additional tissue damage. As injected MSCs lack adhesion to the extracellular matrix (ECM), they suffer from poor cell persistence and survival upon engraftment [24]. These problems limit the ultimate therapeutic potential of MSCs for wound repair.

Compared with MSCs, MSC-derived nanovesicles have several obvious advantages. First, CDNs can directly fuse with target cells and exert a strong biological effect. Second, their cargo is protected from degradation by the lipid bilayer. Third, the concentration, dosage, and route of administration of CDNs is more controllable. Fourth, CDN therapy can avoid the risks of immune rejection and tumor occurrence that may be caused by the cell transplant. Therefore, MSC-derived nanovesicles can be used as an alternative to MSCs in the future. Researchers have reported applications of MSC-derived nanovesicles for wound repair in rat and mouse models since 2015 (Figure 3). In Table 1, we have
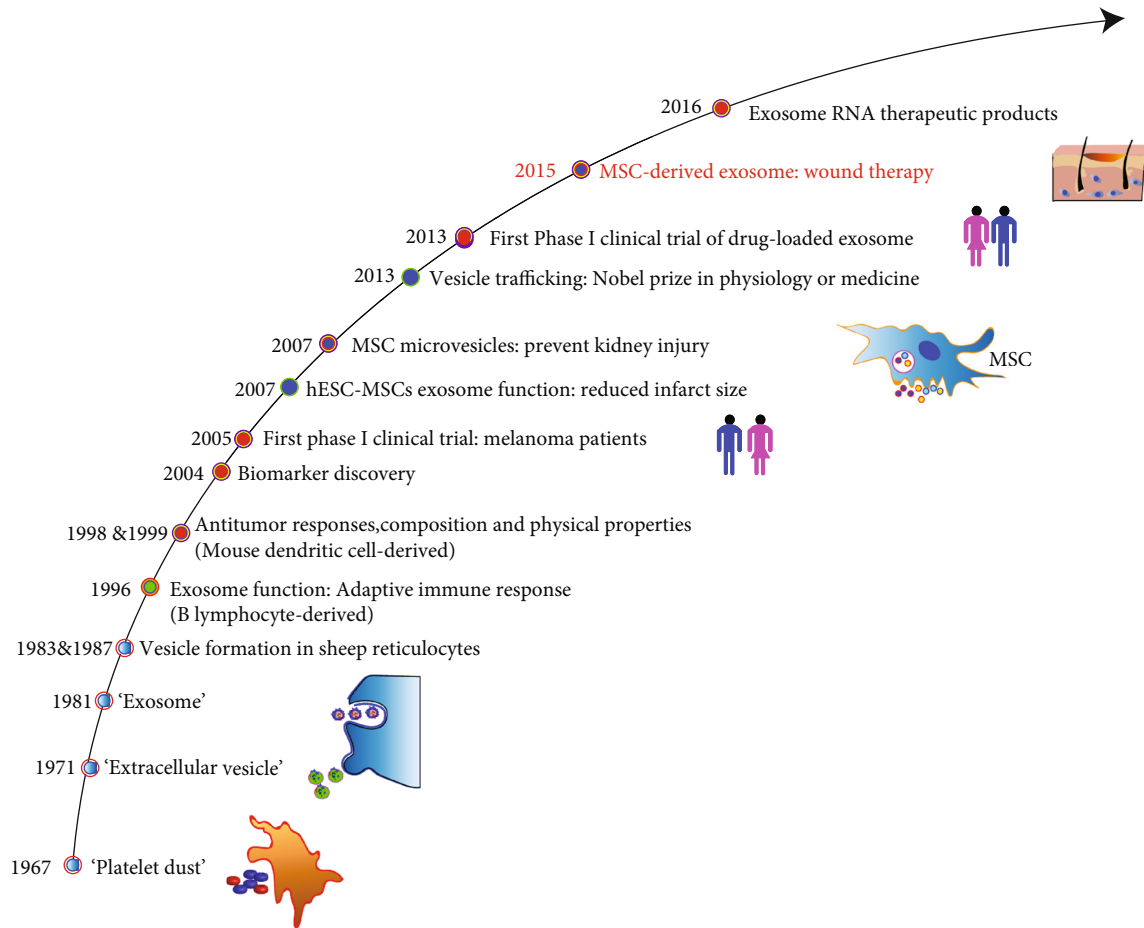
FIGURE 1: Timeline of the discovery and application of CDNs.
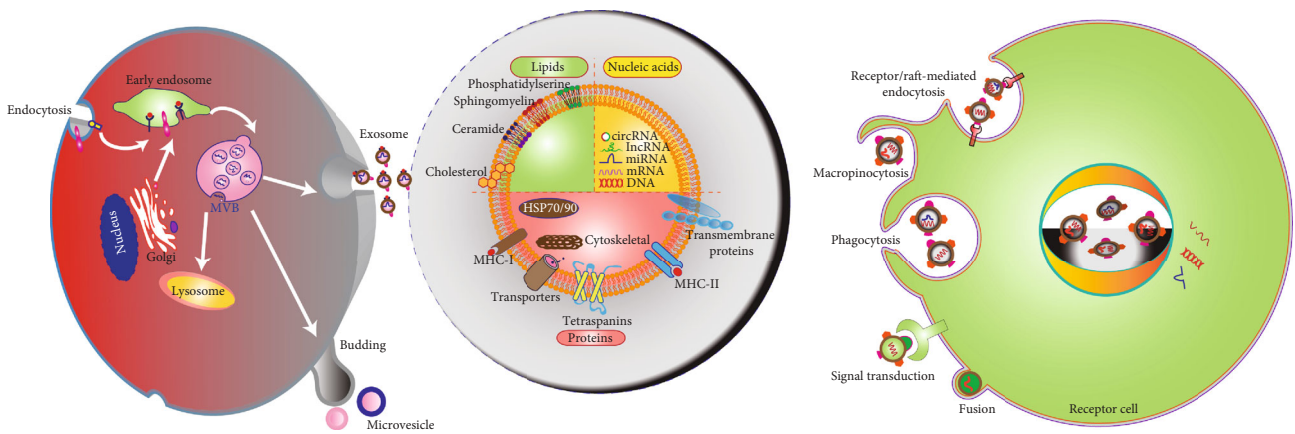
FIGURE 2: Schematic diagram of CDN biogenesis, structural composition, and cellular internalization. Exos are formed following plasma membrane invagination to form MVBs that are then exocytosed. The main components of CDNs are lipids, proteins, and nucleic acids. CDN lipids include cholesterol, ceramides, and phosphatidylserines, while CDN proteins include ubiquitous tetraspanins (CD9, CD63, and CD81) and HSPs. CDNs can (i) trigger cell signal transduction through intracellular signaling pathways and release of secretory contents; (ii) fuse with cell membranes, transfer proteins and genetic content, and enter the cytoplasm of recipient cells; and (iii) be endocytosed through phagocytosis, macropinocytosis, or receptor-mediated endocytosis.

summarized the research on the use of MSC-derived nanovesicles for wound healing. The supernatant of cell culture was used to collect CDNs. Usually, ultracentrifugation was used for purification of CDNs, but the yield is low. Other additional purification steps, including size exclusion chromatography and sucrose or OptiPrep density gradients showed better yield and purity. Standardization is essential for the application of CDNs. Characterization of CDNs
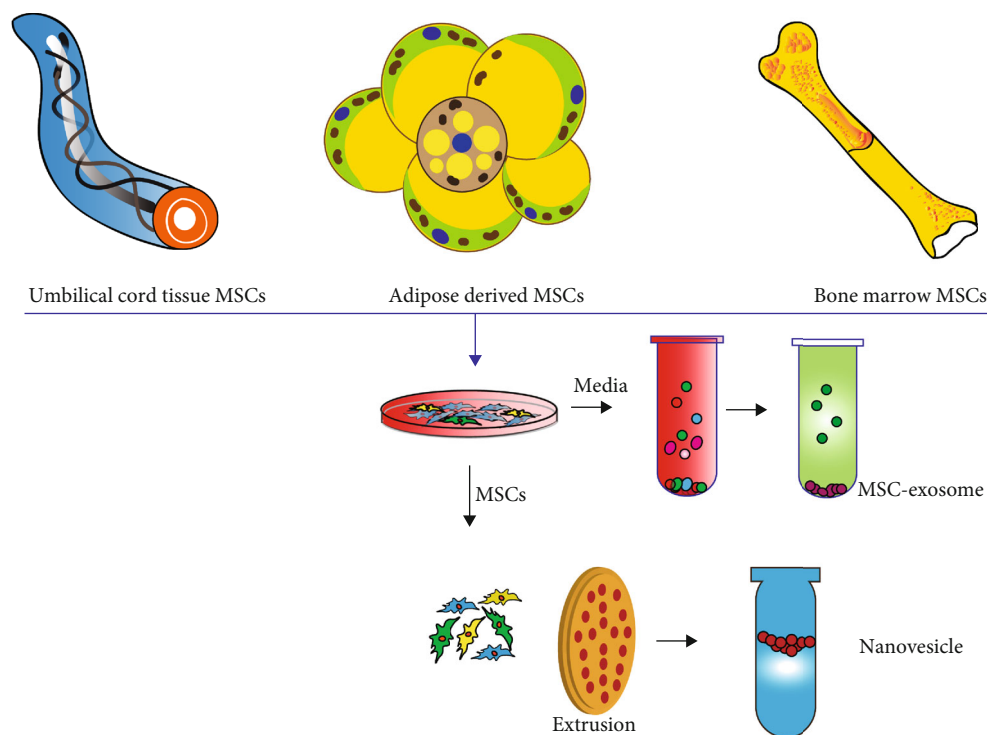
FIGURE 3: MSCs derived nanovesicles as a cell-free therapy for wound repair.

includes western blotting, liquid chromatography, and mass spectrometry for proteomic analysis. The size and concentration of exosomes were assessed by nanoparticle tracking analysis, the morphology was characterized by transmission electron microscopy, and CDN surface analysis can use the flow cytometry technique. Standardization of the storage method of CDN components is also a key step. Storage at 4°C or -20°C will affect the biological activity and protein content of CDNs. It is generally recommended to store at -80°C which is the optimal temperature that has the least effect on the morphology and content of exosomes. We also used a model with a full-thickness incision wound to prove that exosomes derived from hBM-MSC can accelerate the skin wound healing process *in vivo* (Figure 4).

4. Mechanisms of MSC-Derived Nanovesicles in Wound Healing

Wound healing is a highly organized multistep process that restores tissue integrity after injury. It involves interactions between various cell populations and is usually divided into four overlapping stages: hemostasis, inflammation, proliferation, and remodeling [25]. MSC-derived nanovesicles can regulate wound repair during inflammation, cell migration, cell proliferation, angiogenesis, collagen production, and ECM remodeling. At present, CDNs are known to activate a variety of important signaling cascade pathways related to the final three stages of wound repair (Figure 5), including AKT, extracellular signal-regulated kinase (ERK), signal transducer and activator of transcription 3 (STAT3), and Wnt/β-catenin [2, 26, 27]. CDNs can also stimulate several

signaling pathways to induce the expression of several important growth factors related to wound repair, such as insulin-like growth factor 1 (IGF1), HGF, and stromal cell-derived factor 1 (SDF1) [27]. These growth factors can promote angiogenesis, cell migration, cell proliferation, and reepithelialization.

4.1. CDN Function in Hemostasis. Studies have revealed that the main therapeutic effect of platelets during bleeding is dependent on the effect of platelet-derived extracellular vesicles [28]. Neonatal plasma exosomes can be enriched in a large number of proteins involved in platelet function and primary hemostasis, such as platelet activation and signaling proteins, integrins αIIb and β3, platelet chemotactic protein (PF4), filaggrin-A, and ligand receptor (CD36) [29]. The use of platelet exosomes shows the advantage of the hemostatic effect over fresh platelets [30]. Platelet exosomes can improve the outcome of severe trauma by maintaining hemodynamic stability and reducing the development of ischemia and metabolic acidosis, which provide a prohemostatic support for the early wound stage.

4.2. CDN Function in Inflammation. Inflammation is a self-defense mechanism against wound injury that occurs within 24–48 h of ischemia onset. Acute and regulated inflammation can promote wound healing and epithelial regeneration [31]. MSC-derived nanovesicles can downregulate proinflammatory enzymes, such as inducible nitric oxide synthase (iNOS) and cyclooxygenase (COX2), as well as secreted cytokines and chemokines to reduce inflammation during wound repair [32]. In addition, MSC-derived nanovesicles
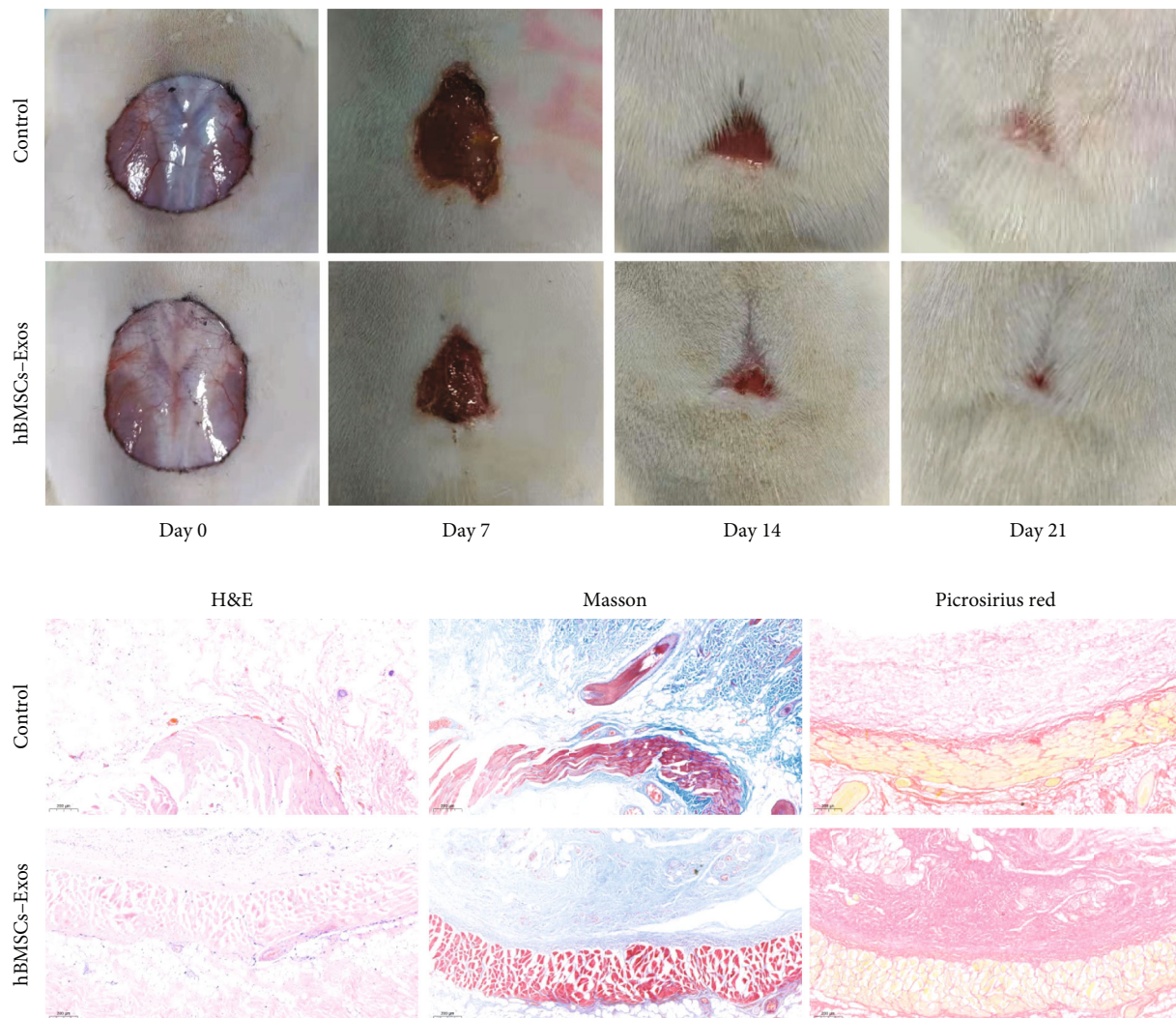
Figure 4: The representative photos shown of full-thickness excision wound area of the rat treated with PBS (control) or hBMSCs-Exos. Reproduced with from Ref. [69]. Copyright 2021 BioMed Central Ltd.

can upregulate the anti-inflammatory cytokine interleukin 10 (IL10), which has been reported to play a vital role in the control of skin wound inflammation and scar formation [33]. Macrophages are prominent inflammatory cells that play an important role in the process of skin regeneration. MSC-derived nanovesicles can promote the significant switch of macrophages to the anti-inflammatory M2 phenotype [34]. Additionally, MSC-derived Exos rely on the Janus kinase 2 (JAK2)/STAT6 pathway to mediate macrophage activation, which can significantly reduce the number of proinflammatory macrophages [35]. Lipopolysaccharide- (LPS-) pretreated MSC-derived Exos have been shown to regulate macrophage polarization and chronic inflammation. Exo-specific let-7b released by LPS-pretreated MSCs can stimulate the toll-like receptor 4 (TLR4) pathway, inhibit inflammation, and promote normal wound healing [36]. In addition, the immunomodulatory effect of human umbilical cord-derived MSCs (hUC-MSCs) preactivated with IL1β is partly caused by Exo-mediated miR-146a transfer [37]. Melatonin-pretreated MSC-derived Exos can

increase M2 polarization relative to M1 polarization by upregulating the expression of phosphatase and tensin homolog (PTEN) and inhibiting phosphorylation of AKT, which can significantly inhibit the proinflammatory factors IL1β and tumor necrosis factor alpha (TNFα) and increase the expression of the anti-inflammatory factor IL10. Thus melatonin-pretreated MSC-derived Exos can significantly facilitate diabetic wound healing [38]. These findings provide research directions for enhancing the anti-inflammatory functions of Exos. MSC-derived Exos can regulate the activation, differentiation, and proliferation of B lymphocytes and T lymphocytes. Moreover, MSC-derived Exos can transform activated T lymphocytes into a T regulatory phenotype, thereby exerting an immunosuppressive effect [39]. Studies have also found that MSC-derived Exos exert immunomodulatory effects through specific miRNAs. Three miRNAs (miRNA-21, miRNA-146a, and miRNA-181c) enriched in hUC-MSC-derived Exos were shown to be related to specific immune responses and inflammation regulation [40]. hUC-MSC-derived Exos overloaded with
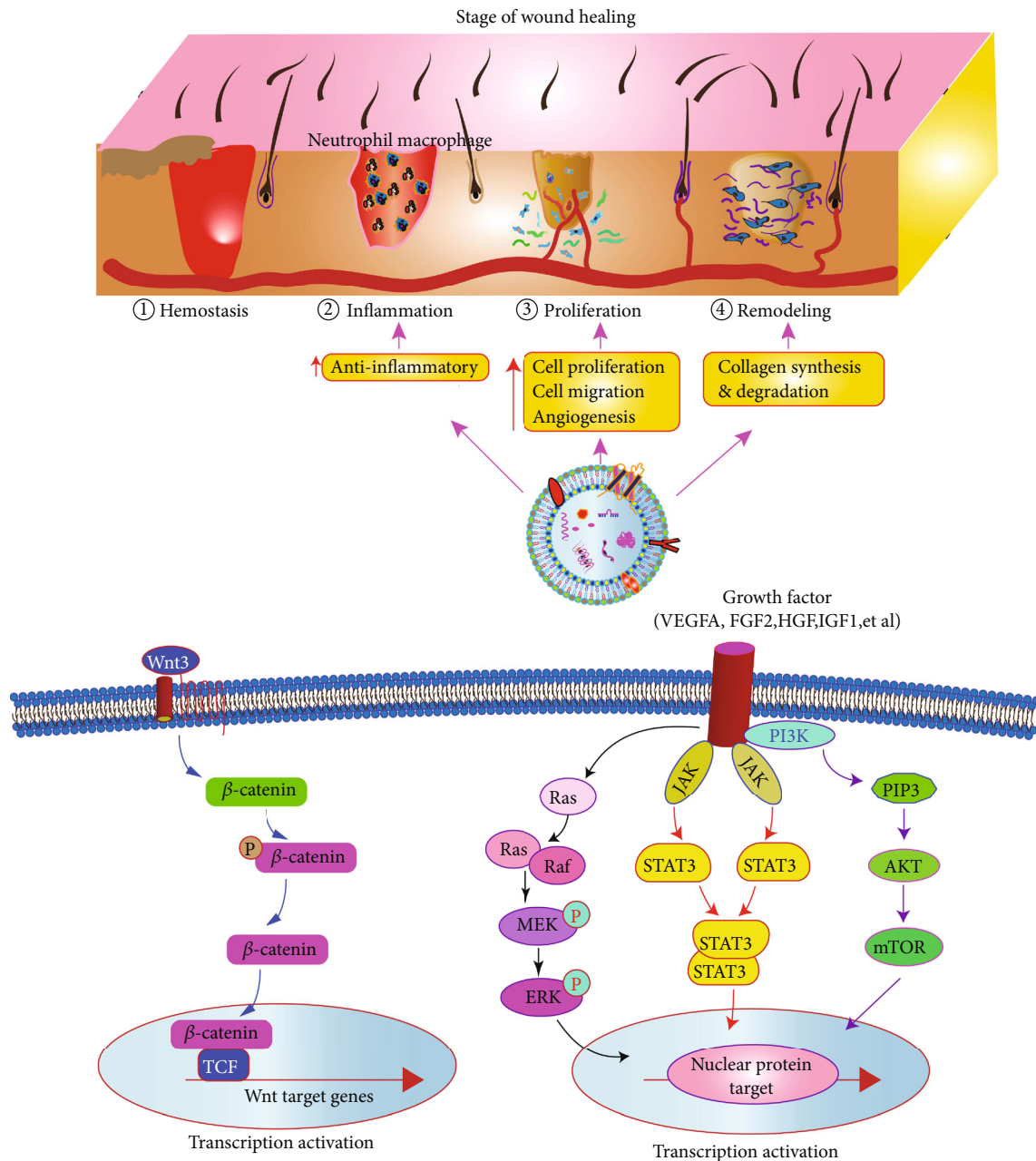
Figure 5: CDNs promote wound healing by enhancing angiogenesis, reducing inflammation, increasing cell proliferation and migration, and restoring tissue integrity. The contribution of signaling pathways in which the exosome can activate the Wnt3/catenin, PI3K/Akt, JAK/STAT3, Ras/ERK signaling pathways to further accelerate wound healing.

miR-181c were found to reduce burn-induced inflammation in rats by downregulating the TLR4 signaling pathway [41]. In general, further research is needed to clarify the specific molecular mechanisms underlying inflammation inhibition by MSC-derived nanovesicles during wound healing and skin regeneration.

4.3. CDN Function in Angiogenesis. Wound angiogenesis is one of the main mechanisms by which CDNs promote skin damage repair. Adequate wound blood provides nutrition, oxygen, and cell migration pathways for the regeneration of damaged tissues. MSC-derived Exos are rich in various

proteins related to angiogenesis and miRNAs that activate multiple signaling pathways in endothelial cells. Previous research showed that MSC-derived nanovesicles contain a large number of angiogenic factors, such as VEGFA, FGF2, MMP, lactadherin (MFG-E8), angiopoietin-related protein 1 (ANGPTL1), and thrombopoietin. Recently, Zhang et al. reported that Exos derived from hUC-MSCs are rich in WNT4 protein, which can activate the Wnt/β-catenin signaling pathway to promote the reconstruction and regeneration of blood vessels after scalding wounds [42]. Exos derived from human umbilical cord blood-derived endothelial progenitor cells (EPCs) can activate the ERK1/2

signaling pathway to upregulate the expression of vascular genes, such as VEGFA, COX2, and FGF2, to promote cutaneous wound healing and regeneration [43]. Exos from human urine-derived stem cells are rich in deleted malignant brain tumor 1 (DMBT1), which has been shown to induce angiogenesis in cultured endothelial cells and promote angiogenesis and wound healing in diabetic mice [44]. In addition, the proangiogenic effect of EPC-derived Exos in endothelial cells may be partly attributed to inhibition of the MMP9 expression [45].

Previous studies have found that EVs are also enriched with a large number of miRNAs that promote angiogenesis. For example, fibrocyte-derived nanovesicles were found to be enriched with miRNA-126, miRNA-130a, and miRNA-132 during wound closure [46]. miR-125a is also enriched in Exos from adipose-derived MSCs (ADSCs), which were found to transfer miR-125a to endothelial cells for targeted knockdown of the angiogenesis inhibitor delta-like canonical Notch ligand 4 (DLL4) [47]. Additionally, exosomally transferred miR-21 can act on the target gene PTEN to activate the downstream mitogen-activated protein kinase (MAPK)/ERK and PI3K/AKT signaling pathways to promote vascularization [48].

Studies on the mechanisms of Exos in angiogenesis will help us better understand various physiological and pathological processes in wound repair. Although some studies have demonstrated the potential roles of exosomal miRNAs and protein factors, further research is needed to determine their overall importance compared to the broader secretory group and the mechanisms that underlie exosomal transport of specific cargo. Further research on miRNAs and proteins transferred from Exos may provide new directions for enhancing the therapeutic regulation of angiogenesis during wound healing.

4.4. CDN Function in Cell Proliferation and Migration. Cell proliferation and skin reepithelialization are essential for wound healing. Skin fibroblasts play an important role in the repair and regeneration of damaged tissue. The basic characteristics of wound proliferation include cell proliferation, migration of various cell types, and matrix protein synthesis. This stage is also described by the formation of a new tissue organization. Epithelial cells begin to migrate to the edge of the injured area, closing the edge of the wound, while matrix proteins provide an external environment to promote cell attachment to the scaffold. The synthesis and deposition of ECM play an important role in this stage. Under certain cell stimulation conditions, fibroblasts can differentiate into myofibroblasts, which play an important role in wound contraction.

MSC-derived Exos can be internalized *in vivo* and their contents (such as proteins and RNAs) transferred to receiving cells to regulate their proliferation and migration. It has been demonstrated that EVs from a variety of cell sources can accelerate the proliferation and migration of fibroblasts and keratinocytes [49]. For example, EVs from ADSCs and bone marrow-derived MSCs (BMSCs) have been shown to promote the growth and migration of fibroblasts from chronic diabetic ulcer wounds in a dose-dependent manner

in vitro [46]. Exos from human-induced pluripotent stem cell- (hiPSC-) derived MSCs were also shown to promote the proliferation and migration of human dermal fibroblasts and epidermal cells in a dose-dependent manner *in vitro* [50]. Exos also promote the proliferation of skin cells and are associated with increased levels of cytokeratin 19 (CK19) and proliferating cell nuclear antigen (PCNA). For example, Exos derived from hUC-MSCs were shown to increase the expressions of CK19, PCNA, and collagen I, which accelerate wound healing and promote epithelial regeneration [2]. In addition, hUC-MSC-derived EVs were shown to inhibit the proliferation and apoptosis of keratinocytes and dermal fibroblasts by inhibiting the proapoptotic protein B cell lymphoma 2 (BCL2) and BCL2-like protein 4 (BAX). In a rat model study, it was found that ADSC-derived Exos can be internalized by fibroblasts, inducing skin wound repair and fibroblast activity. Results from this study showed that the gene expressions of N-cadherin, cyclin 1, PCNA, type I and type III collagen, and elastin were significantly increased in a dose-dependent manner under stimulation by ADSC-derived Exos [51]. It has been reported that the MAPK, Wnt, and mechanistic target of rapamycin (mTOR) pathways all play important roles in the process of wound healing. As a special intercellular signaling pathway, Exos have a common molecular mechanism that regulates the proliferation and migration behavior of skin cells, rather than skin cell specificity. Exos can induce important intracellular signaling pathways, including AKT, STAT3, Wnt, and ERK. These signaling pathways can upregulate various growth factors in target cells (such as HGF, IL6, IGF1, and nerve growth factor). For example, EVs derived from keratinocytes can upregulate the MAPK/ERK pathway. hUC-MSC-derived EVs were shown to activate Wnt/β-catenin in skin cells by transferring WNT4 to promote wound healing in a rat burn model [2]. BMSC-derived Exos also transport WNT3A to enhance fibroblast proliferation and migration [52]. Synovial MSC-derived EVs are enriched in miRNA-126-3p, which regulates the PI3K/AKT and MAPK/ERK pathways to induce the proliferation and migration of dermal fibroblasts [53].

These common signaling pathways provide the potential for applications of Exos in other fields of biology and the treatment of other diseases. Nevertheless, the components of Exos that play functional roles and the upstream and downstream phosphorylation regulation mechanisms in related molecular pathways still need to be investigated.

4.5. CDN Function in Wound Remodeling. ECM remodeling usually lasts from 2 weeks to one year or more after injury. The remodeling stage of wound healing is closely related to the production and reorganization of ECM, which is critical to scar formation. In the later stage of wound repair, related effector cells undergo apoptosis, type I collagen is replaced with type III collagen, MMPs degrade ECM, and other ECM proteins are synthesized. The key to ECM reconstruction is the synthesis and degradation of collagen. EVs regulate the final stage of wound healing by stimulating the secretion of ECM. In the early stage of wound healing, Exos derived from MSCs can increase the amount of collagens I

TABLE 2: Summary of research on immobilized Exos in wound repair.

Exosome	Scaffold	Model	Function	Reference
hUC-MSC-derived Exos	Pluronic F127 hydrogel	Diabetic full-thickness skin wound	Accelerate wound closure and promote tissue regeneration	[85]
pH-responsive Exos	Polysaccharide-based dressing	Chronic diabetic wound	Enhance the angiogenic ability and sustained release of Exos	[86]
Mouse ADSC-derived Exos	Pluronic F127 hydrogel, oxidized hyaluronic acid, and ε-polylysine	Rat diabetic cutaneous injury	Sustained release of Exos; promote angiogenesis, reepithelialization, neovascularization, and cell proliferation	[87]
ADSC-derived Exos	Alginate hydrogel	Full-thickness excisional wound	Enhance wound closure, reepithelization, collagen deposition, and angiogenesis	[88]
ADSC-derived Exos	Porous cryogels	Diabetic and infectious wound	Accelerate wound closure, promote collagen deposition, increase reepithelialization and neovascularization, and decrease oxidative stress	[79]
hUC-MSC-derived Exos	Hydromatrix	Skin wound healing	Inhibit myofibroblast formation and reduce scar formation	[89]
hUC-MSC-derived Exos	Genipin-crosslinked hydrogel	Rat cutaneous wound	Reduce inflammation, promote wound closure, accelerate epithelial regeneration, and increase collagen deposition	[90]
Gingival MSC-derived Exos	Chitosan/silk-based hydrogel	Rat diabetic wound	Promote reepithelialization, deposition and remodeling of collagen, angiogenesis, and skin wound healing	[89]
BMSC-derived Exos	Electrospun fibrous scaffolds	Full-thickness skin wound	Synergistic immunomodulatory functions toward skin wound repair	[58]
ADSC-derived Exos	Pluronic F127 hydrogel, oxidized hyaluronic acid, and ε-polylysine	Diabetic full-thickness cutaneous wound	Sustained release of Exos; promote neovascularization, accelerate the formation of granulation tissue, and enhance reepithelialization and collagen remodeling	[91]
Placental MSC-derived Exos	Aldehyde methylcellulose–chitosan-g-PEG hydrogel	Full-thickness skin defect	Synergistically promote angiogenesis and inhibit cell apoptosis; promote the function of hair follicles and glands	[92]

Abbreviations: ADSC: adipose-derived MSC; BMSC: bone marrow-derived MSC; hUC-MSC: human umbilical cord-derived MSC; PEG: polyethylene glycol.

and III in the wound bed. However, in the late stages of chronic wound healing, the effects of EVs shift to inhibition of collagen expression and fibroblast differentiation into myofibroblasts, which can inhibit scar hyperplasia [54]. EVs from fibroblasts can stimulate the synthesis of collagen in the matrix and enhance the deposition of mature collagen fibers in the wound area [46]. Exos derived from hiPSCs have been observed to enhance the synthesis of type I and III collagen in wound sites [50]. Another study showed that Exos from human amniotic epithelial cells regulate the ratio of collagens I and III by stimulating the expression of MMP1, which promotes wound healing and inhibits scar formation [55]. Intravenous injection of ADSC-derived Exos in full-thickness dorsal wound model mice was shown to inhibit the expressions of collagens III and I in fibroblasts by increasing the transforming growth factor beta 1 (TGFβ1)/TGFβ3 ratio, thereby preventing fibroblast differentiation into myofibroblasts and inhibiting the formation of granulation tissue, which reduced scar formation. In addition, ADSC-derived Exos were shown to activate the MAPK/ERK pathway in skin dermal fibroblasts *in vitro*, increase the ratio of MMP3 to TIMP1, and promote scarless skin repair by regulating ECM remodeling [51]. In addition, during skin regeneration,

hUC-MSC-derived Exos effectively promoted the phosphorylation of yes-associated protein (YAP) by transporting the 14-3-3ζ protein, thereby mediating the binding of YAP and the phosphorylated large tumor suppressor (p-LATS). Phosphorylation of YAP also inhibited Wnt/β-catenin signal transduction, restricting excessive dermal fibroblast expansion and collagen deposition in burn wounds, which played a key role in improving tissue remodeling and reducing scar formation [49].

These studies provide strong *in vitro* and *in vivo* evidence that MSC-derived Exos play important roles in ECM remodeling during wound repair, indicating that Exos have clinical application prospects in tissue wound healing. It is important to note that the roles of Exos in all stages of wound healing are complementary. In addition, a larger range of prospective, blinded, randomized, and placebo-controlled clinical trials is needed to further verify the safety, effectiveness, and durability of Exos.

5. Discussion and Conclusion

In the past few decades, numerous studies have used stem cells and CDNs for wound repair and skin regeneration.

Exo-based therapies are becoming a promising technology that can promote wound healing and minimize scar formation. As cell-free therapies, Exos have many advantages, such as ease of preparation, storage, transport, and administration. They also have demonstrated high therapeutic efficiency without risk of immune rejection and tumor development. MSC-derived Exos have significant wound regeneration potential and can effectively replace MSC-based therapies. The processes in each stage of wound repair are usually carried out in a precise and programmed manner involving a variety of intracellular and extracellular pathways, inflammatory pathways, the immune system, the coagulation cascade, and other complex processes. Thus, the participation of Exos in wound healing is very complicated. Further studies on the content and function of Exos can reveal the molecular mechanisms involved in wound repair and provide sufficient knowledge for the application of cell-free therapies for regenerative medicine. Currently, most of the mechanisms discovered have been studied in rodent models. However, animal physiology cannot always be translated to humans. Therefore, further clinical trials using human cell-derived Exos are needed to clearly demonstrate the therapeutic potential of Exos for wound healing.

Therapeutic applications of Exos are limited by their rapid clearance, short half-lives, and difficult large-scale preparation. Loading Exos into a supporting scaffold can prevent them from being quickly removed from the wound area. Additionally, synergies between Exos and scaffolds have been found that effectively promote wound repair [56, 57]. We have highlighted those studies that utilize Exos loaded in bioactive scaffolds to promote wound healing in Table 2. The application of CDNs in scaffold materials is still at an early stage. Studying the immune response of CDN-laden scaffolds in wound repair is a long-standing topic for the development of biocompatible biomaterial. The development of the active composition of CDN-laden scaffolds that appropriately interact with the immune system is facing a huge challenge. Studies have found that immune cells can absorb exosomes from the scaffold with more priority, which means that the body's immune response is important in tissue response [58].

Although CDNs have great advantages, they do not have the ability to target diseased organs after systemic injection, so that CDNs need multiple injections to achieve a certain therapeutic effect. In order to improve the targeting efficiency of CDNs to diseased organs, we have genetically engineered exosomes to improve the efficiency of targeted delivery for cartilage tissue repair [59–61]. These strategies can also be used to modify stem cells to obtain targeted stem cell-derived nanovesicles.

Although nanovesicles derived from different cell sources have different potentials, their physical and biological functions show high consistency. However, generation of CDNs is closely related to the microenvironment. Recent studies have also shown that the inflammatory microenvironment can significantly increase Exo release from MSCs. Interferon gamma (IFNγ) can enhance the immunomodulatory activity of hUC-MSC-derived Exos [62]. LPS pretreatment of hUC-MSCs was found to significantly alter Exo secretion, and Exos from pretreated cells were rich in the miRNA let-7b, which alleviated inflammation and enhanced wound healing [63]. Furthermore, other studies have shown that under a 1–2% hypoxic environment, TNFα-pretreated 3D culture systems have significantly altered MSC paracrine factor compositions. Therefore, the release and composition of CDNs can be adjusted by changing the cell culture microenvironment to enhance their wound repair functions. In addition, Exos can be loaded with therapeutic small molecule drugs or gene drugs to enhance their effects [64–66].

For extensive clinical application of Exos, there are still some urgent problems that need to be solved. At present, the extraction and purification of Exos is relatively cumbersome. It is not possible to quickly isolate the number of Exos required to meet clinical needs. There also is a lack of standardized methods for identifying Exos from specific cell sources, and proteomic detection and analysis of Exos are currently not available. Most importantly, the clinical implementation of any therapy must be based on safety. Further research is needed to determine the effective Exo dose for specific applications. Since research in the field of Exos is still in its infancy, the biological safety, effectiveness, reproducibility, production potential, formation mechanism, and biological functions of Exos that contribute to wound healing are still unclear. Despite the current challenges, the use of Exos for wound treatment is promising and inspiring. At present, more and more clinical treatment trials for CDNs are also underway, including for cancer, neurodegeneration, and infectious diseases. Stem cells are the main source for therapeutic CDNs, especially for regenerative medicine and immunomodulation. The phase I trial (NCT02138331), led by Nassar et al., uses CDNs derived from hUC-MSCs to ameliorate inflammatory immune reactions in chronic kidney diseases [67]. Previous clinical trials (NCT04276987, NCT04313647) used the immunomodulatory effects of CDNs from ADSCs for the treatment of lung injury [68]. Ongoing phase I clinical trials for the treatment of cutaneous wound healing use autologous exosomes from the participants' own plasma (NCT02565264). We highly expect that more exciting applications of Exos in clinical practice will emerge in the near future.

Data Availability

The data used to support the findings of this study are available from the corresponding author upon request.

Conflicts of Interest

The authors indicate no potential conflicts of interest.

Authors' Contributions

Y.J.L. designed the overall review, wrote the manuscript, drew the figure, and gave final approval of the manuscript; J.H.H. wrote the manuscript, performed the *in vitro* experiments, and analyzed all data. S.Q.S., Z.J., J.X., J.Y.X., and L.Y. provided feedback on the manuscript.

Acknowledgments

References

[1] A. Casado-Díaz, J. M. Quesada-Gómez, and G. Dorado, "Extracellular vesicles derived from mesenchymal stem cells (MSC) in regenerative medicine: applications in skin wound healing," *Frontiers in Bioengineering and Biotechnology*, vol. 8, 2020.

[2] B. Zhang, M. Wang, A. Gong et al., "HucMSC-exosome mediated-Wnt4 signaling is required for cutaneous wound healing," *Stem Cells*, vol. 33, no. 7, pp. 2158–2168, 2015.

[3] X. Y. Li, Y. Wang, L. Y. Shi et al., "Magnetic targeting enhances the cutaneous wound healing effects of human mesenchymal stem cell-derived iron oxide exosomes," *Journal of Nanobiotechnology*, vol. 18, no. 1, p. 113, 2020.

[4] H. N. Wilkinson and M. J. Hardman, "Wound healing: cellular mechanisms and pathological outcomes," *Open Biology*, vol. 10, no. 9, p. 200223, 2020.

[5] C. Gai, A. Carpanetto, M. C. Deregibus, and G. Camussi, "Extracellular vesicle-mediated modulation of angiogenesis," *Histology and Histopathology: Cellular and Molecular Biology*, vol. 31, no. 4, pp. 379–391, 2016.

[6] X. Xian, Q. Gong, C. Li, B. Guo, and H. Jiang, "Exosomes with highly angiogenic potential for possible use in pulp regeneration," *Journal of Endodontics*, vol. 44, no. 5, pp. 751–758, 2018.

[7] H. Tang, Y. He, L. Li et al., "Exosomal MMP2 derived from mature osteoblasts promotes angiogenesis of endothelial cells via VEGF/Erk1/2 signaling pathway," *Experimental Cell Research*, vol. 383, no. 2, article 111541, 2019.

[8] J. Thaler, I. Pabinger, W. R. Sperr, and C. Ay, "Clinical evidence for a link between microparticle-associated tissue factor activity and overt disseminated intravascular coagulation in patients with acute myelocytic leukemia," *Thrombosis Research*, vol. 133, no. 3, pp. 303–305, 2014.

[9] Q. Liu, D. M. Rojas-Canales, S. J. Divito et al., "Donor dendritic cell-derived exosomes promote allograft-targeting immune response," *Journal of Clinical Investigation*, vol. 126, no. 8, pp. 2805–2820, 2016.

[10] J. M. Aliotta, M. Pereira, K. W. Johnson et al., "Microvesicle entry into marrow cells mediates tissue-specific changes in mRNA by direct delivery of mRNA and induction of transcription," *Experimental Hematology*, vol. 38, no. 3, pp. 233–245, 2010.

[11] M. C. Deregibus, V. Cantaluppi, R. Calogero et al., "Endothelial progenitor cell derived microvesicles activate an angiogenic program in endothelial cells by a horizontal transfer of mRNA," *Blood*, vol. 110, no. 7, pp. 2440–2448, 2007.

[12] V. Arcucci, S. A. Stacker, and M. G. Achen, "Control of gene expression by exosome-derived non-coding RNAs in cancer angiogenesis and lymphangiogenesis," *Biomolecules*, vol. 11, no. 2, p. 249, 2021.

[13] A. Gonda, J. Kabagwira, G. N. Senthil, and N. R. Wall, "Internalization of exosomes through receptor-mediated endocytosis," *Molecular Cancer Research*, vol. 17, no. 2, pp. 337–347, 2019.

[14] D. Feng, W. L. Zhao, Y. Y. Ye et al., "Cellular Internalization of exosomes occurs through phagocytosis," *Traffic*, vol. 11, no. 5, pp. 675–687, 2010.

[15] K. J. McKelvey, K. L. Powell, A. W. Ashton, J. M. Morris, and S. A. McCracken, "Exosomes: mechanisms of uptake," *Journal of Circulating Biomarkers*, vol. 4, p. 7, 2015.

[16] S. Neri, "Genetic stability of mesenchymal stromal cells for regenerative medicine applications: a fundamental biosafety aspect," *International Journal of Molecular Sciences*, vol. 20, no. 10, p. 2406, 2019.

[17] H. Li, R. Ghazanfari, D. Zacharaki, H. C. Lim, and S. Scheding, "Isolation and characterization of primary bone marrow mesenchymal stromal cells," *Annals of the New York Academy of Sciences*, vol. 1370, no. 1, pp. 109–118, 2016.

[18] H. J. Jin, Y. Bae, M. Kim et al., "Comparative analysis of human mesenchymal stem cells from bone marrow, adipose tissue, and umbilical cord blood as sources of cell therapy," *International Journal of Molecular Sciences*, vol. 14, no. 9, pp. 17986–18001, 2013.

[19] X. Li, L. Duan, Y. Liang, W. Zhu, J. Xiong, and D. Wang, "Human umbilical cord blood-derived mesenchymal stem cells contribute to chondrogenesis in coculture with chondrocytes," *BioMed Research International*, vol. 2016, Article ID 3827057, 9 pages, 2016.

[20] E. Antoniadou and A. L. David, "Placental stem cells," *Best Practice & Research Clinical Obstetrics & Gynaecology*, vol. 31, pp. 13–29, 2016.

[21] A. Pombero, R. Garcia-Lopez, and S. Martinez, "Brain mesenchymal stem cells: physiology and pathological implications," *Development, Growth & Differentiation*, vol. 58, no. 5, pp. 469–480, 2016.

[22] Z. Jia, Y. Liang, X. Xu et al., "Isolation and characterization of human mesenchymal stem cells derived from synovial fluid by magnetic-activated cell sorting (MACS)," *Cell Biology International*, vol. 42, no. 3, pp. 262–271, 2018.

[23] Z. Jia, Y. Liang, X. Li et al., "Magnetic-activated cell sorting strategies to isolate and purify synovial fluid-derived mesenchymal stem cells from a rabbit model," *Journal of Visualized Experiments*, vol. 138, no. 138, 2018.

[24] S. G. Kwon, Y. W. Kwon, T. W. Lee, G. T. Park, and J. H. Kim, "Recent advances in stem cell therapeutics and tissue engineering strategies," *Biomaterials Research*, vol. 22, no. 1, 2018.

[25] A. J. Singer and R. A. Clark, "Cutaneous wound healing," *New England Journal of Medicine*, vol. 341, no. 10, pp. 738–746, 1999.

[26] X. Li, C. Chen, L. Wei et al., "Exosomes derived from endothelial progenitor cells attenuate vascular repair and accelerate reendothelialization by enhancing endothelial function," *Cytotherapy*, vol. 18, no. 2, pp. 253–262, 2016.

[27] A. Shabbir, A. Cox, L. Rodriguez-Menocal, M. Salgado, and E. Van Badiavas, "Mesenchymal stem cell exosomes induce proliferation and migration of normal and chronic wound fibroblasts, and enhance angiogenesis in vitro," *Stem Cells and Development*, vol. 24, no. 14, pp. 1635–1647, 2015.

[28] S.-C. Tao, S.-C. Guo, and C.-Q. Zhang, "Platelet-derived extracellular vesicles: an emerging therapeutic approach," *International Journal of Biological Sciences*, vol. 13, no. 7, pp. 828–834, 2017.

[29] J. Peñas-Martínez, M. N. Barrachina, E. J. Cuenca-Zamora et al., "Qualitative and quantitative comparison of plasma exosomes from neonates and adults," *International Journal of Molecular Sciences*, vol. 22, no. 4, p. 1926, 2021.

[30] E. Lopez, A. K. Srivastava, J. Burchfield et al., "Platelet-derived-Extracellular Vesicles Promote Hemostasis and Prevent the Development of Hemorrhagic Shock," *Scientific Reports*, vol. 9, no. 1, article 17676, 2019.

[31] M. A. Sugimoto, L. P. Sousa, V. Pinho, M. Perretti, and M. M. Teixeira, "Resolution of inflammation: what controls its onset?," *Frontiers in Immunology*, vol. 7, 2016.

[32] W. Jiang and J. Xu, "Immune modulation by mesenchymal stem cells," *Cell Proliferation*, vol. 53, no. 1, article e12712, 2020.

[33] P. Wu, B. Zhang, H. Shi, H. Qian, and W. Xu, "MSC-exosome: a novel cell-free therapy for cutaneous regeneration," *Cytotherapy*, vol. 20, no. 3, pp. 291–301, 2018.

[34] C. Lo Sicco, D. Reverberi, C. Balbi et al., "Mesenchymal stem cell-derived extracellular vesicles as mediators of anti-inflammatory effects: endorsement of macrophage polarization," *Stem Cells Translational Medicine*, vol. 6, no. 3, pp. 1018–1028, 2017.

[35] X. Sun, A. Shan, Z. Wei, and B. Xu, "Intravenous mesenchymal stem cell-derived exosomes ameliorate myocardial inflammation in the dilated cardiomyopathy," *Biochemical and Biophysical Research Communications*, vol. 503, no. 4, pp. 2611–2618, 2018.

[36] J. Zhao, X. Li, J. Hu et al., "Mesenchymal stromal cell-derived exosomes attenuate myocardial ischaemia-reperfusion injury through miR-182-regulated macrophage polarization," *Cardiovascular Research*, vol. 115, no. 7, pp. 1205–1216, 2019.

[37] Y. Song, H. Dou, X. Li et al., "Exosomal miR-146a contributes to the enhanced therapeutic efficacy of interleukin-1β-primed mesenchymal stem cells against sepsis," *Stem Cells*, vol. 35, no. 5, pp. 1208–1221, 2017.

[38] W. Liu, M. Yu, D. Xie et al., "Melatonin-stimulated MSC-derived exosomes improve diabetic wound healing through regulating macrophage M1 and M2 polarization by targeting the PTEN/AKT pathway," *Stem Cell Research & Therapy*, vol. 11, no. 1, p. 259, 2020.

[39] M. Monguió-Tortajada, S. Roura, C. Gálvez-Montón et al., "Nanosized UCMSC-derived extracellular vesicles but not conditioned medium exclusively inhibit the inflammatory response of stimulated T cells: implications for nanomedicine," *Theranostics*, vol. 7, no. 2, pp. 270–284, 2017.

[40] D. Ti, H. Hao, X. Fu, and W. Han, "Mesenchymal stem cells-derived exosomal microRNAs contribute to wound inflammation," *Science China Life Sciences*, vol. 59, no. 12, pp. 1305–1312, 2016.

[41] X. Li, L. Liu, J. Yang et al., "Exosome derived from human umbilical cord mesenchymal stem cell mediates miR-181c attenuating burn-induced excessive inflammation," *EBioMedicine*, vol. 8, pp. 72–82, 2016.

[42] B. Zhang, X. Wu, X. Zhang et al., "Human umbilical cord mesenchymal stem cell exosomes enhance angiogenesis through the Wnt4/β-catenin pathway," *Stem Cells Translational Medicine*, vol. 4, no. 5, pp. 513–522, 2015.

[43] J. Zhang, C. Chen, B. Hu et al., "Exosomes derived from human endothelial progenitor cells accelerate cutaneous wound healing by promoting angiogenesis through Erk1/2 signaling," *International Journal of Biological Sciences*, vol. 12, no. 12, pp. 1472–1487, 2016.

[44] C. Y. Chen, S. S. Rao, L. Ren et al., "Exosomal DMBT1 from human urine-derived stem cells facilitates diabetic wound repair by promoting angiogenesis," *Theranostics*, vol. 8, no. 6, pp. 1607–1623, 2018.

[45] J. Kong, F. Wang, J. Zhang et al., "Exosomes of Endothelial Progenitor Cells Inhibit Neointima Formation After Carotid Artery Injury," *Journal of Surgical Research*, vol. 232, pp. 398–407, 2018.

[46] A. Geiger, A. Walker, and E. Nissen, "Human fibrocyte-derived exosomes accelerate wound healing in genetically diabetic mice," *Biochemical and Biophysical Research Communications*, vol. 467, no. 2, pp. 303–309, 2015.

[47] X. Liang, L. Zhang, S. Wang, Q. Han, and R. C. Zhao, "Exosomes secreted by mesenchymal stem cells promote endothelial cell angiogenesis by transferring miR-125a," *Journal of Cell Science*, vol. 129, no. 11, pp. 2182–2189, 2016.

[48] Y. An, J. Zhao, F. Nie et al., "Exosomes from adipose-derived stem cells (ADSCs) overexpressing miR-21 promote vascularization of endothelial cells," *Scientific Reports*, vol. 9, no. 1, 2019.

[49] B. Zhang, Y. Shi, A. Gong et al., "HucMSC exosome-delivered 14-3-3ζ orchestrates self-control of the Wnt response via modulation of YAP during cutaneous regeneration," *Stem Cells*, vol. 34, no. 10, pp. 2485–2500, 2016.

[50] J. Zhang, J. Guan, X. Niu et al., "Exosomes released from human induced pluripotent stem cells-derived MSCs facilitate cutaneous wound healing by promoting collagen synthesis and angiogenesis," *Journal of Translational Medicine*, vol. 13, no. 1, 2015.

[51] L. Hu, J. Wang, X. Zhou et al., "Exosomes derived from human adipose mensenchymal stem cells accelerates cutaneous wound healing via optimizing the characteristics of fibroblasts," *Scientific Reports*, vol. 6, no. 1, p. 32993, 2016.

[52] J. D. McBride, L. Rodriguez-Menocal, W. Guzman, A. Candanedo, M. Garcia-Contreras, and E. V. Badiavas, "Bone marrow mesenchymal stem cell-derived CD63+Exosomes transport Wnt3a exteriorly and enhance dermal fibroblast proliferation, migration, and angiogenesis in vitro," *Stem Cells and Development*, vol. 26, no. 19, pp. 1384–1398, 2017.

[53] S.-C. Tao, S. C. Guo, M. Li, Q. F. Ke, Y. P. Guo, and C. Q. Zhang, "Chitosan wound dressings incorporating exosomes derived from microRNA-126-overexpressing synovium mesenchymal stem cells provide sustained release of exosomes and heal full-thickness skin defects in a diabetic rat model," *Stem Cells Translational Medicine*, vol. 6, no. 3, pp. 736–747, 2017.

[54] L. Wang, L. Hu, X. Zhou et al., "Exosomes secreted by human adipose mesenchymal stem cells promote scarless cutaneous repair by regulating extracellular matrix remodelling," *Scientific Reports*, vol. 7, no. 1, article 13321, 2017.

[55] B. Zhao, Y. Zhang, S. Han et al., "Exosomes derived from human amniotic epithelial cells accelerate wound healing and inhibit scar formation," *Journal of Molecular Histology*, vol. 48, no. 2, pp. 121–132, 2017.

[56] J. Huang, J. Xiong, L. Yang, J. Zhang, S. Sun, and Y. Liang, "Cell-free exosome-laden scaffolds for tissue repair," *Nanoscale*, vol. 13, no. 19, pp. 8740–8750, 2021.

[57] X. Xing, S. Han, Z. Li, and Z. Li, "Emerging role of exosomes in craniofacial and dental applications," *Theranostics*, vol. 10, no. 19, pp. 8648–8664, 2020.

[58] N. Su, Y. Hao, F. Wang, W. Hou, H. Chen, and Y. Luo, "Mesenchymal stromal exosome-functionalized scaffolds induce innate and adaptive immunomodulatory responses toward tissue repair," *Science Advances*, vol. 7, no. 20, 2021.

[59] Y. Liang, X. Xu, X. Li et al., "Chondrocyte-targeted microRNA delivery by engineered exosomes toward a cell-free osteoarthritis therapy," *ACS Applied Materials & Interfaces*, vol. 12, no. 33, pp. 36938–36947, 2020.

[60] Y. Liang, L. Duan, J. Lu, and J. Xia, "Engineering exosomes for targeted drug delivery," *Theranostics*, vol. 11, no. 7, pp. 3183–3195, 2021.

[61] X. Xu, Y. Liang, X. Li et al., "Exosome-mediated delivery of kartogenin for chondrogenesis of synovial fluid- derived mesenchymal stem cells and cartilage regeneration," *Biomaterials*, vol. 269, article 120539, 2021.

[62] G. Zhang, Z. Zhu, H. Wang et al., "Exosomes derived from human neural stem cells stimulated by interferon gamma improve therapeutic ability in ischemic stroke model," *Journal of Advanced Research*, vol. 24, pp. 435–445, 2020.

[63] D. Ti, H. Hao, C. Tong et al., "LPS-preconditioned mesenchymal stromal cells modify macrophage polarization for resolution of chronic inflammation via exosome-shuttled let-7b," *Journal of Translational Medicine*, vol. 13, no. 1, p. 308, 2015.

[64] L. Duan, L. Xu, X. Xu et al., "Exosome-mediated delivery of gene vectors for gene therapy," *Nanoscale*, vol. 13, no. 3, pp. 1387–1397, 2021.

[65] L. Duan, X. Xu, L. Xu et al., "Exosome-mediated drug delivery for cell-free therapy of osteoarthritis," *Current Medicinal Chemistry*, vol. 27, 2020.

[66] L. Duan, K. Ouyang, X. Xu et al., "Nanoparticle delivery of CRISPR/Cas9 for genome editing," *Frontiers in Genetics*, vol. 12, article 673286, 2021.

[67] W. Nassar, M. el-Ansary, D. Sabry et al., "Umbilical cord mesenchymal stem cells derived extracellular vesicles can safely ameliorate the progression of chronic kidney diseases," *Biomaterials Research*, vol. 20, no. 1, p. 21, 2016.

[68] Z. Leng, R. Zhu, W. Hou et al., "Transplantation of ACE2-mesenchymal stem cells improves the outcome of patients with COVID-19 pneumonia," *Aging and Disease*, vol. 11, no. 2, pp. 216–228, 2020.

[69] T. Jiang, Z. Wang, and J. Sun, "Human bone marrow mesenchymal stem cell-derived exosomes stimulate cutaneous wound healing mediates through TGF-β/Smad signaling pathway," *Stem Cell Research & Therapy*, vol. 11, no. 1, p. 198, 2020.

[70] Y. Bai, Y.-d. Han, X.-l. Yan et al., "Adipose mesenchymal stem cell-derived exosomes stimulated by hydrogen peroxide enhanced skin flap recovery in ischemia-reperfusion injury," *Biochemical and Biophysical Research Communications*, vol. 500, no. 2, pp. 310–317, 2018.

[71] A. D. Ariyanti, J. Zhang, O. Marcelina et al., "Salidroside-pretreated mesenchymal stem cells enhance diabetic wound healing by promoting paracrine function and survival of mesenchymal stem cells under hyperglycemia," *Stem Cells Translational Medicine*, vol. 8, no. 4, pp. 404–414, 2019.

[72] Y. Hu, R. Tao, L. Chen et al., "Exosomes derived from pioglitazone-pretreated MSCs accelerate diabetic wound healing through enhancing angiogenesis," *Journal of Nanobiotechnology*, vol. 19, no. 1, 2021.

[73] X. Qiu, J. Liu, C. Zheng et al., "Exosomes released from educated mesenchymal stem cells accelerate cutaneous wound healing via promoting angiogenesis," *Cell Proliferation*, vol. 53, no. 8, article e12830, 2020.

[74] Y. J. Kim, S. . Yoo, H. H. Park et al., "Exosomes derived from human umbilical cord blood mesenchymal stem cells stimulates rejuvenation of human skin," *Biochemical and Biophysical Research Communications*, vol. 493, no. 2, pp. 1102–1108, 2017.

[75] L. Liu, Y. Yu, Y. Hou et al., "Human umbilical cord mesenchymal stem cells transplantation promotes cutaneous wound healing of severe burned rats," *PLoS One*, vol. 9, no. 2, article e88348, 2014.

[76] J. Liu, Z. Yan, F. Yang et al., "Exosomes derived from human umbilical cord mesenchymal stem cells accelerate cutaneous wound healing by enhancing angiogenesis through delivering angiopoietin-2," *Stem Cell Reviews and Reports*, vol. 17, no. 2, pp. 305–317, 2021.

[77] M. Oh, J. Lee, Y. Kim, W. Rhee, and J. Park, "Exosomes derived from human induced pluripotent stem cells ameliorate the aging of skin fibroblasts," *International Journal of Molecular Sciences*, vol. 19, no. 6, 2018.

[78] R. Dalirfardouei, K. Jamialahmadi, A. H. Jafarian, and E. Mahdipour, "Promising effects of exosomes isolated from menstrual blood-derived mesenchymal stem cell on wound-healing process in diabetic mouse model," *Journal of Tissue Engineering and Regenerative Medicine*, vol. 13, no. 4, pp. 555–568, 2019.

[79] S.-C. Guo, S. C. Tao, W. J. Yin, X. Qi, T. Yuan, and C. Q. Zhang, "Exosomes derived from platelet-rich plasma promote the re-epithelization of chronic cutaneous wounds via activation of YAP in a diabetic rat model," *Theranostics*, vol. 7, no. 1, pp. 81–96, 2017.

[80] A. Shi, J. Li, X. Qiu et al., "TGF-β loaded exosome enhances ischemic wound healingin vitroand in vivo," *Theranostics*, vol. 11, no. 13, pp. 6616–6631, 2021.

[81] S. Hu, Z. Li, J. Cores et al., "Needle-free injection of exosomes derived from human dermal fibroblast spheroids ameliorates skin photoaging," *ACS Nano*, vol. 13, no. 10, pp. 11273–11282, 2019.

[82] X. Li, C. Jiang, and J. Zhao, "Human endothelial progenitor cells-derived exosomes accelerate cutaneous wound healing in diabetic rats by promoting endothelial function," *Journal of Diabetes and its Complications*, vol. 30, no. 6, pp. 986–992, 2016.

[83] M. Li, T. Wang, H. Tian, G. Wei, L. Zhao, and Y. Shi, "Macrophage-derived exosomes accelerate wound healing through their anti-inflammation effects in a diabetic rat model," *Artificial Cells, Nanomedicine, and Biotechnology*, vol. 47, no. 1, pp. 3793–3803, 2019.

[84] S. Sjöqvist, T. Ishikawa, D. Shimura et al., "Exosomes derived from clinical-grade oral mucosal epithelial cell sheets promote wound healing," *Journal of Extracellular Vesicles*, vol. 8, no. 1, article 1565264, 2019.

[85] J. Yang, Z. Chen, D. Pan, H. Li, and J. Shen, "Umbilical cord-derived mesenchymal stem cell-derived exosomes combined pluronic F127 hydrogel promote chronic diabetic wound healing and complete skin regeneration," *International Journal of Nanomedicine*, vol. 15, pp. 5911–5926, 2020.

[86] H. S. Kim, N. H. Kim, J. Kim, and I. H. Cha, "Inducing re-epithelialization in skin wound through cultured oral mucosal

keratinocytes," *Journal of the Korean Association of Oral and Maxillofacial Surgeons*, vol. 39, no. 2, pp. 63–70, 2013.

[87] J. S. Chin, W. H. Chooi, H. Wang, W. Ong, K. W. Leong, and S. Y. Chew, "Scaffold-mediated non-viral delivery platform for CRISPR/Cas9-based genome editing," *Acta Biomaterialia*, vol. 90, pp. 60–70, 2019.

[88] S. Shafei, M. Khanmohammadi, R. Heidari et al., "Exosome loaded alginate hydrogel promotes tissue regeneration in full-thickness skin wounds: an in vivo study," *Journal of Biomedical Materials Research Part A*, vol. 108, no. 3, pp. 545–556, 2020.

[89] S. Fang, C. Xu, Y. Zhang et al., "Umbilical cord-derived mesenchymal stem cell-derived exosomal microRNAs suppress myofibroblast differentiation by inhibiting the transforming growth factor-β/SMAD2 pathway during wound healing," *Stem Cells Translational Medicine*, vol. 5, no. 10, pp. 1425–1439, 2016.

[90] Q. Li, S. Gong, W. Yao et al., "Exosome loaded genipin cross-linked hydrogel facilitates full thickness cutaneous wound healing in rat animal model," *Drug Delivery*, vol. 28, no. 1, pp. 884–893, 2021.

[91] C. Wang, M. Wang, T. Xu et al., "Engineering bioactive self-healing antibacterial exosomes hydrogel for promoting chronic diabetic wound healing and complete skin regeneration," *Theranostics*, vol. 9, no. 1, pp. 65–76, 2019.

[92] C. Wang, C. Liang, R. Wang et al., "The fabrication of a highly efficient self-healing hydrogel from natural biopolymers loaded with exosomes for the synergistic promotion of severe wound healing," *Biomaterials Science*, vol. 8, no. 1, pp. 313–324, 2020.

Hindawi

Retraction

Retracted: High-Resolution Microscopy to Learn the Nuclear Organization of the Living Yeast Cells

Stem Cells International

This article has been retracted by Hindawi following an investigation undertaken by the publisher [1]. This investigation has uncovered evidence of one or more of the following indicators of systematic manipulation of the publication process:

(1) Discrepancies in scope

(2) Discrepancies in the description of the research reported

(3) Discrepancies between the availability of data and the research described

(4) Inappropriate citations

(5) Incoherent, meaningless and/or irrelevant content included in the article

(6) Manipulated or compromised peer review

The presence of these indicators undermines our confidence in the integrity of the article's content and we cannot, therefore, vouch for its reliability. Please note that this notice is intended solely to alert readers that the content of this article is unreliable. We have not investigated whether authors were aware of or involved in the systematic manipulation of the publication process.

Wiley and Hindawi regrets that the usual quality checks did not identify these issues before publication and have since put additional measures in place to safeguard research integrity.

We wish to credit our own Research Integrity and Research Publishing teams and anonymous and named external researchers and research integrity experts for contributing to this investigation.

The corresponding author, as the representative of all authors, has been given the opportunity to register their agreement or disagreement to this retraction. We have kept a record of any response received.

References

[1] R. Wang, A. Huang, Y. Wang et al., "High-Resolution Microscopy to Learn the Nuclear Organization of the Living Yeast Cells," *Stem Cells International*, vol. 2021, Article ID 9951114, 7 pages, 2021.

Research Article

High-Resolution Microscopy to Learn the Nuclear Organization of the Living Yeast Cells

Renjie Wang ⓘ, Aiwen Huang, Yan Wang, Pengxin Mei, He Zhu, Qianqian Chen, and Sankui Xu ⓘ

College of Materials Science & Engineering, Henan University of Technology, Zhengzhou, China

Correspondence should be addressed to Renjie Wang; renjie_wang@haut.edu.cn and Sankui Xu; sankui_xu@haut.edu.cn

The spatial organization of the nucleus is a key determinant in all genome activities. However, the accurate measurement of the nuclear organization is still technically challenging. Here, the technology NucQuant we created previously was utilized to detect the variation of the nuclear organization, including the heterogeneity of the nuclear geometry, the change of the NPC distribution along different cell cycle stages during interphase, and the organization of the nucleolus. The results confirmed that not only the growth rate and the NPC distribution are influenced by the carbon source; the nuclear shape is also impacted by the carbon source. The nuclei lost their spherical geometry gradually when the cell was cultured from the most to a less favorable carbon source. We also discovered that the nucleolus prefers to locate at the nuclear periphery, which was called the "genes poor region," especially when the cells entered quiescence. Furthermore, the distribution of the NPC along the different stages during the interphase was analyzed. We proposed that with the growth of the cell, the nucleus would grow from the surface of the NE flanking the nucleolus firstly.

1. Introduction

Chromosome spatial organization plays a key role in transcriptional regulation, DNA repair, and replication [1]. In eukaryotic cells in interphase, the chromosomes are segregated away from the cytoplasm by the nuclear envelope (NE). How do chromosomes organize in the eukaryotic nucleus is still an open question. In budding yeast, NE remains closed during the entire cell cycle, including mitosis. Past researches have uncovered few structural features characterizing the budding yeast nucleus in interphase: the spindle pole body (SPB), centromeres (CEN), telomeres (TEL), and nucleolus. In interphase, the nucleolus is organized in a crescent-shaped structure adjacent to the NE and contains quasiexclusively genes coding ribosomal RNA (rDNA) present on the right arm of chromosome XII. The genome structure and the nucleolar organization are intimately connected owing to the efficiency of rDNA transcription that plays an important role in the nucleolar organization [2]. Diametrically opposed to the nucleolus, the SPB tethers the

CEN during the entire cell cycle via microtubules to the centromere-bound kinetochore complex [3–6]. TEL are localized in clusters at the NE [7, 8]. Consequently, chromosome arms extend outwards from CEN to the nuclear periphery, defining a Rabl-like conformation [9, 10]. Nuclear pore complexes (NPCs) are embedded in the envelope to control the nucleocytoplasmic transport of molecules [11]. Besides, components of the NPCs have been proposed to play a key role in the chromatin organization [12]. The NPC components, Nups, are connected to the chromosomes and regulate the expression of certain genes [13–16]. Therefore, the distribution of the NPCs on NE and the nucleolus organization need to be precisely defined to accurately explore eukaryotic nuclear organization.

The nucleus in budding yeast in interphase is always described as a sphere of radius ~1 μm. However, the nuclear shape and size *in vivo* are dynamic [17]. Along the cell cycle, the nucleus adopts different morphologies and sizes. In the G1/S phase (or interphase), the nucleus is often described as a sphere; this structure is clearly established when yeast is

growing in rich medium containing glucose [18]. Differential interference contrast (DIC) microscopy research indicated that the nucleus is more or less spherical [19]. Transmission Electron Microscopy (TEM) analysis of ultrathin (60-80 nm) sections of an entire nucleus showed that the yeast nucleus in interphase undergoes a twofold increase in volume from G1 to S phase [20]. The "Nucloc" program created by Berger et al. to analyze the "genes territories" in the nucleus fits the NE through spherical simulation based on the detection of labeled NPCs; the results of this approach showed that the median budding yeast nucleus in interphase can be approximated as a sphere of ~1 μm radius [17]. However, the approximation of the yeast nucleus as a sphere is oversimplified, the nuclear shape being dynamic along the cell cycle and in different conditions [21]. Additionally, due to the existence of the aberration along the Z axis, the spherical fitting of the nucleus in interphase is not precise [22].

Accurate determination of the nuclear organization using fluorescence microscopy is technically challenging [23, 24]. The fit of the NE position is still controversial because of the resolution barrier in fluorescent microscopy: 200 nm in X-Y and about 500 nm in Z axis [25]. In budding yeast, fluorescent-labeled NPCs appear as typical punctate rings staining the NE which can perfectly be used to reconstruct the NE structure in 3D [20, 23]. Here, we used "NucQuant," an optimized automated image analysis algorithm we developed in our previous work [22], which can automatically localize fluorescently labeled NPCs and correct the detection bias resulting from optical spherical aberration along the Z axis to accurately compute an approximation of the NE in 3D. In addition, it also can detect the structure of the labeled nucleolus. This approach allowed us to precisely measure the heterogeneity of the nuclear shape and the NPC distribution along interphase. Based on this technology we could evaluate the nucleolus structure and organization in interphase. We also detected the change of the NPC distribution along the NE correlated with the cell cycle stage.

2. Materials and Methods

2.1. Yeast Strains.
Genotypes of the strains used in this study are described in Table 1.

2.2. Fluorescence Microscopy of Living Yeast Cells

2.2.1. Cell Culture. Yeast media were used as previously described [22]. The Yeast Extract Peptone Dextrose Medium (YPD) is made of 1% yeast extract, 2% peptone, and 2% dextrose. Synthetic complete media (SC) is made of 0.67% nitrogen base w/o amino acids (BD Difco, USA), 2% dextrose supplemented with amino acid mixture (AA mixture Bio101, USA), adenine, and uracil. Cells were grown overnight at 30°C in the Yeast Extract Peptone (YP) media containing 2% carbon source, cells were diluted at 10^6 cells/mL in rich glucose, galactose, or raffinose containing media. Cells were harvested when OD600 reached 4×10^6 cells/mL and rinsed twice with the corresponding SC media. Cells were spread on slides coated with corresponding SC

patch containing 2% agar and 2% of corresponding carbon source. Cover slides were sealed with "VaLaP" (1/3 vaseline, 1/3 lanoline, and 1/3 paraffin). For short time starvation experiments, when OD600 reached 4×10^6 cells/mL, cell culture was washed twice with YP media, resuspended at OD600 = 4×10^6 cells/mL in YP (15%) media, and incubated for 2 hours at 30°C. For 7 days of progressive starvation experiments, we used YP containing 2% glucose media to culture the cells for 7 days.

2.2.2. Confocal Microscope Image Acquisition. Confocal microscopy was performed as previously described [26]. Confocal microscopy was limited to 20 min after mounting and performed with an Andor Revolution Nipkow-disk confocal system installed on an Olympus IX-81, featuring a CSU22 confocal spinning disk unit (Yokogawa) and an EMCCD camera (DU 888, Andor). The system was controlled using the mode "Revolution FAST" of Andor Revolution IQ1 software (Andor). Images were acquired using an Olympus 100x objective (Plan APO, 1.4 NA, oil immersion). Single laser lines used for excitation were diode-pumped solid-state lasers (DPSSL) exciting GFP fluorescence at 488 nm (50 mW, Coherent) and mCherry fluorescence at 561 nm (50 mW, Cobolt Jive). A Semrock bibandpass emission filter (Em01-R488/568-15) allowed the collection of green and red fluorescence. Pixel size was 65 nm. For 3D analysis, Z-stacks of 41 images with a 250 nm Z-step were used. For microfluidic experiments, the fluorescence images can be acquired for more than 2 hours.

2.3. Image Analysis.
Confocal images were processed and analyzed with a Matlab script NucQuant, the modified version of "Nucloc" combined with the correction of the aberration along the Z axis, which is available to download at GitHub (https://github.com/ogadal/nucquant). The nuclear shape was fitted by the 3D-NE model, and the cumulative distribution functions (CDF) of the sphericity of the NE were generated using the existing function in the NucQuant. The probability density distribution of detected NPCs along NE was generated using the existing function (Matlab). To calculate the position of the nucleolus relative to the NE, here, we modified the NucQuant algorithm about the detection of the nucleolus. All pixels of the nucleolus were detected and then corrected Z-aberration based on the NPC position of one perfect spherical nucleus. Schematical of NucQuant is presented in Figure S1.

3. Results and Discussion

3.1. Heterogeneity of the Nuclear Shape in the Cell Population.
The cell nucleus is typically spheroidal or ellipsoid [17, 18]. However, the nuclear shape has high plasticity: in the same strain, the nuclei also have different shapes from cell to cell [27]. To study the heterogeneity of the nuclear shape in the interphase of one cell population, we utilized NucQuant to determine the NE with a 3D-NE model and measured the sphericity of each cell nucleus. Sphericity is one criterion to reflect how round an object is. The sphericity of a given object is the ratio between the surface area of a

TABLE 1: Genotypes of strain used in this study.

Name	Genotype
ycnod99-1a	MATa His3-Δ1, leu2-Δ0, C, ura3-Δ0, ade2-801, lys2-801, lys2D::KAN-MX, nup49-Δ::HPH-MX6 + pASZ11-NupNop

sphere which would have the same volume as that object to the surface area of the object [28]. For one perfect sphere, the sphericity index equals 1 and is maximal. A sphericity index lower than 1 indicates deviation from a perfect sphere. For one ellipsoid, the sphericity is ~0.92 when $a : b : c = 1 : 1 : 2$ (Figure 1(a)). The sphericity of the yeast nucleus was tested when the carbon source was changed from the most favorable to the less favorable carbon source. We confirmed that most of the nuclei in the interphase were close to spherical (the median sphericity is over 0.99). However, about 20% of the nuclei are rather ellipsoidal (sphericity below 0.95) (Figure 1(b); the samples are presented in Figure 1(d)). We also found that when the carbon source was changed to the less favorable carbon source ethanol, the sphericity clearly decreased compared with the favorable carbon source (Figure 1(b)). Consider the ~twofold reduction of the nuclear volume when changing from the most to a less favorable carbon source [22], we proposed that, when the carbon source changed from the most to a less favorable carbon source, the nuclear volume decreased anisotropic, which resulted in the nuclear shape tends to much more nonspherical. Actually, after the cells entered quiescence, ~70% nuclear lost their sphericity. So, we also explored the heterogeneity of the nuclear shape after the cells entered quiescence. The results clearly showed that after 7 days of starvation, most of the nuclei lost their sphericity (Figure 1(c)). We supposed that the nuclei will anisotropically shrink, which leads to most of the nuclei lost their spherical geometry, to control the limited consumption when the cells entered quiescence.

3.2. Heterogeneity of NPC Distribution in Different Interphase Stages.

NPC probability density map reflects the distribution of the NPC clusters along the nuclear envelope (NE). In this research, to assess the NPC distribution along the interphase, we sorted nuclei in G1, S, and G2. During interphase, nuclear volume is continuously increasing, from G1 to G2 [29]. This property has an implication: the closer the cell is from the G1 stage, the smaller is the nucleus. Therefore, we sorted nuclei according to their volume: the small newborn G1 nuclei and the mother nuclei in the G1 phase, the middle nuclei in the late G1 phase and S phase, and the bigger nuclei in the late S phase and early G2 phase. The NPC distribution in small, middle, and big nuclei of cells grown on different carbon sources was analyzed with "NucQuant." The results interestingly showed that the NPC distribution varied along the interphase stages, the NPCs gradually moved away from the NE flanking the nucleolus in interphase (Figure 2). In addition, it was also obvious that the NE elongated along the nucleolus direction with the cells growing.

The mechanism of the NPCs concentrated around the nucleolus for the small nuclei are still unclear. There is more and more evidence proving that in most mutants

altering the nuclear shape, the NE preferentially elongates at the nucleolar side [30–33]. The nucleolus contacts extensively with the NE. NE flanking the nucleolus has very specific properties [32]. Previous research suggested that these specialized properties can prompt the transfer of the nucleolar materials to the cytoplasm without passing through the nucleoplasm [34]. We would prefer to link these properties to the cell cycle. After cell division, in the small nuclei, we can observe the NPCs are concentrated at the NE flanking the nucleolus. This might be a consequence of mitosis, with the hourglass shape and the nucleolus being the last nuclear domain to segregate. In the late G1, S, and G2 phases, the surface of the nucleus is increased from the NE flanking the nucleolus [35]. Thus, the NPCs at this site are gradually shifted away from the nucleolus. In addition, because of the increase of the nuclear surface, the distance between clustered NPCs increased which allows the localization microscopy to distinguish the close NPCs; this is also why we can detect more NPC from the big nuclei.

3.3. The Organization of the Nucleolus.

The budding yeast has 100-200 ribosomal DNA (rDNA) units tandemly located on chromosome XII which is confined in the nucleolus. Only half of the rDNA copies are actively transcribed in S. cerevisiae [36]. Quantifying the intranuclear position of the nucleolus is essential for studying the spatial conformation of chromosomes. In budding yeast, the nucleolus contacts extensively with the nuclear envelope (NE) (Figure 3(a)). The research on the nuclear periphery, which was always seen as the silenced region, is significant to help us to understand the relation between chromosome organization and transcription activity. By using "NucQuant," the peripheral location of the nucleolus in 3D could be accurately explored.

Our previous work has shown that the growth of cells was stopped and the nucleolar size decreased after the cells enter quiescence [22]. We were wondering if this change in the nucleolar size impacts its localization with respect to the nuclear periphery. To answer this question, we calculated the fraction of the nucleolus located at the nuclear periphery. We defined periphery as 1/3 of the nuclear volume uniformly distributed along the NE. The nucleolar periphery percentage is the proportion of the nucleolus at the nuclear periphery. It is clear that with such definition, the nucleolus was not restricted to the peripheral region: in asynchronous cells, we measured a median of ~60% of the nucleolus located at the nuclear periphery. After cells entered quiescence, the percentage of the nucleolus at the nuclear periphery is massively increased (Figure 3(b)). We proposed that the transcription of the rDNA was repressed; more rDNA units would be organized to the periphery region which caused the peripheral localization of the nucleolus, when the cells entered quiescence.

Sphere   Ellipsoid

Sphericity = 1   Sphericity = 0.92

(a)

(b)

— Glucose   — Raffinose
— Galactose   — Ethanol

(c)

— G1   — 72 h
— 48 h   — 7 d

Sphericity = 0.996   Sphericity = 0.984

(d)
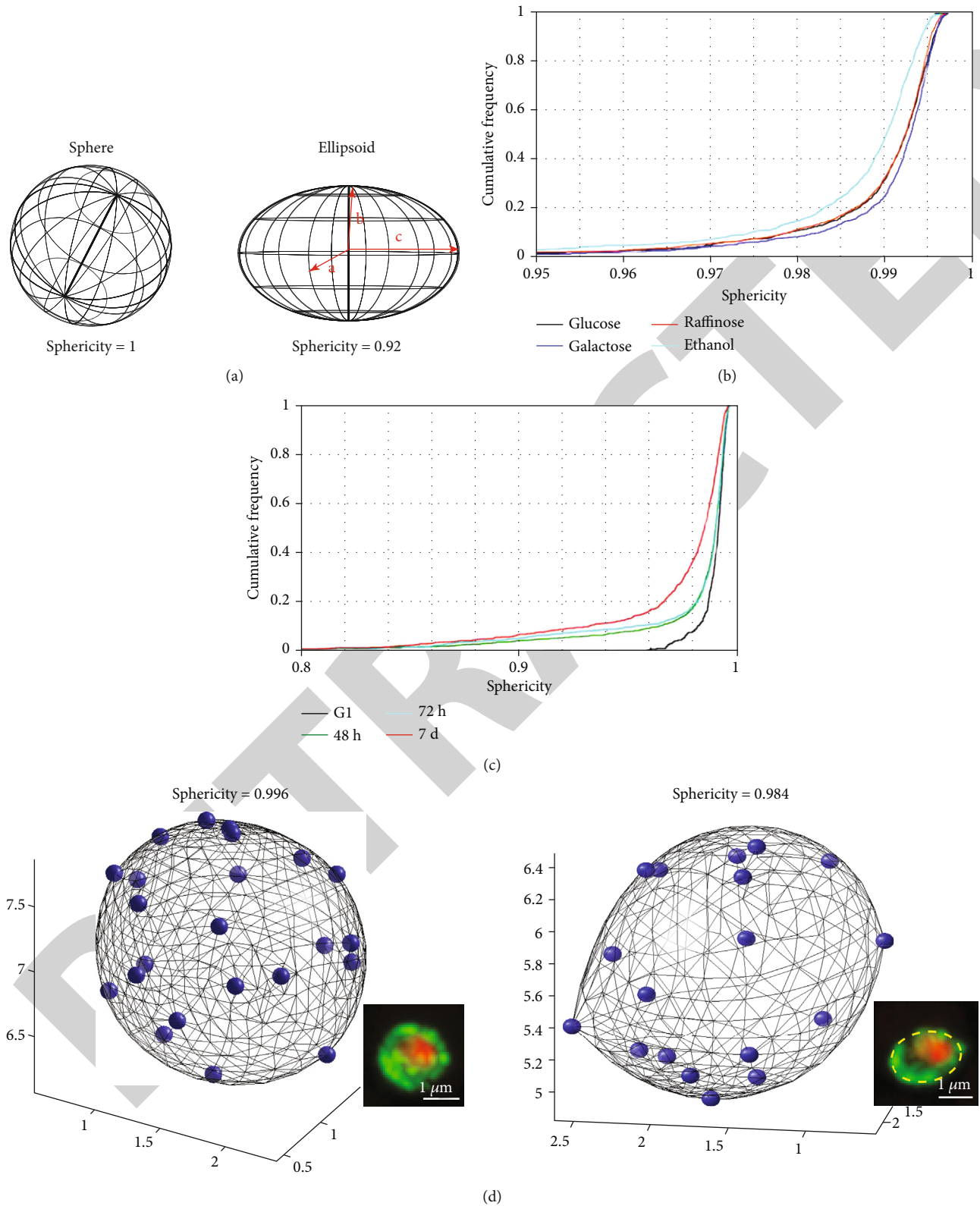
FIGURE 1: The heterogeneity of the nuclear shape in the cell population. (a) The sphericity of the perfect sphere (sphericity = 1) and the ellipsoid (sphericity = 0.92). (b) The change of the nuclear geometry in cell population cultured by different carbon sources, the sphericity of the nuclei decreases when the carbon source changed from the most favorable to the less favorable. (c) The distribution of the nuclear geometry after the cell population enters quiescence. (d) Two typical examples of the nucleus with different geometry *in vivo*, small blue spheres represent the detected NPC clusters.
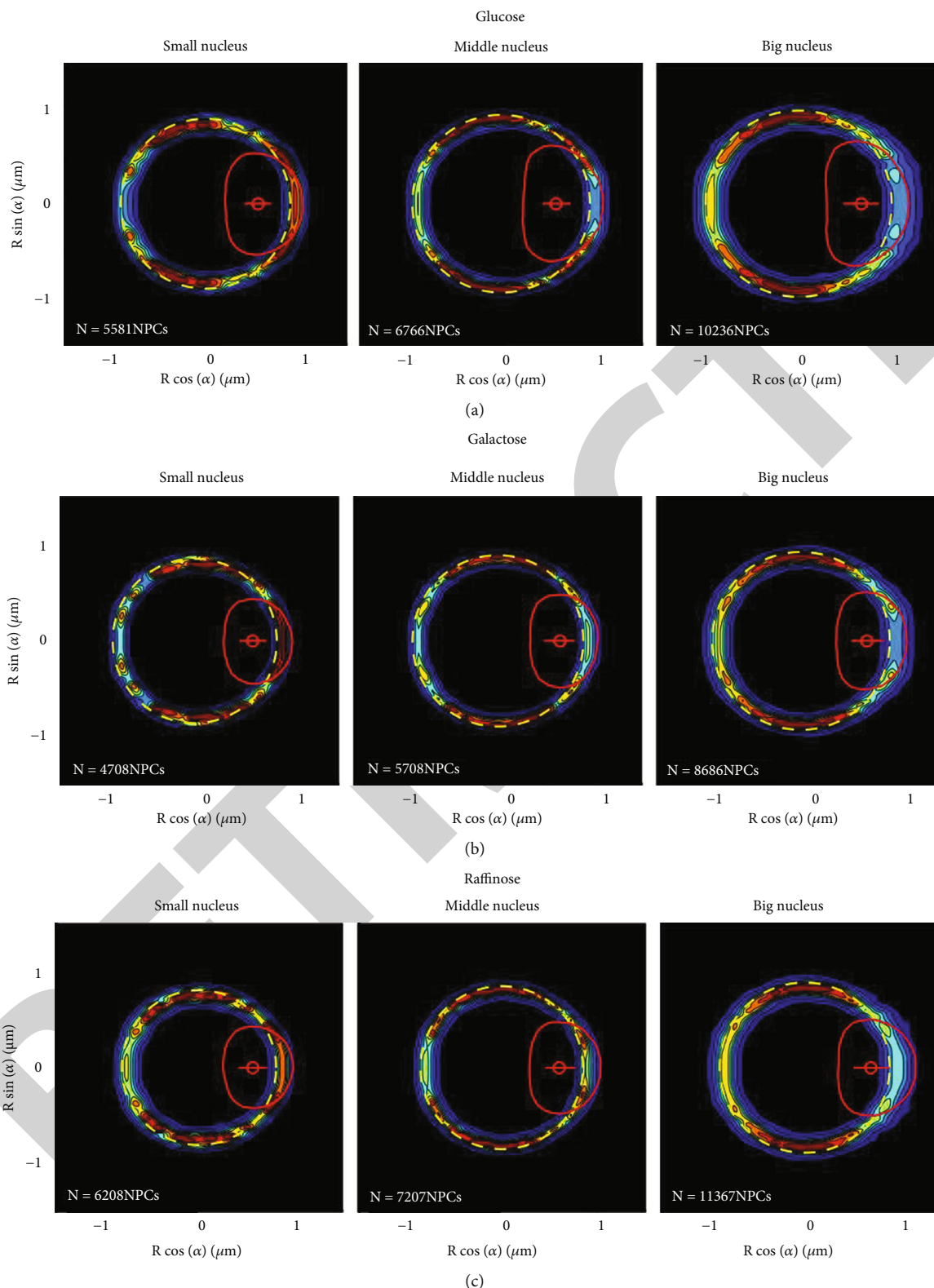
FIGURE 2: The variety of the NPC distribution along the NE according to carbon sources. The NPC probability density maps based on analysis of asynchronous cells cultured with glucose (a), galactose (b), and raffinose (c). The small-sized nuclei are composed of the newborn nuclei and the mother nuclei in the G1 phase; the middle-sized nuclei consist of the nucleus in the later G1 phase and S phase. The nuclei in the later S phase and early G2 phase constitute the bigger-sized nuclei. The dashed yellow circle represents the nuclear envelope determined according to the "NucQuant" technology; the red curve represents the median nucleolus contour; the red small circle represents the median nucleolar centroid; N represents the number of the NPC clusters used to generate the cumulative percentage maps.

(a)

(b)
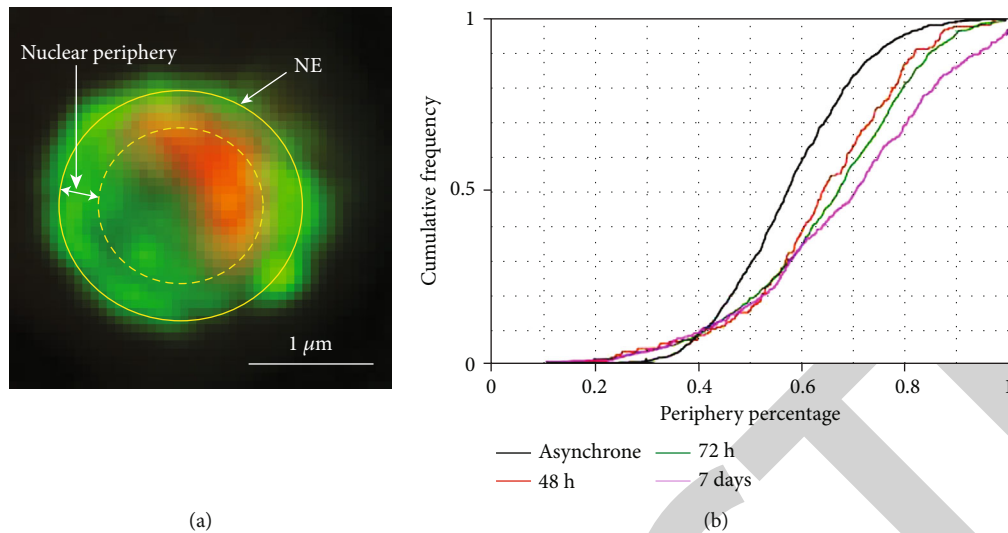
Figure 3: The change of the nucleolar organization after the cell population enters quiescence. (a) Schematic of the nucleus, nucleolus, and nuclear periphery region. Here, the periphery region was defined as the region that occupied 1/3 of the total nucleus at the periphery. The solid and dashed yellow circles represent the NE and the boundary of the nuclear periphery, respectively. (b) The reorganization of the nucleolus after the cell population enters quiescence, the nucleolus localized to the nuclear envelope closer.

4. Conclusion

In this study, the heterogeneity of the nuclear organization, including the nuclear geometry, the distribution of the NPC along the NE, and the nucleolus organization, was successfully determined through the "NucQuant" technology. The nuclear would shrink anisotropically to control the limited consumption of the cell, which resulted in the nuclei lost their sphericity, when the carbon source changed from the most to a less favorable. Moreover, the NE increased from the surface of the NE flanking the nucleolus with the growing of the nuclear, which caused the variety of the NPC distribution along the NE close to the nucleolus. Furthermore, accompanying the shrink of the nucleus, the nucleolus also reorganized to the periphery region since the transcription of the rDNA was repressed.

Data Availability

The data used to support the findings of this study are available from the corresponding author upon request.

Disclosure

This work is completed based on the author's Ph.D. thesis paper "Quantitative Analysis of Chromatin Dynamics and Nuclear Geometry in Living Yeast Cells".

Conflicts of Interest

We declare that we have no financial and personal relationships with other people or organizations that can inappropriately influence our work, there is no professional or other personal interest of any nature or kind in any product, service, and/or company that could be construed as influencing the position presented in, or the review of, the manuscript entitled.

Supplementary Materials

Supplementary Figure S1 shows the schematic illustration of the "NucQuant" technology. (Supplementary Materials)

References

[1] P. R. Cook, "The organization of replication and transcription," Science, vol. 284, no. 5421, pp. 1790–1795, 1999.

[2] P. Therizols, T. Duong, B. Dujon, C. Zimmer, and E. Fabre, "Chromosome arm length and nuclear constraints determine the dynamic relationship of yeast subtelomeres," Proceedings of the National Academy of Sciences of the United States of America, vol. 107, no. 5, pp. 2025–2030, 2010.

[3] Z. Duan, M. Andronescu, K. Schutz et al., "A three-dimensional model of the yeast genome," Nature, vol. 465, no. 7296, pp. 363–367, 2010.

[4] K. Bystricky, T. Laroche, G. van Houwe, M. Blaszczyk, and S. M. Gasser, "Chromosome looping in yeast: telomere pairing and coordinated movement reflect anchoring efficiency and territorial organization," The Journal of Cell Biology, vol. 168, no. 3, pp. 375–387, 2005.

[5] C. H. Yang, E. J. Lambie, J. Hardin, J. Craft, and M. Snyder, "Higher order structure is present in the yeast nucleus: autoantibody probes demonstrate that the nucleolus lies opposite the

Retraction

Retracted: Study of the Structure and Properties of ZnS Utilized in a Fluorescence Biosensor

Stem Cells International

This article has been retracted by Hindawi following an investigation undertaken by the publisher [1]. This investigation has uncovered evidence of one or more of the following indicators of systematic manipulation of the publication process:

(1) Discrepancies in scope

(2) Discrepancies in the description of the research reported

(3) Discrepancies between the availability of data and the research described

(4) Inappropriate citations

(5) Incoherent, meaningless and/or irrelevant content included in the article

(6) Manipulated or compromised peer review

The presence of these indicators undermines our confidence in the integrity of the article's content and we cannot, therefore, vouch for its reliability. Please note that this notice is intended solely to alert readers that the content of this article is unreliable. We have not investigated whether authors were aware of or involved in the systematic manipulation of the publication process.

Wiley and Hindawi regrets that the usual quality checks did not identify these issues before publication and have since put additional measures in place to safeguard research integrity.

We wish to credit our own Research Integrity and Research Publishing teams and anonymous and named external researchers and research integrity experts for contributing to this investigation.

The corresponding author, as the representative of all authors, has been given the opportunity to register their agreement or disagreement to this retraction. We have kept a record of any response received.

References

[1] Y. Ren, H. Zhou, X. Wang, Q. W. Liu, X. D. Hou, and G. F. Zhang, "Study of the Structure and Properties of ZnS Utilized in a Fluorescence Biosensor," *Stem Cells International*, vol. 2021, Article ID 7067146, 6 pages, 2021.

Research Article

Study of the Structure and Properties of ZnS Utilized in a Fluorescence Biosensor

Y. Ren [iD],[1] H. Zhou,[1] X. Wang,[2] Q. W. Liu,[2] X. D. Hou,[2] and G. F. Zhang [iD][2]

[1]*Henan University of Technology, School of Materials Science and Engineering, Engineering Laboratory of High Temperature Resistance-Wear Materials, Zhengzhou 450007, China*
[2]*Key Laboratory of Materials Modification by Laser, Ion and Electron Beams (Ministry of Education), School of Materials Science and Engineering, Dalian University of Technology, Dalian, 116024 Liaoning Province, China*

Correspondence should be addressed to Y. Ren; ying_ren@haut.edu.cn and G. F. Zhang; gfzhang@dlut.edu.cn

ZnS materials have been widely used in fluorescence biosensors to characterize different types of stem cells due to their excellent fluorescence effect. In this study, ZnS was prepared by vulcanizing nano-Zn particles synthesized using a DC arc plasma. The composition and structure of the ZnS materials were studied by X-ray diffraction (XRD), and their functional group information and optical properties were investigated by using IR spectrophotometry and UV-vis spectrophotometry. It has been found that the synthesized materials consist of Zn, cubic ZnS, and hexagonal ZnS according to the vulcanization parameters. Crystalline ZnS was gradually transformed from a cubic to a hexagonal structure, and the cycling properties first increase, then decrease with increasing sulfurization temperature. There is an optimal curing temperature giving the best cycling performance and specific capacity: the material sulfurized thereat mainly consists of cubic β-ZnS phase with a small quantity of Zn and hexagonal α-ZnS. The cubic phase ZnS has better conductivity than hexagonal ZnS, as evinced by electrochemical impedance spectroscopy (EIS). The ZnS (as prepared) shows board absorption, which can be used in fluorescence biosensors in cell imaging systems.

1. Introduction

Fluorescence biosensors are used in qualitative or quantitative analysis by fluorescence enhancement, quenching, or shift of emission wavelength by fluorescence signals; they are used for cell imaging, so organic fluorescent dyes have been developed, including fluorescein, rhodamine, and coumarin. [1, 2] Compared with these traditional organic fluorescent dyes, ZnS nanomaterials, as important II-VI compound semiconductors, have attracted much attention. Its band gap at room temperature is 3.66 eV, resulting in excellent fluorescence and electroluminescence function, making it a good fluorescent host material.

ZnS quantum dots (QDs) have been developed as promising materials for different uses in devices such as chemical sensors [3], in antibacterial applications, [4] and biological imaging and diagnosis [5–9]. Furthermore, ZnS nanomaterials can be thought of as candidate anode materials of

lithium-ion batteries, replacing graphite carbon materials [10]. The performance of lithium-ion batteries depends largely on anode materials [11, 12]. The anode performance, moreover, will deteriorate due to the large volume changes before and after lithium intercalation. Solvothermal synthesis and microwave synthesis are the main methods used to prepare ZnS [13–17]. As a solution, carbon-coated ZnS has been prepared by the solvothermal method in recent years [18]. To prepare ZnS with excellent performance, the new synthetic methods at low cost, with high yield, good stability, and effective elimination of surface defects need to be explored.

In the present work, a simple and low-cost method was used to synthesize ZnS nanomaterials. Firstly, Zn powders were prepared by DC arc plasma and then vulcanized to form ZnS [19]. The advantage therein is that the degree of vulcanizing and the structure of ZnS can be controlled by altering various vulcanizing parameters. Whether it is used
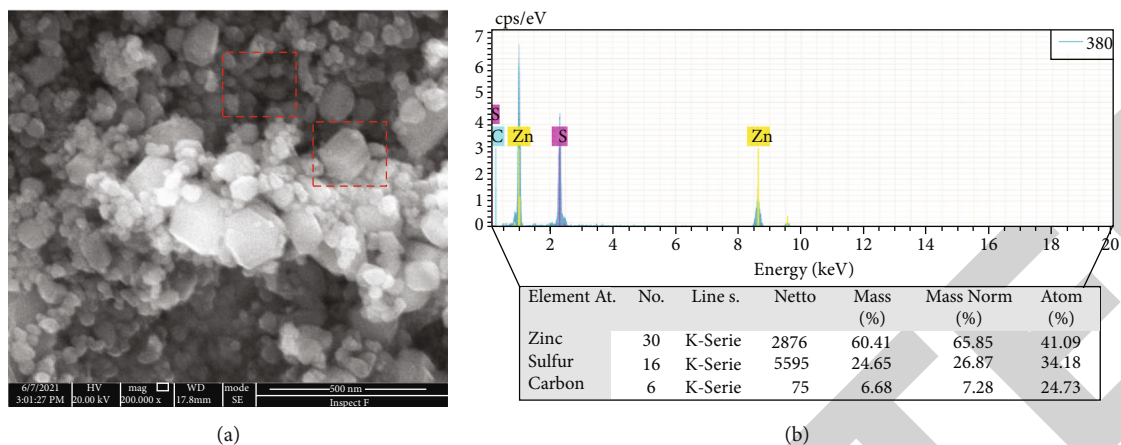
FIGURE 1: (a) SEM image of the ZnS materials at the sulfurization temperature of 350°C and (b) the corresponding EDX spectra.

as a fluorescent probe or anode material, we are trying to obtain high-performance ZnS materials in terms of their optical and electrochemical properties. The electrochemical properties can be improved and are superior to those of pure Zn or ZnS materials [20].

2. Experiments

In a DC arc-discharge plasma evaporation system, the arc was maintained between the bulk Zn (99.99%) anode and the W cathode for 5 min at a current of about 50 A using argon at 0.03 MPa and hydrogen at 0.01 MPa as the carrier gas. After cooling for 120 min and then allowing inflow of air at 0.025 MPa to deactivate the system for 12 h, the vacuum chamber was opened to collect the resulting Zn powder. The uniform mixture of precursors and sublimated sulfur in the ratio of 1 : 1 was put in a closed reactor located at the flat-temperature zone of a tube-type vacuum furnace. The mixture was heated at 200, 250, 300, and 350°C, respectively, at a rate of 10°C/min, then maintained thereat for 2 h. After cooling to room temperature in the furnace, the reactant was dispersed in a porcelain boat and reheated to 200°C for 2 h to remove the remaining sulfur. Finally, the ZnS powders were obtained.

SEM and energy-dispersive X-ray spectrometry (EDX) were used to assess the surface morphology and composition of the ZnS powders (FEI inspect F50). The structure of the ZnS materials was characterized by an XRD-6000 diffractometer with a scanning rate of 4°/min. Functional group information was acquired from Fourier-transform infrared spectroscopy (FTIR, Prestige-21). The optical absorbance was measured on a UV-vis spectrophotometer (SHIMADZU UV-2600i). The electrochemical performance was evaluated using CR2025 coin-type half cells. The anode active material was mixed with conductive additive (Ketjen black) and binder (poly(acrylic acid) (PAA)) in a mass ratio of 8 : 1 : 1. A homogeneous slurry was formed by stirring and dissolving an appropriate amount of deionized water in the mixture. The slurry was uniformly coated onto a copper foil current collector. After drying at 70°C for 12 h and suppressing the reaction, an electrode disk (14 mm in diameter) was obtained with a mass loading of 0.8 mg/cm^2. The CR2025
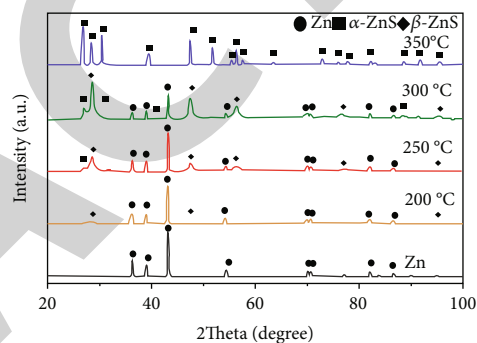
FIGURE 2: XRD spectra of the ZnS materials at different sulfurization temperatures.

button cells were assembled in an argon-filled glovebox using lithium metal as counter electrode. The separator and electrolyte were a microporous polypropylene film and 1 M LiPF$_6$ solution in ethylene carbonate (EC)/diethyl carbonate (DEC) (1 : 1 by volume), respectively. The galvanostatic charge-discharge and rate capability were carried out using a Land CT2001A testing system in a voltage window of 0.01–3 V vs. Li/Li+. The cyclic voltammogram (CV) curves were obtained using a CHI660E electrochemical workstation at a scanning rate of 0.1 mV s^{-1} between 0.01 and 3 V. The electrochemical impedance spectroscopy (EIS) analysis was conducted over the frequency range from 0.01 to 100 kHz at an amplitude of 0.5 mV.

3. Results and Discussion

The morphology of the ZnS powders was examined using an SEM, as shown in Figure 1. It was observed that powders with different sizes and irregular shapes consisted of smaller particles (<100 nm) and nanosheets (~200 nm) indicated by boxes in Figure 1(a). The EDX spectra evinced the chemical composition of the synthesized powders as mainly composed of zinc and sulfur (Figure 1(b)).

The XRD spectra of the ZnS materials under various sulfurization temperatures are shown in Figure 2. It was found
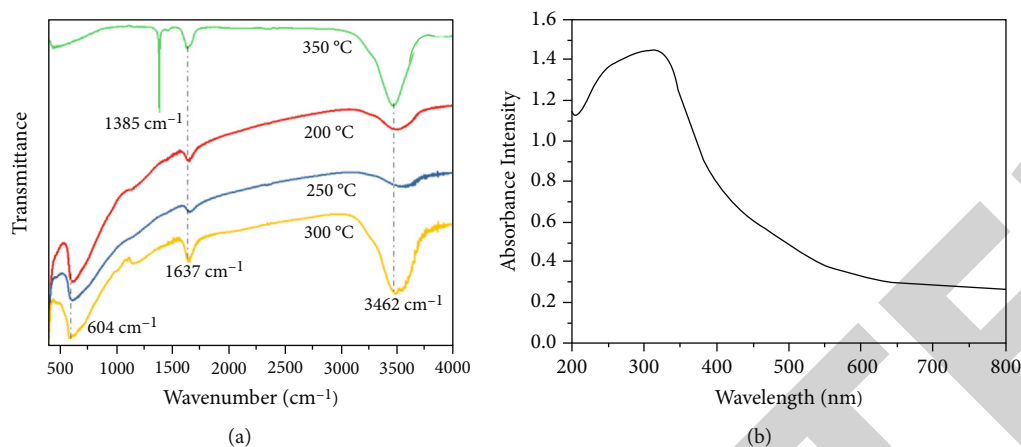
Figure 3: (a) FTIR spectra of ZnS and (b) UV spectrum of ZnS at 350°C.

Table 1: Cycle performance of Zn/ZnS materials prepared at various sulfurization temperatures.

Temperature (°C)	First discharge capacity (mAh/g)	First charge capacity (mAh/g)	Discharge capacity after 300 cycles (mAh/g)	Retention ratio after 300 cycles (%)
25 (pure Zn)	527.8	405.3	<81.3	<15.4
200	627.4	305.1	99.6	16.0
250	894.8	407.6	156.3	17.5
300	998.8	465.2	230.3	23.1
350	1052.0	511.6	96.7	9.2

that there were three phases of Zn, β-ZnS, and α-ZnS in the vulcanization products. Diffraction peaks located at 36.1°, 38.9°, and 43.1° are assigned to the (002), (010), and (011) planes of Zn, at 28.6°, 47.5°, and 56.3° to (111), (220), and (101) of cubic β-ZnS, and at 26.9°, 28.5°, and 30.6° to (100), (002), and (011) of hexagonal α-ZnS, respectively.

The intensity of Zn diffraction peaks gradually decreased with increasing sulfurization temperature and the Zn diffraction peak disappeared at about 350°C. Moreover, cubic β-ZnS had begun to form at 200°C. The main product was cubic β-ZnS between 250 and 300°C: this became hexagonal α-ZnS at 350°C. It is noteworthy that the phase transformation temperature from β-ZnS to α-ZnS was greater than 1000°C [12], which indicates that the high surface energy of the Zn nanoparticles plays an important role in the sulfurization process [21].

In the FTIR spectra of the ZnS materials at different sulfurization temperatures as shown in Figure 3(a), the absorption peaks occur at about $3462 \, cm^{-1}$ and $1637 \, cm^{-1}$, which can be ascribed to the stretching and bending vibration of the O-H and H-O-H bands from external surface water molecules, respectively. [22, 23] Another absorption peak appears at $604 \, cm^{-1}$ when the sulfurization temperature increases from 200°C to 300°C. The characteristic vibration of ZnS was observed at 669 or $642 \, cm^{-1}$, which was confirmed in Ref.[23, 24] However, with increasing the sulfurization temperature to 350°C, the sharper peak located at $1385 \, cm^{-1}$ could be indexed to the stretching vibration of C-O-C bonds. [22] In this study, the excellent optical char-

acteristics of ZnS nanoparticles were observed by absorption spectra. The UV absorption spectrum of ZnS at the sulfurization temperature of 350°C is shown in Figure 3(b): ZnS nanoparticles had a wider range of absorption and show a peak corresponding to 1s-1s electronic transitions therein [22]. The absorption peak position of ZnS was 313 nm, but the maximum absorbance cut-off wavelength was observed at about 500 nm (albeit weak).

At a constant current density of 0.5 A/g, the charge/discharge tests of the cells assembled from the ZnS materials prepared at various sulfurization temperatures were conducted (Table 1). With increasing sulfurization temperature, the first discharge capacity increases from 527.8 to 1052.0 mAh/g and first charge capacity from 405.3 to 511.6 mAh/g. Unexceptionally, the capacity of all such cells decreases with increased cycling. The discharge capacity retention ratio after 300 cycles increases slowly with increasing sulfurization temperature, reaching a maximum of 23.1% at 300°C, and then falling to 9.2%. Under same conditions, the discharge capacity retention ratio of the pure Zn is only 15.4% after 100 cycles: the cycling performance of the Zn/ZnS composites is superior to that of Zn or ZnS. Two main reasons for this are the volumetric expansion of the ZnS materials and the shuttle effects of the elemental S therein; moreover, these two reasons act in mutual opposition. The first factor dominates under lower sulfurization, and the second at higher degrees of vulcanizing, which leads to the existence of an optimal cycle performance.
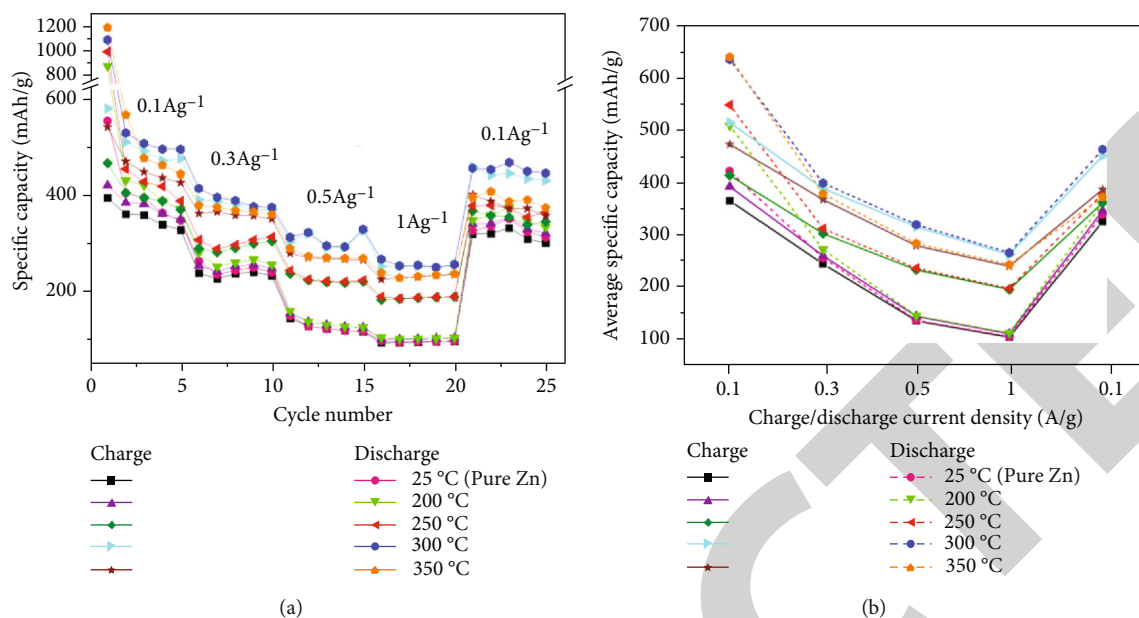
FIGURE 4: (a) Rate capability and (b) the average specific capacity of the ZnS materials vulcanized at various temperatures.
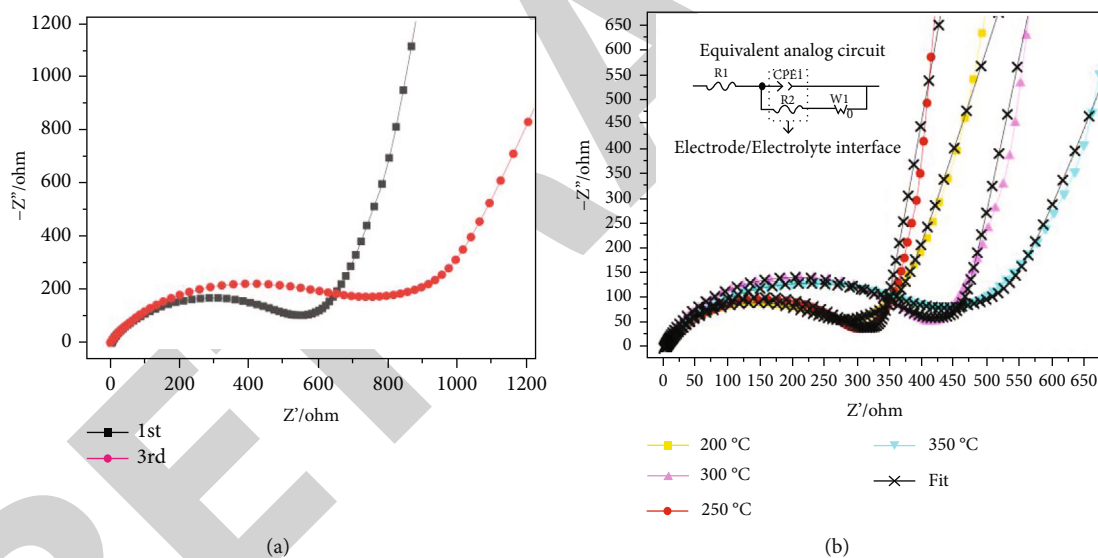
FIGURE 5: (a) EIS of Zn. (b) EIS and the corresponding equivalent analogue circuits of the ZnS materials at different sulfurization temperatures.

The rate capability of the ZnS materials was measured in a range of charge/discharge current density 0.1-1.0 A/g. As shown in Figure 4(a), the current density was changed every five cycles. The average specific capacity on each stage for different samples is illustrated in Figure 4(b): the rate capability of samples presents stepped characteristics. The capability can recover if the current density returns from 1.0 A/g to 0.1 A/g. This means that this loss of capacity is reversible, and there is a maximum capability in the tested range of charge/discharge current density at a sulfurization temperature of 300°C.

To further reveal the relationship of the composition of different phases with the electrochemical performance, EIS

is applied to specimens in the initial state (Figure 5). The larger the diameter of the semicircle, the more difficult the migration of the lithium ion at the interface. The shallower the slope, the greater the barrier to lithium-ion diffusion inside the electrodes [25]. As shown in Figure 5(a), the diameter increases and the slope for specimens of pure Zn decreases with increased cycling, suggesting that it is more difficult for lithium ions both to enter the electrode and to migrate within.

The equivalent circuit (inset, Figure 4(b)) matches that in an actual battery because the corresponding fitting curves are completely consistent with those measured. This is attributable to the influences of the sulfurization temperature on the

composition and phase of the ZnS materials. When vulcanized at 250°C and 300°C, the slope of the linear portion of the sample is greater, which is due to a higher cubic β-ZnS content. Compared with the dense hexagonal α-ZnS, the lattice gap of β-ZnS is greater and the lithium-ion conductivity is better. The semicircle diameter in the high-frequency region increases with increasing vulcanization temperature; the difficulty of lithium-ion migration at the interface increases due to the increase in the amount of hexagonal α-ZnS phase with its lower ionic conductivity.

4. Conclusions

A zinc precursor was prepared by DC arc plasma method, then sulfurized at different temperatures to obtain Zn/ZnS composite powders. The microstructure and electrochemical properties of the Zn/ZnS materials with varying degrees of vulcanization were investigated. With increasing sulfurization temperature, pure Zn gradually changes into cubic β-ZnS and then cubic β-ZnS into hexagonal α-ZnS. The cycling performance gradually increases to a maximum at 300°C, declining thereafter. The capability of the ZnS vulcanized at 300°C is maintained at 232.1 mAh/g after 300 cycles under conditions involving a 500 mA/g charge/discharge current density. Diffusion migration of lithium ions is easier in the cubic β-ZnS, as confirmed by electrochemical impedance spectroscopy. Furthermore, ZnS nanoparticles present good optical properties and have potential applications in biological tagging and cell imaging.

Data Availability

Data sharing not applicable to this article as no datasets were generated or analysed during the current study.

Conflicts of Interest

The authors declare that they have no conflicts of interest.

Acknowledgments

References

[1] A. Loudet and K. Burgess, "BODIPY dyes and their derivatives: syntheses and spectroscopic properties," *Chemical Reviews*, vol. 107, no. 11, pp. 4891–4932, 2007.

[2] H. Katerinopoulos, "The coumarin moiety as chromophore of fluorescent ion indicators in biological systems," *Current Pharmaceutical Design*, vol. 10, no. 30, pp. 3835–3852, 2004.

[3] J. Liu, H. Chen, Z. Lin, and J. M. Lin, "Preparation of surface imprinting polymer capped Mn-doped ZnS quantum dots and their application for chemiluminescence detection of 4-nitrophenol in tap water," *Analytical Chemistry*, vol. 82, no. 17, pp. 7380–7386, 2010.

[4] S. Kumar, A. Jain, S. Panwar et al., "Effect of silica on the ZnS nanoparticles for stable and sustainable antibacterial applica-

[5] T. Pellegrino, S. Kudera, T. Liedl, A. Muñoz Javier, L. Manna, and W. . J. Parak, "On the development of colloidal nanoparticles towards multifunctional structures and their possible use for biological applications," *Small*, vol. 1, no. 1, pp. 48–63, 2005.

[6] N. Hildebrandt, "Biofunctional quantum dots: controlled conjugation for multiplexed biosensors," *ACS Nano*, vol. 5, no. 7, pp. 5286–5290, 2011.

[7] W. C. Chan and S. Nie, "Quantum dot bioconjugates for ultrasensitive nonisotopic detection," *Science*, vol. 281, no. 5385, pp. 2016–2018, 1998.

[8] W. Liu, M. Howarth, A. B. Greytak et al., "Compact biocompatible quantum dots functionalized for cellular imaging," *Journal of the American Chemical Society*, vol. 130, no. 4, pp. 1274–1284, 2008.

[9] S. K. Mahto, C. Park, T. H. Yoon, and S. W. Rhee, "Assessment of cytocompatibility of surface-modified CdSe/ZnSe quantum dots for BALB/3T3 fibroblast cells," *Toxicol in Vitro*, vol. 24, no. 4, pp. 1070–1077, 2010.

[10] Muthukumaraswamy Rangaraj, Achazhiyath Edathil, P. Kadirvelayutham, and Banat, "Chicken feathers as an intrinsic source to develop ZnS/carbon composite for Li-ion battery anode material," *Materials Chemistry and Physics*, vol. 248, p. 122953, 2020.

[11] Q. H. Cui, Y. T. Zhong, L. Pan et al., "Recent advances in designing high-capacity anode nanomaterials for Li-ion batteries and their atomic-scale storage mechanism studies," *Advanced Science*, vol. 5, no. 7, 2018.

[12] V. Etacheri, R. Marom, R. Elazari, G. Salitra, and D. Aurbach, "Challenges in the development of advanced Li-ion batteries: a review," *Energy & Environmental Science*, vol. 4, no. 9, pp. 3243–3262, 2011.

[13] E. M. Nolan and S. J. Lippard, "Small-molecule fluorescent sensors for investigating zinc metalloneurochemistry," *Accounts of Chemical Research*, vol. 42, no. 1, pp. 193–203, 2009.

[14] G. Palanisamy, T. Pazhanivel, K. Bhuvaneswari, G. Bharathi, G. Marimuthu, and T. Maiyalagan, "Spinel oxide $ZnCr_2O_4$ incorporated with ZnS quantum dots for application on visible light driven photocatalyst Azo dye degradation," *Colloids and Surfaces A: Physicochemical and Engineering Aspects*, vol. 590, p. 124505, 2020.

[15] A. Błażewicz, W. Dolliver, S. Sivsammye et al., "Determination of cadmium, cobalt, copper, iron, manganese, and zinc in thyroid glands of patients with diagnosed nodular goitre using ion chromatography," *Journal of Chromatography B*, vol. 878, no. 1, pp. 34–38, 2010.

[16] Z. Li, M. Yu, L. Zhang et al., "A "switching on" fluorescent chemodosimeter of selectivity to Zn^{2+} and its application to MCF-7 cells," *Chemical Communications*, vol. 46, no. 38, pp. 7169–7171, 2010.

[17] Z. X. Han, X. B. Zhang, Z. Li et al., "Efficient fluorescence resonance energy transfer-based ratiometric fluorescent cellular imaging probe for Zn2+Using a rhodamine spirolactam as a trigger," *Analytical Chemistry*, vol. 82, no. 8, pp. 3108–3113, 2010.

[18] L. He, X. Z. Liao, K. Yang, Y. S. He, W. Wen, and Z. F. Ma, "Electrochemical characteristics and intercalation mechanism of ZnS/C composite as anode active material for lithium-ion

Review Article

The Influence of the Surface Topographical Cues of Biomaterials on Nerve Cells in Peripheral Nerve Regeneration: A Review

Fang Liu [ID],[1,2,3,4] **Jiawei Xu** [ID],[1,2,3] **Linliang Wu** [ID],[1,2,3] **Tiantian Zheng** [ID],[1,2,3] **Qi Han** [ID],[1,2,3] **Yunyun Liang** [ID],[1,2,3] **Liling Zhang** [ID],[1,2,3] **Guicai Li** [ID],[1,2,3] **and Yumin Yang** [ID][1,2,3,4]

[1]*Key Laboratory of Neuroregeneration of Jiangsu and Ministry of Education, Nantong University, 226001 Nantong, China*
[2]*Coinnovation Center of Neuroregeneration, Nantong University, 226001 Nantong, China*
[3]*School of Medicine, Nantong University, 226001 Nantong, China*
[4]*NMPA Key Laboratory for Research and Evaluation of Tissue Engineering Technology Products, Nantong University, 226001 Nantong, China*

Correspondence should be addressed to Guicai Li; gcli1981@ntu.edu.cn and Yumin Yang; yangym@ntu.edu.cn

The surface topographies of artificial implants including surface roughness, surface groove size and orientation, and surface pore size and distribution have a great influence on the adhesion, migration, proliferation, and differentiation of nerve cells in the nerve regeneration process. Optimizing the surface topographies of biomaterials can be a key strategy for achieving excellent cell performance in various applications such as nerve tissue engineering. In this review, we offer a comprehensive summary of the surface topographies of nerve implants and their effects on nerve cell behavior. This review also emphasizes the latest work progress of the layered structure of the natural extracellular matrix that can be imitated by the material surface topology. Finally, the future development of surface topographies on nerve regeneration was prospectively remarked.

1. Introduction

Peripheral nerve injury is the most common disease in clinical medicine, which brings much trouble to the patients in their life. The pathogenic factors are varied, including trauma, traffic accidents, or artificially excised nerve tissue by surgery, sports injury, etc. [1]. Although most of the peripheral nerve damage will not endanger a human's life, it could hinder the function of normal surrounding tissues [2], lead to mobility difficulties and sensory abnormalities, and have a negative impact on people's daily life. From a biological point of view, nerve damage and scarring at the site of injury are major contributors to the healing of damaged nerves, which may limit the functional recovery of peripheral nerves [3]. Therefore, repairing peripheral nerves remains an urgent clinical problem that has not been adequately addressed. In today's medical field, the functional repair of damaged tissues in the nervous system is still a huge problem. After nerve tissue damage, the formed glial scar will produce

inhibitory molecules to block the regeneration of nerve axons [4]. In order to achieve the functional replacement of damaged tissues in neural tissue, more and more artificial nerve grafts made of synthetic or natural biomaterials have been developed to promote the growth, proliferation, and differentiation of nerve cells [5] .

Tissue engineering is aimed at solving the problem of organ shortage by developing biological substitutes that can help restore or enhance the function of damaged tissue [6]. With the continuous deepening of the research on tissue engineering, the research on nerve grafts is also transitioning from simple primary preparation to advanced bionic and functional preparation [7]. More and more studies have shown that the microenvironment constructed by the surface properties of tissue engineering product materials has an important impact on tissue engineering and organ regeneration [8–10]. For example, biomaterials not only provide mechanical and three-dimensional structural support for tissue and organ regeneration, but some of its own properties

and factors can also regulate tissue and organ regeneration. These characteristics and factors include the surface characteristics of materials (such as surface topology), which are now gradually becoming a research hotspot [8–10]. The surface topology of a material plays a very important role in guiding cell behavior, including morphology, adhesion, differentiation, and axon guidance [8, 11]. Nerve cells or neurons are responsible for transmitting signals to other cells. They collect signals through dendrites and cell soma and transmit signals through synapses at the end of axons [12]. Therefore, numerous studies have been devoted to the manufacture of the surface pattern of biomaterials for exploring the role of contact guidance. In recent years, two-photon polymerization nanolithography micro/nanomanufacturing technology has become a powerful and useful manufacturing tool, which can generate two-dimensional (2D) to three-dimensional (3D) arbitrary micro/nanotopologies of various materials with high spatial resolution, thus arousing great interest in cell and tissue engineering [13].

Material surface topology was reported to have a significant effect on nerve regeneration [6, 14]. The normal nerve tissue is distributed on a long-strip structure with good orientation growth. Thus, simulating this structure will be beneficial for nerve regeneration. Miller et al. found that the stripe-shaped distribution of the PDLA pattern could regulate the orientation growth behavior of Schwann cells, which had the best alignment when the groove width was 10-20 μm, but the depth of the grooves showed little effect [15]. Song and Uhrich studied the size effect of laminin micropatterns on the axon growth rate, length, and tropism of DRG; they found that when the protein pattern width was 40 μm, DRG cells had the fastest axon growth rate and best orientation [16]. The above two studies indicated that when the appropriate topography size, i.e., approaching to cell size, was designed, the process of nerve regeneration could be significantly promoted. The studies have an important reference value for revealing the effect of the surface size of the biomaterial on nerve regeneration. Blong et al. found that the patterned surface of collagen and laminin could better regulate the orientation and distribution of neural progenitor cells but had little effect on their differentiation ability [17]. Researchers have also used micrographic methods to successfully differentiate neural stem cells into neural cells, astrocytes, and oligodendrocytes [18]. The latest report by Liu et al. displayed that the 3D topology of biomaterials (porosity, pore size, etc.) and the geometric topology of sub-cell size could affect the specific differentiation of progenitor cells and stem cells [19]. In addition, Lu et al. found that basal stiffness and topology can coordinately regulate stem cell morphology and differentiation [20]. Therefore, the micropatterns on the surface of biomaterials can build a physical microenvironment that is conducive to cell growth and orientation, to promote and regulate the growth and spatial distribution of nerve cells for achieving better and faster nerve regeneration. However, numerous studies are currently limited to the regulation of topographies on cell morphology, while the molecular mechanism of how nerve cells sense the surface topology of materials, and how surface topology affect the inner reaction of cells, such as

gene variation and signal pathway activation, is still not fully understood.

Thus, understanding how nerve cells respond to different biomaterial surface topologies is critical to the development of suitable nerve grafts used in regenerative medicine and tissue engineering. The purpose of this review is mainly to emphasize the significance of the surface topology of biomaterial implants and their effect on the behavior of nerve cells, including proliferation, differentiation, adhesion, migration, alignment growth, and neurite guidance and relevant mechanism (Figure 1).

2. Different Features of Topographies and Their Influence on Cell Behavior

2.1. Topography Affects Cell Proliferation and Differentiation. Cell proliferation is one of the important physiological functions of living cells and an important life characteristic of organisms, which is the basis of organism growth, development, reproduction, and heredity, and could be seriously affected by the structure of the surrounding microenvironment. In recent years, many studies have applied various microfabrication methods to prepare concrete topographical maps, at sub-micro- and microscales. A new technology has been developed to prepare microgrooves with adsorbed proteins on a biodegradable polymer substrate made of poly(D,L-lactic acid) [6, 10, 15, 21]. The effect of matrix-mediated chemical and physical guidance on the growth and arrangement of Schwann cells in vitro was studied. The preparation of surface nanotopography by Onesto et al. and others can guide nerve cells to assemble into efficient computational networks, providing new tools and standards for tissue engineering and regenerative medicine [6, 10, 15, 21]. Generally, the natural physiological tissues have a specific microtopological structure, with the repetition or regular arrangement of certain geometric features in space. The morphology and structure are closely related to the physiological functions it undertakes. Besides, the specific microtopology could provide space for cell growth and diffusion in the tissue. The difference of microtopology in different tissues may be one of the factors that regulate the biological behavior of cells. As a substrate for promoting cell or tissue growth, microtopological structures have begun to be used in various tissue engineering fields. According to the natural structure of physiological tissues, various types or sizes of porous or microgrooved arrays for regulating cell or tissue growth have been designed and fabricated [22, 23]. Previous studies have shown that microtopology could regulate the growth of nerve cells and tissues and promote cell proliferation and differentiation. The suitable topographical types fabricated on biomaterials can be used to regulate cell expansion, direction differentiation, and migration [24, 25]. Moreover, understanding the mechanism of cell surface topographical interaction is of great significance for scaffold design in nerve tissue engineering [26, 27].

Many studies have shown that microtopography can promote the proliferation of adherent cells including most nerve cells. In previous studies, a simple method of combining freeze-drying and micromolding to efficiently and expandably
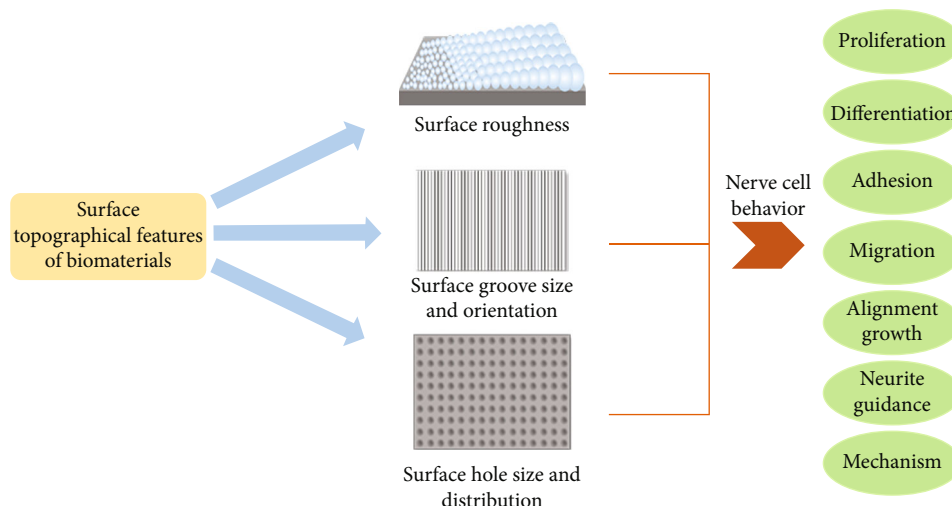
FIGURE 1: Schematic diagram of the influence of the surface topographical features of biomaterials on the behavior of nerve cells.

manufacture a biomaterial conduit with a seamless sidewall and longitudinally arranged structures on the inner wall was developed. The highly arranged microstructures could speed up the directional growth of neonatal nerve tissues, and the foraminous sidewalls were expected to be in favor of loading biological factors and reducing nutrient leakiness or axon out-growth [28]. The number of proliferating cells was largely dependent on the diameter of the nanofibers, and the prolifer-ation increases with the decrease of the fiber size. Christopher-son et al. also found a similar phenomenon by culturing rat neural stem cells on a grid composed of nanofibers, which further confirmed the extreme sensitivity of cell proliferation to specific sizes of nanoscale features [29].

In numerous differentiation clues such as ECM composi-tion, soluble factors, material component, and structure, the nanomorphology around the cell plays a vital role [30]. Embryonic stem cells (ESC), as a renewable source of cells, have great application potential in nerve injury repair. In order to study the response of ESC to uneven surfaces, Chen et al. [31] used a simple self-assembly method to prepare highly ordered hexagons with completely opposite curva-tures. The array and honeycomb structure surface were formed by the cell sequence, and experiments proved that in the concave honeycomb structure, the cells could not enter the honeycomb pores, but penetrate the honeycomb pores, which promoted the elongation of cells. The release of gravity promoted homosexual diffusion and cell proliferation. Alvarez et al. [32] designed a biomimetic PLA nanofiber scaf-fold that could release L-lactic acid. The topological structure of PLA nanofibers could promote the growth of neurons and glial cells. They showed that the release of L-lactic acid through the bionic scaffold composed of electrospun PLA fibers reproduced the three-dimensional organization and supported functions of embryonic radial glial cells, thereby simulating physical and biochemical characteristics of the embryonic NSC niche. Although there is still a long way before clinical transformation, the results of the research opened unexpected and exciting prospects for the design of

cell-free implant devices. By promoting glial cell generation, neurogenesis, and vascularization, the functional nerve tissue lost after injury can be restored without growth factors, genetic manipulation, or exogenous cells.

Cheong et al. [33] designed natural polymer scaffolds with bionic topologies. They found that a mussel adhesion protein could be fused with biological functional peptides in the extracellular matrix to strengthen differentiation and proliferation of neuron and Schwann cells. Additionally, the contact between nerve cells and aligned nanofibers can greatly promote functional recovery after nerve regeneration. Therefore, by synergistically providing physical adhesion for cell proliferation, integrin-mediated stimulation for cell differentiation, and contact guidance for cell alignment, the proposed multidimensional bioinspiration strategy realized by aligned nanofiber scaffolds can be an effective and univer-sal bioinspired method in the field of neuroregenerative medicine. However, because the secretion of mussel protein is very low, the price of products extracted directly from mussels is relatively expensive, and it is thus very compli-cated to obtain genetically engineered products with the characteristics of natural adhesion proteins [34]. Islam et al. [35] conducted the first neuron-like PC12 growth study on untreated and easily available micro-nano-surfaces. Micro-reactive ion etching provided a fast and economical method to fabricate a nanostructured substrate for neuron-like cell culture. It was found that even in the absence of any extracel-lular matrix treatment (such as collagen and laminin), nano-structures could stimulate the growth of cultured PC12 cells. The neuron-like structure on the nanostructured glass cover slip was increased by 200% compared with the ordinary glass cover slip. Morphological studies showed that the attachment and growth of PC12 cells on the nanostructured substrate did not initiate any apoptosis mechanism of the cells. Coupled with the ability to induce and enhance the proliferation of PC12 cells, these substrates had excellent potential for neural cell attachment. Neural cell attachment is a precursor for enhanced differentiation, which can be used to manipulate

axon regeneration and guide neural circuit reconstruction, thus showing a great potential for treatment of nervous system trauma. Nanostructures can also promote the differentiation of mouse embryonic stem cells into neuronal lineages. For example, the diameter of the nanofibers affected the differentiation of neural progenitor cells in rats. The differentiation of oligodendrocytes on 283 nanofibers was increased by 40%, and differentiation of neurons on 749 nanofibers was increased by 20%, in contrast to the standard tissue culture surface [29].

The topographic signal of the substrate will have a certain guiding role in the process of cell development and tissue repair, and control the fate of cells. Moe et al. [36] fabricated a simple, customizable, cost-effective topology array that can combine different nano- to microtopologies with various aspect ratios and complexity levels. Anisotropic topographic maps (2-micron gratings, nanometer gratings) and isotropic topographic maps (1-micron column) promoted neuron differentiation. The isotropic 1-micron column and 2-micron holes were conducive to the differentiation of primary glial cells. In general, it showed that a multiarchitecture chip (MARC) could identify the best combination of topographical and biochemical cues by analyzing different topographies at the same time, which is beneficial for the cell-topography interaction. Therefore, the customizable MARC as a topological chip was a novel and unique platform with a wide range of potential biological applications. Choi et al. [37] used the engineered concave microarray to regulate the formation of the shape and size of the intermediate products of embryonic stem cells. The PDMS was used as the base material, and the differentiation of cardiomyocytes and neurons was induced by controlling the size of the concave microarray, which proved that the size of the concave microarray may be a main factor in regulating the differentiation of embryonic stem cells and a potential tool to guide the fate of embryonic stem cells. Fernandez et al. [38] designed and produced polycaprolactone/polyethylene oxide–polycaprolactone-blended fiber materials using electrospinning technology, and it was found that this blend promoted the growth of rat neural stem cells by culturing neural stem cells isolated from mouse brain fiber materials, and neural stem cells even differentiated into neurons and astrocytes without adding any growth factors. Tachizawa et al. [39] used hydroxyl propyl cellulose (HPC) and sodium alginate (Na-Alg) to prepare a neuronal cell-oriented scaffold with a bundle-like structure. These bundled fibers allowed neuronal cells to follow the axon direction and fiber long axis elongation, and experiments had shown that human-induced pluripotent stem cells could successfully differentiate into neuronal cells based on the fiber bundle structure. In addition, microtopology can effectively adjust to the differentiation and proliferation of cells [40]. In clinic, on the basis of effective treatment, microtopology could provide a way to enhance the differentiation and proliferation of nerve cells in order to reduce the damage of nerve tissue defects to the human body [41, 42]. The foundation of the topographical structure shortens the treatment time and improves the treatment efficiency. A list of the impacts of the topographical structure on the proliferation and differentiation of nerve cells is presented in Table 1.

2.2. Topography Affects Cell Adhesion and Migration.

Adhesion is an important condition for anchoring dependent cell survival, growth, and proliferation on the matrix. Poor adhesion may lead to cell immobility or even apoptosis [43]. Cell adhesion is the basis of communication between cells and the external environment and plays a major role in organizational development [44]. Thus, the adhesion is considered to be the first indicator of the interaction of cells with their surrounding environment, prior to other properties, such as proliferation, differentiation, and migration. Early studies showed that the surface topographical properties of biomaterials could guide nerve cell adhesion and the migration process [45]. The topographic maps submitted through nanofibers had been shown to promote the regeneration of peripheral nerves with a damaged gap. However, its basic mechanism has not yet been fully elucidated. For example, topography [9], wettability [46], chemical composition [47] are usually interrelated properties. An increase in the hydrophobicity of the surface of a fluorinated polystyrene material could cause a decrease in human MG63 osteosarcoma cell adhesion [46]. Adsorption of fibronectin (FN) on the hydroxyl functional groups (functional group as compared with -CH$_3$) showed high levels of $\alpha_5\beta_1$ level, resulting in an increase of cell adhesion and the structural strength of the signal component levels associated with focal adhesion of cells [48]. The topographies have a huge influence on cell adhesion and migration behavior. Jia et al. [49] prepared neatly arranged poly(L-lactic acid-co-e-caprolactone) (P(LLA-CL)) nanofibers. The Schwann cells that migrated and the number of axons on the neatly arranged nanofibers were 2.0 times and 2.84 times that of the random group, respectively. The nerve guide channels constructed by the aligned nanofibers obviously enhance peripheral nerve regeneration through stimulating a more promacrophage phenotype.

Radhakrishnan et al. [50] used polylactide-glycolide copolymers to prepare random and longitudinally arranged electrospun fibers including two-dimensional films and three-dimensional scaffolds. Compared with two-dimensional films and random fibers, oriented nanofiber scaffolds showed a significant increase in the adhesion of Schwann cells after culture for 3, 6, and 12 hours, respectively. The orientation structure of the scaffold promoted the maturation of Schwann cells, thereby promoting the formation of the myelin sheath to maintain Schwann cells' function. A new method for preparing polycaprolactone scaffolds that mimic the natural structure of peripheral nerves with a micropatterned ridge/groove structure on the surface by combining electrospinning and micromolding has previously been developed. The micropatterned polycaprolactone scaffold exhibits a porous structure, and its hydrophobicity and mechanical properties increased with the electrospinning flow rate of the polycaprolactone solution, while the chemical properties did not change. The micropatterned polycaprolactone scaffold had good stability and could effectively regulate the attachment and orientation of Schwann cells in the early stage after cell culture. The results showed that the flow rate of the PCL electrospinning solution had an important influence on the morphology of the scaffold and the adsorption

TABLE 1: Summary of the influence of topographical features on the proliferation and differentiation of cells.

Feature type	Cell type	Effects on cell behaviors	Reference
PLA nanofiber stents	Neurons and glial cells	Promote neuron and glial cell growth	[32]
Mussel protein glue-based nanofiber conduit	Nerve and Schwann cells	Promote nerve and Schwann cell proliferation and differentiation	[33]
Nanotextured glass coverslips	PC12 cell	Promote the proliferation of neuronal cells and provide treatment for central nervous system trauma	[35]
A customizable multilevel architecture array	Neurons	Enhance the differentiation of neurons	[36]
The engineered concave microarray	Cardiomyocytes and neurons	The differentiation of cardiomyocytes and neurons	[37]
Polycaprolactone/polyethylene oxide–polycaprolactone-blended fiber materials using electrospinning technology	Neural stem cells	Promotes the growth of rat neural stem cells, differentiates into neurons and astrocytes	[38]

behavior of cells and proteins. The micropatterned scaffold with a flow rate of 0.12 mL/h^{-1} had a good regulation effect on the adhesion and arrangement of Schwann cells, without negatively affecting the normal biological functions of the cells. This research could provide important design concepts for artificial nerve implants, and provide an experimental and theoretical foundation for the development of implants in tissue engineering [51]. Although polycaprolactone has excellent mechanical properties and plasticity, PCL's biological properties and functions are low, and the degradation rate in the body is slow. Thus, the performance of PCL including biocompatibility and biodegradation should be further improved for future applications [52]. Xie et al. [53] used electrospinning technology to prepare a single layer of nonoriented and neatly arranged nanofibers for dorsal root ganglion (DRG) culture, and it was proved that on nonoriented nanofibers, the DRG neurites spread radially from the body with no particular orientation. In contrast, when DRG was cultured in single-layer-oriented nanofibers, neurites extended preferentially along the long axis. Yao et al. [54] combined electrospinning and molecular self-assembly technology to prepare an aligned fibrin hydrogel (AFG), which is a three-dimensional layered arrangement with a directional morphology to simulate the spinal cord tissue in the natural environment. The results proved that the motor function recovery rate of the AFG group was significantly faster than that of the control group and the stochastic fibrin hydrogel group (RFG). The AFG scaffold supplied an induction array for promoting directional host cell invasion, reconstruction of the vascular system, and axon regeneration, which could facilitate and buttress a wide range of axon regeneration and recovery of motor function. Zhang et al. [55] prepared aligned poly(3-hydroxybutyrate-co-3-hydroxyvalerate) PHBV nanofibers doped with polyethylene oxide (PEO) by electrospinning. Compared with randomly oriented nanofibers, aligned nanofibers showed clear guidance for cell extension. The surface of the nanotube enhanced the interaction between nerve cells and the scaffold. The aligned fiber was then treated with plasma and modified with laminin to fabricate a nerve conduit. The functionally arranged nanofibers effectively promoted the

adhesion and proliferation of Schwann cells. In vivo animal experiments showed that the PHBV/PEO nanofiber nerve conduit coated with laminin on the inner surface could promote the regeneration of sciatic nerve defects. However, the defects of PHBV, including high crystallinity and large spherulite size caused brittleness and slow degradation (more than two years for complete degradation), extremely limiting its application in biomedicine [56].

Cell migration is critical to a wide range of pathological and physiological processes, including wound repair, metastasis, and embryogenesis [57–59]. The surface structure of biomaterials is essential to control their interaction with the biological environment [60]. It is well known that the micro- and nanoscale geometric cues presented by the extracellular matrix of cells affect cell behavior, such as migration, adhesion, and dispersion [61]. Therefore, it is important to understand the interaction between cells and different surface morphologies of artificial graft, which may improve the biological performance of medical implants [62]. Topological structure can also regulate cell functions, such as differentiation [63] or migration [64]. Researchers [65] studied the influence of surface topographical properties on the migration and dispersion of the cytoskeleton of stem cells. The surface of titanium alloy was firstly treated with a pulsed laser to form parallel grooves and matrix holes to evaluate the dispersion behavior of the cytoskeleton. The experimental results showed that the cell cytoskeleton was influenced not only by the surface roughness (Ra and Sa) but also by the surface flatness and area.

Microscale grooves could induce cells to form a high-aspect ratio cytoskeleton and restrict the migration and diffusion of the cytoskeleton. Li et al. [66] developed chitosan micropatterns with various pattern sizes for peripheral nerve regeneration. The 30 μm size pattern showed the best regulation effect on Schwann cell migration. In addition, compared with the unpatterned sample, the micropatterned chitosan film could well retain the physiological function of SCs, indicating that chitosan micropatterning and SCs have good biocompatibility. Thus, chitosan micropatterning can effectively regulate the directional growth of SCs, and may have potential application value in the repair of peripheral nerve

injury. Although chitosan has been widely used for constructing artificial grafts for tissue engineering, several disadvantages limit its application, such as its dependence on low pH and the risk of allergic reactions. The neonerve tissue migrated much faster in a chitosan conduit with surface micropatterning compared to the controlled conduit without topography [67]. Walter et al. [68] used a polystyrene colloidal template to fabricate a surface with controlled feature sizes. The results of fluorescence microscopy, WST analysis, and morphological analysis showed that the surface feature size had a strong effect on bone marrow-derived rat stromal cells (ST2). Quantitative analysis showed that compared with flat surfaces, when the surface feature size was reduced to less than 200 nm, cell adhesion, diffusion, viability, and activity were enhanced, while larger feature size was not conducive to cell adhesion. The effects of topography on nerve cell adhesion and migration are presented in Table 2.

2.3. Topography Affects Cell Alignment Growth and Neurite Guidance.

The characteristic functions of complex tissues are largely determined by the shape and polarity of the cells [69–71]. By means of a process known as contact guidance, the polarity of many different cell types can be strongly influenced by substrate morphology [72–74]. Cells can adjust their arrangement according to the local geometry of their adhesion surface [75]. This process is called contact guidance and has been well established, but little is known about it. One of the challenges is the varied natural surface topologies associated with cell movement guidance. Many studies have reported that the surface topography could facilitate contact guidance of cell morphology and achieve controlled neurite outgrowth under the guidance of a combination of chemical cues and physical patterns, which was important in the treatment of damaged nerve in regenerative medicine [76, 77]. In a previous study, the effect of collagen gradient micropatterns on peripheral nerve regeneration was investigated. The prepared gradient collagen micropatterns could well regulate the directional growth of Schwann cells. At the same time, it could be used as gradient micropatterns with higher collagen concentration and larger pattern size [78].

Generally, at least two different types of stress fibers exist in the cell, one is the long top stress fiber arranged in the axial direction, and the other is the short base stress fiber arranged in the circumferential direction. A small guanosine triphosphatase (Rho) that regulates the assembly of stress fibers can realize the manipulation of stress fibers and achieve the purpose of guiding and controlling cell arrangement [79]. It has been documented that in organisms, cells treat the microscopic nanofiber matrix network as a physical signal, which affects the arrangement of cells in the range of tens to hundreds of microns. Many studies reported that the microgroove could cause neurite arrangement, and the surface topography increases the stimulation of discrete retinal neurites and enhances the orientation of neurites [80–83]. Observations have also shown that topographical features could provide guidance for the direction and growth of hippocampal neurons, and these directional cues contribute to the long-term organization of axons and dendrites [82]. In addition, it has also been reported that the growth cone of

neurons can perceive nanoshaped extracellular matrix tips to produce stable neurites [83]. Moreover, it was found that microRNA is involved in the growth of neurites guided by topological cues [84]. The engineered mussel protein glue-based nanofiber catheters were also used to carry out multidimensional biologically inspired strategies to accelerate the regeneration of functional nerves [33]. The results showed that the AFG biomimetic composition is comprised of a protein of a natural fiber cable, and the aligned organization could facilitate rapid biological function recovery in peripheral nerve regeneration [85].

According to previous studies, the scale of the topography has an effect on the growth of neurites on electrospun nanofibers. In previous studies, it was found that the fiber diameter strongly affects the morphology and differentiation [86], neurite length [87], and neurite arrangement of nerve cells [88–90]. Topographical structures, such as the width and height of a groove have a significant impact on the alignment and elongation of various types of cells. The aligned PLLA nanofiber scaffold highly improved the neurite outgrowth, NSC displayed an obvious bipolar elongated morphology of the cell soma, and the neurites grew outward [86]. Topographical size was also shown to have an important influence on the differentiation and growth of nerve cells. The results of the research may provide valuable reference information for developing effective tissue remodeling matrices and optimizing existing biomaterials for neural tissue engineering applications. The neatly arranged electrospun fibers have shown great promise in promoting the growth of directed neurites in cells and animal models. Although electrospun fiber diameter affected cell behavior, it is unclear how directional spun fiber scaffolds of different diameters affect neurite growth and Schwann cell migration. Therefore, the study firstly established highly arranged electrospun fiber scaffolds with different diameters, and then evaluated the neurites and stem cell behavior of dorsal root ganglion (DRG) explants. Three groups of highly aligned electrospun polylactic acid (PLLA) fibers (1325 + 383 nanometers: large diameter fibers; 759 + 179 nanometers: medium diameter fibers; and 293 + 65 nanometers: small diameter fibers) were produced. Moreover, the extension of DRG neurites in chicks was found to be affected by the fiber diameter [88]. Small fiber diameters (293 ± 65 nm) did not promote the extension of DRG neurites, moderate fiber diameters (759 ± 179 nm) could promote the directional expansion of neurites, while large fiber diameters (1325 ± 383 nm) could obviously promote the directional growth and extension of DRG neurites. The packing density of fibers may also affect the extension of axons and the migration of Schwann cells [88]. Therefore, when constructing aligned electrospun fiber constructs for nerve regeneration applications, careful consideration should be given to fiber diameter and spacing between fibers. As a material with a relatively slow degradation rate, PLLA may cause some problems, such as incomplete degradation and lower local pH. Therefore, PLLA implants may cause late inflammation, cell necrosis, and delayed axonal recovery in the body [91], which should also be considered for future clinical applications.

TABLE 2: Summary of the effects of sizes on cell adhesion and migration.

Feature type	Effects on cell behaviors	Reference
Prepared poly(L-lactic acid-co-e-caprolactone) (P(LLA-CL)) nanofibers	Have different regulatory effects on macrophage activation	[49]
Polylactide-glycolide copolymers were used to prepare random and longitudinally arranged electrospun fibers such as two-dimensional films and three-dimensional films	Increase in the adhesion of Schwann cells	[50]
Arranged nanofibers	Neurites extended preferentially along the long axis	[53]
Poly(3-hydroxybutyrate-co-3-hydroxyvalerate) PHBV nanofibers doped with polyethylene oxide (PEO)	Promoted adhesion and proliferation of Schwann cells	[55]
Micron-scale groove	Limiting the migration and diffusion of the cytoskeleton	[65]
Used a polystyrene colloidal template to make a surface with controlled feature sizes	When the surface feature size is reduced to less than 200 nm, cell adhesion, diffusion, viability, and activity are enhanced	[68]

Human embryonic stem cell-derived neural stem cells on silk fibroin scaffolds with different diameters (i.e., 400 and 800 nanometers) and orientations (i.e., random and arrangement) were used to analyze the effects of fiber diameter and arrangement on nerves derived from human embryonic stem cells including cell viability, neuron differentiation, and neurite growth. Compared with random thyroid-stimulating hormone-releasing factor scaffolds, the arranged thyroid-stimulating hormone-releasing factor scaffolds could significantly promote the differentiation and axon growth of human embryonic stem cell-derived neurons. In addition, on the aligned 400-nanometer fibers, cell viability, neuron differentiation, and neurite outgrowth were greater than those on the aligned 800-nanometer fibers. Their results indicated that the 400-nanometer directional thyroid-stimulating hormone-releasing factor scaffold was more suitable for the development of neural stem cells derived from human embryonic stem cells, which was helpful for optimizing the therapeutic potential of human embryonic stem cells for nerve regeneration [83]. However, although natural silk has good mechanical properties, the mechanical properties of silk protein after degumming are impaired, which further affects the performance of silk fibroin nerve conduits. A previous study showed that the aligned PLLA fiber scaffold could promote the elongation of neural stem cells, and their neurites grew along with the fiber direction, while the fiber diameter had no significant effect on cell orientation. Interestingly, it was reported that the NSC differentiation rate on nanofibers was higher than microfibers, but it had no relationship with fiber orientation degree [86]. Besides, the aligned silk fibroin nanofibers with different diameters were shown to support astrocyte attachment and growth. An obvious enhancement of the astrocyte migration area was observed on SF scaffolds with a diameter of 400 nm compared to those with a diameter of 1200 nm [89]. In our previous research, we also used a combination of micromodeling and freeze-drying to prepare porous chitosan micropatterns with different sizes of surface ridges/grooves. The Schwann cells on the chitosan micropattern appeared to display orientation adhesion and began to grow in a certain direction after having been cultured for 2 h. After further culture for 3 and 5 d, the minimum orienta-

tion angle and maximum length appeared on the 30/30 μm micropattern. Therefore, the results showed that the porous chitosan micropatterns with a suitable size could well regulate the growth of Schwann cells and had potential application value in nerve regeneration [67].

The rapid vascularization of the nerve graft at the wound site is very important for nerve regeneration [92]. Vascular endothelial cells (VEC) are one of the most important core cells for angiogenesis [93]. Endothelial cells change their phenotype and could grow guided by the topography. The topography with a larger microsize (width range of 4.8 to 9.9 μm and height range of 1015 to 2169 nm) resulted in cell alignment and inhibited vascular network formation, while the topography with a nano/microsize (width range from 1.5 μm to 3.8 μm and height range from 176 nm to 780 nm) could lead to the formation of early vascular networks [94]. Moreover, it was found that the scaffolds with aligned topologies could form a fused endothelium with enhanced endothelial cell (EC) adhesion for vascularization. The cells on the scaffolds with aligned fibers of 100 nm and 300 nm diameter had a significantly larger aspect ratio and long axis length compared with those on aligned fibers of 1200 nm and random fibers. Fiber orientation had a great influence on the alignment of guided cells on the scaffolds with diameters of 100 nm and 300 nm, while the cells on the 1200 nm scaffold did not show aligned growth [95]. Previous reports have demonstrated that cell-topography interactions can affect the gene expression, neurite branching, growth, and reprogramming efficiency of induced neurons (iNs) [96]. Cell arrangement and neuron guidance stimulated by topological structure with different sizes is summarized in Table 3.

2.4. Topography-Nerve Cell-Relevant Mechanism. Cell responses to topographical cues can be caused by direct changes in cytoskeletons and indirect changes in signaling pathways. However, the mechanism of how neuronal cells sense and react to topography is rarely reported. For nonneuronal cells, it is generally believed that the recognition mechanism between cells and topographical features in the extracellular environment is based on integrin adhesion molecules [97]. Integrin expresses widely in the nervous

TABLE 3: Summary of the effects of sizes on cell alignment and neurite guidance.

|	Diameter	Material	Cell type	Effects on cell behaviors	Reference
Silk nanofibers/scaffold	400 ± 67 nm 800 ± 35 nm	Silk fibroin	Human embryonic stem cell-(hESC-) derived neural precursors (NPs)	Cell viability, neuronal differentiation, and neurite outgrowth are greater on aligned 400 nm fibers	[83]
Poly (L-lactic acid) (PLLA) nano/microfibrous scaffolds	300 nm (nanometer scale) 1.5 mm (submicron scale)	PLLA	Neural stem cells (NSCs)	Aligned nanofibers highly supported the NSC culture and improved the neurite outgrowth	[86]
Silk fibroin (SF)	400 nm 1200 nm	Silk fibroin (SF)	Astrocytes	Significant increase in astrocyte diffusion area on SF scaffolds at 400 nm	[89]
Poly-L-lactic acid (PLLA) fibers	293 ± 65 nm 759 ± 179 nm 1325 ± 383 nm	Poly-L-lactic acid (PLLA) fibers	DRG neurites in chicks	Large fiber diameters (1325 ± 383 nm) obviously promote the directional growth and extension of neurites	[88]
Gradients	Wavelengths ranging from 1.5 μm to 3.8 μm and amplitudes ranging from 176 nm to 780 nm Wavelengths ranging from 4.8 to 9.9 μm and amplitudes ranging from 1015 to 2169 nm	Polydimethylsiloxane (PDMS)	Human pulmonary microvascular endothelial cells (ECs)	Caused formation of early networks that can be stabilized by the use of the guidance layer of adipogenic stromal cells (ASC) Caused cell alignment and inhibited vascular endothelial network formation	[94]
Electrospun scaffolds	100 nm and 300 nm 1200 nm	Poly(ε-caprolactone) (PCL) and type I collagen	Endothelial cell (EC)	Significantly larger aspect ratio and long axis length	[95]
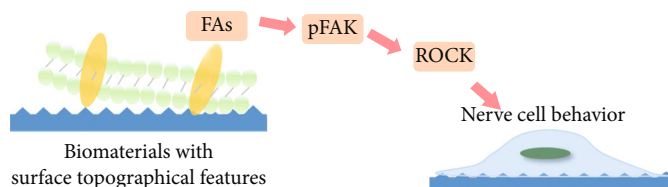
FIGURE 2: Schematic diagram of material surface topographical features regulating nerve cell behavior. Nerve cells perceive stimuli of different topographical features through the focal adhesion-pFAK-Rho A signaling pathway.

system. The presence of integrin is related to various developmental processes of the nervous system, such as neuron migration, axon growth, and guidance through attachment to extracellular matrix proteins such as tenascin laminin and fibronectin [98–100]. In addition, it has been detected in many growth cones of focal adhesion protein, such as tallin and vinculin, indicating that the integrin-cytoskeleton coupling may play a major role in the movement of growth cones and the processes of neurons [100, 101]. Therefore, most of the reported influence mechanisms of topographical features on nerve cells mainly focused on the activation of integrin, the cytoskeleton, ROCK signaling, and focal adhesion [102–104]. Activation of integrin leads to the organization of focal adhesions (FAs), the actin filaments that connect integrin to the cytoskeleton [105]. FAs include proteins such as talin or vincinin, which transfer mechanical forces through the whole actin-myosin cytoskeletal network, and directly leads to changes in cytoskeletal assembly, and finally cell morphology [97, 106]. In addition, the FA proteins are comprised of an activation signal cascade of biochemical signals such as paxillin [106]. These cascades, which include activation of phosphorylation-mediated signaling pathways and activation of G-protein- (such as Rho-) mediated signaling pathways (such as ROCK), may cause long-term changes in cell proliferation, differentiation, survival, and transcriptional regulation [97]. A receptor for activated protein kinase C (RACK1) inhibits the nanoscale response to contact guidance and promotes adhesion as well [107]. Under the different characteristics of the surface topographical structure, the single adhesion may change to the protein aggregation and reorganization, which affects the quantity and distribution of FAs [108]. In short, the surface topographical cues of the material can regulate the behavior of nerve cells through the focal adhesion-pFAK-RhoA signaling pathway (Figure 2).

3. Outlook

Tissue engineering is an interdisciplinary research field that applies materials and biological sciences to create artificial organs and tissue matrices [13]. Micro-/nanostructured biomaterials with specific characteristics and functions are in great demand in biomedical applications. Neural tissue engineering relies on combining biological materials and external cues, such as cell-matrix interactions [109]. For application in peripheral nerve regeneration, the surface topography of the biomaterial plays an important role in regulating nerve cell behavior. The surface topography could present with different morphologies and structures, thereby providing a

superior microenvironment that is suitable for nerve tissue regeneration. Many researches have reported that the cell proliferation, differentiation, adhesion, migration, arrangement, and neurite guidance could be manipulated by the interaction of cell-biomaterial surfaces with different topological structures and sizes. In addition, the unique topography and structure of the surface of biomaterials may affect the differentiation type of nerve cells. Further on, the surface topographical specification of biomaterials (surface roughness, surface groove size and direction, and surface pore size and distribution) will significantly affect the molecular pathways that control the fate of nerve cells.

4. Conclusions

This review gives a broad overview of the powerful influence of the topological structure of the material surface on different neuronal cell types, including neurons and glial cells. Feature roughness, groove size and orientation, and surface pore size are important parameters that regulate cell behavior on topological structures. The review illustrated that different topographical features have a great impact on cell proliferation, differentiation, adhesion, migration, arrangement, and neurite guidance. In particular, the cell's behaviour would be most significantly improved across different topographical features. Future research will further reveal the regulatory mechanisms of topography on cellular response, which will significantly influence nerve regeneration. The correct design and fabrication of appropriate dimensions and shapes of topographical features will be helpful for the development of artificial nerve grafts with excellent biological performance in nerve tissue engineering and neuroregenerative medicine.

Data Availability

Data sharing is not applicable to this article as no datasets were generated or analyzed during the current study.

Conflicts of Interest

We declare that we do not have any commercial or associative interest that represents a conflict of interest in connection with the work submitted.

Acknowledgments

References

[1] J. Moskow, B. Ferrigno, N. Mistry et al., "Review. Bioengineering approach for the repair and regeneration of peripheral nerve," *Bioactive materials*, vol. 4, no. 1, pp. 107–113, 2019.

[2] T. Kornfeld, P. M. Vogt, and C. Radtke, "Nerve grafting for peripheral nerve injuries with extended defect sizes," *Wiener Medizinische Wochenschrift*, vol. 169, no. 9-10, pp. 240–251, 2019.

[3] J. J. Kim, D. V. Bax, R. Murphy, S. M. Best, and R. E. Cameron, "Collagen film activation with nanoscale IKVAV-capped dendrimers for selective neural cell response," *Nanomaterials*, vol. 11, no. 5, 2021.

[4] J. Liu, B. Yang, M. Li, J. Li, and Y. Wan, "Enhanced dual network hydrogels consisting of thiolated chitosan and silk fibroin for cartilage tissue engineering," *Carbohydrate Polymers*, vol. 227, 2020.

[5] F. Wang, Y. Pang, G. Chen, W. Wang, and Z. Chen, "Enhanced physical and biological properties of chitosan scaffold by silk proteins cross-linking," *Carbohydrate Polymers*, vol. 229, 2020.

[6] N. Mansouri and S. Bagheri, "The influence of topography on tissue engineering perspective," *Materials Science and Engineering: C*, vol. 61, pp. 906–921, 2016.

[7] L. Zhang, T. Zheng, L. Wu et al., "Fabrication and characterization of 3D-printed gellan gum/starch composite scaffold for Schwann cells growth," *Nanotechnology Reviews*, vol. 10, no. 1, pp. 50–61, 2021.

[8] S. Baudis, F. Nehl, S. C. Ligon et al., "Elastomeric degradable biomaterials by photopolymerization-based CAD-CAM for vascular tissue engineering," *Biomedical Materials*, vol. 6, no. 5, article 055003, 2011.

[9] P. Viswanathan, M. G. Ondeck, S. Chirasatitsin et al., "3D surface topology guides stem cell adhesion and differentiation," *Biomaterials*, vol. 52, pp. 140–147, 2015.

[10] N. Sagar, K. Khanna, V. S. Sardesai et al., "Bioconductive 3D nano-composite constructs with tunable elasticity to initiate stem cell growth and induce bone mineralization," *Materials Science and Engineering: C*, vol. 69, pp. 700–714, 2016.

[11] E. Ueda and P. A. Levkin, "Micropatterning hydrophobic liquid on a porous polymer surface for long-term selective cell-repellency," *Advanced healthcare materials*, vol. 2, no. 11, pp. 1425–1429, 2013.

[12] H. Arzaghi, B. Adel, H. Jafari et al., "Nanomaterial integration into the scaffolding materials for nerve tissue engineering: a review," *Reviews in the Neurosciences*, vol. 31, no. 8, pp. 843–872, 2020.

[13] G. Zyla, N. Surkamp, E. L. Gurevich et al., "Two-photon polymerization with diode lasers emitting ultrashort pulses with high repetition rate," *Optics Letters*, vol. 45, no. 17, pp. 4827–4830, 2020.

[14] C. R. Carvalho, J. Silva-Correia, J. M. Oliveira, and R. L. Reis, "Nanotechnology in peripheral nerve repair and reconstruction," *Advanced Drug Delivery Reviews*, vol. 148, pp. 308–343, 2019.

[15] C. Miller, H. Shanks, A. Witt, G. Rutkowski, and S. Mallapragada, "Oriented Schwann cell growth on micropatterned biodegradable polymer substrates," *Biomaterials*, vol. 22, no. 11, pp. 1263–1269, 2001.

[16] M. Song and K. E. Uhrich, "Optimal micropattern dimensions enhance neurite outgrowth rates, lengths, and orientations," *Annals of biomedical engineering*, vol. 35, no. 10, pp. 1812–1820, 2007.

[17] C. C. Blong, C. J. Jeon, J. Y. Yeo et al., "Differentiation and behavior of human neural progenitors on micropatterned substrates and in the developing retina," *Journal of neuroscience research*, vol. 88, no. 7, pp. 1445–1456, 2010.

[18] A. Béduer, C. Vieu, F. Arnauduc, J. C. Sol, I. Loubinoux, and L. Vaysse, "Engineering of adult human neural stem cells differentiation through surface micropatterning," *Biomaterials*, vol. 33, no. 2, pp. 504–514, 2012.

[19] X. Liu, R. Liu, B. Cao et al., "Subcellular cell geometry on micropillars regulates stem cell differentiation," *Biomaterials*, vol. 111, pp. 27–39, 2016.

[20] D. Lü, C. Luo, C. Zhang, Z. Li, and M. Long, "Differential regulation of morphology and stemness of mouse embryonic stem cells by substrate stiffness and topography," *Biomaterials*, vol. 35, no. 13, pp. 3945–3955, 2014.

[21] V. Onesto, L. Cancedda, M. L. Coluccio et al., "Nano-topography enhances communication in neural cells networks," *Scientific reports*, vol. 7, no. 1, p. 9841, 2017.

[22] J. Shao, Z. Ding, L. Li, Y. Chen, J. Zhu, and Q. Qian, "Improved accumulation of TGF-β by photopolymerized chitosan/silk protein bio-hydrogel matrix to improve differentiations of mesenchymal stem cells in articular cartilage tissue regeneration," *Journal of Photochemistry and Photobiology B: Biology*, vol. 203, 2020.

[23] R. Hedayati, S. M. Ahmadi, K. Lietaert et al., "Isolated and modulated effects of topology and material type on the mechanical properties of additively manufactured porous biomaterials," *Journal of the mechanical behavior of biomedical materials*, vol. 79, pp. 254–263, 2018.

[24] G. Doron and J. S. Temenoff, "Culture substrates for improved manufacture of mesenchymal stromal cell therapies," *Advanced Healthcare Materials*, no. article e2100016, 2021.

[25] J. Minguela, D. W. Müller, F. Mücklich et al., "Peptidic biofunctionalization of laser patterned dental zirconia: a biochemical-topographical approach," *Materials Science and Engineering: C*, vol. 125, p. 112096, 2021.

[26] M. S. Pacheco, G. E. Kano, P. L. de Almeida, P. S. Lopes, and M. A. de Moraes, "Silk fibroin/chitosan/alginate multilayer membranes as a system for controlled drug release in wound healing," *International Journal of Biological Macromolecules*, vol. 152, pp. 803–811, 2020.

[27] S. Asadpour, S. Kargozar, L. Moradi, A. Ai, H. Nosrati, and J. Ai, "Natural biomacromolecule based composite scaffolds from silk fibroin, gelatin and chitosan toward tissue engineering applications," *International Journal of Biological Macromolecules*, vol. 154, pp. 1285–1294, 2020.

[28] G. Li, C. Xue, H. Wang et al., "Spatially featured porous chitosan conduits with micropatterned inner wall and seamless sidewall for bridging peripheral nerve regeneration," *Carbohydrate polymers*, vol. 194, pp. 225–235, 2018.

[29] G. T. Christopherson, H. Song, and H. Q. Mao, "The influence of fiber diameter of electrospun substrates on neural

stem cell differentiation and proliferation," *Biomaterials*, vol. 30, no. 4, pp. 556–564, 2009.

[30] D. H. Kim, D. J. Beebe, and A. Levchenko, "Micro- and nanoengineering for stem cell biology: the promise with a caution," *Trends in biotechnology*, vol. 29, no. 8, pp. 399–408, 2011.

[31] S.-S. Chen, X.-M. Lu, and Q.-H. Lu, "Effects of concave and convex substrate curvature on cell mechanics and the cytoskeleton," *Chinese Chemical Letters*, vol. 28, no. 4, pp. 818–826, 2017.

[32] Z. Álvarez, O. Castaño, A. A. Castells et al., "Neurogenesis and vascularization of the damaged brain using a lactate-releasing biomimetic scaffold," *Biomaterials*, vol. 35, no. 17, pp. 4769–4781, 2014.

[33] H. Cheong, J. Kim, B. J. Kim et al., "Multi-dimensional bioinspired tactics using an engineered mussel protein glue-based nanofiber conduit for accelerated functional nerve regeneration," *Acta biomaterialia*, vol. 90, pp. 87–99, 2019.

[34] D. S. Hwang, Y. Gim, and H. J. Cha, "Expression of functional recombinant mussel adhesive protein type 3A in Escherichia coli," *Biotechnology progress*, vol. 21, no. 3, pp. 965–970, 2005.

[35] M. Islam, R. Atmaramani, S. Mukherjee, S. Ghosh, and S. M. Iqbal, "Enhanced proliferation of PC12 neural cells on untreated, nanotextured glass coverslips," *Nanotechnology*, vol. 27, no. 41, p. 415501, 2016.

[36] A. A. Moe, M. Suryana, G. Marcy et al., "Microarray with micro- and nano-topographies enables identification of the optimal topography for directing the differentiation of primary murine neural progenitor cells," *Small*, vol. 8, no. 19, pp. 3050–3061, 2012.

[37] Y. Y. Choi, B. G. Chung, D. H. Lee, A. Khademhosseini, J. H. Kim, and S. H. Lee, "Controlled-size embryoid body formation in concave microwell arrays," *Biomaterials*, vol. 31, no. 15, pp. 4296–4303, 2010.

[38] D. Fernández, M. Guerra, J. G. Lisoni et al., "Fibrous materials made of poly(epsilon-caprolactone)/poly(ethylene oxide)-b-poly (epsilon-caprolactone) blends support neural stem cells dblends support neural stem cells differentiation," *Polymers*, vol. 11, no. 10, 2019.

[39] S. Tachizawa, H. Takahashi, Y. J. Kim et al., "Bundle gel fibers with a tunable microenvironment for in vitro neuron cell guiding," *ACS applied materials & interfaces*, vol. 9, no. 49, pp. 43250–43257, 2017.

[40] J. Huang, J. Qin, P. Zhang et al., "Facile preparation of a strong chitosan-silk biocomposite film," *Carbohydrate Polymers*, vol. 229, p. 115515, 2020.

[41] A. V. Sapelkin, S. C. Bayliss, B. Unal, and A. Charalambou, "Interaction of B50 rat hippocampal cells with stain-etched porous silicon," *Biomaterials*, vol. 27, no. 6, pp. 842–846, 2006.

[42] G. Wang, Q. Ao, K. Gong et al., "The effect of topology of chitosan biomaterials on the differentiation and proliferation of neural stem cells," *Acta biomaterialia*, vol. 6, no. 9, pp. 3630–3639, 2010.

[43] Z. Ma, Z. Liu, D. P. Myers, and L. S. Terada, "Mechanotransduction and anoikis: death and the homeless cell," *Cell Cycle*, vol. 7, no. 16, pp. 2462–2465, 2008.

[44] B. Honig and L. Shapiro, "Adhesion protein structure, molecular affinities, and principles of cell-cell recognition," *Cell*, vol. 181, no. 3, pp. 520–535, 2020.

[45] B. Kundu, M. Eltohamy, V. K. Yadavalli, S. C. Kundu, and H. W. Kim, "Biomimetic designing of functional silk nanotopography using self assembly," *Acs Applied Materials & Interfaces*, vol. 8, no. 42, pp. 28458–28467, 2016.

[46] D. P. Dowling, I. S. Miller, M. Ardhaoui, and W. M. Gallagher, "Effect of surface wettability and topography on the adhesion of osteosarcoma cells on plasma-modified polystyrene," *Journal of Biomaterials Applications*, vol. 26, no. 3, pp. 327–347, 2011.

[47] P. Thevenot, W. J. Hu, and L. P. Tang, "Surface chemistry influences implant biocompatibility," *Current Topics in Medicinal Chemistry*, vol. 8, no. 4, pp. 270–280, 2008.

[48] B. G. Keselowsky, D. M. Collard, and A. J. Garcia, "Surface chemistry modulates focal adhesion composition and signaling through changes in integrin binding," *Biomaterials*, vol. 25, no. 28, pp. 5947–5954, 2004.

[49] Y. Jia, W. Yang, K. Zhang et al., "Nanofiber arrangement regulates peripheral nerve regeneration through differential modulation of macrophage phenotypes," *Acta Biomaterialia*, vol. 83, pp. 291–301, 2019.

[50] J. Radhakrishnan, A. A. Kuppuswamy, S. Sethuraman, and A. Subramanian, "Topographic cue from electrospun scaffolds regulate myelin-related gene expressions in Schwann cells," *Journal of Biomedical Nanotechnology*, vol. 11, no. 3, pp. 512–521, 2015.

[51] L. Zhang, S. Chen, R. Liang et al., "Fabrication of alignment polycaprolactone scaffolds by combining use of electrospinning and micromolding for regulating Schwann cells behavior," *Journal of Biomedical Materials Research Part A*, vol. 106, no. 12, pp. 3123–3134, 2018.

[52] H. Tseng, D. S. Puperi, E. J. Kim et al., "Anisotropic poly(ethylene glycol)/polycaprolactone hydrogel-fiber composites for heart valve tissue engineering," *Tissue Engineering Part A*, vol. 20, no. 19-20, pp. 2634–2645, 2014.

[53] J. Xie, M. E. MR, X. Li, S. E. Sakiyama-Elbert, and Y. Xia, "Neurite outgrowth on nanofiber scaffolds with different orders, structures, and surface properties," *Acs Nano*, vol. 3, no. 5, pp. 1151–1159, 2009.

[54] S. Yao, S. Yu, Z. Cao et al., "Hierarchically aligned fibrin nanofiber hydrogel accelerated axonal regrowth and locomotor function recovery in rat spinal cord injury," *International Journal of Nanomedicine*, vol. 13, pp. 2883–2895, 2018.

[55] X. F. Zhang, H. X. Liu, L. S. Ortiz, Z. D. Xiao, and N. P. Huang, "Laminin-modified and aligned poly (3-hydroxybutyrate-co-3-hydroxyvalerate)/polyethylene oxide nanofibrous nerve conduits promote peripheral nerve regeneration," *Journal of Tissue Engineering and Regenerative Medicine*, vol. 12, no. 1, pp. E627–E636, 2018.

[56] S. Luo and A. N. Netravali, "A study of physical and mechanical properties of poly(hydroxybutyrate-co-hydroxyvalerate) during composting," *Polymer Degradation and Stability*, vol. 80, no. 1, pp. 59–66, 2003.

[57] E. Sahai, "Illuminating the metastatic process," *Nature Reviews Cancer*, vol. 7, no. 10, pp. 737–749, 2007.

[58] R. J. Petrie, A. D. Doyle, and K. M. Yamada, "Random versus directionally persistent cell migration," *Nature reviews Molecular cell biology*, vol. 10, no. 8, pp. 538–549, 2009.

[59] P. Friedl and K. Wolf, "Plasticity of cell migration: a multiscale tuning model," *Journal of Cell Biology*, vol. 188, no. 1, pp. 11–19, 2010.

[60] M. M. Stevens, "Exploring and engineering the cell-surface interface," *Biophysical Journal*, vol. 100, no. 3, pp. 189–189, 2011.

[61] V. Vogel and M. Sheetz, "Local force and geometry sensing regulate cell functions," *Nature Reviews Molecular Cell Biology*, vol. 7, no. 4, pp. 265–275, 2006.

[62] M. Nikkhah, F. Edalat, S. Manoucheri, and A. Khademhosseini, "Engineering microscale topographies to control the cell-substrate interface," *Biomaterials*, vol. 33, no. 21, pp. 5230–5246, 2012.

[63] X. Li, Y. Huang, L. Zheng et al., "Effect of substrate stiffness on the functions of rat bone marrow and adipose tissue derived mesenchymal stem cells," *Journal of Biomedical Materials Research Part A*, vol. 102, no. 4, pp. 1092–1101, 2014.

[64] G. Vidal, B. Delord, W. Neri et al., "The effect of surface energy, adsorbed RGD peptides and fibronectin on the attachment and spreading of cells on multiwalled carbon nanotube papers," *Carbon*, vol. 49, no. 7, pp. 2318–2333, 2011.

[65] Y. F. Wang, Z. Yu, K. M. Li, and J. Hu, "Effects of surface properties of titanium alloys modified by grinding, sandblasting and acidizing and nanosecond laser on cell proliferation and cytoskeleton," *Applied Surface Science*, vol. 501, 2020.

[66] G. Li, X. Zhao, L. Zhang, C. Wang, Y. Shi, and Y. Yang, "Regulating Schwann cells growth by chitosan micropatterning for peripheral nerve regeneration in vitro," *Macromolecular bioscience*, vol. 14, no. 8, pp. 1067–1075, 2014.

[67] G. Li, X. Zhao, W. Zhao et al., "Porous chitosan scaffolds with surface micropatterning and inner porosity and their effects on Schwann cells," *Biomaterials*, vol. 35, no. 30, pp. 8503–8513, 2014.

[68] T. Walter, A. Gruenewald, R. Detsch, A. R. Boccaccini, and N. Vogel, "Cell interactions with size-controlled colloidal monolayers: toward improved coatings in bone tissue engineering," *Langmuir*, vol. 36, no. 7, pp. 1793–1803, 2020.

[69] A. A. Saidova and I. A. Vorobjev, "Lineage commitment, signaling pathways, and the cytoskeleton systems in mesenchymal stem cells," *Tissue Engineering Part B-Reviews*, vol. 26, no. 1, pp. 13–25, 2020.

[70] Z. T. Berent and A. J. W. Johnson, "Cell seeding simulation on micropatterned islands shows cell density depends on area to perimeter ratio, not on island size or shape," *Acta Biomaterialia*, vol. 107, pp. 152–163, 2020.

[71] N. Saito, H. Adachi, H. Tanaka et al., "Interstitial fluid flow-induced growth potential and hyaluronan synthesis of fibroblasts in a fibroblast-populated stretched collagen gel culture," *Biochimica Et Biophysica Acta-General Subjects*, vol. 1861, no. 9, pp. 2261–2273, 2017.

[72] D. H. Kim, E. A. Lipke, P. Kim et al., "Nanoscale cues regulate the structure and function of macroscopic cardiac tissue constructs," *Proceedings of the National Academy of Sciences of the United States of America*, vol. 107, no. 2, pp. 565–570, 2010.

[73] Y. J. Cheng, S. Y. Zhu, and S. W. Pang, "Directing osteoblastic cell migration on arrays of nanopillars and nanoholes with different aspect ratios," *Lab on a Chip*, vol. 21, no. 11, pp. 2206–2216, 2021.

[74] A. Fertin, L. Laforgue, A. Duperray, V. M. Laurent, Y. Usson, and C. Verdier, "Displacement fields using correlation methods as a tool to investigate cell migration in 3D collagen gels," *Journal of Microscopy*, vol. 275, no. 3, pp. 172–182, 2019.

[75] M. K. Driscoll, X. Sun, C. Guven, J. T. Fourkas, and W. Losert, "Cellular contact guidance through dynamic sensing of nanotopography," *ACS Nano*, vol. 8, no. 4, pp. 3546–3555, 2014.

[76] M. J. Dalby, M. O. Riehle, D. S. Sutherland, H. Agheli, and A. S. Curtis, "Changes in fibroblast morphology in response to nano-columns produced by colloidal lithography," *Biomaterials*, vol. 25, no. 23, pp. 5415–5422, 2004.

[77] C. H. Choi, S. H. Hagvall, B. M. Wu, J. C. Dunn, and R. E. Beygui, "Cell interaction with three-dimensional sharp-tip nanotopography," *Biomaterials*, vol. 28, no. 9, pp. 1672–1679, 2007.

[78] G. Li, S. Chen, M. Zeng et al., "Hierarchically aligned gradient collagen micropatterns for rapidly screening Schwann cells behavior," *Colloids Surf B Biointerfaces*, vol. 176, pp. 341–351, 2019.

[79] N. D. Bade, R. D. Kamien, R. K. Assoian, and K. J. Stebe, "Curvature and Rho activation differentially control the alignment of cells and stress fibers," *Science advances*, vol. 3, no. 9, article e1700150, 2017.

[80] T. Leng, P. Wu, N. Z. Mehenti et al., "Directed retinal nerve cell growth for use in a retinal prosthesis interface," *Investigative ophthalmology & visual science*, vol. 45, no. 11, pp. 4132–4137, 2004.

[81] R. M. Smeal, R. Rabbitt, R. Biran, and P. A. Tresco, "Substrate curvature influences the direction of nerve outgrowth," *Annals of Biomedical Engineering*, vol. 33, no. 3, pp. 376–382, 2005.

[82] N. M. Dowell-Mesfin, M. A. Abdul-Karim, A. M. Turner et al., "Topographically modified surfaces affect orientation and growth of hippocampal neurons," *Journal of neural engineering*, vol. 1, no. 2, pp. 78–90, 2004.

[83] K. J. Jang, M. S. Kim, D. Feltrin, N. L. Jeon, K. Y. Suh, and O. Pertz, "Two distinct filopodia populations at the growth cone allow to sense nanotopographical extracellular matrix cues to guide neurite outgrowth," *PLoS One*, vol. 5, no. 12, article e15966, 2010.

[84] H. Cheng, L. Zhou, B. Li, M. Zhu, H. P. Too, and W. K. Choi, "Nano-topology guided neurite outgrowth in PC12 cells is mediated by mi RNAs," *Nanomedicine*, vol. 10, no. 8, pp. 1871–1875, 2014.

[85] J. Du, J. Liu, S. Yao et al., "Prompt peripheral nerve regeneration induced by a hierarchically aligned fibrin nanofiber hydrogel," *Acta Biomaterialia*, vol. 55, pp. 296–309, 2017.

[86] F. Yang, R. Murugan, S. Wang, and S. Ramakrishna, "Electrospinning of nano/micro scale poly(L-lactic acid) aligned fibers and their potential in neural tissue engineering," *Biomaterials*, vol. 26, no. 15, pp. 2603–2610, 2005.

[87] L. He, S. Liao, D. Quan et al., "Synergistic effects of electrospun PLLA fiber dimension and pattern on neonatal mouse cerebellum C17.2 stem cells," *Acta Biomaterialia*, vol. 6, no. 8, pp. 2960–2969, 2010.

[88] H. B. Wang, M. E. Mullins, J. M. Cregg, C. W. McCarthy, and R. J. Gilbert, "Varying the diameter of aligned electrospun fibers alters neurite outgrowth and Schwann cell migration," *Acta Biomaterialia*, vol. 6, no. 8, pp. 2970–2978, 2010.

[89] J. Qu, D. Wang, H. Wang et al., "Electrospun silk fibroin nanofibers in different diameters support neurite outgrowth and promote astrocyte migration," *Journal of Biomedical*

Materials Research Part A, vol. 101, no. 9, pp. 2667–2678, 2013.

[90] J. Wang, R. Ye, Y. Wei et al., "The effects of electrospun TSF nanofiber diameter and alignment on neuronal differentiation of human embryonic stem cells," *Journal of Biomedical Materials Research Part A*, vol. 100, no. 3, pp. 632–645, 2012.

[91] S. K. Yoon, J. H. Yang, H. T. Lim et al., "In vitro and in vivo biosafety analysis of resorbable polyglycolic acid-polylactic acid block copolymer composites for spinal fixation," *Polymers*, vol. 13, no. 1, 2021.

[92] T. M. Saffari, M. Bedar, C. A. Hundepool, A. T. Bishop, and A. Y. Shin, "The role of vascularization in nerve regeneration of nerve graft," *Neural regeneration research*, vol. 15, no. 9, pp. 1573–1579, 2020.

[93] L. Coultas, K. Chawengsaksophak, and J. Rossant, "Endothelial cells and VEGF in vascular development," *Nature*, vol. 438, no. 7070, pp. 937–945, 2005.

[94] A. M. Suarez, I. van der Ham, M. G. Brinker, P. van Rijn, and M. C. Harmsen, "Topography-driven alterations in endothelial cell phenotype and contact guidance," *Heliyon*, vol. 6, no. 6, article e04329, 2020.

[95] B. M. Whited and M. N. Rylander, "The influence of electrospun scaffold topography on endothelial cell morphology, alignment, and adhesion in response to fluid flow," *Biotechnology and bioengineering*, vol. 111, no. 1, pp. 184–195, 2014.

[96] K. Kulangara, A. F. Adler, H. Wang et al., "The effect of substrate topography on direct reprogramming of fibroblasts to induced neurons," *Biomaterials*, vol. 35, no. 20, pp. 5327–5336, 2014.

[97] B. Geiger, J. P. Spatz, and A. D. Bershadsky, "Environmental sensing through focal adhesions," *Nature reviews Molecular cell biology*, vol. 10, no. 1, pp. 21–33, 2009.

[98] R. O. Hynes and A. D. Lander, "Contact and adhesive specificities in the associations, migrations, and targeting of cells and axons," *Cell*, vol. 68, no. 2, pp. 303–322, 1992.

[99] L. F. Reichardt and K. J. Tomaselli, "Extracellular matrix molecules and their receptors: functions in neural development," *Annual review of neuroscience*, vol. 14, pp. 531–570, 1991.

[100] D. M. Suter and P. Forscher, "Substrate-cytoskeletal coupling as a mechanism for the regulation of growth cone motility and guidance," *Journal of neurobiology*, vol. 44, no. 2, pp. 97–113, 2000.

[101] A. M. Sydor, A. L. Su, F. S. Wang, A. Xu, and D. G. Jay, "Talin and vinculin play distinct roles in filopodial motility in the neuronal growth cone," *Journal of Cell Biology*, vol. 134, no. 5, pp. 1197–1207, 1996.

[102] J. Xie, W. Liu, M. E. MR, P. C. Bridgman, and Y. Xia, "Neurite outgrowth on electrospun nanofibers with uniaxial alignment: the effects of fiber density, surface coating, and supporting substrate," *ACS Nano*, vol. 8, no. 2, pp. 1878–1885, 2014.

[103] A. Rajnicek, S. Britland, and C. Mc Caig, "Contact guidance of CNS neurites on grooved quartz: influence of groove dimensions, neuronal age and cell type," *Journal of cell science*, vol. 110, Part 23, pp. 2905–2913, 1997.

[104] K. Kang, S. Y. Yoon, S. E. Choi et al., "Cytoskeletal actin dynamics are involved in pitch-dependent neurite outgrowth on bead monolayers," *Angewandte Chemie International Edition*, vol. 53, no. 24, pp. 6075–6079, 2014.

[105] S. Di Cio and J. E. Gautrot, "Cell sensing of physical properties at the nanoscale: mechanisms and control of cell adhe-sion and phenotype," *Acta Biomaterialia*, vol. 30, pp. 26–48, 2016.

[106] M. J. Dalby, N. Gadegaard, and R. O. Oreffo, "Harnessing nanotopography and integrin-matrix interactions to influence stem cell fate," *Nature materials*, vol. 13, no. 6, pp. 558–569, 2014.

[107] M. J. Dalby, A. Hart, and S. J. Yarwood, "The effect of the RACK1 signalling protein on the regulation of cell adhesion and cell contact guidance on nanometric grooves," *Biomaterials*, vol. 29, no. 3, pp. 282–289, 2008.

[108] F. Guilak, D. M. Cohen, B. T. Estes, J. M. Gimble, W. Liedtke, and C. S. Chen, "Control of stem cell fate by physical interactions with the extracellular matrix," *Cell Stem Cell*, vol. 5, no. 1, pp. 17–26, 2009.

[109] W. H. Chooi and S. Y. Chew, "Modulation of cell-cell interactions for neural tissue engineering: potential therapeutic applications of cell adhesion molecules in nerve regeneration," *Biomaterials*, vol. 197, pp. 327–344, 2019.

Research Article

Therapeutic Study of Thermosensitive Hydrogel Loaded with Super-Activated Platelet Lysate Combined with Core Decompression Technology for the Treatment of Femoral Head Necrosis

Zhipeng Huang,[1] **Zhe Zhao,**[2] **Jun Lang,**[1] **Wantao Wang,**[1] **Yinsheng Fu,**[3] **and Wenbo Wang** [1,2]

[1]*The First Affiliated Hospital of Harbin Medical University, 23 You Zheng Street, Harbin 150001, China*
[2]*Southern University of Science and Technology Hospital, 6019 Liuxian Avenue, Xili, Nanshan District, Shenzhen 518000, China*
[3]*Tianqing Stem Cell Co., Ltd., Jubao Second Road, Science and Technology Innovation City, Songbei District, Harbin 150000, China*

Correspondence should be addressed to Wenbo Wang; wenbowang1967@163.com

Received 16 April 2021; Accepted 1 June 2021; Published 28 June 2021

Academic Editor: Kun Zhang

Super activated platelet lysate (sPL) is a derivative of platelet-rich plasma (PRP) that contains high levels of several growth factors. In this study, we synthesized a temperature-sensitive hydrogel that contained temperature-sensitive Poly(DL-lactide-glycolide-glycolide acid) (PLGA), $SrCl_2$, and HA, and loaded it with different concentrations of sPL. The hydrogel showed satisfactory encapsulation efficiency and release of the growth factors in a sustained manner, indicating its suitability as a drug carrier. The sPL-loaded hydrogel was inserted into the necrotic femoral head of a rat model and core decompression was applied and resulted in significantly accelerated bone repair and regeneration. Therefore, encapsulation of sPL in a hydrogel scaffolding may be an effective strategy for treating femoral head necrosis.

1. Introduction

Femoral head necrosis (ONFH) is characterized by osteocytic necrosis and bone marrow necrosis as a result of insufficient or a complete lack of blood supply to the subchondral bone. There are currently 30 million diagnosed cases of ONFH worldwide, of which 8.12 million are in China alone, and the rate of incidence has been increasing annually [1]. A recent multicenter study conducted on ONFH patients in China found that steroid use was identified as the causative factor in 26.35% of males patients and 55.75% of female patients [2]. Long-term use of high-dose glucocorticoids (GC) may affect the differentiation of cells in the femoral head and alter bone metabolism, thereby decreasing the angiogenic activity of the femoral head and triggering ischemic hypoxia.

In the absence of an effective method of treatment, ONFH can progress into subchondral bone collapse in 80% of patients within 1-3 years. Subchondral bone collapse causes resulting in considerable pain and impaired hip joint function and will eventually require total hip arthroplasty (THA). However, since THA is not the best option for younger patients, action needs to be taken as early as possible to slow down the progression of ONFH and delay the age of joint replacement.

Core decompression (CD) is a joint-preserving surgery [3] that is suitable for the early stage ONFH patients with an intact joint surface [4]. It can reduce intramedullary pressure on the femoral head, accelerate bone regeneration that may form a cavity after core decompression, and reverse femoral head necrosis [5], thereby delaying the progression of the disease and preventing femoral head collapse. However, 37% of patients that undergo core decompression therapy will progress to femoral head collapse [4].

Platelet-rich plasma (PRP) can accelerate bone formation by restoring osteoblast proliferation and activating pathways

that promote angiogenesis and osteogenesis [6], which is a strategy that can be used to the pathological progression of ONFH. Growth factors in PRP can promote cartilage formation [7] and osteogenesis [8] and can therefore alleviate ONFH [9]. In addition, platelet lysate (PL) growth factors also promote the chemotactic migration of various cells [10, 11]. PL can be incorporated into biological scaffolds that can retain its beneficial effects for a longer period [7, 12] based on the preparation method, activation, initial platelet concentration, and donor [12, 13]. Super-active platelet lysate (sPL) is prepared from PRP via ultralow temperature freeze-thawing. It is enriched in bioactive factors that can promote tissue regeneration and vascular remodeling. However, the short half-life of the growth factors in sPL limits their biological effects *in vivo*. In addition, high dosageses and/or the frequent administration of sPL is not economically viable, and may lead to toxic side effects. The controlled release of sPL loaded with hydrophilic macromolecules such as growth factors can significantly improve its efficacy *in vivo*.

Polymers with a high molecular weight [14], such as poly lactic-co-glycolic acid (PLGA), can be used as effective *in vivo* drug delivery systems due to their biocompatibility and biodegradability. The polymer material can protect sPL from the tissue microenvironment, leading to controlled release. Bone is a natural organic-inorganic-inorganic composite material that is mainly composed of collagen and hydroxyapatite (HA, $Ca_{10}(PO_4)_6(OH)_2$)). A variety of organic-inorganic composite materials that can mimic the composition and structure of bones have been developed. Strontium (Sr) is a trace element found in the human body that promotes bone formation and the healing of osteoporotic tissues. Therefore, we designed a composite hydrogel that consisted temperature-sensitive PLGA, the bone mineral hydroxyapatite (HA), and strontium [15, 16]. However, the hydrogel can flow into other parts of the defect, and the properties of the hydrogel need to be changed to prevent the hydrogel from flowing out.

Temperature-sensitive PLGA/HA/SrCl$_2$ hydrogel loaded with sPL was used to reconstruct the degenerated bone tissue in combination with CD surgery. sPL was slowly released from the hydrogel in a temperature-sensitive manner and resulted in accelerated bone repair after core decompression of the femoral head and ONFH. Therefore, our study has laid the foundation for the clinical application of heat-sensitive hydrogel materials, and also for a considerable reduction in the cost of treating ONFH patients.

2. Materials and Methods

2.1. Materials. Temperature-sensitive PLGA was purchased from Jinan Daigang Biomaterial Co., Ltd, SrCl2 was purchased from Sinopharm Chemical Reagent Co. Ltd., HA was purchased from Aladdin, lipopolysaccharide was purchased from Sigma-Aldrich Inc. (USA), while Methylsulfonate was purchased from Pfizer Pharmaceuticals (Hangzhou, China).

2.2. sPL Preparation. sPL was isolated from human blood via ultralow temperature freezing, as previously described [17].

In brief, PRP was extracted by centrifuging fresh whole blood. The PRP was ultralow-frozen using melt preparation and patented cytokine culture technologies, sPL can be efficiently induced, activated, and cultivated.

2.3. Synthesis and Characterization of Hydrogels. The temperature-sensitive PLGA\SrCl$_2$ and HA were mixed at a ratio of $94 : 5 : 1$, and the mixture was added to 0, 250, and $500\,\mu$l of sPL placed in a magnetic stirrer. The resulting PLS0, PLS1, and PLS2 hydrogels were lyophilized and sprayed with gold, and their morphology was observed under a scanning electron microscope (SEM) (Japan Electronics Co. Ltd.).

To measure the sustained release of bioactive factors from the PLS hydrogels created, the latter were placed in clean vials ($n = 4$ per group) and completely submerged in 4 ml of simulated body fluid (SBF). The vials were then sealed and incubated in a water bath, and the aliquots in the medium were collected on days 3, 6, 9, 12, 15, 18, 21, 24, 27, and 30. The concentration of VEGF and TGF-β was measured using specific ELISA kits (Jingmei, Jiangsu).

Preweighed lyophilized gels were incubated in deionized water at 30°C, 34°C, 38°C, and 42°C for 1 hour to measure hydrogel swelling. The swollen gels were retrieved, blotted to remove excess water, and weighed. The colloidal water content (SR) was calculated using the formula: $(W1 - W0)/W0$, where $W0$ and $W1$ indicate dry weight and temperature weight, respectively.

2.4. In Vivo Experiments

2.4.1. Establishment of an ONFH Model and Treatment. All animal experiments were conducted in accordance with the guidelines on the humane use and care of animals formulated by the National Institutes of Health, all experimental animals are taken care of, and all operations on animals are approved by the Experimental Animal Use and Welfare Ethics Committee of the First Affiliated Hospital of Harbin Medical University (Ethical approval number:2019029).

Male SD rats weighing 280-300 g were reared at the animal center of the First Affiliated Hospital of Harbin Medical University and fed *ad libitum* on a standard laboratory diet and water. A total of 27 rats were intravenously injected with $10\,\mu$g/kg lipopolysaccharide (LPS), followed by 24 h later with three intramuscular injections of 20 mg/kg methylsulfonate (MPS) then at 24 h intervals. Osteonecrotic lesions first appeared two weeks after the procedure and continued to appear until 6 weeks after the procedure [18]. Three of the rats were euthanized, and tissue samples were collected for CT and histopathological examination. Once a diagnosis of ONFH was confirmed, the other rats were randomly assigned to the PLS0, PLS1, and PLS2 groups ($n = 8$). The rats were anesthetized using 3% pentobarbital sodium, and the right hip was exposed using an anterior and posterior approach while preserving the main blood vessels in the femoral head. The hip joint was prevented from shifting by cutting the switch capsule, and the femoral head and neck were exposed. Decompression was performed from the greater trochanter to the core of the femoral head using a drill, and the lesion
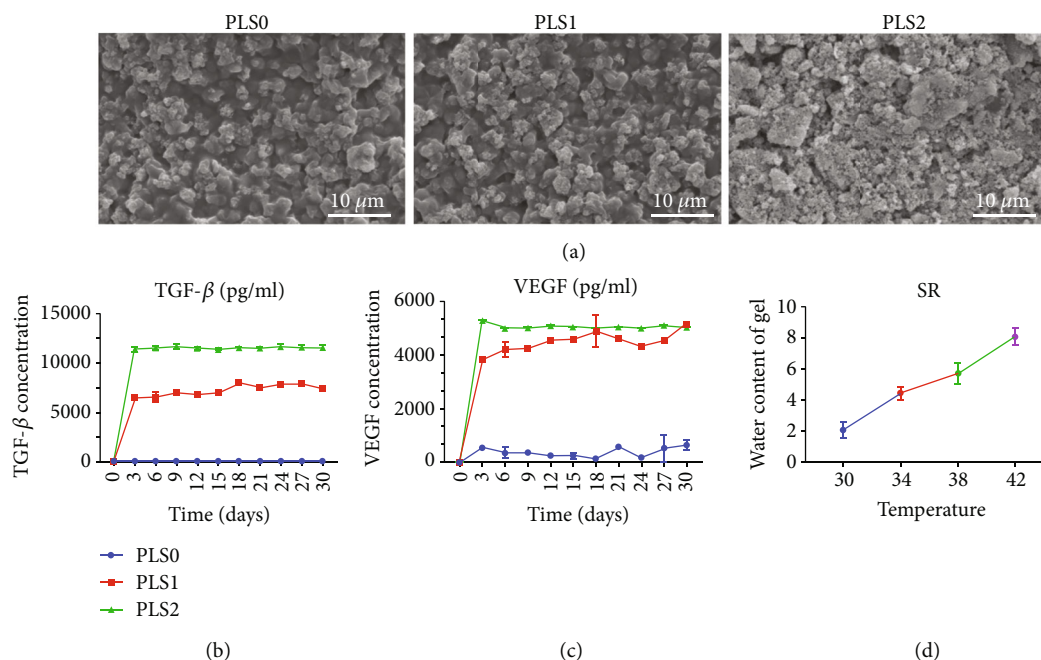
FIGURE 1: (a) Representative SEM images showing the structure of lyophilized thermosensitive hydrogel. (b, c) Release of growth factors from the loaded sPL hydrogel. (d) Temperature-dependent change in water content.

was filled with PLS. The implanted region was covered with bone wax, and the wound was closed. All animals were intramuscularly injected with gentamicin (4 mg/kg) before and after the operation to prevent any wound infections.

2.4.2. Radiological Analysis. Four animals from each group were sacrificed to be used for the Micro-CT analysis on the 4th and 12th weeks postsurgery. Changes in the femoral head were monitored using a QuantumGX CT imaging system (PerkinElmer, USA). An isotropic 20 mm voxel pitch dataset was obtained using a total rotation of 360° and step length of 0.5° under a power of 80 kV, and computer-generated three-dimensional model of the femoral head was constructed.

2.4.3. Histopathological Analysis. Animals from each group were used for the histological observations made on the 4th and 12th weeks after surgery. The tissue samples were fixed using 4% paraformaldehyde for a period of 1 week and decalcified using 20% EDTA solution for a period of a month. Then, the samples were dehydrated using an alcohol gradient and clarified using xylene. Thereafter, the tissues were embedded in paraffin and cut into 4 μm thick sections, followed by hematoxylin and eosin (HE), Masson, and ALP staining, as per standard protocols.

2.4.4. Tunel Assay. The tissue sections were incubated with the Tunel reagent using the specific Tunel kit as per the manufacturer's instructions. The color was developed by applying 0.03% DAB for 5 minutes, and the slides were counterstained with hematoxylin. The number of Tunel-positive cells were counted in four random microscopic fields at 200x magnification. The apoptosis rate (%) was calculated as the ratio of the number of Tunel-positive cells to the total number of cells.

2.4.5. Immunohistochemistry. The tissue sections were probed using primary antibodies against type I collagen and CD31, followed by a secondary antibody with/out Cy5 conjugate. After counterstaining with hematoxylin, the slides were observed under a fluorescence microscope (Leica, Mannheim, Germany) or a light microscope (Leica, Mannheim, Germany).

2.5. Statistical Analysis. Data are expressed as mean ± standard deviation (SD). One-way analysis of variance (ANOVA) was used to compare data between the groups. A P value of <0.05 was considered to be statistically significant.

3. Results and Discussion

3.1. Characterization of the Hydrogels. We loaded sPL into a temperature-sensitive hydrogel for sustainable release and stronger therapeutic effects. As shown in Figure 1(a), the freeze-dried hydrogel had a partially porous structure, and the incorporation of sPL decreased the size of the particles.

The polymer hydrogel steadily released TGF-β and VEGF over a period of 30 days (Figures 1(b) and 1(c)) depending on the amount of encapsulated sPL. As expected, there was no obvious release of growth factors from PLS0. In addition, the hydrogel swelled to 2.1, 2.8, and 3.9 times to its volume at 30°C when heated to 34°C, 38°C, and 42°C, respectively (Figure 1(d)).

3.2. The sPL-Loaded Hydrogel Alleviated Osteonecrosis and Promoted Bone Formation. An ONFH model was established using LPS and MPS, as previously described by Wu et al. [19]. Imaging and histological tests clearly demonstrated a diagnosis of osteonecrosis at 6 weeks, along with bone marrow necrosis, abnormal fat distribution, and increased internal
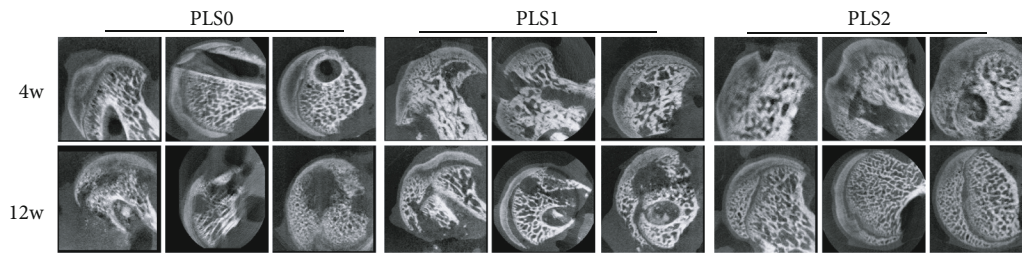
FIGURE 2: Representative coronal, transverse and sagittal micro-CT scans of the different treatment groups.
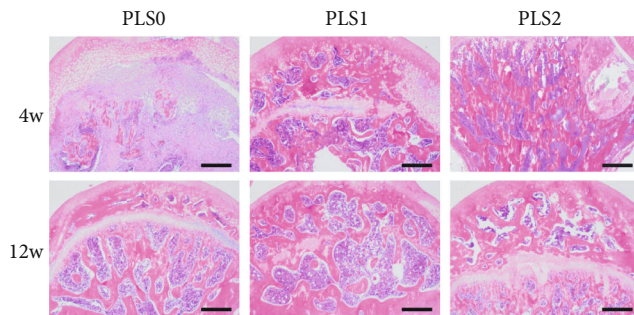
FIGURE 3: HE staining after treatment for femoral head necrosis (40x).
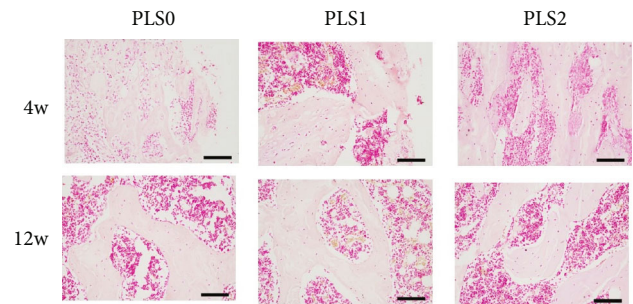
FIGURE 5: ALP staining of the histopathological osteogenic marker (200x).
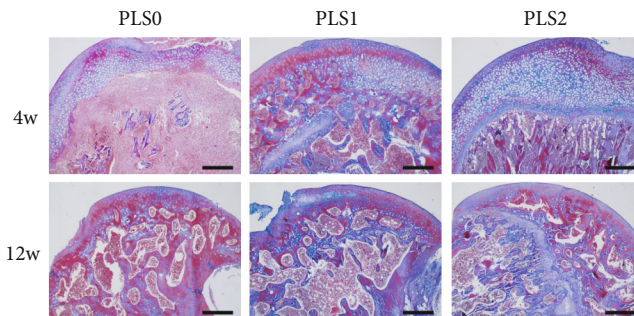
FIGURE 4: Histopathology Masson staining conducted 4 weeks and 12 weeks after ONFH treatment (40x).
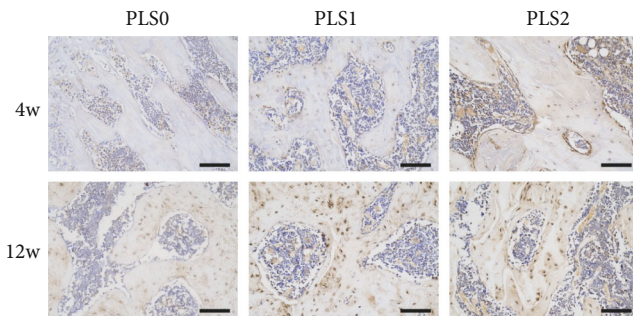
FIGURE 6: Histopathological type I staining demonstrated the composition of bone tissue (200x).

pressure of the femoral head. The core decompression channel for femoral head necrosis was well constructed, and the hydrogel was accurately implanted without any damage to the muscles, nerves, or blood vessels. All animals were healthy and no obvious signs of infection were observed. Several studies have reported the presence of osteogenic growth factors in PL [10, 20], and encapsulation of sPL in a hydrogel scaffolding enhances the retention capacity of constituent growth factors. As shown in Figure 2, the cross-sectional and longitudinal CT images show that PLS1 was partially repaired in the necrotic region, 4 weeks after the implantation, compared with the PLS0 group, whereas PLS2 showed a stronger therapeutic effect. Necrotic areas were still visible even after 12 weeks in the PLS0 groups but had been mostly reconstituted in rats treated with PLS1 and PLS2.

Histological examination of the femoral head necrosis showed that ONFH induction resulted in sparse cavities, diffuse spot-like bone marrow necrosis, and a sparse trabecular
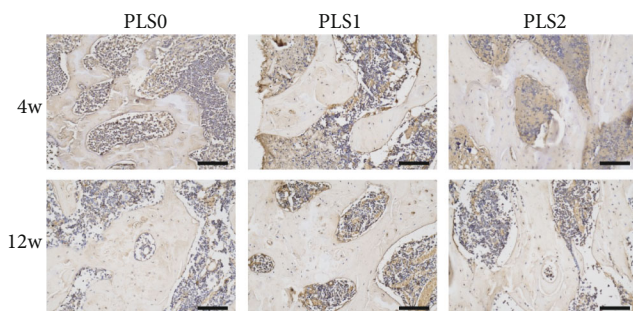
FIGURE 7: Histopathological CD31 staining demonstrating the formation of blood vessels in the femoral head (200x).

bone marrow cavity with large fat cells. Implantation of the hydrogels did not trigger any localized inflammatory reaction or fibrosis. PLS2 resulted in the formation of new bone and trabeculae by the 4th week after implantation with causing osteonecrosis and hematopoietic necrosis. Likewise, PLS0

(a)

(b)
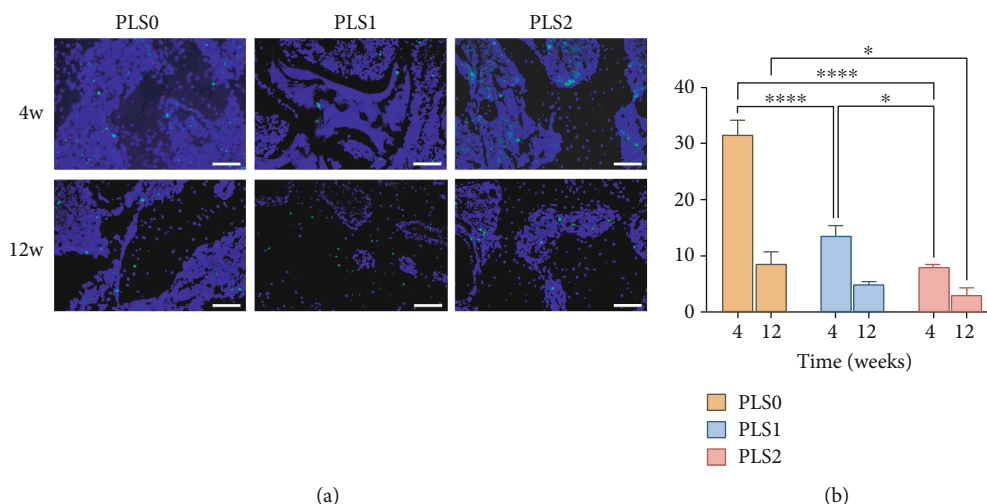
FIGURE 8: (a) Tunel staining conducted on the 4th week and 12th week after ONFH treatment (200x). (b) The apoptotic rate was calculated using the Tunel-staining results.

and PLS1 administration caused the formation of new bones but did not induce a trabecular arrangement (Figures 3 and 4). Consistent with the observations mentioned above, bone tissues expressing the osteogenic factor ALP and collagen I were observed in all groups, and the degree of positive staining increased in the PLS-implanted groups in a sPL concentration-dependent manner (Figures 5 and 6).

3.3. The sPL-Loaded Hydrogel Promoted Angiogenesis.

In addition to, the growth factors in sPL promote the adherence and proliferation of osteoblasts, while also facilitating angiogenesis via the proliferation of vascular endothelial cells. Platelet endothelial cell adhesion molecule-1 (CD31), which is typical for the endothelial lineage [21]. As shown in Figure 7, compared with the PLS0 group, CD31 staining increased in the PLS1 and PLS2 treatment groups during the 4th week of treatment. The number of CD31-positive cells increased in a time and sPL concentration-dependent manner and peaked in the PLS2 treatment group, 12 weeks after surgery. Vadasz et al. [22] found that the decrease in VEGF (vascular endothelial growth factor, promote angiogenesis) levels was correlated with ONFH progression and promoted VEGF synthesis induced angiogenesis in the trabecular space in femoral head necrosis. Bai et al. [23] found that compared to BMP-2 alone, the combination of VEGF and BMP-2 increased the formation of the vascular networks and significantly enhanced the formation of ectopic bone. Consistent with previous reports, angiogenic factor CD31 was highly expressed in the PLS2-treated group (Figure 7).

3.4. The sPL-Loaded Hydrogel Inhibited Apoptosis in the Femoral Head Tissue.

Numerous Tunel-positive apoptotic bone cells were observed in the necrotic femoral head, while the number of positive cells decreased significantly after hydrogel implantation. As shown in Figure 8, the rate of apoptosis in the PLS0, PLS1, and PLS2 groups were $31.48 \pm 1.80\%$, $13.60 \pm 1.27\%$, and $8.05 \pm 0.27\%$, respectively, after 4 weeks, and $8.59 \pm 1.55\%$, $4.97 \pm 0.29\%$, and $3.08 \pm 0.92\%$,

respectively, after 12 weeks (Figure 8(b)). In the 4th week, compared with the PLS0 group, the apoptosis rate of the PLS1 and PLS2 groups was significantly reduced ($P < 0.05$). With the addition of sPL, the apoptosis rate in the tissues was also significantly reduced ($P < 0.05$). In the 12th week, compared with the PLS0 group, the apoptosis rate of PLS1 and PLS2 groups was significantly reduced ($P < 0.05$). With the addition of sPL, the apoptosis rate between PLS0 and PLS1 groups, and PLS1 and PLS2 groups had no significant statistical significance. In the PLS0 group, PLS1 group, and PLS2 group, compared with 4 weeks, the apoptosis rate in tissues at 12 weeks after operation was significantly reduced ($P < 0.05$).

ER stress-induced apoptosis can be inhibited by PRP exosomes in a manner independent of the PERK/CHOP pathway [24]. Bone mesenchymal stem cells (BMSCs) treated with PRP exosomes and dexamethasone showed enhanced phosphorylated Akt (protein kinase B) and Bad (Bcl-2 related death promoter) levels, as well as enhanced Bcl-2 expression, indicating that PRP exosomes can inhibit apoptosis by activating the Akt/Bad/Bcl-2 signaling pathway [24].

Despite the encouraging results, our study has two main limitations. First, we established an ONFH rat model in rats, which did not develop femoral head collapse. However, when we performed core decompression, the cartilage surface was partially destroyed, simulating the destruction of cartilage as a result of the femoral head collapse. The pathological condition of ONFH was not consistent with the actual clinical situation and also precluded the long-term effects of the use of the hydrogel. Therefore, at this stage, it is impossible to determine whether the hydrogel can prevent collapse. Instead, femoral collapse would have to be established in a large animal model to demonstrate cartilage repair. Second, we evaluated angiogenesis based only on CD31 expression levels, and microangiography can be used to observe the formation of new blood vessels in a more accurate manner.

4. Conclusion

Compared to thermosensitive hydrogel, the sPL-loaded thermosensitive hydrogel steadily released biological factors that reduced the level of osteoblast apoptosis, promoted osteogenesis and angiogenesis, and effectively prevented the development of ONFH in a rat model. Therefore, treatment using sPL-loaded thermosensitive hydrogel can be used in combination with core decompression surgery to improve the outcomes of femoral head necrosis treatment.

Data Availability

The data used to support the findings of this study are included within the article.

Conflicts of Interest

The authors have declared that there are no competing interests.

Acknowledgments

References

[1] D. W. Zhao, M. Yu, K. Hu et al., "Prevalence of nontraumatic osteonecrosis of the femoral head and its associated risk factors in the Chinese population: results from a nationally representative survey," *Chinese Medical Journal*, vol. 128, no. 21, pp. 2843–2850, 2015.

[2] D. Li, X. Xie, Z. Yang, C. Wang, Z. Wei, and P. Kang, "Enhanced bone defect repairing effects in glucocorticoid-induced osteonecrosis of the femoral head using a porous nano-lithium-hydroxyapatite/gelatin microsphere/erythropoietin composite scaffold," *Biomaterials Science*, vol. 6, no. 3, pp. 519–537, 2018.

[3] M. Chughtai, N. S. Piuzzi, A. Khlopas, L. C. Jones, S. B. Goodman, and M. A. Mont, "An evidence-based guide to the treatment of osteonecrosis of the femoral head," *The Bone & Joint Journal*, vol. 99-b, no. 10, pp. 1267–1279, 2017.

[4] D. R. Marker, T. M. Seyler, S. D. Ulrich, S. Srivastava, and M. A. Mont, "Do modern techniques improve core decompression outcomes for hip osteonecrosis?," *Clinical Orthopaedics and Related Research*, vol. 466, no. 5, pp. 1093–1103, 2008.

[5] J. R. Lieberman, S. M. Engstrom, R. M. Meneghini, and N. F. SooHoo, "Which factors influence preservation of the osteonecrotic femoral head?," *Clinical Orthopaedics and Related Research*, vol. 470, no. 2, pp. 525–534, 2012.

[6] V. T. Nguyen, M. Nardini, A. Ruggiu, R. Canceda, F. Descalzi, and M. Mastrogiacomo, "Platelet Lysate Induces in Human Osteoblasts Resumption of Cell Proliferation and Activation of Pathways Relevant for Revascularization and Regeneration of Damaged Bone," *International Journal of Molecular Sciences*, vol. 21, no. 14, p. 5123, 2020.

[7] L. S. Moreira Teixeira, J. C. Leijten, J. W. Wennink et al., "The effect of platelet lysate supplementation of a dextran-based hydrogel on cartilage formation," *Biomaterials*, vol. 33, no. 14, pp. 3651–3661, 2012.

[8] V. E. Santo, A. R. Duarte, E. G. Popa, M. E. Gomes, J. F. Mano, and R. L. Reis, "Enhancement of osteogenic differentiation of human adipose derived stem cells by the controlled release of platelet lysates from hybrid scaffolds produced by supercritical fluid foaming," *Journal of Controlled Release*, vol. 162, no. 1, pp. 19–27, 2012.

[9] J. Han, F. Gao, Y. Li et al., "The use of platelet-rich plasma for the treatment of osteonecrosis of the femoral head: a systematic review," *BioMed Research International*, vol. 2020, Article ID 2642439, 11 pages, 2020.

[10] M. C. Phipps, Y. Xu, and S. L. Bellis, "Delivery of platelet-derived growth factor as a chemotactic factor for mesenchymal stem cells by bone-mimetic electrospun scaffolds," *PLoS One*, vol. 7, no. 7, article e40831, 2012.

[11] Y. Yu, S. Zhu, Y. Hou, J. Li, and S. Guan, "Sulfur contents in sulfonated hyaluronic acid direct the cardiovascular cells fate," *ACS Applied Materials & Interfaces*, vol. 12, no. 41, pp. 46827–46836, 2020.

[12] P. S. Babo, R. L. Pires, L. Santos et al., "Platelet lysate-loaded photocrosslinkable hyaluronic acid hydrogels for periodontal endogenous regenerative technology," *ACS Biomaterials Science & Engineering*, vol. 3, no. 7, pp. 1359–1369, 2017.

[13] J. M. de Leon, V. R. Driver, C. P. Fylling et al., "The clinical relevance of treating chronic wounds with an enhanced near-physiological concentration of platelet-rich plasma gel," *Advances in Skin & Wound Care*, vol. 24, no. 8, pp. 357–368, 2011.

[14] R. Xu, K. Zhang, J. Liang, F. Gao, J. Li, and F. Guan, "Hyaluronic acid/polyethyleneimine nanoparticles loaded with copper ion and disulfiram for esophageal cancer," *Carbohydrate Polymers*, vol. 261, article 117846, 2021.

[15] S. C. Verberckmoes, M. E. De Broe, and P. C. D'Haese, "Dose-dependent effects of strontium on osteoblast function and mineralization," *Kidney International*, vol. 64, no. 2, pp. 534–543, 2003.

[16] B. Zhao, X. Li, H. Xu, Y. Jiang, D. Wang, and R. Liu, "Influence of simvastatin-strontium-hydroxyapatite coated implant formed by micro-arc oxidation and immersion method on osteointegration in osteoporotic rabbits," *International Journal of Nanomedicine*, vol. 15, pp. 1797–1807, 2020.

[17] Z. Huang, W. Wang, Q. Wang et al., "Coaxial nanofiber scaffold with super-active platelet lysate to accelerate the repair of bone defects," *RSC Advances*, vol. 10, no. 59, pp. 35776–35786, 2020.

[18] L. Qin, G. Zhang, H. Sheng et al., "Multiple bioimaging modalities in evaluation of an experimental osteonecrosis induced by a combination of lipopolysaccharide and methylprednisolone," *Bone*, vol. 39, no. 4, pp. 863–871, 2006.

[19] X. Wu, S. Yang, D. Duan, Y. Zhang, and J. Wang, "Experimental osteonecrosis induced by a combination of low-dose lipopolysaccharide and high-dose methylprednisolone in rabbits," *Joint, Bone, Spine*, vol. 75, no. 5, pp. 573–578, 2008.

[20] E. Jain, S. Sheth, A. Dunn, S. P. Zustiak, and S. A. Sell, "Sustained release of multicomponent platelet-rich plasma proteins from hydrolytically degradable PEG hydrogels," *Journal of Biomedical Materials Research. Part A*, vol. 105, no. 12, pp. 3304–3314, 2017.

[21] M. Hristov, W. Erl, and P. C. Weber, "Endothelial progenitor cells: mobilization, differentiation, and homing," *Arteriosclerosis,*

Thrombosis, and Vascular Biology, vol. 23, no. 7, pp. 1185–1189, 2003.

[22] Z. Vadasz, I. Misselevich, D. Norman, E. Peled, and J. H. Boss, "Localization of vascular endothelial growth factor during the early reparative phase of the rats' vessels deprivation-induced osteonecrosis of the femoral heads," *Experimental and Molecular Pathology*, vol. 77, no. 2, pp. 145–148, 2004.

[23] Y. Bai, Y. Leng, G. Yin et al., "Effects of combinations of BMP-2 with FGF-2 and/or VEGF on HUVECs angiogenesis in vitro and CAM angiogenesis in vivo," *Cell and Tissue Research*, vol. 356, no. 1, pp. 109–121, 2014.

[24] S. C. Tao, T. Yuan, B. Y. Rui, Z. Z. Zhu, S. C. Guo, and C. Q. Zhang, "Exosomes derived from human platelet-rich plasma prevent apoptosis induced by glucocorticoid-associated endoplasmic reticulum stress in rat osteonecrosis of the femoral head via the Akt/Bad/Bcl-2 signal pathway," *Theranostics*, vol. 7, no. 3, pp. 733–750, 2017.

Review Article

3D Electrospun Nanofiber-Based Scaffolds: From Preparations and Properties to Tissue Regeneration Applications

Shanshan Han,[1,2] Kexin Nie,[1,2] Jingchao Li,[3] Qingqing Sun,[4] Xiaofeng Wang,[1,2] Xiaomeng Li ⓘ,[1,2] and Qian Li ⓘ[1,2]

[1]*School of Mechanics and Safety Engineering, Zhengzhou University, Zhengzhou 450001, China*
[2]*National Center for International Joint Research of Micro-nano Moulding Technology, Zhengzhou University, Zhengzhou 450001, China*
[3]*School of Chemical and Biomedical Engineering, Nanyang Technological University, Singapore 637457, Singapore*
[4]*Center for Functional Sensor and Actuator, National Institute for Materials Science, 1-1 Namiki, Tsukuba, Ibaraki 305-0044, Japan*

Correspondence should be addressed to Xiaomeng Li; xiaomeng.li@zzu.edu.cn and Qian Li; qianli@zzu.edu.cn

Shanshan Han and Kexin Nie contributed equally to this work.

Electrospun nanofibers have been frequently used for tissue engineering due to their morphological similarities with the extracellular matrix (ECM) and tunable chemical and physical properties for regulating cell behaviors and functions. However, most of the existing electrospun nanofibers have a closely packed two-dimensional (2D) membrane with the intrinsic shortcomings of limited cellular infiltration, restricted nutrition diffusion, and unsatisfied thickness. Three-dimensional (3D) electrospun nanofiber-based scaffolds can provide stem cells with 3D microenvironments and biomimetic fibrous structures. Thus, they have been demonstrated to be good candidates for *in vivo* repair of different tissues. This review summarizes the recent developments in 3D electrospun nanofiber-based scaffolds (ENF-S) for tissue engineering. Three types of 3D ENF-S fabricated using different approaches classified into electrospun nanofiber 3D scaffolds, electrospun nanofiber/hydrogel composite 3D scaffolds, and electrospun nanofiber/porous matrix composite 3D scaffolds are discussed. New functions for these 3D ENF-S and properties, such as facilitated cell infiltration, 3D fibrous architecture, enhanced mechanical properties, and tunable degradability, meeting the requirements of tissue engineering scaffolds were discovered. The applications of 3D ENF-S in cartilage, bone, tendon, ligament, skeletal muscle, nerve, and cardiac tissue regeneration are then presented with a discussion of current challenges and future directions. Finally, we give summaries and future perspectives of 3D ENF-S in tissue engineering and clinical transformation.

1. Introduction

Tissue engineering that combines cells, biomaterials, and biochemical and biophysical factors to improve or replace biological tissues provides an ideal treatment option for tissue damages [1, 2]. It involves isolation and expansion of target cells *in vitro* and their seeding and growth in implanted biomaterials to allow the formation of new tissues with defined shapes and functions [3]. By utilizing these autogenous cells, tissue engineering has the advantages of autografts, which overcomes the limited self-repairing capacity

of many tissues [4]. To date, this therapeutic approach has demonstrated success in the repair of skin, cartilage, bone, bladder, and blood vessels, among others [5–9].

Biomaterials play essential roles in tissue engineering as they can provide designable biophysical and biochemical milieus to support cell attachment, proliferation, differentiation, and neo tissue genesis [10–12]. With the increasing understanding of the interactions between cells and the surrounding microenvironment, more and more attention is focused on developing biomaterials that mimic ECM's native components, properties, and structures [13–15]. An optimal

scaffold for tissue regeneration should mimic the mechanical and functional properties of ECM of those tissues to be regenerated. To date, a significant number of biomaterials, including hydrogels, porous scaffolds, and fibers, have been extensively developed and explored in tissue engineering.

Among them, fibrous scaffolds have recently attracted a lot of attention since native ECM consists of abundant protein fibers with different structures and arrangements [1, 16]. Electrospun nanofibers with controllable diameters, alignments and components, and large surface areas are often used to meet the requirements of tissue engineering [17–21]. However, these traditional 2D electrospun membranes have an intrinsic limitation of relatively poor cellular infiltration due to their limited thickness and relatively high packing density [22, 23]. Therefore, these scaffolds, in practice, act as 2D surfaces rather than 3D microenvironments. Although porous scaffolds and hydrogels can provide a suitable 3D microenvironment for implanted cells and have exhibited extensive applications in regenerative medicine [24–26], they often lack fibrous structures and the anisotropy character of native tissue ECM [27, 28]. Thus, researchers are seeking to develop 3D electrospun nanofiber scaffolds to recapitulate ECM's architecture and morphology better [29].

There are some review articles about electrospinning and nanofiber-hydrogel composite scaffolds [30–32]. However, a comprehensive summary of fabrication strategies, required functions, and advanced performances in tissue engineering is missing. This review article summarizes the recent design approaches of 3D ENF-S and their applications in tissue engineering. It starts with a brief introduction to the traditional electrospun nanofibers and their limitations. Subsequently, recent advances in the fabrications of three types of 3D ENF-S are presented. The applications of 3D ENF-S with improved features and functions in various types of tissue engineering are then highlighted (Figure 1). Finally, we give a brief conclusion and discuss the perspectives on current challenges and future directions of 3D ENF-S in tissue engineering.

2. Preparation of ENF-S from 2D to 3D

2.1. Traditional Electrospinning and Its Limitation. Electrospun nanofibers are often fabricated using electrospinning facilities which consist of three elements: an electrical generator (high voltage supply), a needle with or without solvent pump (jet source), and a metal collector (target) [33]. When voltage is applied on the nozzle and electrostatic repulsion counteracts the surface tension, the droplet will be stretched. At the critical voltage point (the threshold voltage), a "Taylor cone" (disintegration of water drops in an electric field) is formed, and a jet of liquid erupts from the surface. The jet flow created at the "Taylor cone" is stretched to whip into continuous ultrafine fibers in the electric field while the solvent is evaporating. By adjusting experimental parameters such as the applied voltage, the designated distance between the nozzle and collector, and the property of the solution, fibers with uniform diameters can be routinely produced, and an electrospun membrane with packed density is gradually fabricated. The nanofibers' diameters and orientations
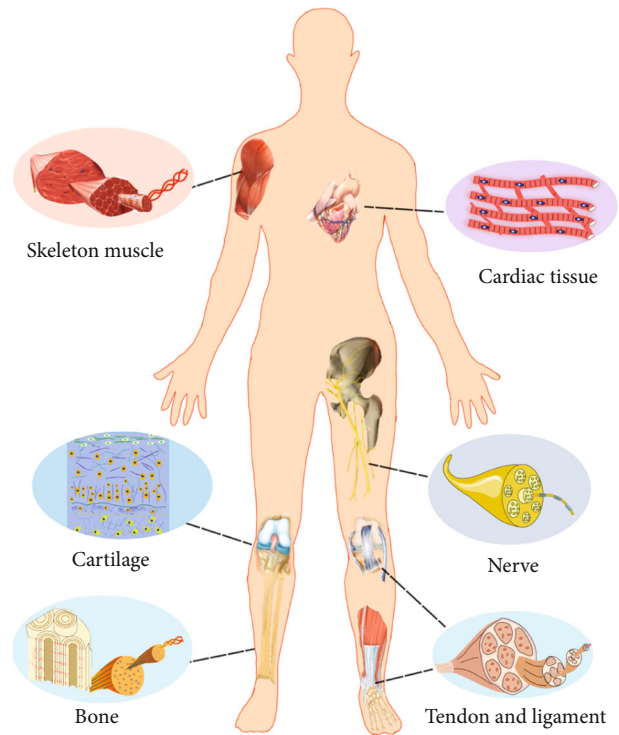
FIGURE 1: Illustration of typical tissues with fibrous structures whose regeneration can be mediated by 3D ENF-S.

can be controlled by adjusting the solution viscosity or the type of collectors, which leads to an apparent influence on cell behaviors and functions [34, 35]. However, electrospun membrane produced by traditional strategy possesses a very thin thickness (<1 mm) [36] and high dense packing attributed to the nature of electrospinning, which hampers cell infiltration, and limits extensive applications in tissue regeneration.

2.2. Preparation of 3D Electrospun Nanofiber-Based Scaffolds (ENF-S). 3D scaffolds are required for most tissue regeneration because their biomimetic 3D environment will promote cell differentiation, neo tissue development, and higher genetic material expression, such as ECM secretion and cell metabolism. Therefore, 3D ENF-S with thick thickness and the capacity for cell infiltration is highly needed for tissue engineering. In this section, 3D ENF-S are classified into (i) electrospun nanofiber 3D scaffolds, (ii) electrospun nanofiber/hydrogel composite 3D scaffolds, and (iii) electrospun nanofiber/porous matrix composite 3D scaffolds according to the different fabrication approaches (Figure 2).

2.2.1. Electrospun Nanofiber 3D Scaffolds. Electrospun nanofiber 3D scaffolds with high porosity and thickness can be fabricated by direct electrospinning through postprocessing techniques, tuning fiber collection techniques, or combining the two. Electrospun membranes can be changed into scaffolds with desirable 3D structures, tailored sizes, and mechanical properties by facile and direct postprocessing techniques such as stacking, rolling, and braiding the electrospun membrane [37]. Besides, gas foaming is also successfully
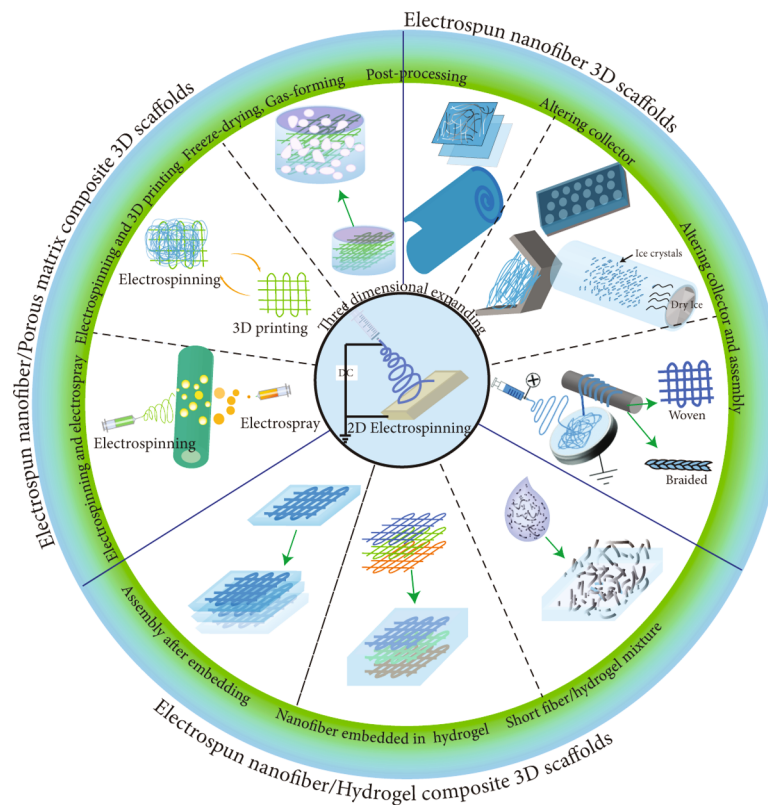
Figure 2: The summary of representative design approaches of 3D ENF-S.

used to expand 2D electrospun nanofiber sheets to 3D scaffolds. For example, electrospun nanofiber mats were successfully grown into a 3D scaffold after treatment with $NaBH_4$ aqueous solutions [38]. The distributions of gap widths and layer thicknesses are directly dependent on nanofiber mats processing time within the gas bubble forming solution. Similarly, a porous poly(ε-caprolactone) (PCL) electrospun structure was fabricated by adding a chemical blowing agent, azodicarbonamide, which generated micro-sized pores through decomposition after deposing at 100°C for 2-3 seconds [39]. The montmorillonite-reinforced poly(L-lactide) (PLLA) electrospun nanofibers with a 3D and dual-porosity structure were fabricated through a cold compression molding process and salt leaching/gas-forming method [40]. Other postprocessing methods, such as hole forming by punching or laser ablation, can enhance electrospun mats' porosity and promote tissue regeneration performance by improving cell infiltration and migration [41, 42].

Electrospun nanofiber 3D scaffolds with significantly increased thickness can also be prepared by tuning fiber collection techniques, such as regulating the electrospinning collector or the environment during electrospinning. According to a study conducted by Subramanian et al., a 3D tubular scaffold was fabricated by adding an insulating gap as an auxiliary electrode, which resulted in a longitudinal deposition of fibers [43]. Similarly, spherical dish and double-bevel collectors were also used to fabricate 3D fibrous scaffolds [44, 45]. Patterned collectors could increase the thickness and pore size of electrospun nanofiber scaffolds to improve cell infiltration [46–50]. Besides the geometry of

the collector, Olvera et al. found that electrospun nanofiber 3D scaffolds could be fabricated readily by varying the rotational speed of the mandrel collector during electrospinning [51]. Moreover, cryogenic electrospinning was also used to fabricate electrospun nanofiber 3D scaffold with high porosity and thickness utilizing ice crystal as templates [52–54]. For instance, a poly(D, L-lactide) scaffold with large pores ranging from 10 to 500 μm was fabricated by the cryogenic electrospinning technique [55]. Besides, centrifugal electrospinning, using centrifugal forces to produce fibers from melts or solutions, has also been reported to produce 3D fibrous scaffolds. This technology is high throughput, and the scaffolds prepared by this technology have open porous structures facilitating deep cell penetration [56, 57].

Tuning collectors and postprocessing techniques are often combined to increase further the thickness and porosity of electrospun nanofiber scaffolds. For example, 3D porous electrospinning PCL with nanohydroxyapatite (nHA) scaffolds were prepared using the stainless-steel porous mesh collector and layer-by-layer (LbL) assembly technique [58]. Another popular strategy is the electrospinning-based yarn assembly technique, forming yarns by regulating the collection system and further postprocessing by 3D assembling [59–61]. For example, the yarns obtained through a liquid support system can produce 3D scaffolds with different shapes [62]. Similarly, yarns can be collected through an "electro-wet spinning," in which a water vortex is formed to twist the collected fibers into yarns in a dynamic liquid collection system [63, 64]. A combination of this hydroelectrospinning and LbL assembly can produce 3D scaffolds [65].

Further, the yarn-based 3D scaffolds could be prepared by postprocessing treatment [66]. Moreover, the yarns can be used to weave 3D anisotropy scaffolds, which exhibited excellent anisotropy mechanical properties for specific tissue regeneration [67].

2.2.2. Electrospun Nanofiber/Hydrogel Composite 3D Scaffolds. Hydrogels have been utilized for various biomedical field applications, including drug loading, cell delivery, and tissue engineering, because of their 3D spatial architecture and elastic properties [68–70]. However, hydrogels have poor mechanical strength and lack native ECM's fibrous structure [31]. The amalgamation of electrospun fibers and hydrogels can simulate the structures and properties of ECM [71]. Nanofiber components can increase cell viability, adhesion, and differentiation because the nanofibers can resist the contractile forces, providing adhesion sites and maintaining the oriented morphology [72]. The mechanical properties and cell in infiltration ability of such composite constructs are significantly enhanced compared to the individual counterparts [73]. The design approaches to integrate hydrogels with electrospun nanofibers will be summarized in this part. Simultaneously, their roles and synergy functions in various tissue regeneration will also be emphasized.

Electrospun nanofiber/hydrogel composite 3D scaffolds can be fabricated by embedding the postassembled electrospun nanofibers in hydrogel precursor solution or assembled after combining electrospun nanofibrous membranes and hydrogels. For example, electrospun PLA nanofiber sheets were coated with poly(lactide-co-ethylene oxide fumarate) (PLEOF) hydrogels. They were assembled into composite scaffolds through the LbL assembly and crosslinking. In this approach, the precursor solution acted as a "glue" to hold the fiber layers together [74]. The formed laminated or rolled nanofiber/hydrogel composite scaffolds possess significantly higher mechanical strength than the pure hydrogels [74, 75]. Besides, the embedded nanofibers were reported to improve hydrogels' mechanical and biological properties, such as the ability to act against contraction or degradation during tissue regeneration and provide the attachment signal and directional cues to cells [72]. Also, the interaction between nanofibers and hydrogels would affect the performance of final products [76].

Short nanofibers via cutting or degrading the electrospun nanofibers can be suspended in hydrogel precursor solutions before gelation [77, 78]. This integration process retains the injectability of the constructs. For instance, gelatin/PCL electrospun short fibers were mixed with gelatin solution and then crosslinked with glutaraldehyde to prepare composite scaffolds. These composite scaffolds showed more robust mechanical properties than pure hydrogels due to the strong interfacial bonding between the nanofibers and the hydrogels [79, 80]. Short electrospun nanofiber/hydrogel mixture could also be processed into bioinks suitable for 3D bioprinting to fabricate constructs with complex structure and improved mechanical properties [81].

2.2.3. Electrospun Nanofiber/Porous Matrix Composite 3D Scaffolds. Scaffolds with interconnected porous structures are attractive for tissue engineering because the porous structures provide spaces for cell migration, proliferation, nutrition/waste transportation, and neo tissue regeneration [12, 25]. It was reported that fibrous structures in porous scaffolds could further accelerate cell adhesion and migration due to their similarities with native ECM [82]. Therefore, many recent studies have introduced nanofibers into porous scaffolds. The methods, such as freeze-drying, electrospray, and 3D printing, for porous scaffold fabrication, can be integrated with electrospinning to make nanofiber-based 3D scaffolds. Therefore, combining electrospinning with other 3D porous structure forming technologies is also an effective approach to fabricate 3D ENF-S.

3D ENF-S with porous structures can be easily formed by freeze-drying. For example, regenerated cellulose (RC) and PLA nanofibrous composite scaffolds were fabricated by freeze-drying and followed by crosslinking with citric acid. These RC/PLA composite scaffolds with dual pore structures exhibited superabsorbent, good stability, and mechanical property [83]. Similarly, bilayer collagen-nanofiber composite porous scaffolds were prepared by compression and freeze-drying. There is no apparent gap between the porous and nanofiber layer, showing a good integration [84]. Poly(ethylene oxide) (PEO) microparticles and PLA nanofibers produced by electrospray and electrospinning, respectively, are deposited on the collector simultaneously to form the nanofiber/microparticle composite scaffolds. The thickness can significantly increase after introducing microparticles, which can release electric charge and build the construct during electrospinning [85, 86].

3D printing is a frequently used method to fabricate porous scaffolds, especially for scaffolds with complex structures. Combined with 3D printing, the dimension of the structure and the scale of electrospun nanofibers pore will increase from nanoscale to the macroscale resembling the ECM's topographic characteristic [87]. Yu et al. fabricated a composite 3D scaffold by printing PCL grid scaffold with the macroscale pores as the fundus and infusing PCL/gelatin short nanofibers into the printed scaffolds [88]. 3D-printed PCL grid was reported to have a smooth surface, while electrospinning PCL nanofibers connected by simply gluing improved the chondrocyte viability, adhesion, and infiltration [89]. The short nanofibers were also used for porous and fibrous scaffold fabrication. For example, a semifluid mixture of HA/PEO solution and gelatin/poly(lactide-co-glycolide) (PLGA) electrospun short nanofibers working as a novel ink was extruded to fabricate 3D-printed fiber-based scaffolds. By tuning parameters (the inner diameters of the nozzle, the moving speed of the plotting head, and the dosing speed) and adjusting the distance and diameters of the strands, the composite scaffolds with different shapes and pore sizes can be achieved [90].

Moreover, direct polymer melt deposition was also combined with electrospinning to fabricate 3D scaffolds with fibrous structures. Park et al. deposited the electrospun polycaprolactone/collagen nanofibers between the polycaprolactone microfiber layers prepared by direct polymer melt deposition to form 3D ECM-like tissue engineering scaffolds. This nano/microfiber composite 3D scaffold provided the

optimal environment for chondrocyte adhesion and proliferation due to the improvement of biocompatibility and inner surface's enlargement [91]. Other approaches, such as selected laser sintering [92] and stereolithography [93], were also used to fabricate tissue engineering scaffolds with 3D porous and fibrous structures, which can accelerate cell infiltration and tissue regeneration [94].

3. Advanced Functional Properties of 3D ENF-S

3D ENF-S with cell-permeable structure and controllable thickness is more practical than 2D electrospun membrane in most tissue regeneration. As a critical factor in tissue engineering, the tissue engineering scaffold should substitute for the native ECM while mimicking its structure and mechanical properties. Compared with other kinds of scaffolds, such as porous or hydrogel scaffolds, these 3D ENF-S have also exhibited many other advanced functional properties, such as 3D fibrous architecture and tunable mechanical properties, making them a focus of recent studies.

3.1. 3D Fibrous Architecture. It is widely accepted that the creation of biomimetic niches closely resembling the native biological environment is critical to guide cell growth and differentiation and promote target tissue regeneration. Although there are already many studies involving bioinspired ECM design, related studies are still developing rapidly [95]. 3D ENF-S has drawn extensive attention due to its nanofibrous structures, which can resemble the various tissues of native ECM's fibrillar features [96]. This fibrous structure has been demonstrated to play a vital role in regulating how cells interact with the native ECM, influencing cell adhesion, spreading, proliferation, and differentiation. Therefore, 3D ENF-S with these biomimetic fibrous structures have been developed for various kinds of tissue regeneration.

3.2. Mechanical Properties. Scaffolds' mechanical properties are essential for their successful performance in tissue regeneration. Considering the *in vivo* implantation and clinical application, mechanical strength and suture retention strength are vital for tissue engineering scaffolds. Among the different types of scaffolds, 3D ENF-S with excellent and adjustable mechanical properties have great potential for clinical transplantation.

3.2.1. Mechanical Strength. Scaffolds must be sufficiently strong to match the mechanical properties of the native tissue at the implantation site to support cell adhesion, cell spreading, and ECM synthesis. Additionally, when applied *in vivo*, the scaffold must withstand external forces acting upon it to maintain its integrity and support its function without collapsing. Recently, many studies reported that 3D electrospun nanofiber-based scaffolds with outstanding mechanical properties have been successfully applied in tissue engineering, especially in force loading tissues, such as cartilage, tendon, and ligament [97, 98]. Biomimicing the collagen nanofibers in native tissue, aligned electrospun nanofibers have exhibited extraordinary mechanical strength, enhancing tissue engineering scaffolds' mechanical properties [60]. In composite scaffolds, electrospun nanofibers can improve mechanical strength through strain transfer between the matrix and the nanofiber reinforcement.

3.2.2. Suture Retention Strength. Suture is a common method to fix implants to surrounding tissues [99]. The limited suture ability of scaffolds may hinder the in situ implantation and then impede the *in vivo* experiments and clinical transplantation, especially for the tissues or organs that require high and dynamic loads, such as vascular, tendon, and ligament [100]. However, few studies on engineered scaffolds measure suture retention strength, despite its established importance for clinical implementation. 3D ENF-S presents suture ability and enough suture retention strength for *in vivo* implantation. For example, Vaquette et al. braided electrospun PCL mesh with cell seeding to develop a tissue-engineered ligament construct that can be sutured with the surrounding tissue [101].

3.3. Structural and Mechanical Anisotropy. Anisotropy, which refers to the directional dependence of physical properties, is one fundamental property of some tissues, such as cartilage, muscle, tendon, and ligament [27, 102, 103]. Anisotropy gives ECM the ability to maximize its function along the direction of use. For instance, these unique structures can impose effective force transmission and contractility for the regeneration of functional muscle fibers [104–106]. Anisotropic scaffolds with structural and mechanical anisotropy are highly needed to mimic the target tissue properties and provide a specific microenvironment for cell differentiation. Many 3D ENF-S with required anisotropy properties have been prepared by controlling electrospun nanofibers' alignment and arrangement [107, 108].

3.4. Degradability. One of the requirements of tissue engineering scaffolds is biodegradation. Degradation itself is a regulatory factor that controls cell behavior and differentiation [2]. Biomaterials can undergo degradation through ester hydrolysis, enzymatic hydrolysis, or photolytic cleavage of the polymer chains *in vitro* and *in vivo*. Based on these mechanisms, scaffolds with good biodegradability and ideal degradation rate can be designed as temporary supports and gradually degraded and replaced by regenerated tissue. Generally, natural polymers, such as gelatin and collagen, have excellent biocompatibilities but a rapid degradation rate. Most synthetic polymers lead to mechanically stable electrospun nanofibers. Electrospun nanofiber composite scaffolds with tailored degradation rates can be designed for tissue engineering applications [52, 74].

Based on the functional properties discussed above, it is found that 3D ENF-S have shown substantial advantages in architecture and mechanical properties compared with other types of scaffolds, thus shortening the distance for clinical applications. However, most studies have performed mechanical tests before implantation. In a dynamic microenvironment *in vivo*, scaffolds will exhibit significantly different performance, such as rapid degradation. Therefore, changes in the mechanical properties of 3D ENF-S under *in vivo* environment are particularly worthy of attention, especially for heavy-duty tissues, such as muscle, tendon, and ligament.

4. Tissue Regeneration Application

4.1. Cartilage and Bone. Osteoarthritis commonly known as the cartilage defect is a disease induced by traumatic injury or degenerative joint diseases. With an aging population and the growing problem of obesity, the number of osteoarthritis cases is estimated to multiply in the future [109]. The popular treatments for articular cartilage repair include microfracture, autologous chondrocyte transplantation, and osteochondral allograft transplantation [110]. Although these techniques have successfully relieved pain and improved joint function, their disadvantages restricted their long-term clinical application [111]. Cartilage tissue engineering as a promising strategy has attracted considerable efforts in the past several decades [112]. Recently, electrospun nanofibers have been used for cartilage tissue engineering due to their nanofibrous network structure [113, 114]. Chen et al. prepared gelatin/PLA nanofiber-based 3D porous scaffold by using nanofiber membrane suspended solution through freeze-drying and heating processes to fabricate a 3D nanofibrous scaffold and overcome the limitations of commonly produced electrospun nanofiber 2D membrane. This type of scaffold could be crosslinked with hyaluronic acid using 1-ethyl-3-(3-dimethyl aminopropyl) carbodiimide (EDC)/N-hydroxysuccinimide (NHS) to promote the function for cartilage regeneration further [115]. The composite scaffold promoted cartilage regeneration, indicated by positive collagen type II and aggrecan immunohistochemical staining results after implantation *in vivo* for 12 weeks (Figures 3(a)–3(c)). Electrospun nanofiber/porous matrix scaffolds also exhibited good performance in cartilage tissue regeneration [116, 117]. For instance, the collagen-poly(vinyl alcohol) nanofibers were electrospun on the surface of a freeze-dried porous collagen sponge to fabricate a composite scaffold, which was designed to replicate the superficial and transitional zones of articular cartilage [118].

Cartilage ECM consists of fibrous collagen II and proteoglycan-based ground substance. Therefore, it was believed that fiber/hydrogel composite 3D scaffold could mimic both the structure and function of native cartilage ECM [119]. For example, a cooled mandrel collector at -78°C was used to prepare electrospun PCL nanofibers to mimic the fibrillar component of cartilage. With the ice crystallization process, the deposited PCL fibers exhibited loose fibrous structure and increased thickness. After sublimation, the macropores are created to allow cell infiltration. The O_2 plasma treatment was used to make the fibers with a hydrophilic surface, ensuring good contact with cell-laden alginate hydrogel. The cryoelectrospun PCL fiber scaffolds with a thicker thickness (1.5 mm) could enhance alginate hydrogels' mechanical property and stability. After three weeks of *in vitro* culture and three weeks *in vivo* implantation, such a hydrogel/fiber composite scaffold still existed and showed many chondrogenic ECM deposition while the pure hydrogel scaffold was degraded (Figures 3(d) and 3(e)) [52].

Bioactive hydrogels' insufficient mechanical property is a severe challenge in cartilage tissue engineering [97]. Nanofiber/hydrogel composite scaffolds with an improved mechanical property and a chondrocyte preferred 3D microenvironment have become a promising candidate [98, 120]. Sharifi et al. fabricated a composite scaffold using fragmented electrospun PLA fibers and alginate-graft-hyaluronate hydrogel. The compressive modulus of such a composite scaffold increased by 81% compared with hydrogel without mixing with nanofibers. The chondrocytes cultured in this composite scaffold showed a round cell shape and produced a cartilage-specific matrix [121]. The mechanical property and the stability of 3D-printed alginate hydrogels were improved after reinforcement with PLA submicrofibers [81].

The interaction between fiber and hydrogel matrix is essential for chondrogenesis in electrospun nanofiber/hydrogel composite scaffolds. For example, silk fiber (SF) enhanced chondrogenesis when embedded in silk hydrogel rather than standard agarose hydrogel. The newly synthesized proteoglycan was found to be around the silk microfibers in SF-silk hydrogel. In contrast, poor stress transfer and ECM deposition occurred in SF-agarose hydrogel without fiber/hydrogel binding [122]. The nanofiber component can also accelerate the proliferation and secretion of chondrogenic ECM by tuning the constructs' structural morphology and chemical composition [123].

Bone tissue engineering also requires a scaffold with extremely high mechanical strength. The combination of electrospun nanofibers is a practical approach to increase mechanical strength and provides an option for using hydrogel as a scaffold for bone tissue engineering. Shojai and coworkers prepared a trilayered scaffold that consisted of polyhydroxybutyrate (PHB), hydroxyapatite (HA), and gelatin methacryloyl (GelMA) hydrogel for bone tissue engineering (Figures 4(a) and 4(b)). In their work, electrospun PHB mats were punched and soaked in GelMA precursor solution with suspended HA nanoparticles for 20 min, which was then sandwiched between GelMA with HA nanoparticle layers. The 3D nanofiber/hydrogel composite scaffold was formed by UV crosslinking. Compared with electrospun fiber or hydrogel alone, this trilayered scaffold exhibited the required mechanical strength and superior microenvironment. Also, the matrix mineralization and alkaline phosphatase (ALP) activity were improved in this hybrid scaffold due to the presence of HA nanoparticles (Figure 4(c)) [124]. Lamination of PLA fiber/PLEOF hydrogel composite scaffold was fabricated by LbL assembly and further crosslinking of hydrogel component. The fiber mesh gave this composite scaffold strong mechanical strength, and the hydrogel components connecting these different layers accelerated the diffusion of oxygen and nutrients.

Furthermore, with hydrogel degradation, there will be more space for cell proliferation and ECM deposition. After combining HA nanocrystal and Arg-Gly-Asp (RGD) peptide in the hydrogel phase, this laminated composite scaffold promoted the osteogenic differentiation, which was confirmed by detecting higher ALP activity and expressing osteogenic markers (osteopontin and osteocalcin) [74]. Similarly, Naghieh et al. produced hierarchical scaffolds stacked with PLA microfiber layers prepared by fused deposition modeling and nanocomposite gelatin-forsterite fibrous layers fabricated through electrospinning. The elastic modulus of this composite scaffold was increased by more than 1.5-fold
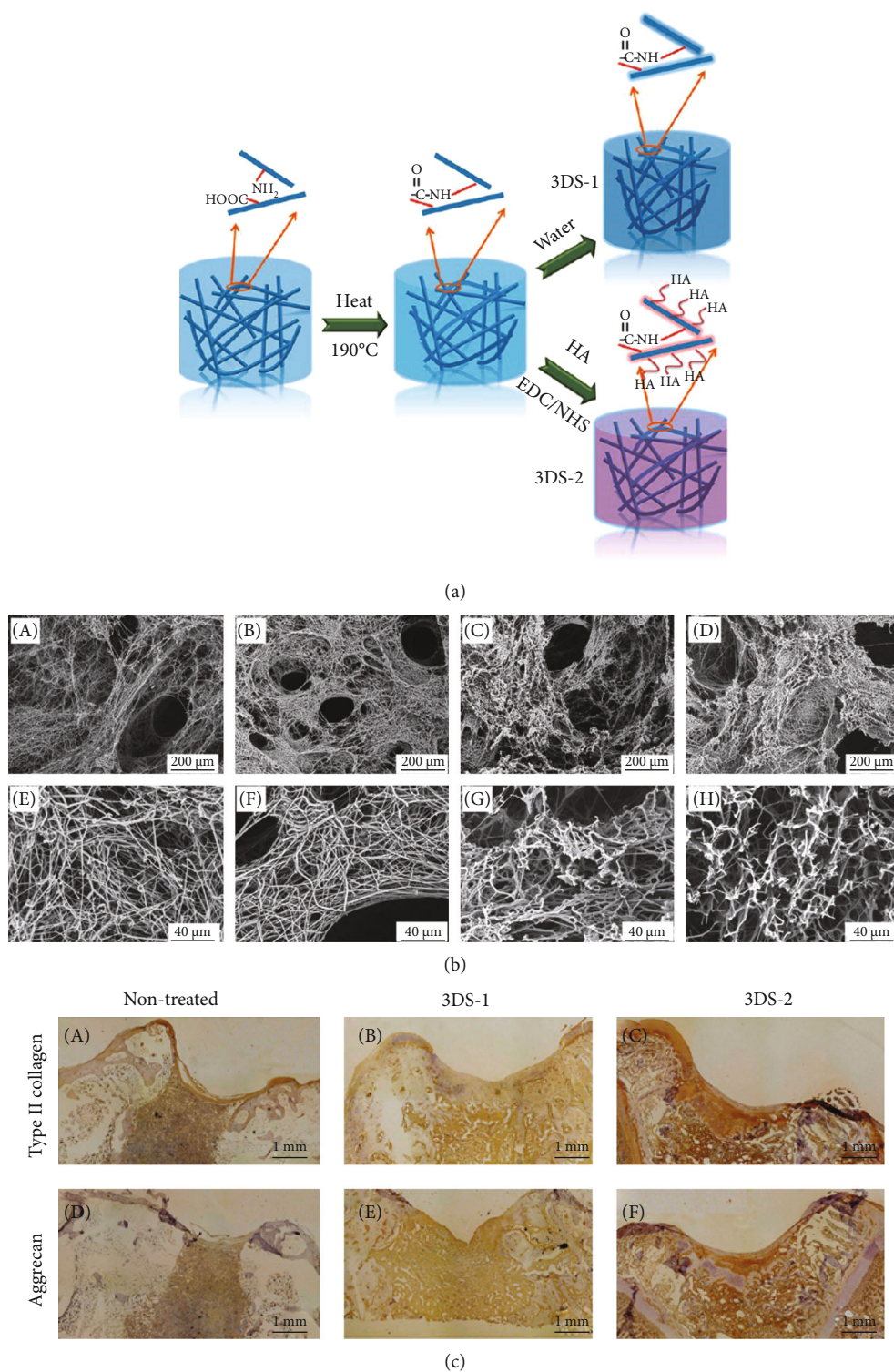
(a)
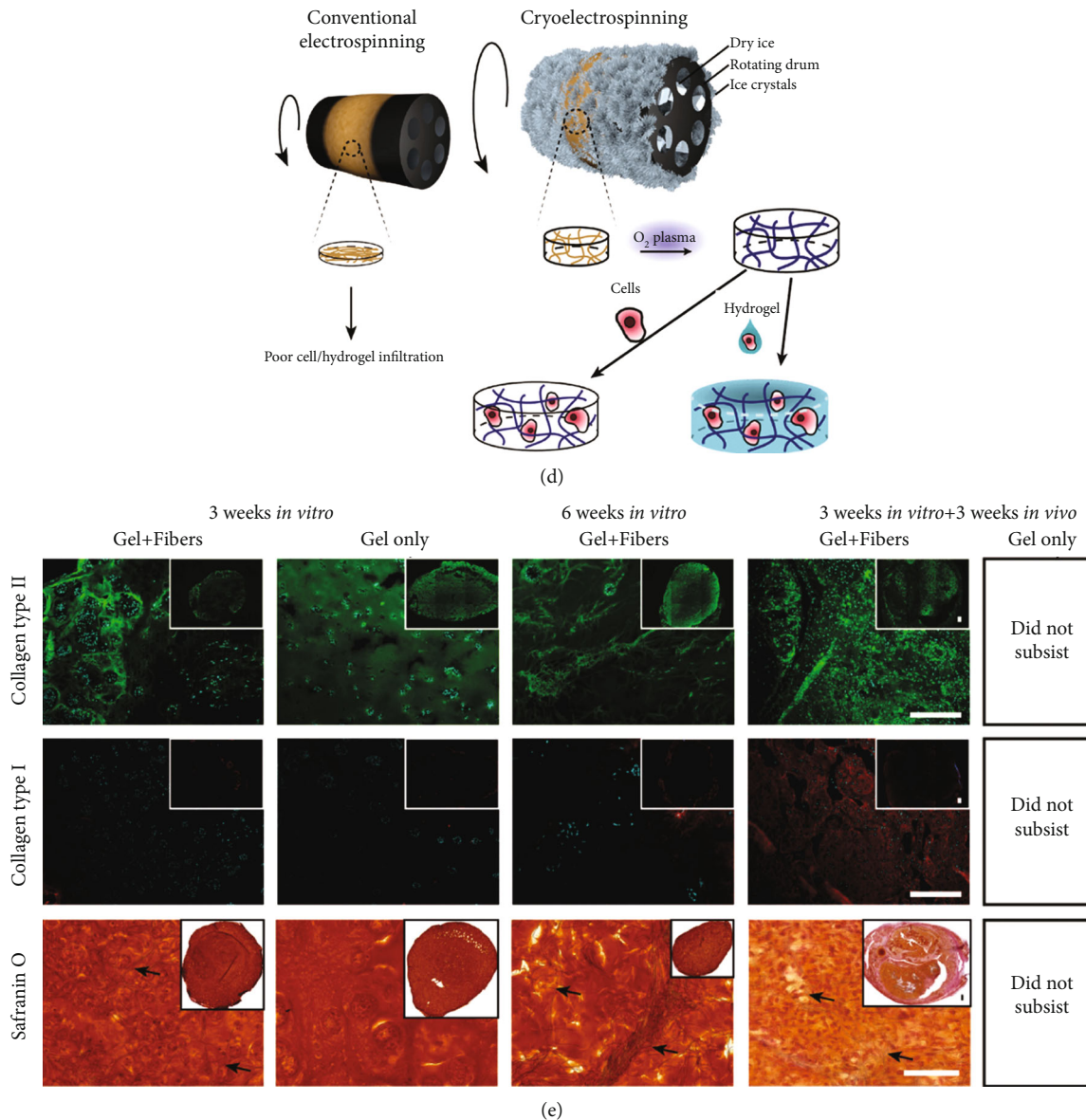

(b)

(c)

Figure 3: Continued.

(d)

(e)

Figure 3: 3D electrospun nanofiber-based scaffolds for cartilage tissue regeneration. (a) The schematic illustration for fabrication and crosslinking of electrospun nanofiber porous 3D scaffold (3DS-1) and crosslinked with hyaluronic acid scaffold (3DS-2). (b) The porous and fibrous structure of uncrosslinked (A, E), heat-treated (B, F), crosslinked 3DS-1 group (C, G), and 3DS-2 group (D, H). (c) Collagen type II and aggrecan immunohistochemical staining results of nontreated, 3DS-1, and 3DS-2 scaffolds after *in vivo* implantation for 12 weeks. Reproduced with permission from [115]. Copyright © 2021, American Chemical Society. (d) Conventional electrospinning formed dense nanofiber membrane. Cryoelectrospinning (on a mandrel collector at -78°C) induced 3D porous PCL scaffold due to the ice crystal formation. (e) Hydrogel/nanofiber composite constructs exhibited good chondrogenic ECM deposition and higher stability than pure hydrogel scaffold *in vitro* cell culture and *in vivo* implantation. Reproduced with permission from [52]. Copyright © 2021, WILEY-VCH Verlag GmbH & Co. KGaA, Weinheim.

compared with the PLA scaffolds without the combination of electrospun fibers. After soaking in a simulated body fluid (SBF) solution for 28 days, HA crystals were found on the struts of the composite scaffold, indicating a bioactive candidate for bone tissue regeneration [125].

3D ENF-S are also promising for osteochondral tissue regeneration. In the natural osteochondral region, the ingredient and structure vary from bone to cartilage, in which the complex environment cannot be satisfied by a homogeneous scaffold. Previously, collagen porous scaffolds and electro-

spun nanofibers have been proven to promote cartilage and bone regeneration, respectively [11, 25]. Therefore, a bilayer collagen/PLLA nanofiber composite scaffold was developed for osteochondral tissue repair (Figures 5(a) and 5(b)). The top layer was a freeze-dried collagen porous scaffold, and the bottom layer consisted of nanofiber strips with 100-300 μm pores (Figure 5(c)) [84]. Mesenchymal stem cells (MSCs) cultured on this collagen/nanofiber composite scaffold showed stronger osteogenic differentiation, which was evidenced by the higher expression of osteocalcin (OCN) and
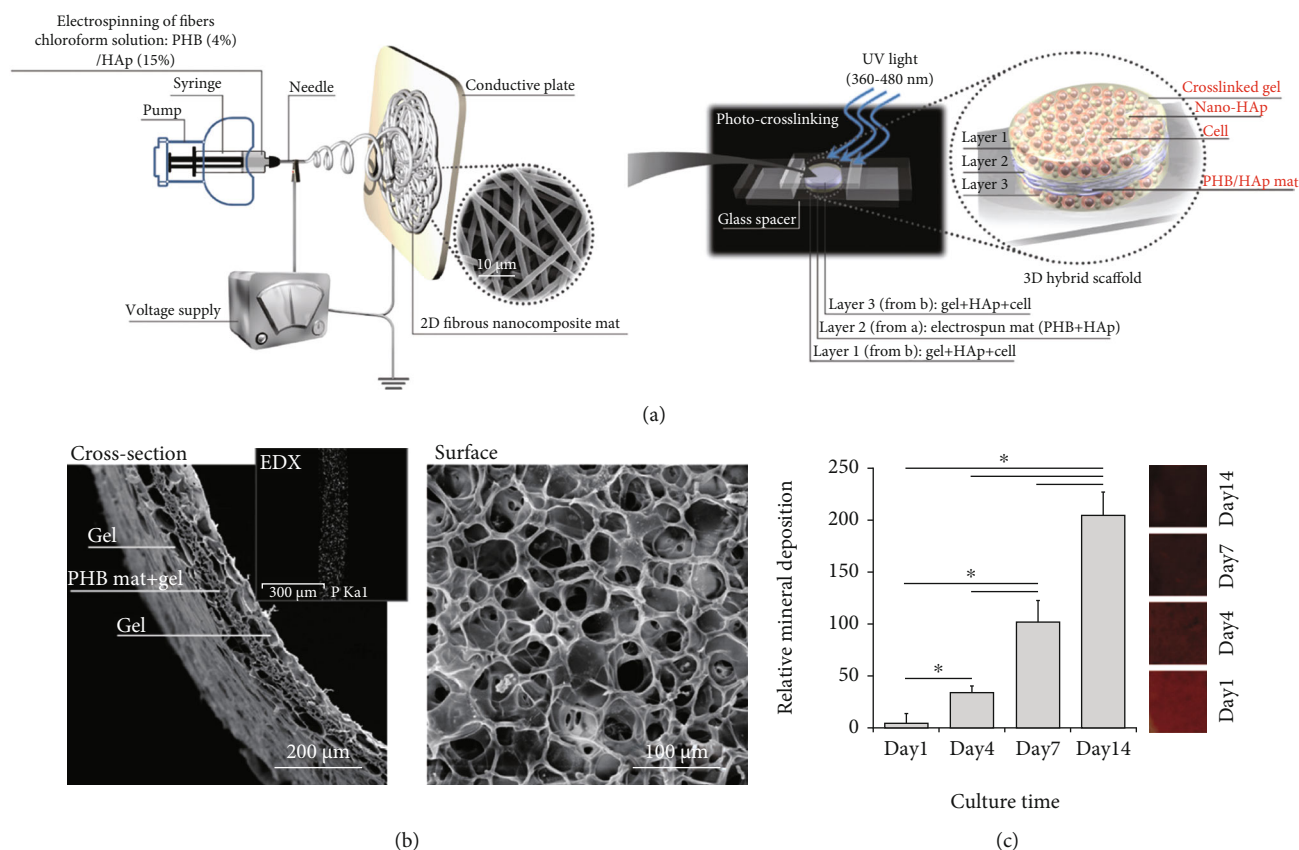
(a)

(b)

(c)

FIGURE 4: Electrospun nanofiber/hydrogel 3D scaffolds for bone tissue regeneration. (a) Schematic diagram of the experimental steps and the structure of 3D cell-laden hybrid scaffolds. (b) SEM micrographs of surface and cross-section of the freeze-dried hybrid scaffold. (c) Gross appearance of Alizarin Red staining and mineral quantification of hybrid scaffolds after incubation in SBF at 37°C for specific periods (mean ± SD of six replicates). Reproduced with permission from [124]. Copyright © 2016, Elsevier B.V.

runt-related transcription factor 2 (runx2) osteogenic genes. In the rabbit osteochondral defect model, rapid subchondral bone emergence and better cartilage formation were observed in collagen/nanofiber composite scaffold. Further, the subchondral bone with a bridge-like structure was also observed using μ-CT, which was expected to contribute to the top cartilage regeneration (Figure 5(d)) [84].

4.2. Tendon and Ligament. Tendons and ligaments are tough connective tissues that connect bone to muscle and bone to bone, respectively. They have strong tensile strength due to their dense fibrous microstructure. Therefore, fiber-based composite scaffolds have drawn much attention for tendon and ligament tissue regeneration [126]. For example, aligned electrospun nano/microfiber scaffolds were developed by mimicking the aligned collagen fibrils of native tendon and ligament [127, 128]. Braided or stacked electrospun PLLA and PCL fiber were prepared to meet the clinical requirements of tensile and suture strength [37]. It was indicated that braided scaffolds with substantial mechanical properties could promote tenogenic markers' expression. Stacked scaffolds have better cell infiltration than braided ones, resulting in a higher total cell number and ECM content. Similarly, Vaquette et al. braided electrospun PCL mesh with cell-laden to develop a tissue-engineered ligament construct

[101]. This PCL mesh/cell sheet composite construct had a stress/displacement J-curve, similar to that of the native ligament. *In vivo* experiments showed that ECM was distributed homogenously within the scaffolds after incorporating the cell sheet.

Electrospun nanofibers and hydrogel composite scaffolds were also selected to achieve the cell-laden and excellent mechanical properties. PCL-polyamide electrospun membranes possessed excellent mechanical properties for tendon replacement but lacked biocompatibility and 3D structure. Therefore, GelMA/alginate thin hydrogel layers were coated on the electrospun nanofibers, providing an ECM-like microenvironment for encapsulated MSCs. Under mechanical stimulation generated by a custom-built bioreactor, the cell viability, proliferation, alignment, and tenogenic differentiation of MSCs were promoted (Figure 6(a)) [129]. Kim et al. also presented a fiber/hydrogel composite scaffold for tendon tissue engineering. The aligned fibers produced by hybrid electrospinning of PCL and silk fibroin provided topological cues for cell alignment and differentiation. Alginate hydrogel with MSCs laden was injected into the fibrous scaffolds after rolling the fibrous layers around a needle to improve cell infiltration and provide a 3D microenvironment. With basic fibroblast growth factor (bFGF) supplements, MSCs exhibited a ligament phenotype, which was
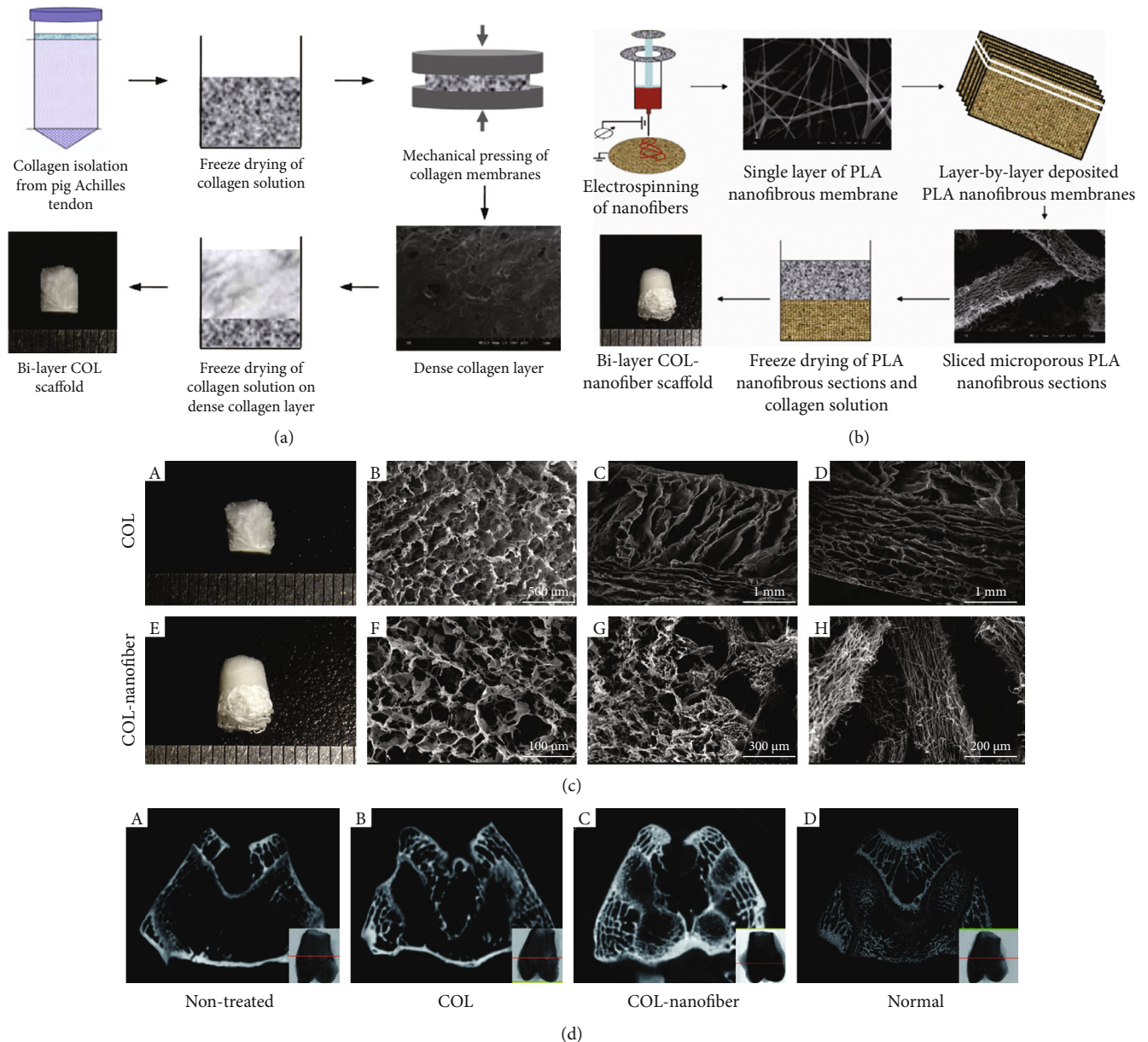
(a)

(b)

(c)

(d)

FIGURE 5: Electrospun PLA nanofiber/freeze-dried collagen bilayer composite scaffold for osteochondral tissue engineering. (a) The fabrication process of freeze-dried collagen bilayer scaffolds and (b) nanofiber/freeze-dried collagen bilayer composite scaffolds, and (c) their microstructures. (d) Architecture evaluation of the repaired tissues after 12 weeks of implantation by μ-CT images ((A) nontreated group, (B) freeze-dried collagen bilayer scaffold group, (C) nanofiber/freeze-dried collagen bilayer composite scaffold group, and (D) normal joints). There were abundant subchondral bones formed in the nanofiber-collagen porous scaffold group. Adapted with permission from [84]. Copyright © 2013, Acta Materialia Inc. Published by Elsevier Ltd.

approved by the secretion and deposition of related ECM proteins in the composite scaffold (Figures 6(b)–6(d)) [130].

Tendons consist of aligned collagen fibers and surrounding glycosaminoglycan sheath, mainly dermatan sulfate and chondroitin sulfate. Therefore, nanofiber/hydrogel composite scaffolds have also been designed for tendon regeneration. For example, the aligned PLLA nanofibers were manufactured by electrospinning. A chitosan/collagen hydrogel was layered on the nanofiber, rolled into tubes, and then coated with alginate hydrogel to prepare a composite construct. As expected, the mechanical strength of this composite scaffold

was significantly enhanced, which was sufficient for the flexor tendon. The aligned nanofibers could guide cell attachment and growth. The hydrogel phase promoted cell infiltration, and the alginate component prevented peritendinous adhesion. The excellent mechanical property and biocompatibility proved that electrospun nanofiber-based composite scaffolds are good candidates for tendon regeneration [75]. The bFGF growth factor and dynamic stimulation were further applied to the braided PCL/collagen fibrous scaffold for tendon regeneration. This composite scaffold with mechanical and biochemical stimulation showed enhanced proliferation,
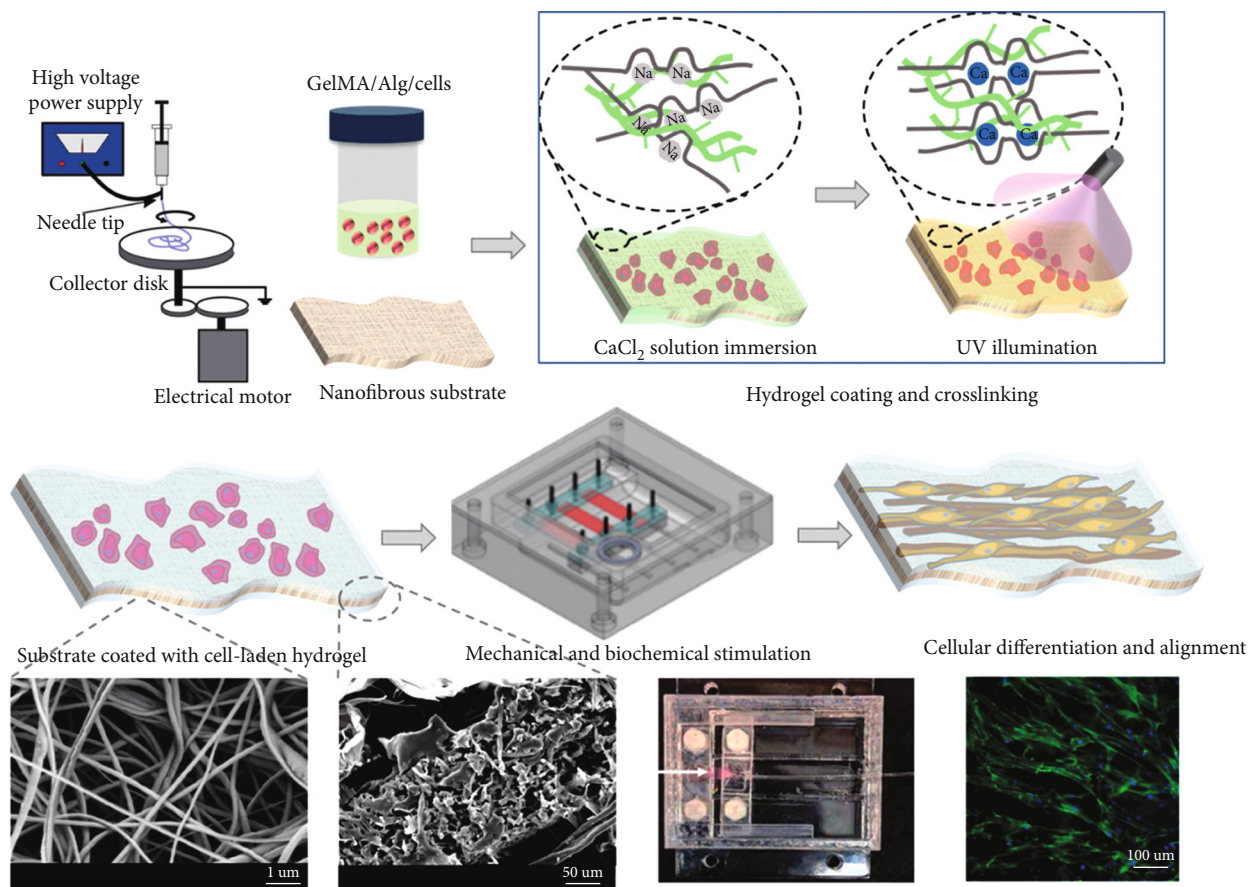
(a)
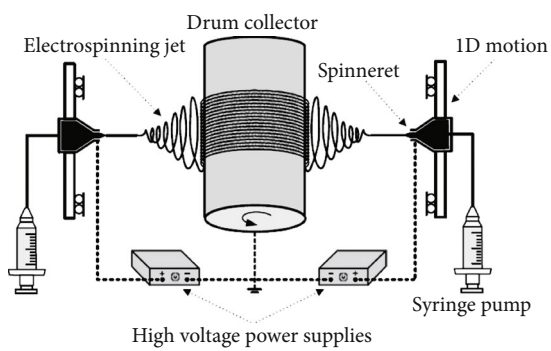
(b)
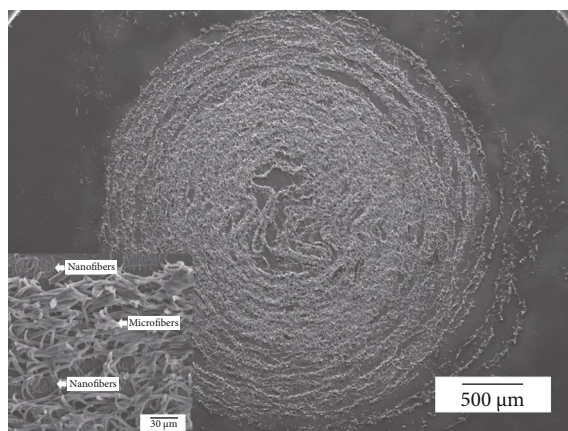
(c)

FIGURE 6: Continued.
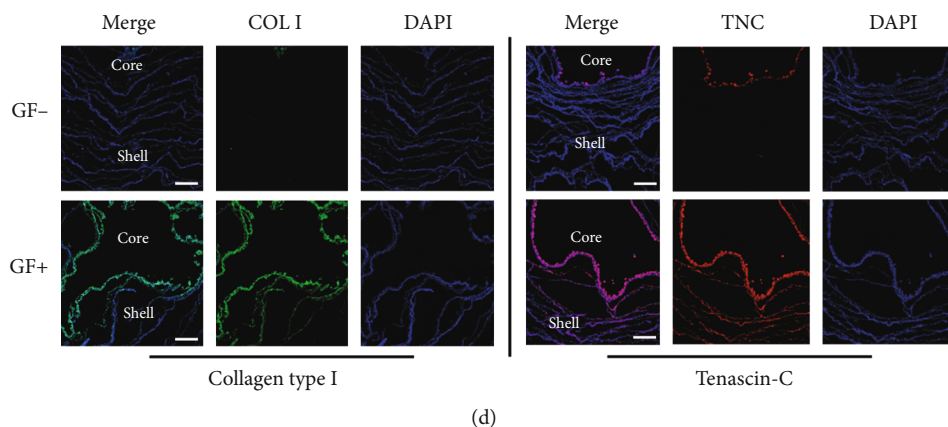
(d)

Figure 6: 3D electrospun nanofiber-based scaffolds for tendon and ligament regeneration. (a) Schematic illustration of fabrication and stimulation of composite scaffold consisted of electrospun nanofibers and cell-laden hydrogel coating crosslinked by Ca^{2+} and UV light. Reproduced with permission from [129]. Copyright © 2019, American Chemical Society. (b) Electrospinning equipment for fabrication of silk fibroin-PCL nano/microfiber mat. (c) SEM images of cell-laden fiber/hydrogel 3D composite construct (cross-section). (d) Immunofluorescent staining of collagen type I and tenascin-C in the hybrid constructs. Scale bar = 200 μm. Copyright [130].

tenogenic marker expression, and aligned collagen morphology after 12 weeks of *in vivo* implantation, further proving the promising application of electrospun nanofiber-based 3D composite scaffold in tendon tissue reconstruction [131].

4.3. Skeletal Muscle. Skeletal muscles, comprising between 40 and 45% of an adult human body mass, are mainly responsible for generating force and controlling body locomotion [103]. However, muscle tissues are easily injured. Unfortunately, after severe injuries, the endogenic regeneration of itself is helpless [132]. According to reports, skeletal muscle tissue engineering, designing constructs to meet tissue regeneration's functional and aesthetic requirements in muscle defects, has good prospects [104]. Cellular alignment and elongated myotube are crucial in muscle tissue engineering because skeletal muscle is composed of aligned myofibers and connective tissues [103]. Moreover, scaffolds used to support skeletal muscle regeneration should accommodate and promote the formation of densely packed, highly aligned myofibers, which exert effective force transmission and contractility for the revival of functional muscle fibers [105].

Recent studies have shown that anisotropic materials may be preferred for developing muscle tissue engineering constructs as their morphology and function are more similar to native tissues [106, 134]. 3D scaffolds with anisotropic properties are needed to provide a 3D microenvironment for implanted cells [134]. Combining hydrogels with electrospun nanofibers offers an excellent solution to this problem. For example, fibers with fibrous 3D bundle structures were fabricated with an electrohydrodynamic jet technique followed by wet electrospinning. After a uniaxial stretch, the fibers become aligned direction from a random structure. Cell encapsulated collagen/PEO bioink was printed on this 3D bundle. The fibers provided the cell-laden hydrogel with typical topographic stimulus, and the collagen-coated surface exhibited biochemical cues. They synergically promoted myotube formation and myoblast differentiation [135]. Nanofiber yarn and hydrogel were assembled to prepare a composite scaffold with a core-shell structure (Figure 7(a))

[133]. The fiber yarn core comprised of PCL, polyaniline, and silk fibroin was fabricated through dry-wet electrospinning, which had the function of inducing 3D cellular alignment and elongation. The photocrosslinked PEG hydrogel was used as a shell to embed the cell-seeded yarns. This hydrogel shell showed the protection for cell proliferation and the 3D environment for cell arrangement. Moreover, the hydrogel with a similar stiffness of muscle tissue could prevent the random winding and twining of yarns during operation, thereby reducing the possibility of cell detachment. Finally, C2C12 myoblast cultured within this yarn/hydrogel core-shell scaffolds *in vitro* showed enhanced cellular alignment and myogenic differentiation, further proving the advantages and promising prospects of nanofiber/hydrogel composite scaffolds in the application of skeletal muscle regeneration (Figures 7(b) and 7(c)).

4.4. Nerve. Nerve injuries caused by diseases, trauma, or tumor operations can lead to loss of movement dysfunctions and extreme pains. Spontaneous regeneration produces unsatisfied recovery results, and the availability of donor's nerves limits the autologous nerve graft. Therefore, different kinds of neural tissue engineering scaffolds have become promising for nerve repair [136]. Among them, electrospun nanofibers with various mechanical and biochemical stimuli are often used. The physical properties of electrospun fibers, such as alignments [137], stiffness, and topography [138], and the biochemical properties, such as RGD and growth factor [139, 140], have been systematically studied. Also, conductive polymers (e.g., polyaniline [141]) and nanoparticles (e.g., graphene [142]) have been fabricated or added to the nanofibers to promote neural tissue regeneration [143, 144].

3D environment is critical for cell activities and cell-cell interactions, which affect cell differentiation and neo tissue regeneration [145–147]. It was reported that aligned nanofibers could provide physical cues for guiding neural differentiation in the 2D surface. Based on this principle, aligned nanofiber/hydrogel 3D composited scaffolds were designed, which exhibited practical nerve tissue engineering functions.

(a)

(b)

(c)
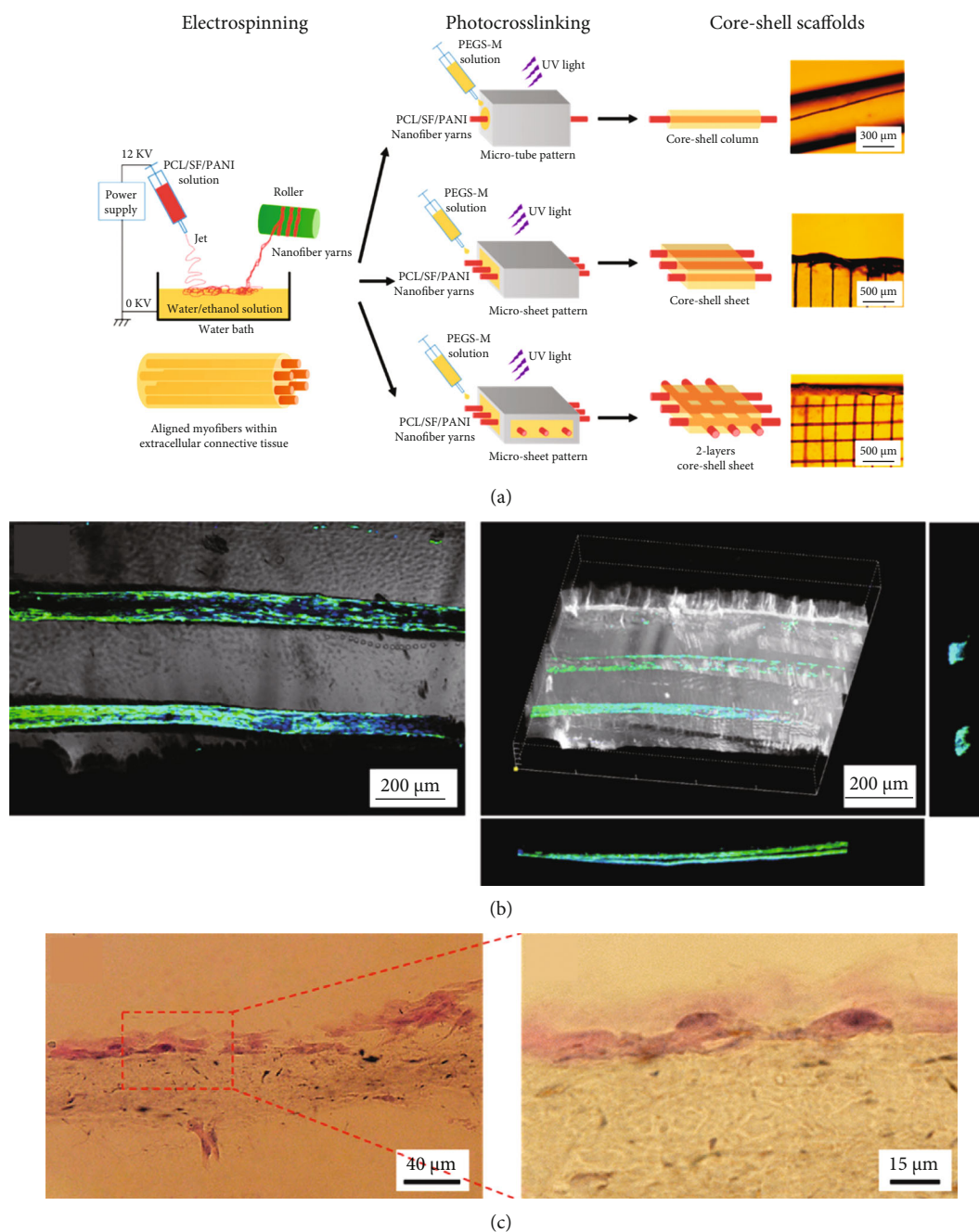
FIGURE 7: Nanofiber yarn/hydrogel composite 3D scaffolds for myoblast alignment and differentiation. (a) Preparation illustration of yarn/hydrogel composite 3D scaffolds with native skeletal muscle mimicking core-shell structure (aligned nanofiber yarns by electrospinning and PEG-based hydrogel shell via photocrosslinking). (b) Highly organized C2C12 myotubes within the 3D hydrogel. (c) H&E staining images of the construct with C2C12 cell encapsulation after cultivation for seven days. Reproduced with permission from [133]. Copyright © 2015, American Chemical Society.

An external magnetic field could control the alignment of short fibers suspended in the hydrogel before complete gelation of the matrix, which endowed the anisotropic property of this composite matrix. Cells encapsulated in the aligned fibers/hydrogel construct stretched F-actin filaments in the direction of fibers. The experiment confirmed that the neurons encapsulated in this matrix had a spontaneous electrical activity with calcium signals propagating along with the orientation of these iron oxide-loaded PLGA short fibers

(Figures 8(a) and 8(b)) [80]. Similarly, an aligned fibrin nanofibrous hydrogel for peripheral nerve regeneration was prepared by electrospinning and self-assembly methods. This fibrous hydrogel/chitosan composite scaffold promoted the regrowth of axons *in vivo* [148]. In addition, due to the matrix stiffness which is another important biomechanical cue for cell differentiation, a fibrous and aligned fibrin hydrogel scaffold with soft elasticity was fabricated by electrospinning. This construct promoted the stem cells' neurogenic

(a)

(b)

(c)

(d)
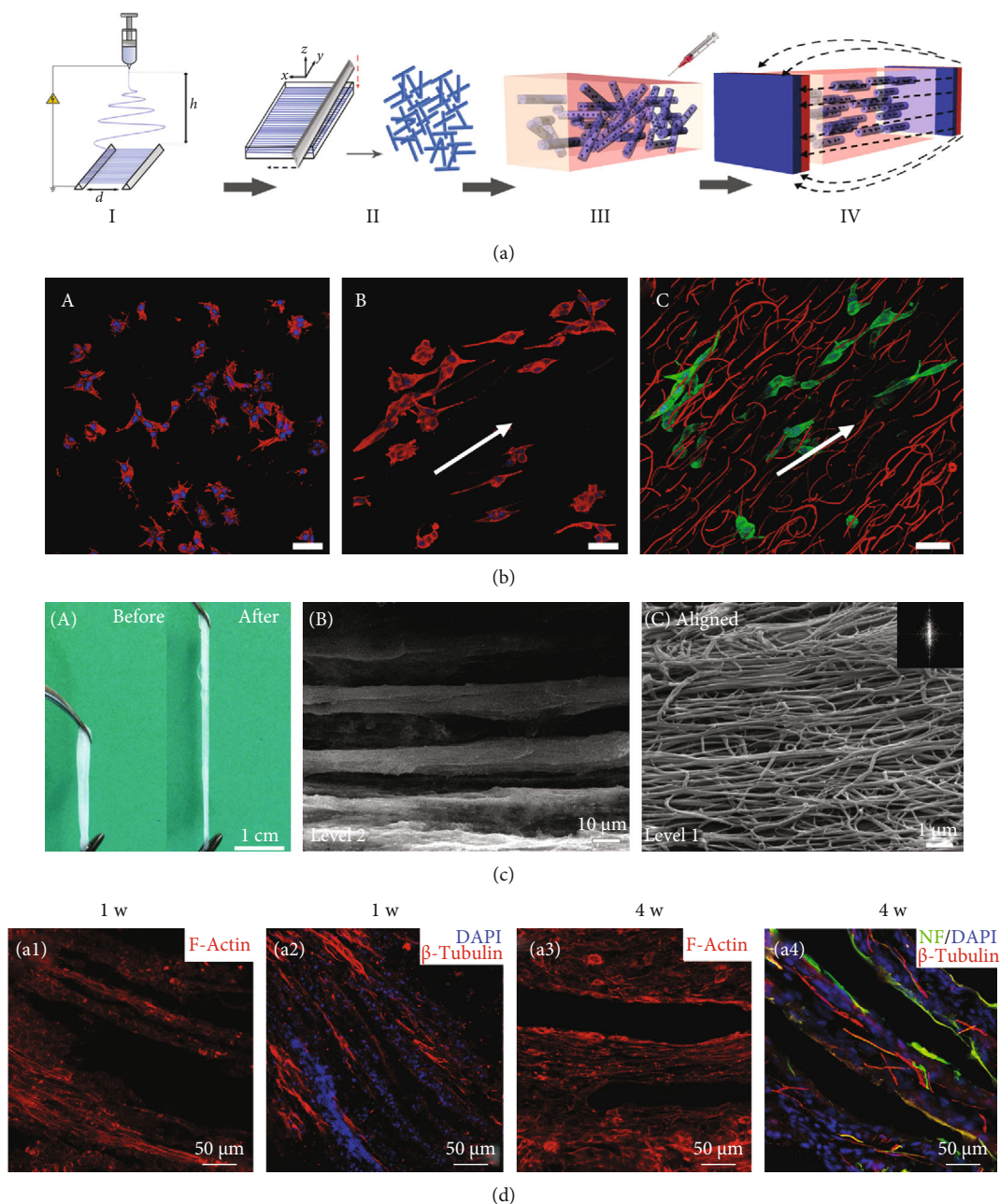
FIGURE 8: Electrospun nanofibers in 3D scaffolds and their effects on cell alignment and neural differentiation. (a) A schematic illustration of the fabrication process of Anisogel. Electrospinning of aligned fibers (step I). Short fibers forming by cryosectioning (step II). Randomly oriented short fibers mixed within the hydrogel precursor solution before gelation and applying the magnetic field (step III). Fiber orientation under low magnetic field and hydrogel crosslinking result in the Anisogel (step IV). (b) The ability of the Anisogel to direct cell growth. (A) Fibroblasts mixed within a fibrin gel without fibers, (B) fibroblasts mixed within a fibrin gel with short oriented fibers, and (C) fibroblasts elongate in the direction of the oriented fibers. Scale bars 50 μm. Reproduced with permission from [80], Copyright © 2017, WILEY-VCH Verlag GmbH & Co. KGaA, Weinheim. (c, A) Electrospun-aligned fibrillar fibrin hydrogel with good flexibility. (B, C) Hierarchically aligned microstructure at different magnifications. (d) Immunofluorescence staining images of the longitudinal tissue section from the T8–T10 spinal cord segment at 1 and 4 weeks after scaffold implantation. Reused with permission from [149]. Copyright © 2016, Royal Society of Chemistry.

differentiation and rapid neurite outgrowth *in vivo* spinal cord injury model (Figures 8(c) and 8(d)) [149].

Furthermore, it has been reported that the hydrogel matrix can provide a protective barrier to shield the transplanted cell from a toxic environment, under which most of the transplanted cells will gradually die, resulting in minor effects on tissue regeneration [150]. Biomimetic multichannel silk conduits were prepared by an electrospinning technique followed by manual manipulation to create perineurium-like structures, mimicking the architecture of the native nerve

FIGURE 9: Nanofiber yarn/hydrogel composite 3D scaffolds with alignment, conductivity, and anisotropy for cardiac tissue engineering. Schematic illustration of (a) PCL/SF/CNT nanofiber yarns prepared by wet-dry electrospinning and (b) NFYs-NET scaffolds fabricated by a weaving technique. (c) 3D composite scaffold fabricated via encapsulating two layers of NFYs-NET with orthogonal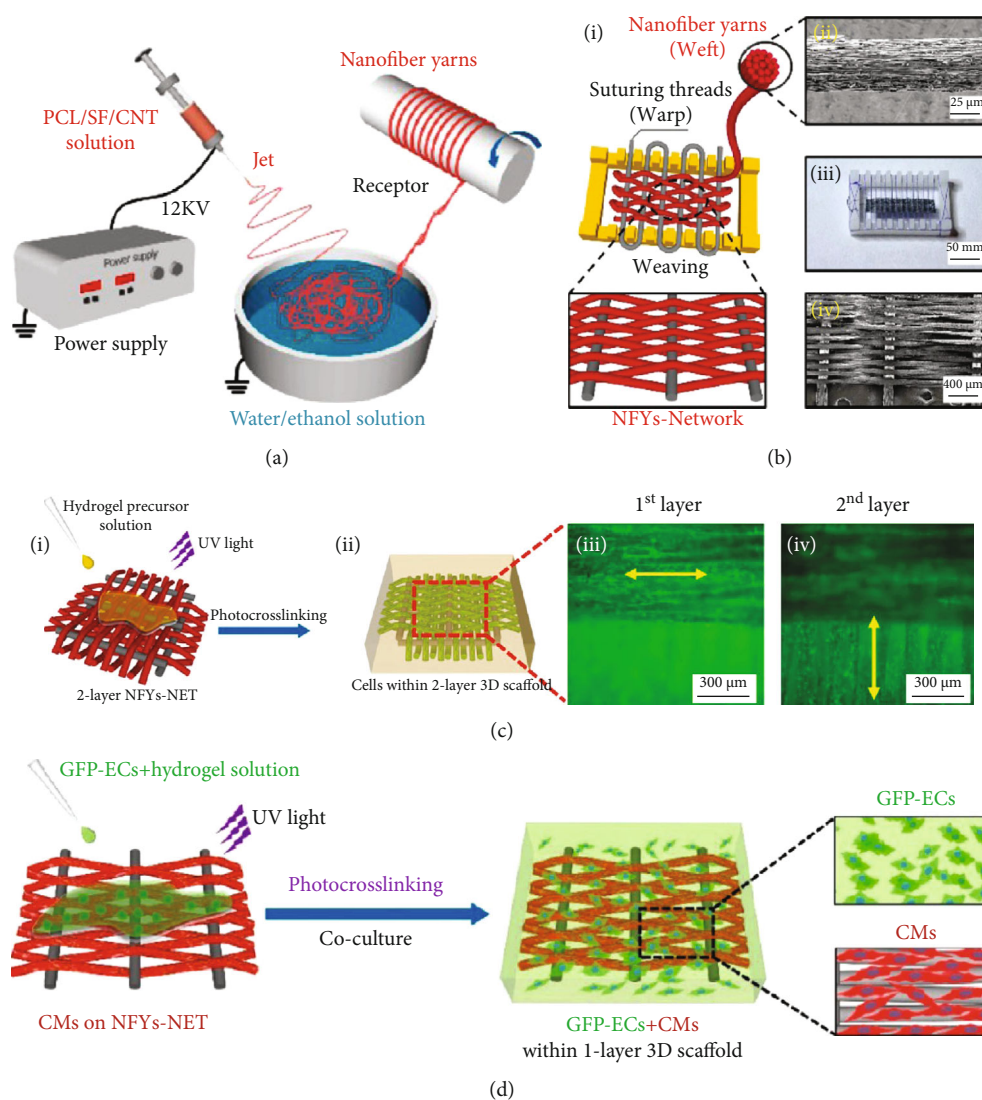 orientation within UV crosslinked GelMA hydrogel (i). F-Actin (green) staining of CMs cultured on the NFYs-NET layer with horizontal direction (iii) and vertical direction (iv) within a 2-layer 3D scaffold. (d) Coculture of CMs and ECs within yarn/hydrogel 3D composite scaffolds. CMs were cultured on the NFYs-NET layer while ECs with green fluorescent protein were encapsulated within a hydrogel shell. Reproduced with permission from [67]. Copyright © 2017, American Chemical Society.

[151]. Surrounded hydrogels prevented the cells from being directly exposed to the harsh environment and thus presented low oxygen and nutrient level, apoptotic cytokines, and some toxic reactive oxygen species. Therefore, electrospun nanofiber-based 3D composite scaffolds have exhibited improved controllability in mechanical properties, cell protection, and good performances *in vivo*, showing promising applications in neural tissue engineering.

4.5. Cardiac Tissue. As the major tissue for systole and diastole, the myocardium exhibits a hierarchical structure with aligned cells embedded into micropatterned and anisotropy ECM [27]. Therefore, electrospun nanofibers have been widely explored for myocardial tissue regeneration, which can mimic the myocardium anisotropic structure, direct the alignment of cardiomyocytes (CMs), and provide a suitable microenvironment for cell phenotype and neo tissue regeneration [152]. Electrospun nanofibers with different mechanical and biochemical properties for cardiac tissue engineering can be fabricated using different polymers, hybridization with other polymers, or nanoparticles, loading with growth factors or drugs.

Strong mechanical properties of scaffolds are required to restore heart functions, such as systole. However, many studies have shown that CMs prefer the matrix with soft stiffness [153, 154]. Electrospun nanofiber-based 3D composite scaffolds afford an optimized approach for resolving this challenge. For example, the multiple aligned fiber

layer-incorporated hydrogel scaffold was created through wet-dry electrospinning and photocrosslinking techniques, respectively (Figures 9(a) and 9(b)) [67]. The conductive nanofiber yarn network (NFY-NET) was fabricated with poly-caprolactone, silk fibroin, and carbon nanotubes through wet-dry electrospinning. The hydrogel was made of biocompatible GelMA hydrogel, which had the function to provide a preferred 3D environment for cell differentiation, nutrition exchange, thickness increase, and mechanical protection (Figure 9(c)). CMs cultured on the NEYs-NET scaffolds showed more robust and synchronized beating than that cultured on the 2D glass surface. Furthermore, the scaffold's mechanical property and structure stability were improved after incorporating with GelMA hydrogels. CMs and endothelial cells (ECs) could be separately seeded on the surface of yarns and encapsulated in GelMA hydrogel for coculture, indicating the potential for using integrated cardiovascular organoids (Figure 9(d)).

Heart valve tissue engineering is a promising approach for injured or diseased heart value repairing. An electrospun fiber mesh with heterogeneous and anisotropic properties was created by textile techniques to mimic the native features of heart value tissue. After combining with cell-laden methacrylated hyaluronic acid/GelMA hydrogel, this composite scaffold exhibited better mechanical strength, enhanced proliferation, and balanced ECM remodeling against degradation and shrinkage compared with single materials [155]. The nanofiber composite scaffold can also be designed for coronary artery vessel regeneration, comprised of separate collagen and elastin fibers [156]. For example, an electrospun mesh was cut into a rectangular piece with the short edge parallel with the orientation of the fibers and rolled wrapping around a latex tube. Then, a hollow Teflon cylinder was placed around the wrapped tube as a mold, and a thrombin/-fibrinogen-cell suspension was added into the structure. After crosslinking and removing the latex tube and Teflon cylinder, a fiber/hydrogel composite was left. This composite scaffold was biphasic in the mechanical property due to the different mechanical performance with the inner electrospun fibers and outer hydrogel, making it a potential construct for coronary artery vessel tissue engineering [157].

5. Conclusion and Future Perspectives

3D ENF-S represent a novel class of materials and have shown great promise for tissue engineering due to their intrinsic merits. These scaffolds with improved fibrous structure and thickness are superior to the 2D electrospun nanofiber membrane in cell infiltration and homogenous tissue regeneration. Besides, the tunable fibrous structure and mechanical properties of 3D ENF-S are attractive for tissue regeneration. Moreover, the ability to provide 3D biochemical and biophysical stimulus and cell protection from harsh environments is also present in electrospun nanofiber/hydrogel composite 3D scaffolds. Therefore, these 3D ENF-S have demonstrated effectiveness for cartilage and bone, tendon and ligament, skeletal muscle, nerve, and cardiac tissue engineering.

Despite the encouraging progress, utilizing 3D ENF-S for tissue engineering still faces many challenges. Ideally, bioinspired tissue engineering scaffolds should have highly ordered architecture because natural tissues or organs consist of multiscale hierarchical structures. Future studies focusing on the biomimetic hierarchical structure may bring additional functions for cell migration, proliferation, and neo tissue deposition. Moreover, it is necessary to study the interface between the fiber and porous scaffold/hydrogel matrix, which is related to the mechanical properties of the construct and affects cell activities and functions. It was reported that the interfacial bonding between fiber and hydrogel has the effect of promoting angiogenesis [158].

Finally, the long-term safety and performance of 3D ENF-S *in vivo* are the direction of future study in clinical transplantation. 3D ENF-S are usually prepared from two or more materials, and the synthetic polymers are generally electrospun in an organic solvent. Therefore, the toxicity of degradation products *in vivo* should be thoroughly evaluated. Also, the predesigned mechanical properties, hierarchical and anisotropic structures, and degradation profiles tested *in vitro* cannot reflect the results in the dynamic environment *in vivo*. All these performances will change with the scaffold degradation and the ingrowth of new tissue after implantation in the body. Therefore, the dynamic changes of the microenvironment *in vivo* should be taken into consideration when designing and preparing the 3D ENF-S with functional structure and properties.

Data Availability

The figures and data supporting this review are from previously reported studies and datasets, which have been cited and obtained permissions.

Conflicts of Interest

The authors declare no conflict of interest.

Authors' Contributions

Shanshan Han and Kexin Nie contributed equally to this work. Kexin Nie is co-first author.

Acknowledgments

References

[1] L. G. Griffith and G. Naughton, "Tissue engineering–current challenges and expanding opportunities," *Science*, vol. 295, no. 5557, pp. 1009–1014, 2002.

[2] X. Li, Q. Sun, Q. Li, N. Kawazoe, and G. Chen, "Functional hydrogels with tunable structures and properties for tissue engineering applications," *Frontiers in Chemistry*, vol. 6, 2018.

[3] C. F. Guimarães, L. Gasperini, A. P. Marques, and R. L. Reis, "The stiffness of living tissues and its implications for tissue engineering," *Nature Reviews Materials*, vol. 5, no. 5, pp. 351–370, 2020.

[4] S. J. Hollister, "Porous scaffold design for tissue engineering," *Nature Materials*, vol. 4, no. 7, pp. 518–524, 2005.

[5] L. Ma, C. Gao, Z. Mao et al., "Collagen/chitosan porous scaffolds with improved biostability for skin tissue engineering," *Biomaterials*, vol. 24, no. 26, pp. 4833–4841, 2003.

[6] G. Chen, T. Sato, T. Ushida, N. Ochiai, and T. Tateishi, "Tissue engineering of cartilage using a hybrid scaffold of synthetic polymer and collagen," *Tissue Engineering*, vol. 10, no. 3-4, pp. 323–330, 2004.

[7] Y. Chen, N. Kawazoe, and G. Chen, "Preparation of dexamethasone-loaded biphasic calcium phosphate nanoparticles/collagen porous composite scaffolds for bone tissue engineering," *Acta Biomaterialia*, vol. 67, pp. 341–353, 2018.

[8] J. Rouwkema, N. C. Rivron, and C. A. van Blitterswijk, "Vascularization in tissue engineering," *Trends in Biotechnology*, vol. 26, no. 8, pp. 434–441, 2008.

[9] M. Horst, D. Eberli, R. Gobet, and S. Salemi, "Tissue engineering in pediatric bladder reconstruction–the road to success," *Frontiers in Pediatrics*, vol. 7, p. 91, 2019.

[10] X. Mo, B. Sun, T. Wu, and D. Li, *Electrospun nanofibers for tissue engineering. Electrospinning: Nanofabrication and Applications*, Elsevier, 2019.

[11] X. Gao, S. Han, R. Zhang, G. Liu, and J. Wu, "Progress in electrospun composite nanofibers: composition, performance and applications for tissue engineering," *Journal of Materials Chemistry B*, vol. 7, no. 45, pp. 7075–7089, 2019.

[12] G. Chen, T. Ushida, and T. Tateishi, "Scaffold design for tissue engineering," *Macromolecular Bioscience*, vol. 2, no. 2, pp. 67–77, 2002.

[13] X. Li, S. Chen, J. Li et al., "3D culture of chondrocytes in gelatin hydrogels with different stiffness," *Polymers*, vol. 8, no. 8, p. 269, 2016.

[14] X. Li, Y. Chen, N. Kawazoe, and G. Chen, "Influence of microporous gelatin hydrogels on chondrocyte functions," *Journal of Materials Chemistry B*, vol. 5, no. 29, pp. 5753–5762, 2017.

[15] X. Wang, B. Ding, and B. Li, "Biomimetic electrospun nanofibrous structures for tissue engineering," *Materials Today*, vol. 16, no. 6, pp. 229–241, 2013.

[16] Y. Li, M. S. Budamagunta, J. Luo, W. Xiao, J. C. Voss, and K. S. Lam, "Probing of the assembly structure and dynamics within nanoparticles during interaction with blood proteins," *ACS Nano*, vol. 6, no. 11, pp. 9485–9495, 2012.

[17] O. S. Manoukian, R. Matta, J. Letendre, P. Collins, A. D. Mazzocca, and S. G. Kumbar, *Electrospun nanofiber scaffolds and their hydrogel composites for the engineering and regeneration of soft tissues*, Biomedical Nanotechnology: Springer, 2017.

[18] J. Xue, J. Xie, W. Liu, and Y. Xia, "Electrospun nanofibers: new concepts, materials, and applications," *Accounts of Chemical Research*, vol. 50, no. 8, pp. 1976–1987, 2017.

[19] J. Lannutti, D. Reneker, T. Ma, D. Tomasko, and D. Farson, "Electrospinning for tissue engineering scaffolds," *Materials Science and Engineering: C*, vol. 27, no. 3, pp. 504–509, 2007.

[20] K. Nie, S. Han, J. Yang et al., "Enzyme-crosslinked electrospun fibrous gelatin hydrogel for potential soft tissue engineering," *Polymers*, vol. 12, no. 9, p. 1977, 2020.

[21] D. Wang, X. Wang, Z. Zhang et al., "Programmed release of multimodal, cross-linked vascular endothelial growth factor and heparin layers on electrospun polycaprolactone vascular grafts," *ACS Applied Materials & Interfaces*, vol. 11, no. 35, pp. 32533–32542, 2019.

[22] W. Chen, J. Ma, L. Zhu et al., "Superelastic, superabsorbent and 3D nanofiber-assembled scaffold for tissue engineering," *Colloids and Surfaces, B: Biointerfaces*, vol. 142, pp. 165–172, 2016.

[23] L. Du, W. Li, Z. Jiang et al., "Hierarchical macro/microporous silk fibroin scaffolds for tissue engineering," *Materials Letters*, vol. 236, pp. 1–4, 2019.

[24] Y. Du, H. Liu, Q. Yang et al., "Selective laser sintering scaffold with hierarchical architecture and gradient composition for osteochondral repair in rabbits," *Biomaterials*, vol. 137, pp. 37–48, 2017.

[25] Q. Zhang, H. Lu, N. Kawazoe, and G. Chen, "Pore size effect of collagen scaffolds on cartilage regeneration," *Acta Biomaterialia*, vol. 10, no. 5, pp. 2005–2013, 2014.

[26] X. Li, J. Zhang, N. Kawazoe, and G. Chen, "Fabrication of highly crosslinked gelatin hydrogel and its influence on chondrocyte proliferation and phenotype," *Polymers*, vol. 9, no. 12, p. 309, 2017.

[27] G. C. Engelmayr, M. Cheng, C. J. Bettinger, J. T. Borenstein, R. Langer, and L. E. Freed, "Accordion-like honeycombs for tissue engineering of cardiac anisotropy," *Nature Materials*, vol. 7, no. 12, pp. 1003–1010, 2008.

[28] W.-J. Li, R. L. Mauck, J. A. Cooper, X. Yuan, and R. S. Tuan, "Engineering controllable anisotropy in electrospun biodegradable nanofibrous scaffolds for musculoskeletal tissue engineering," *Journal of Biomechanics*, vol. 40, no. 8, pp. 1686–1693, 2007.

[29] S. Chen, J. V. John, A. McCarthy, and J. Xie, "New forms of electrospun nanofiber materials for biomedical applications," *Journal of Materials Chemistry B*, vol. 8, no. 17, pp. 3733–3746, 2020.

[30] M. Rahmati, D. K. Mills, A. M. Urbanska et al., "Electrospinning for tissue engineering applications," *Progress in Materials Science*, vol. 117, article 100721, 2021.

[31] L. A. Bosworth, L. A. Turner, and S. H. Cartmell, "State of the art composites comprising electrospun fibres coupled with hydrogels: a review," *Nanomedicine: Nanotechnology, Biology and Medicine*, vol. 9, no. 3, pp. 322–335, 2013.

[32] Q. Fu, C. Duan, Z. Yan et al., "Nanofiber-based hydrogels: controllable synthesis and multifunctional applications," *Macromolecular Rapid Communications*, vol. 39, no. 10, p. 1800058, 2018.

[33] A. Varesano, R. A. Carletto, and G. Mazzuchetti, "Experimental investigations on the multi-jet electrospinning process," *Journal of Materials Processing Technology*, vol. 209, no. 11, pp. 5178–5185, 2009.

[34] X. Li, X. Wang, D. Yao et al., "Effects of aligned and random fibers with different diameter on cell behaviors," *Colloids and Surfaces, B: Biointerfaces*, vol. 171, pp. 461–467, 2018.

[35] T. Jiang, E. J. Carbone, K. W. H. Lo, and C. T. Laurencin, "Electrospinning of polymer nanofibers for tissue regeneration," *Progress in Polymer Science*, vol. 46, pp. 1–24, 2015.

[36] M. B. Fisher, E. A. Henning, N. Söegaard, J. L. Esterhai, and R. L. Mauck, "Organized nanofibrous scaffolds that mimic the macroscopic and microscopic architecture of the knee meniscus," *Acta Biomaterialia*, vol. 9, no. 1, pp. 4496–4504, 2013.

[37] B. B. Rothrauff, B. B. Lauro, G. Yang, R. E. Debski, V. Musahl, and R. S. Tuan, "Braided and stacked electrospun nanofibrous scaffolds for tendon and ligament tissue engineering," *Tissue Engineering Part A*, vol. 23, no. 9-10, pp. 378–389, 2017.

[38] J. Jiang, M. A. Carlson, M. J. Teusink, H. Wang, M. R. MacEwan, and J. Xie, "Expanding two-dimensional electrospun nanofiber membranes in the third dimension by a modified gas-foaming technique," *ACS Biomaterials Science & Engineering*, vol. 1, no. 10, pp. 991–1001, 2015.

[39] G. Kim and W. D. Kim, "Highly porous 3D nanofiber scaffold using an electrospinning technique," *Journal of Biomedical Materials Research Part B: Applied Biomaterials*, vol. 81B, no. 1, pp. 104–110, 2007.

[40] Y. H. Lee, J. H. Lee, I.-G. An et al., "Electrospun dual-porosity structure and biodegradation morphology of montmorillonite reinforced PLLA nanocomposite scaffolds," *Biomaterials*, vol. 26, no. 16, pp. 3165–3172, 2005.

[41] L. Fu, J. Xie, M. A. Carlson, and D. A. Reilly, "Three-dimensional nanofiber scaffolds with arrayed holes for engineering skin tissue constructs," *MRS Communications*, vol. 7, no. 3, pp. 361–366, 2017.

[42] B. L.-P. Lee, H. Jeon, A. Wang et al., "Femtosecond laser ablation enhances cell infiltration into three-dimensional electrospun scaffolds," *Acta Biomaterialia*, vol. 8, no. 7, pp. 2648–2658, 2012.

[43] A. Subramanian, U. M. Krishnan, and S. Sethuraman, "Fabrication of uniaxially aligned 3D electrospun scaffolds for neural regeneration," *Biomedical Materials*, vol. 6, no. 2, article 025004, 2011.

[44] B. A. Blakeney, A. Tambralli, J. M. Anderson et al., "Cell infiltration and growth in a low density, uncompressed three-dimensional electrospun nanofibrous scaffold," *Biomaterials*, vol. 32, no. 6, pp. 1583–1590, 2011.

[45] G. Z. Tan and Y. Zhou, "Tunable 3D nanofiber architecture of polycaprolactone by divergence electrospinning for potential tissue engineering applications," *Nano-Micro Letters*, vol. 10, no. 4, p. 73, 2018.

[46] C. Vaquette and J. J. Cooper-White, "Increasing electrospun scaffold pore size with tailored collectors for improved cell penetration," *Acta Biomaterialia*, vol. 7, no. 6, pp. 2544–2557, 2011.

[47] S. Nedjari, S. Eap, A. Hébraud, C. R. Wittmer, N. Benkirane-Jessel, and G. Schlatter, "Electrospun honeycomb as nests for controlled osteoblast spatial organization," *Macromolecular Bioscience*, vol. 14, no. 11, pp. 1580–1589, 2014.

[48] A. Garcia Garcia, A. Hébraud, J. L. Duval et al., "Poly (ε-caprolactone)/hydroxyapatite 3D honeycomb scaffolds for a cellular microenvironment adapted to maxillofacial bone reconstruction," *ACS Biomaterials Science & Engineering*, vol. 4, no. 9, pp. 3317–3326, 2018.

[49] N. Lavielle, A. Hébraud, C. Mendoza-Palomares, A. Ferrand, N. Benkirane-Jessel, and G. Schlatter, "Structuring and molding of electrospun nanofibers: effect of electrical and topographical local properties of micro-patterned collectors," *Macromolecular Materials and Engineering*, vol. 297, no. 10, pp. 958–968, 2012.

[50] S. Nedjari, G. Schlatter, and A. Hébraud, "Thick electrospun honeycomb scaffolds with controlled pore size," *Materials Letters*, vol. 142, pp. 180–183, 2015.

[51] D. Olvera, R. Schipani, B. N. Sathy, and D. J. Kelly, "Electrospinning of highly porous yet mechanically functional microfibrillar scaffolds at the human scale for ligament and tendon tissue engineering," *Biomedical Materials*, vol. 14, no. 3, article 035016, 2019.

[52] F. A. Formica, E. Öztürk, S. C. Hess et al., "A bioinspired ultraporous nanofiber-hydrogel mimic of the cartilage extracellular matrix," *Advanced Healthcare Materials*, vol. 5, no. 24, pp. 3129–3138, 2016.

[53] M. F. Leong, W. Y. Chan, and K. S. Chian, "Cryogenic electrospinning: proposed mechanism, process parameters and its use in engineering of bilayered tissue structures," *Nanomedicine*, vol. 8, no. 4, pp. 555–566, 2013.

[54] M. Simonet, O. D. Schneider, P. Neuenschwander, and W. J. Stark, "Ultraporous 3D polymer meshes by low-temperature electrospinning: use of ice crystals as a removable void template," *Polymer Engineering & Science*, vol. 47, no. 12, pp. 2020–2026, 2007.

[55] M. F. Leong, M. Z. Rasheed, T. C. Lim, and K. S. Chian, "In vitro cell infiltration and in vivo cell infiltration and vascularization in a fibrous, highly porous poly (D, L-lactide) scaffold fabricated by cryogenic electrospinning technique," *Journal of Biomedical Materials Research Part A*, vol. 91, no. 1, pp. 231–240, 2009.

[56] V. Lukášová, M. Buzgo, K. Vocetková et al., "Needleless electrospun and centrifugal spun poly-ε-caprolactone scaffolds as a carrier for platelets in tissue engineering applications: a comparative study with hMSCs," *Materials Science and Engineering: C*, vol. 97, pp. 567–575, 2019.

[57] K. Vocetkova, M. Buzgo, V. Sovkova et al., "A comparison of high throughput core–shell 2D electrospinning and 3D centrifugal spinning techniques to produce platelet lyophilisate-loaded fibrous scaffolds and their effects on skin cells," *RSC Advances*, vol. 7, no. 85, pp. 53706–53719, 2017.

[58] J. Song, G. Zhu, L. Wang, G. An, X. Shi, and Y. Wang, "Assembling of electrospun meshes into three-dimensional porous scaffolds for bone repair," *Biofabrication*, vol. 9, no. 1, article 015018, 2017.

[59] Y. Z. Cai, G. R. Zhang, L. L. Wang, Y. Z. Jiang, H. W. Ouyang, and X. H. Zou, "Novel biodegradable three-dimensional macroporous scaffold using aligned electrospun nanofibrous yarns for bone tissue engineering," *Journal of Biomedical Materials Research Part A*, vol. 100, no. 5, pp. 1187–1194, 2012.

[60] T. Wu, D. Li, Y. Wang et al., "Laminin-coated nerve guidance conduits based on poly (l-lactide-co-glycolide) fibers and yarns for promoting Schwann cells' proliferation and migration," *Journal of Materials Chemistry B*, vol. 5, no. 17, pp. 3186–3194, 2017.

[61] J. Ma, Y. He, X. Liu et al., "A novel electrospun-aligned nanoyarn/three-dimensional porous nanofibrous hybrid scaffold for annulus fibrosus tissue engineering," *International Journal of Nanomedicine*, vol. 13, pp. 1553–1567, 2018.

[62] R. A. O'Connor and G. B. McGuinness, "Electrospun nanofibre bundles and yarns for tissue engineering applications: a review," *Proceedings of the Institution of Mechanical Engineers, Part H: Journal of Engineering in Medicine*, vol. 230, no. 11, pp. 987–998, 2016.

[63] E. Smit, U. Bűttner, and R. D. Sanderson, "Continuous yarns from electrospun fibers," *Polymer*, vol. 46, no. 8, pp. 2419–2423, 2005.

[64] W.-E. Teo, R. Gopal, R. Ramaseshan, K. Fujihara, and S. Ramakrishna, "A dynamic liquid support system for continuous electrospun yarn fabrication," *Polymer*, vol. 48, no. 12, pp. 3400–3405, 2007.

[65] R. Tzezana, E. Zussman, and S. Levenberg, "A layered ultraporous scaffold for tissue engineering, created via a hydrospinning method," *Tissue Engineering. Part C, Methods*, vol. 14, no. 4, pp. 281–288, 2008.

[66] W. Teo, S. Liao, C. Chan, and S. Ramakrishna, "Remodeling of three-dimensional hierarchically organized nanofibrous assemblies," *Current Nanoscience*, vol. 4, no. 4, pp. 361–369, 2008.

[67] Y. Wu, L. Wang, B. Guo, and P. X. Ma, "Interwoven aligned conductive nanofiber yarn/hydrogel composite scaffolds for engineered 3D cardiac anisotropy," *ACS Nano*, vol. 11, no. 6, pp. 5646–5659, 2017.

[68] Y. Ding, A. S. Zhao, T. Liu et al., "An injectable nanocomposite hydrogel for potential application of vascularization and tissue repair," *Annals of Biomedical Engineering*, vol. 48, no. 5, pp. 1511–1523, 2020.

[69] W. Hu, Z. Wang, Y. Xiao, S. Zhang, and J. Wang, "Advances in crosslinking strategies of biomedical hydrogels," *Biomaterials Science*, vol. 7, no. 3, pp. 843–855, 2019.

[70] J. L. Drury and D. J. Mooney, "Hydrogels for tissue engineering: scaffold design variables and applications," *Biomaterials*, vol. 24, no. 24, pp. 4337–4351, 2003.

[71] A. T. Wood, D. Everett, K. I. Budhwani, B. Dickinson, and V. Thomas, "Wet-laid soy fiber reinforced hydrogel scaffold: Fabrication, mechano- morphological and cell studies," *Materials Science and Engineering: C*, vol. 63, pp. 308–316, 2016.

[72] A. L. Butcher, G. S. Offeddu, and M. L. Oyen, "Nanofibrous hydrogel composites as mechanically robust tissue engineering scaffolds," *Trends in Biotechnology*, vol. 32, no. 11, pp. 564–570, 2014.

[73] S. Xu, L. Deng, J. Zhang, L. Yin, and A. Dong, "Composites of electrospun-fibers and hydrogels: a potential solution to current challenges in biological and biomedical field," *Journal of Biomedical Materials Research. Part B, Applied Biomaterials*, vol. 104, no. 3, pp. 640–656, 2016.

[74] W. Xu, J. Ma, and E. Jabbari, "Material properties and osteogenic differentiation of marrow stromal cells on fiber-reinforced laminated hydrogel nanocomposites," *Acta Biomaterialia*, vol. 6, no. 6, pp. 1992–2002, 2010.

[75] S. Deepthi, M. Nivedhitha Sundaram, J. Deepti Kadavan, and R. Jayakumar, "Layered chitosan-collagen hydrogel/aligned PLLA nanofiber construct for flexor tendon regeneration," *Carbohydrate Polymers*, vol. 153, pp. 492–500, 2016.

[76] N. B. Shelke, P. Lee, M. Anderson et al., "Neural tissue engineering: nanofiber-hydrogel based composite scaffolds," *Polymers for Advanced Technologies*, vol. 27, no. 1, pp. 42–51, 2016.

[77] T. Wu, X. Mo, and Y. Xia, "Moving electrospun nanofibers and bioprinted scaffolds toward translational applications," *Advanced Healthcare Materials*, vol. 9, no. 6, article 1901761, 2020.

[78] S. K. Boda, Y. Almoshari, H. Wang et al., "Mineralized nanofiber segments coupled with calcium-binding BMP-2 pep-

tides for alveolar bone regeneration," *Acta Biomaterialia*, vol. 85, pp. 282–293, 2019.

[79] D. Kai, M. P. Prabhakaran, B. Stahl, M. Eblenkamp, E. Wintermantel, and S. Ramakrishna, "Mechanical properties and in vitro behavior of nanofiber–hydrogel composites for tissue engineering applications," *Nanotechnology*, vol. 23, no. 9, article 095705, 2012.

[80] A. Omidinia-Anarkoli, S. Boesveld, U. Tuvshindorj, J. C. Rose, T. Haraszti, and L. de Laporte, "An injectable hybrid hydrogel with oriented short fibers induces unidirectional growth of functional nerve cells," *Small*, vol. 13, no. 36, p. 1702207, 2017.

[81] A. Kosik-Kozioł, M. Costantini, T. Bolek et al., "PLA short sub-micron fiber reinforcement of 3D bioprinted alginate constructs for cartilage regeneration," *Biofabrication*, vol. 9, no. 4, article 044105, 2017.

[82] W. Lu, J. Sun, and X. Jiang, "Recent advances in electrospinning technology and biomedical applications of electrospun fibers," *Journal of Materials Chemistry B*, vol. 2, no. 17, pp. 2369–2380, 2014.

[83] J. Chen, T. Zhang, W. Hua, P. Li, and X. Wang, "3D Porous poly(lactic acid)/regenerated cellulose composite scaffolds based on electrospun nanofibers for biomineralization," *Colloids and Surfaces A: Physicochemical and Engineering Aspects*, vol. 585, p. 124048, 2020.

[84] S. Zhang, L. Chen, Y. Jiang et al., "Bi-layer collagen/microporous electrospun nanofiber scaffold improves the osteochondral regeneration," *Acta Biomaterialia*, vol. 9, no. 7, pp. 7236–7247, 2013.

[85] C. R. Wittmer, A. Hébraud, S. Nedjari, and G. Schlatter, "Well-organized 3D nanofibrous composite constructs using cooperative effects between electrospinning and electrospraying," *Polymer*, vol. 55, no. 22, pp. 5781–5787, 2014.

[86] L. Ma, G. Yang, N. Wang et al., "Trap effect of three-dimensional fibers network for high efficient cancer-cell capture," *Advanced Healthcare Materials*, vol. 4, no. 6, pp. 838–843, 2015.

[87] S.-J. Lee, M. Nowicki, B. Harris, and L. G. Zhang, "Fabrication of a highly aligned neural scaffold via a table top stereolithography 3D printing and electrospinning," *Tissue Engineering Part A*, vol. 23, no. 11-12, pp. 491–502, 2017.

[88] Y. Yu, S. Hua, M. Yang et al., "Fabrication and characterization of electrospinning/3D printing bone tissue engineering scaffold," *RSC Advances*, vol. 6, no. 112, pp. 110557–110565, 2016.

[89] M. Rampichová, E. Košťáková Kuželová, E. Filová et al., "Composite 3D printed scaffold with structured electrospun nanofibers promotes chondrocyte adhesion and infiltration," *Cell Adhesion & Migration*, vol. 12, no. 3, pp. 271–285, 2018.

[90] W. Chen, Y. Xu, Y. Liu et al., "Three-dimensional printed electrospun fiber-based scaffold for cartilage regeneration," *Materials and Design*, vol. 179, p. 107886, 2019.

[91] S. H. Park, T. G. Kim, H. C. Kim, D. Y. Yang, and T. G. Park, "Development of dual scale scaffolds via direct polymer melt deposition and electrospinning for applications in tissue regeneration," *Acta Biomaterialia*, vol. 4, no. 5, pp. 1198–1207, 2008.

[92] T. Niino, D. Hamajima, K. Montagne et al., "Laser sintering fabrication of three-dimensional tissue engineering scaffolds with a flow channel network," *Biofabrication*, vol. 3, no. 3, article 034104, 2011.

[93] F. P. Melchels, J. Feijen, and D. W. Grijpma, "A review on stereolithography and its applications in biomedical engineering," *Biomaterials*, vol. 31, no. 24, pp. 6121–6130, 2010.

[94] P. D. Dalton, C. Vaquette, B. L. Farrugia, T. R. Dargaville, T. D. Brown, and D. W. Hutmacher, "Electrospinning and additive manufacturing: converging technologies," *Biomaterials Science*, vol. 1, no. 2, pp. 171–185, 2013.

[95] L. Min, H. Pan, S. Chen et al., "Recent progress in bioinspired electrospun materials," *Composites Communications*, vol. 11, pp. 12–20, 2019.

[96] F. Xu, H. Sheardown, and T. Hoare, "Reactive electrospinning of degradable poly (oligoethylene glycol methacrylate)-based nanofibrous hydrogel networks," *Chemical Communications*, vol. 52, no. 7, pp. 1451–1454, 2016.

[97] D. Gan, T. Xu, W. Xing et al., "Mussel-inspired dopamine oligomer intercalated tough and resilient gelatin methacryloyl (GelMA) hydrogels for cartilage regeneration," *Journal of Materials Chemistry B*, vol. 7, no. 10, pp. 1716–1725, 2019.

[98] O. Bas, E. M. de-Juan-Pardo, C. Meinert et al., "Biofabricated soft network composites for cartilage tissue engineering," *Biofabrication*, vol. 9, no. 2, article 025014, 2017.

[99] F. Küng, D. W. Schubert, P. Stafiej, F. E. Kruse, and T. A. Fuchsluger, "A novel suture retention test for scaffold strength characterization in ophthalmology," *Materials Science and Engineering: C*, vol. 69, pp. 941–946, 2016.

[100] X. Meng, X. Wang, Y. Jiang, B. Zhang, K. Li, and Q. Li, "Suture retention strength of P(LLA-CL) tissue-engineered vascular grafts," *RSC Advances*, vol. 9, no. 37, pp. 21258–21264, 2019.

[101] C. Vaquette, P. T. Sudheesh Kumar, E. B. Petcu, and S. Ivanovski, "Combining electrospinning and cell sheet technology for the development of a multiscale tissue engineered ligament construct (TELC)," *Journal of Biomedical Materials Research. Part B, Applied Biomaterials*, vol. 106, no. 1, pp. 399–409, 2018.

[102] P. Datta, V. Vyas, S. Dhara, A. R. Chowdhury, and A. Barui, "Anisotropy properties of tissues: a basis for fabrication of biomimetic anisotropic scaffolds for tissue engineering," *Journal of Bionic Engineering*, vol. 16, no. 5, pp. 842–868, 2019.

[103] T. H. Qazi, D. J. Mooney, M. Pumberger, S. Geißler, and G. N. Duda, "Biomaterials based strategies for skeletal muscle tissue engineering: existing technologies and future trends," *Biomaterials*, vol. 53, pp. 502–521, 2015.

[104] B. J. Kwee and D. J. Mooney, "Biomaterials for skeletal muscle tissue engineering," *Current Opinion in Biotechnology*, vol. 47, pp. 16–22, 2017.

[105] S. Chen, T. Nakamoto, N. Kawazoe, and G. Chen, "Engineering multi-layered skeletal muscle tissue by using 3D microgrooved collagen scaffolds," *Biomaterials*, vol. 73, pp. 23–31, 2015.

[106] S. Jana, A. Cooper, and M. Zhang, "Chitosan scaffolds with unidirectional microtubular pores for large skeletal myotube generation," *Advanced Healthcare Materials*, vol. 2, no. 4, pp. 557–561, 2013.

[107] S. Wu, B. Duan, P. Liu, C. Zhang, X. Qin, and J. T. Butcher, "Fabrication of aligned nanofiber polymer yarn networks for anisotropic soft tissue scaffolds," *ACS Applied Materials & Interfaces*, vol. 8, no. 26, pp. 16950–16960, 2016.

[108] M. Jiang, M. Wang, S. Wei, Z. Chen, and S. Mu, "Aligned nanofibers based on electrospinning technology," *Progress in Chemistry*, vol. 28, p. 711, 2016.

[109] A. Turkiewicz, I. F. Petersson, J. Björk et al., "Current and future impact of osteoarthritis on health care: a population-based study with projections to year 2032," *Osteoarthritis and Cartilage*, vol. 22, no. 11, pp. 1826–1832, 2014.

[110] S. Apprich, S. Trattnig, G. Welsch et al., "Assessment of articular cartilage repair tissue after matrix-associated autologous chondrocyte transplantation or the microfracture technique in the ankle joint using diffusion-weighted imaging at 3 Tesla," *Osteoarthritis and Cartilage*, vol. 20, no. 7, pp. 703–711, 2012.

[111] C. Chung and J. A. Burdick, "Engineering cartilage tissue," *Advanced Drug Delivery Reviews*, vol. 60, no. 2, pp. 243–262, 2008.

[112] X. Nie, Y. J. Chuah, P. He, and D. A. Wang, "Engineering a multiphasic, integrated graft with a biologically developed cartilage–bone interface for osteochondral defect repair," *Journal of Materials Chemistry B*, vol. 7, no. 42, pp. 6515–6525, 2019.

[113] L. Roseti, V. Parisi, M. Petretta et al., "Scaffolds for bone tissue engineering: state of the art and new perspectives," *Materials Science and Engineering: C*, vol. 78, pp. 1246–1262, 2017.

[114] Y. Zhang, X. Liu, L. Zeng et al., "Polymer fiber scaffolds for bone and cartilage tissue engineering," *Advanced Functional Materials*, vol. 29, no. 36, p. 1903279, 2019.

[115] W. Chen, S. Chen, Y. Morsi et al., "Superabsorbent 3D scaffold based on electrospun nanofibers for cartilage tissue engineering," *ACS Applied Materials & Interfaces*, vol. 8, no. 37, pp. 24415–24425, 2016.

[116] K. Athanasiou, M. P. Rosenwasser, J. A. Buckwalter, T. I. Malinin, and V. C. Mow, "Interspecies comparisons of in situ intrinsic mechanical properties of distal femoral cartilage," *Journal of Orthopaedic Research*, vol. 9, no. 3, pp. 330–340, 1991.

[117] S. Gao, M. Chen, P. Wang et al., "An electrospun fiber reinforced scaffold promotes total meniscus regeneration in rabbit meniscectomy model," *Acta Biomaterialia*, vol. 73, pp. 127–140, 2018.

[118] H.-Y. Lin, W. C. Tsai, and S. H. Chang, "Collagen-PVA aligned nanofiber on collagen sponge as bi-layered scaffold for surface cartilage repair," *Journal of Biomaterials Science Polymer Edition*, vol. 28, no. 7, pp. 664–678, 2017.

[119] A. de Mori, M. Peña Fernández, G. Blunn, G. Tozzi, and M. Roldo, "3D printing and electrospinning of composite hydrogels for cartilage and bone tissue engineering," *Polymers*, vol. 10, no. 3, p. 285, 2018.

[120] C. Boyer, L. Figueiredo, R. Pace et al., "Laponite nanoparticle-associated silated hydroxypropylmethyl cellulose as an injectable reinforced interpenetrating network hydrogel for cartilage tissue engineering," *Acta Biomaterialia*, vol. 65, pp. 112–122, 2018.

[121] F. Mohabatpour, A. Karkhaneh, and A. M. Sharifi, "A hydrogel/fiber composite scaffold for chondrocyte encapsulation in cartilage tissue regeneration," *RSC Advances*, vol. 6, no. 86, pp. 83135–83145, 2016.

[122] S. Yodmuang, S. L. McNamara, A. B. Nover et al., "Silk microfiber-reinforced silk hydrogel composites for functional cartilage tissue repair," *Acta Biomaterialia*, vol. 11, pp. 27–36, 2015.

[123] Y. P. Singh, M. Adhikary, N. Bhardwaj, B. K. Bhunia, and B. B. Mandal, "Silk fiber reinforcement modulates in vitro chondrogenesis in 3D composite scaffolds," *Biomedical Materials*, vol. 12, no. 4, article 045012, 2017.

[124] M. Sadat-Shojai, M. T. Khorasani, and A. Jamshidi, "A new strategy for fabrication of bone scaffolds using electrospun nano- HAp/PHB fibers and protein hydrogels," *Chemical Engineering Journal*, vol. 289, pp. 38–47, 2016.

[125] S. Naghieh, E. Foroozmehr, M. Badrossamay, and M. Kharaziha, "Combinational processing of 3D printing and electrospinning of hierarchical poly(lactic acid)/gelatin-forsterite scaffolds as a biocomposite: Mechanical and biological assessment," *Materials and Design*, vol. 133, pp. 128–135, 2017.

[126] C. Zhang, H. Yuan, H. Liu et al., "Well-aligned chitosan-based ultrafine fibers committed teno-lineage differentiation of human induced pluripotent stem cells for Achilles tendon regeneration," *Biomaterials*, vol. 53, pp. 716–730, 2015.

[127] D. Little, F. Guilak, and D. S. Ruch, "Ligament-derived matrix stimulates a ligamentous phenotype in human adipose-derived stem cells," *Tissue Engineering Part A*, vol. 16, no. 7, pp. 2307–2319, 2010.

[128] A. Chainani, K. J. Hippensteel, A. Kishan et al., "Multilayered electrospun scaffolds for tendon tissue engineering," *Tissue Engineering Part A*, vol. 19, no. 23-24, pp. 2594–2604, 2013.

[129] C. Rinoldi, A. Fallahi, I. K. Yazdi et al., "Mechanical and biochemical stimulation of 3d multilayered scaffolds for tendon tissue engineering," *ACS Biomaterials Science & Engineering*, vol. 5, no. 6, pp. 2953–2964, 2019.

[130] J. H. Kim, Y.-J. Choi, H.-G. Yi, J. H. Wang, D.-W. Cho, and Y. H. Jeong, "A cell-laden hybrid fiber/hydrogel composite for ligament regeneration with improved cell delivery and infiltration," *Biomedical Materials*, vol. 12, no. 5, article 055010, 2017.

[131] A. Jayasree, S. Kottappally Thankappan, R. Ramachandran et al., "Bioengineered braided micro–nano (multiscale) fibrous scaffolds for tendon reconstruction," *ACS Biomaterials Science & Engineering*, vol. 5, no. 3, pp. 1476–1486, 2019.

[132] K. Garg, B. T. Corona, and T. J. Walters, "Therapeutic strategies for preventing skeletal muscle fibrosis after injury," *Frontiers in Pharmacology*, vol. 6, p. 87, 2015.

[133] L. Wang, Y. Wu, B. Guo, and P. X. Ma, "Nanofiber yarn/hydrogel core–shell scaffolds mimicking native skeletal muscle tissue for guiding 3D myoblast alignment, elongation, and differentiation," *ACS Nano*, vol. 9, no. 9, pp. 9167–9179, 2015.

[134] S. Jana, S. K. L. Levengood, and M. Zhang, "Anisotropic materials for skeletal-muscle-tissue engineering," *Advanced Materials*, vol. 28, no. 48, pp. 10588–10612, 2016.

[135] M. Yeo and G. H. Kim, "Three-dimensional microfibrous bundle structure fabricated using an electric field-assisted/cell printing process for muscle tissue regeneration," *ACS Biomaterials Science & Engineering*, vol. 4, no. 2, pp. 728–738, 2018.

[136] X. Gu, "Progress and perspectives of neural tissue engineering," *Frontiers in Medicine*, vol. 9, no. 4, pp. 401–411, 2015.

[137] S. J. Lee, M. Heo, D. Lee, D. N. Heo, H. N. Lim, and I. K. Kwon, "Fabrication and design of bioactive agent coated, highly-aligned electrospun matrices for nerve tissue engineering: preparation, characterization and application," *Applied Surface Science*, vol. 424, pp. 359–367, 2017.

[138] H. Hajiali, A. Contestabile, E. Mele, and A. Athanassiou, "Influence of topography of nanofibrous scaffolds on functionality of engineered neural tissue," *Journal of Materials Chemistry B*, vol. 6, no. 6, pp. 930–939, 2018.

[139] J. Hu, L. Tian, M. Prabhakaran, X. Ding, and S. Ramakrishna, "Fabrication of nerve growth factor encapsulated aligned poly (ε-caprolactone) nanofibers and their assessment as a potential neural tissue engineering scaffold," *Polymers*, vol. 8, no. 2, p. 54, 2016.

[140] L. Tian, M. P. Prabhakaran, J. Hu, M. Chen, F. Besenbacher, and S. Ramakrishna, "Coaxial electrospun poly (lactic acid)/silk fibroin nanofibers incorporated with nerve growth factor support the differentiation of neuronal stem cells," *RSC Advances*, vol. 5, no. 62, pp. 49838–49848, 2015.

[141] S. Das, M. Sharma, D. Saharia, K. K. Sarma, E. M. Muir, and U. Bora, "Electrospun silk-polyaniline conduits for functional nerve regeneration in rat sciatic nerve injury model," *Biomedical Materials*, vol. 12, no. 4, article 045025, 2017.

[142] M. Soleimani, S. Mashayekhan, H. Baniasadi, A. Ramazani, and M. Ansarizadeh, "Design and fabrication of conductive nanofibrous scaffolds for neural tissue engineering: process modeling via response surface methodology," *Journal of Biomaterials Applications*, vol. 33, no. 5, pp. 619–629, 2018.

[143] J. Thunberg, T. Kalogeropoulos, V. Kuzmenko et al., "In situ synthesis of conductive polypyrrole on electrospun cellulose nanofibers: scaffold for neural tissue engineering," *Cellulose*, vol. 22, no. 3, pp. 1459–1467, 2015.

[144] S. Hamsici, G. Cinar, A. Celebioglu, T. Uyar, A. B. Tekinay, and M. O. Guler, "Bioactive peptide functionalized aligned cyclodextrin nanofibers for neurite outgrowth," *Journal of Materials Chemistry B*, vol. 5, no. 3, pp. 517–524, 2017.

[145] G. Jin, R. He, B. Sha et al., "Electrospun three-dimensional aligned nanofibrous scaffolds for tissue engineering," *Materials Science and Engineering: C*, vol. 92, pp. 995–1005, 2018.

[146] T. C. Tseng, L. Tao, F. Y. Hsieh, Y. Wei, I. M. Chiu, and S. H. Hsu, "An injectable, self-healing hydrogel to repair the central nervous system," *Advanced Materials*, vol. 27, no. 23, pp. 3518–3524, 2015.

[147] K.-C. Cheng, C. F. Huang, Y. Wei, and S. H. Hsu, "Novel chitosan-cellulose nanofiber self-healing hydrogels to correlate self- healing properties of hydrogels with neural regeneration effects," *NPG Asia Materials*, vol. 11, no. 1, p. 25, 2019.

[148] J. Du, J. Liu, S. Yao et al., "Prompt peripheral nerve regeneration induced by a hierarchically aligned fibrin nanofiber hydrogel," *Acta Biomaterialia*, vol. 55, pp. 296–309, 2017.

[149] S. Yao, X. Liu, S. Yu et al., "Co-effects of matrix low elasticity and aligned topography on stem cell neurogenic differentiation and rapid neurite outgrowth," *Nanoscale*, vol. 8, no. 19, pp. 10252–10265, 2016.

[150] R. J. Miller, C. Y. Chan, A. Rastogi et al., "Combining electrospun nanofibers with cell-encapsulating hydrogel fibers for neural tissue engineering," *Journal of Biomaterials Science. Polymer Edition*, vol. 29, no. 13, pp. 1625–1642, 2018.

[151] T. Dinis, R. Elia, G. Vidal et al., "3D multi-channel bi-functionalized silk electrospun conduits for peripheral nerve regeneration," *Journal of the Mechanical Behavior of Biomedical Materials*, vol. 41, pp. 43–55, 2015.

[152] M. Kitsara, O. Agbulut, D. Kontziampasis, Y. Chen, and P. Menasché, "Fibers for hearts: a critical review on electrospinning for cardiac tissue engineering," *Acta Biomaterialia*, vol. 48, pp. 20–40, 2017.

[153] T. P. Kraehenbuehl, P. Zammaretti, A. J. van der Vlies et al., "Three-dimensional extracellular matrix-directed cardioprogenitor differentiation: Systematic modulation of a synthetic

cell-responsive PEG- hydrogel," *Biomaterials*, vol. 29, no. 18, pp. 2757–2766, 2008.

[154] B. Bhana, R. K. Iyer, W. L. K. Chen et al., "Influence of substrate stiffness on the phenotype of heart cells," *Biotechnology and Bioengineering*, vol. 105, no. 6, pp. 1148–1160, 2010.

[155] S. Wu, B. Duan, X. Qin, and J. T. Butcher, "Living nano-micro fibrous woven fabric/hydrogel composite scaffolds for heart valve engineering," *Acta Biomaterialia*, vol. 51, pp. 89–100, 2017.

[156] Z. Wang, C. Liu, Y. Xiao et al., "Remodeling of a cell-free vascular graft with nanolamellar intima into a neovessel," *ACS Nano*, vol. 13, no. 9, pp. 10576–10586, 2019.

[157] R. E. McMahon, X. Qu, A. C. Jimenez-Vergara et al., "Hydrogel–electrospun mesh composites for coronary artery bypass grafts," *Tissue Engineering Part C, Methods*, vol. 17, no. 4, pp. 451–461, 2011.

[158] X. Li, B. Cho, R. Martin et al., "Nanofiber-hydrogel composite–mediated angiogenesis for soft tissue reconstruction," *Science Translational Medicine*, vol. 11, no. 490, article eaau6210, 2019.

Retraction

Retracted: Loading Gentamicin and Zn^{2+} on TiO$_2$ Nanotubes to Improve Anticoagulation, Endothelial Cell Growth, and Antibacterial Activities

Stem Cells International

This article has been retracted by Hindawi following an investigation undertaken by the publisher [1]. This investigation has uncovered evidence of one or more of the following indicators of systematic manipulation of the publication process:

(1) Discrepancies in scope
(2) Discrepancies in the description of the research reported
(3) Discrepancies between the availability of data and the research described
(4) Inappropriate citations
(5) Incoherent, meaningless and/or irrelevant content included in the article
(6) Manipulated or compromised peer review

The presence of these indicators undermines our confidence in the integrity of the article's content and we cannot, therefore, vouch for its reliability. Please note that this notice is intended solely to alert readers that the content of this article is unreliable. We have not investigated whether authors were aware of or involved in the systematic manipulation of the publication process.

In addition, our investigation has also shown that one or more of the following human-subject reporting requirements has not been met in this article: ethical approval by an Institutional Review Board (IRB) committee or equivalent, patient/ participant consent to participate, and/or agreement to publish patient/participant details (where relevant).

Wiley and Hindawi regrets that the usual quality checks did not identify these issues before publication and have since put additional measures in place to safeguard research integrity.

We wish to credit our own Research Integrity and Research Publishing teams and anonymous and named external researchers and research integrity experts for contributing to this investigation.

The corresponding author, as the representative of all authors, has been given the opportunity to register their agreement or disagreement to this retraction. We have kept a record of any response received.

References

[1] Y. Lin, L. Zhang, Y. Yang et al., "Loading Gentamicin and Zn^{2+} on TiO$_2$ Nanotubes to Improve Anticoagulation, Endothelial Cell Growth, and Antibacterial Activities," *Stem Cells International*, vol. 2021, Article ID 9993247, 13 pages, 2021.

Research Article

Loading Gentamicin and Zn^{2+} on TiO$_2$ Nanotubes to Improve Anticoagulation, Endothelial Cell Growth, and Antibacterial Activities

Yuebin Lin (iD),[1] **Li Zhang,**[2] **Ya Yang,**[2] **Minhui Yang,**[1] **Qingxiang Hong,**[1] **Keming Chang,**[1] **Juan Dai,**[1] **Lu Chen,**[1] **Changjiang Pan** (iD),[1] **Youdong Hu,**[2] **Li Quan,**[1] **Yanchun Wei,**[1] **Sen Liu,**[1] **and Zhongmei Yang**[1]

[1]*Faculty of Mechanical and Material Engineering, Huaiyin Institute of Technology, Huai'an 223003, China*
[2]*The Affiliated Huai'an Hospital of Xuzhou Medical University, Huai'an 223003, China*

Correspondence should be addressed to Yuebin Lin; lybzyt@hyit.edu.cn and Changjiang Pan; panchangjiang@hyit.edu.cn

Titanium and its alloys are widely used in blood-contacting implantable and interventional medical devices; however, their biocompatibility is still facing great challenges. In the present study, in order to improve the biocompatibility and antibacterial activities of titanium, TiO$_2$ nanotubes were firstly in situ prepared on the titanium surface by anodization, followed by the introduction of polyacrylic acid (PAA) and gentamicin (GS) on the nanotube surface by layer-by-layer assembly, and finally, zinc ions were loaded on the surface to further improve the bioactivities. The nanotubes displayed excellent hydrophilicity and special nanotube-like structure, which can selectively promote the albumin adsorption, enhance the blood compatibility, and promote the growth of endothelial cells to some degree. After the introduction of PAA and GS, although the superhydrophilicity cannot be achieved, the results of platelet adhesion, cyclic guanosine monophosphate (cGMP) activity, hemolysis rate, and activated partial thromboplastin time (APTT) showed that the blood compatibility was improved, and the blood compatibility was further enhanced after zinc ion loading. On the other hand, the modified surface showed good cytocompatibility to endothelial cells. The introduction of PAA and zinc ions not only promoted the adhesion and proliferation of endothelial cells but also upregulated expression of vascular endothelial growth factor (VEGF) and nitric oxide (NO). The slow and continuous release of GS and Zn^{2+} over 14 days can significantly improve the antibacterial properties. Therefore, the present study provides an effective method for the surface modification of titanium-based blood-contacting materials to simultaneously endow with good blood compatibility, endothelial growth behaviors, and antibacterial properties.

1. Introduction

Blood-contacting implantable and interventional medical devices, such as artificial heart valves and vascular stents, have saved thousands of lives [1, 2]. Titanium and its alloys have been widely used in blood-contacting medical devices, but they still face great challenges in clinical applications, such as inflammation, thrombosis, and infection. Generally speaking, ideal implants should have the abilities to integrate and communicate with surrounding tissues or cells, trigger specific cell responses and maintain the func-

tion of tissues and organs, and prevent infections caused by microorganisms after the implantation [3, 4]. In this regard, surface functionalization represents one of the straightforward and effective methods to endow biomaterials with excellent properties and functions [5–7]. According to the mechanism of the interactions between the implant and the surrounding physiological microenvironment, the introduction of bioactive substances on the surface by physical or chemical conjugation can endow the inert biomaterial with good biological activities, so as to regulate the cell-material interaction behaviors, induce

specific cell responses, and prevent the infection caused by implantation [8–11].

Although great progress has been made in the surface functionalization of titanium-based biomaterials, there are still many issues to be solved, including the delayed surface endothelialization, thrombosis, and infection after implantation [12, 13]. Studies have shown that the surface properties of the implant are related not only to the surface bioactivities but also to the surface topographies. In recent years, the nanomaterials with special tubular structure have attracted great attention in the blood-contacting biomaterials [14]. Anodization is a surface modification technology that can in situ prepare nanotubes on the titanium surface [15, 16]. The as-prepared nanotubes not only do not change the mechanical properties of bulk materials but also provide an excellent platform for loading bioactive molecules to enhance the surface bioactivities [17–19]. Our previous results showed that the anodized TiO_2 nanotubes with the different dimensions have different effects on hemocompatibility and endothelial cell behaviors, demonstrating that the interfacial biological behaviors between the implanted materials and tissues can be regulated by the surface morphologies [20]. Therefore, loading the bioactive factors into the nanotubes can further enhance the biocompatibility from two aspects of surface bioactivities and surface morphologies.

Zinc is the second most abundant trace element in the human body, which participates in a large number of physiological reactions and is an important substance involved in cell growth behavior and cell function expression [21]. Zinc ions also play an important role in the cardiovascular system, and it can prevent local vascular ischemia and vascular infarction [22]. Zinc deficiency is closely related to atherosclerosis, and zinc can protect the integrity of the vascular endothelium by preventing nuclear factor apoptosis and inflammation-related genes [23]. Moreover, zinc ions can induce bacterial apoptosis by changing the charge balance of bacteria [24]. Therefore, the loading of zinc ions into the anodized TiO_2 nanotubes can not only improve the anticoagulant and antibacterial activities but also promote the growth of endothelial cells.

In addition, intravascular devices should have good antibacterial properties because the implant-centered infection is often one of the important reasons of the implantation failure [25]. Loading or immobilization of antibacterial substances on the surface is an important approach to endow devices with antibacterial properties [26]. Polyacrylic acid (PAA) is a cheap and environmentally friendly water-soluble organic polymer. The carboxylic acid groups of PAA can absorb a large number of metal ions, drugs, and other positively charged substances, so it is widely used in the field of biomaterials [27]. Gentamicin (GS), a widely used antibacterial substance in the clinic, is a kind of aminoglycoside, and it has a broad spectrum of antimicrobial activity and especially has excellent antibacterial activity for Gram-negative bacteria [28]. Therefore, in the present study, we first prepared TiO_2 nanotubes on the titanium surface by anodization, and then, PAA was further introduced on the surface followed by loading GS through layer-by-layer (LBL) and zinc ions with the help of carboxylic acid groups of PAA. The results indicated that PAA and the continuous released zinc ions can significantly improve the anticoagulant and endothelial cell growth, and the excellent and long-lasting antibacterial properties can be achieved through the release of GS and zinc ions.

2. Materials and Methods

2.1. Preparation of TiO_2 Nanotubes on Titanium Surface. Titanium plates (TA2) with a diameter of 15 mm and a thickness of 2 mm were successively polished with sandpapers of 400#, 800#, 1200#, 1500#, and 2000# and then polished to the mirror with a polishing machine. After being ultrasonically cleaned for 10 min with acetone, ethanol, and deionized water, the titanium plates were immersed in 50 mL electrolyte (ethylene glycol solution containing 0.25%wt NH_4F and 6 mL deionized water) to anodize 3 h at 30 V using the plate as the anode. After anodization, the plates were cleaned ultrasonically for 30 min in ethylene glycol solution and for 5 min in ethanol. In order to change the synthesized TiO_2 nanotubes into an anatase-type structure, the sample was dried and heat-treated at 500°C in air for 3 h and named TNT.

2.2. Loading GS and Zn^{2+} on TiO_2 Nanotubes. The TNT samples were firstly immersed in 2 mg/mL dopamine solution (pH 8.0) for 12 h and then washed with the deionized water. The process was repeated three times, and the as-prepared samples were named as TNT-Dopa. The TNT-Dopa samples were immersed in a polyethyleneimine (PEI) solution (5 mg/mL, pH 10.0) for 30 min. After cleaning, the sample was immersed in 1 mg/mL PAA solution (pH 7.4) for 10 min, and the obtained sample was labelled as TNT-PAA. For loading gentamicin (GS), the TNT-PAA sample was alternately immersed in GS (1 mg/mL) and PAA solutions (1 mg/mL), and the process was repeated 10 times; the obtained sample was named as TNT-PAA/GS, and the outermost layer was PAA. Finally, the sample was immersed in 1 M $ZnSO_4$ for 2 h to load Zn^{2+}, and the final sample was labelled as TNT-PAA/GS-Zn.

2.3. Sample Characterization. The surface morphologies of the samples were observed by scanning electron microscopy (SEM, FEI Quanta 250). The changes of chemical groups on the surface were examined by attenuated total reflection Fourier transform infrared spectroscopy (ATR-FTIR, TENSOR 27, Bruker of Germany); the measurements were carried out at room temperature, and the scanning range was from $650 \, cm^{-1}$ to $4000 \, cm^{-1}$. The surface atomic concentrations of the different samples were measured by X-ray photoelectron spectroscopy (XPS, VG Science, East Grinstead, UK). Water contact angle measurement (DSA25, Krüss GmbH, Germany) was used to characterize the surface hydrophilicity, and five parallel samples were measured and averaged.

2.4. Protein Adsorption. The adsorption behaviors of fibrinogen (FIB) and bovine serum albumin (BSA) were measured by the BCA method. The samples were firstly immersed in ethanol for 30 min and then in phosphate buffer (PBS) for 10 h. After that, the samples were placed into 1 mg/mL BSA

solution and 1 mg/mL FIB solution for 2 h at 37°C, respectively. After washing twice by PBS, the sample was put into 2 mL SDS (sodium dodecyl sulfate, 1%wt) solution for ultrasonic desorbing for 30 min. We take 150 μL eluent and 150 μL BCA working solution (reagent A : reagent B : reagent C = 25 : 24 : 1) to react 1 h at 60°C, and then 200 μL mixing solution was transferred into a 96-well plate to measure the absorbance at 562 nm by the microplate reader (BioTek, Eons), and the adsorption amount of protein was calculated according to the standard curve.

2.5. Release Profiles of GS and Zn^{2+}.

The TNT-PAA/GS-Zn sample was immersed in 5 mL 37°C PBS solution for 1 h, 3 h, 5 h, 7 h, 1 d, 3 d, 7 d, and 14 d, and then, 200 μL solution was transferred into the 96-well plate. The absorbance at 562 nm was measured by a microplate reader (BioTek, Eons), and the release amount of GS was calculated according to the standard curve. The concentration of zinc ions was measured by an inductively coupled plasma emission spectrometer (Optima 7000 DV), and the release concentration was calculated according to the standard curve. Three parallel samples were measured and averaged, and the release profiles were further plotted.

2.6. Blood Compatibility

2.6.1. Hemolysis Assay.

The hemolysis rate was measured according to the ISO10993-4 standard. Fresh human blood from a healthy volunteer was centrifuged at 1500 rpm for 10 min to obtain the red blood cells. The red blood cells were prepared into 2% suspension with physiological saline. The samples were incubated 1 h in the suspension solution at 37°C. The solution was then centrifuged 5 min at 3000 rpm. We take 100 μL supernatant into a 96-well plate, and the absorbance (A) was measured at 450 nm by the microplate reader. Under the same conditions, the absorbance value (B) of the mixed solution of 2% red blood cells and 98% normal saline was measured as the negative control, and the absorbance value (C) of the solution of 2% red blood cells and 98% deionized water was recorded as the positive controls. Three parallel samples were measured, and the values were averaged. The hemolysis rate was calculated according to the following formula.

$$\text{Hemolysis rate (\%)} = \frac{A - B}{C - B} \times 100\%. \tag{1}$$

2.6.2. Adhesion and Activation.

Fresh healthy human whole blood was centrifuged at 1500 rpm for 15 min to obtain platelet-rich plasma (PRP). 200 μL PRP was fully covered on each sample surface to incubate 2 h at 37°C, and then, the samples were rinsed thrice with PBS. The adherent platelets were fixed with 2.5% glutaraldehyde (in PBS buffer) for 24 h and then rinsed with PBS. The samples were successively dehydrated with 30%, 50%, 75%, 90%, and 100% ethanol solutions for 10 min each, and the samples were dried in the air. After spraying gold on the surface, the morphologies of the platelets were observed by SEM (FEI Quanta 250). Five SEM images with small magnification (×1000) were ran-

domly selected for calculating the number of platelets, and the values were averaged and expressed as platelets per mm².

For the platelet activation assay, an enzyme-linked immunosorbent assay (ELISA kit, Beyotime Biotechnology, Shanghai, China) was used to measure the activity of cGMP (cyclic guanosine monophosphate) secreted by platelets. In brief, 200 μL PRP was dropped on each sample surface to cover the whole surface. After incubating at 37°C for 2 h, the plasma on the surface was diluted 5 times; subsequently, the plasma was transferred to the enzyme plate for culturing 30 min at 37°C. 50 μL of enzyme-labeled reagent was added to each well, cultured at 37°C for 30 min. Then, 50 μL chromogenic agent A and 50 μL chromogenic agent B were added to each well and kept away from light for 10 min at 37°C. Finally, the terminating solution was added to stop the reaction. The absorbance at 450 nm was measured, and the concentration of cGMP was calculated according to the standard curve.

2.6.3. APTT.

Fresh human anticoagulant whole blood was centrifuged 15 min at 3000 rpm to obtain platelet-poor plasma (PPP). 100 μL PPP was covered onto the sample surface and cultured 15 min at 37°C. Subsequently, 50 μL PPP and 50 μL APTT reagent (Sysmex, Japan) were added into the test tube and cultured at 37°C for 3 min. 50 μL 0.025 M CaCl₂ solution was finally added. The clotting time was measured by an automatic coagulation meter (CA-1500, Sysmex, Japan), and the average values of three parallel samples were measured.

2.7. Endothelial Cell Growth Behaviors

2.7.1. Cell Adhesion and Proliferation.

The samples were firstly placed in a 24-well culture plate and sterilized overnight with ultraviolet light on the superclean table, and then, 0.5 mL endothelial cell suspension (5×10^4 cells/mL) and 1.5 mL cell culture medium (DMEM/F-12 supplemented with 10% fetal bovine serum and 1% penicillin-streptomycin, HyClone) were added to each sample surface. After incubating at 37°C and 5% CO_2 for 1 and 3 days, respectively, the samples were washed with PBS for 3 times. Each sample surface was stained with 200 μL rhodamine (in PBS, 1 : 400) for 20 min and then washed with PBS for 3 times. Finally, 200 μL of DAPI (PBS, 1 : 400) was added to the surface for 3 min. After being washed 3 times with PBS, the cells were observed by fluorescence microscopy (Zeiss, inverted A2).

For cell proliferation, endothelial cells were cultured in the same way as mentioned above. After 1 and 3 days, the samples were washed with PBS for 3 times. 0.5 mL CCK-8 (Sigma-Aldrich, Shanghai, China) solution (10% in cell culture medium) was added and incubated in a 37°C incubator for 3.5 h. After that, 200 μL medium was transferred into a 96-well plate, and the absorbance at 450 nm was measured by a microplate reader (BioTek, Eons) to determine the proliferation activity of endothelial cells.

2.7.2. NO and VEGF Expression.

The NO release from endothelial cells was measured by the Griess method. The endothelial cells were cultured on the sample surface for 1 day and 3 days, the supernatant was added to the 96-well
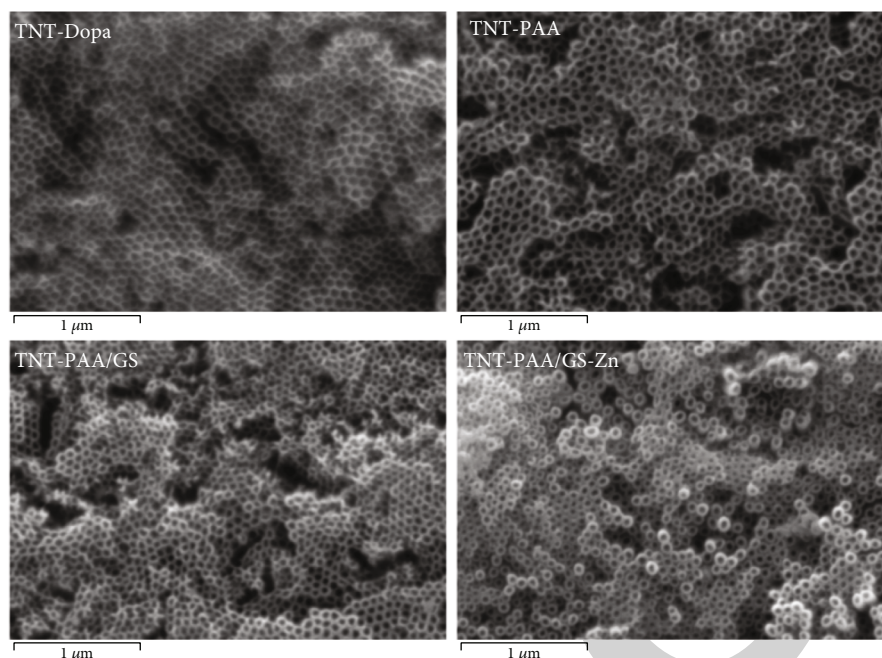
Figure 1: The representative SEM images of surface-modified titanium oxide nanotubes on the titanium surfaces.

plate, and then, Griess Reagents I and II (Beyotime Bio-technology, Shanghai, China) were added successively. The absorbance at 540 nm was determined by a microplate reader, and the NO concentration was calculated according to the standard curve.

For the VEGF assay, according to the instructions of the enzyme-linked immunosorbent assay kit (Jiangsu Enzymatic Immunity Industry Co., Ltd.), endothelial cells were cultured on the sample surface for 1 day and 3 days, and then, the supernatant was absorbed to dilute 5 times and finally added to the enzyme plate. After being incubated at 37°C for 30 min, 50 μL of the enzyme labeled reagent was added and incubated at 37°C for another 30 min, and then, 50 μL chromogenic agent A and 50 μL chromogenic agent B were added to each well to react 10 min at 37°C in the dark. Finally, the terminating solution was added to stop the reaction, and the OD value at 450 nm was determined by a microplate reader. Three parallel samples were measured and averaged. The VEGF concentration was determined according to the standard curve.

2.8. Antibacterial Activities

2.8.1. Bacterial Adhesion. Escherichia coli (ATCC 25922; HuanKai Microbial, Guangzhou, China) was cultured in the mixture of 0.2% liquid medium (5 g/L yeast extract and 10 g/L tryptone) and 99.8% 10 g/L NaCl solution for 20 h; 10 mL solution was centrifuged at 2000 rpm for 3 min and then dispersed evenly. The bacterial solution was diluted 10 times, and 50 μL bacterial suspension was dropped on the sample surface to culture 2 h. The sample was then washed 3 times with PBS and fixed 2.5 h with 2.5% glutaraldehyde solution, followed by washing the sample with PBS, and finally dehydrated with 50%, 70%, 90%, and 100% ethanol solutions for 10 min each time. After spraying gold on the

sample surface, the adhered bacteria were observed by SEM (FEI Quanta 250).

2.8.2. Antibacterial Activities. Escherichia coli (ATCC 25922) was cultured overnight as mentioned above; 10 mL bacteria solution was taken and centrifuged at 1300 rpm for 5 min to determine the survival and number of bacteria. The sample was placed into a 12-well plate, and then, 500 μL bacterial solution was added. After being cultured at 37°C for 30 min, 1500 mL sterilized deionized water was added and continued to culture at 37°C for 24 h. 50 μL of bacterial liquid was evenly covered on the surface of the solid medium. After being cultured at 37°C overnight, the bacteria was observed by taking pictures using a Huawei Mobile (Nova 6).

2.9. Statistical Analysis. Statistical analysis was performed using the SPSS software. All data were expressed as mean ± standard derivation (SD) and statistically analyzed using one-way analysis of variance (ANOVA). $p < 0.05$ is considered to be statistically significant. All of the tests were conducted with no less than three parallel samples.

3. Results and Discussion

3.1. Surface Characterization. Figure 1 shows the representative SEM images of the titanium dioxide nanotubes modified by the different bioactive factors. It is obvious that after different surface modification processes, the surface nanotube structure remains intact. Compared with TNT-Dopa, the surface immobilization of PAA and the loading of GS and Zn^{2+} gradually reduced the diameter of the nanotube and increased the thickness of the tube wall. Furthermore, the chemical group changes on the surface were examined by ATR-FTIR. It can be seen from Figure 2(a) that there was almost no infrared absorption on the unmodified titanium
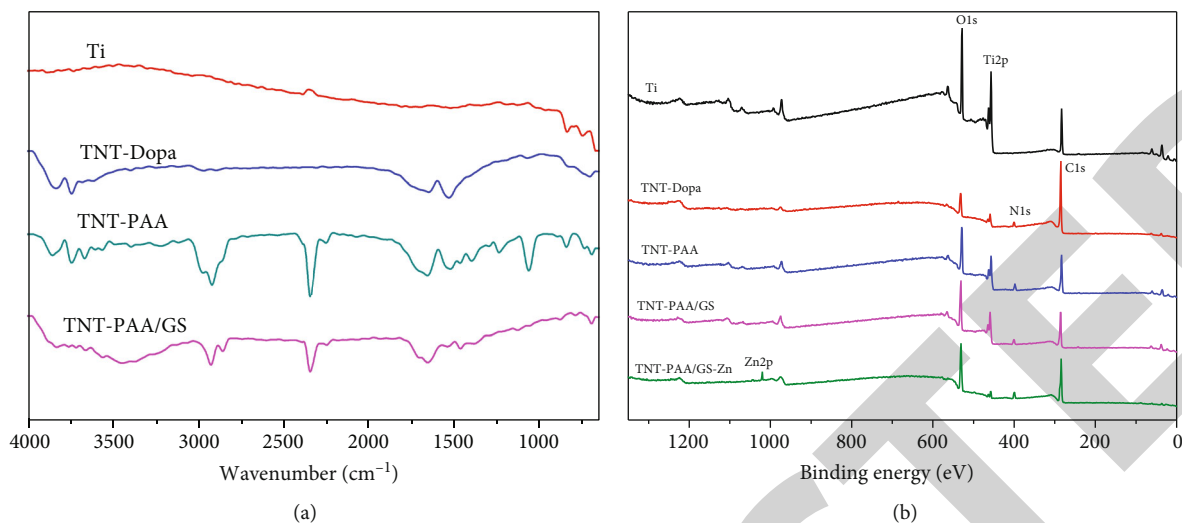
Figure 2: The ATR-FTIR spectra (a) and XPS spectra (b) of the different samples.

surface. Our previous work showed that the anodized TiO_2 nanotubes have a small amount of hydroxyl on the surface [20], but it cannot be directly used to immobilize the bioactive molecules. Dopamine can self-polymerize on the surfaces of almost all solid materials to form polydopamine, which is widely used in the surface modification of biomaterials. The polydopamine coating can easily react with amine or thiol through Michael addition reaction and Schiff base reaction to introduce bioactive substances on the surface. PEI contains rich amine groups and has a large number of positive charges, so it can easily react with polydopamine to form a positively charged surface. PAA is a kind of polymer with rich negative charges and good biocompatibility, which can combine with GS or zinc ions. Therefore, GS and zinc ions can be loaded on the surface by the electrostatic interaction between PEI and PAA. The results of Figure 2(a) show that the stretching vibration and in-plane bending vibration of the -NH bond and -OH bond appeared on the TNT-Dopa surface at 1590 cm^{-1} and 3300 cm^{-1}, respectively, and the stretching vibration of the -OH bond occurred at around 3700 cm^{-1}, indicating that the polydopamine coating had been successfully prepared on the surface. After grafting of PEI, the in-plane bending vibration and stretching vibration of the -CH$_2$ bond can be observed at 1462 cm^{-1} and 2832 cm^{-1}, and the bending vibration of the -NH bond of the primary amine and secondary amine and the stretching vibration of the C-N bond can be detected at 1200 cm^{-1} and 1656 cm^{-1}, indicating that PEI had successfully covalently linked with the polydopamine coating. For TNT-PAA/GS, the stretching vibrations of the C=O bond and the -COOH group appeared at 1519 cm^{-1} and 1694 cm^{-1}, respectively, suggesting that PAA and GS were successfully self-assembled onto the PEI-modified surface. In order to further clarify the surface element composition, the surface element composition of the modified sample was further analyzed by XPS. Figure 2(b) is the XPS diagram of the different samples, and the element compositions are shown in Table 1; it can be seen that the characteristic peaks of C1s (285.2 eV) and N1s (400.3 eV) appeared on the TNT-Dopa. After the

Table 1: The surface element concentration of the different samples measured by XPS.

Sample	Atomic concentration (at.%)				
	Ti	O	C	N	Zn
Ti	61.12	29.86	9.02	0	0
TNT-Dopa	9.28	14.30	71.83	4.59	0
TNT-PAA	9.97	30.42	56.41	3.20	—
TNT-PAA/GS	3.27	31.77	56.20	8.76	—
TNT-PAA/GS-Zn	1.86	28.78	59.73	6.26	3.37

immobilization of PAA, the characteristic peak of O1s (531.8 eV) increased obviously; concurrently, the characteristic peak of C1s (285.2 eV) and carbon content on the surface was reduced, indicating that PAA was successfully grafted onto the surface. For the TNT-PAA/GS, the increased nitrogen content indicated that GS was successfully loaded on the surface. The occurrence of the Zn2p peak (1020.9 eV) on TNT-PAA/GS-Zn proved that the Zn ions were successfully chelated to the surface.

3.2. GS and Zn^{2+} Release Profiles, Surface Hydrophilicity, and Protein Adsorption.
In order to characterize the release profiles of gentamicin and Zn^{2+}, TNT-PAA/GS-Zn was immersed in the PBS solution for different times, and gentamicin and Zn ions were collected to measure the release kinetics curves. As can be seen from the release curve of Figure 3(a), both gentamicin and zinc ions were released over 14 days. After being immersed in PBS solution for 4 h, the release concentration of gentamicin reached 3.9 μg/mL, and the total release concentration was 13.54 μg/mL at the 14th day. Previous studies have shown that the working concentration of gentamicin is 4-20 μg/mL [29]; therefore, the continuous antibacterial activities can last at least 14 days. At the same time, it can also be seen from Figure 3(a) that there was an obvious burst release period of one day for gentamicin and Zn^{2+}. The release rate was relatively large before 1 day, and gentamicin reached 5.5 μg/mL, more than 40% of the total
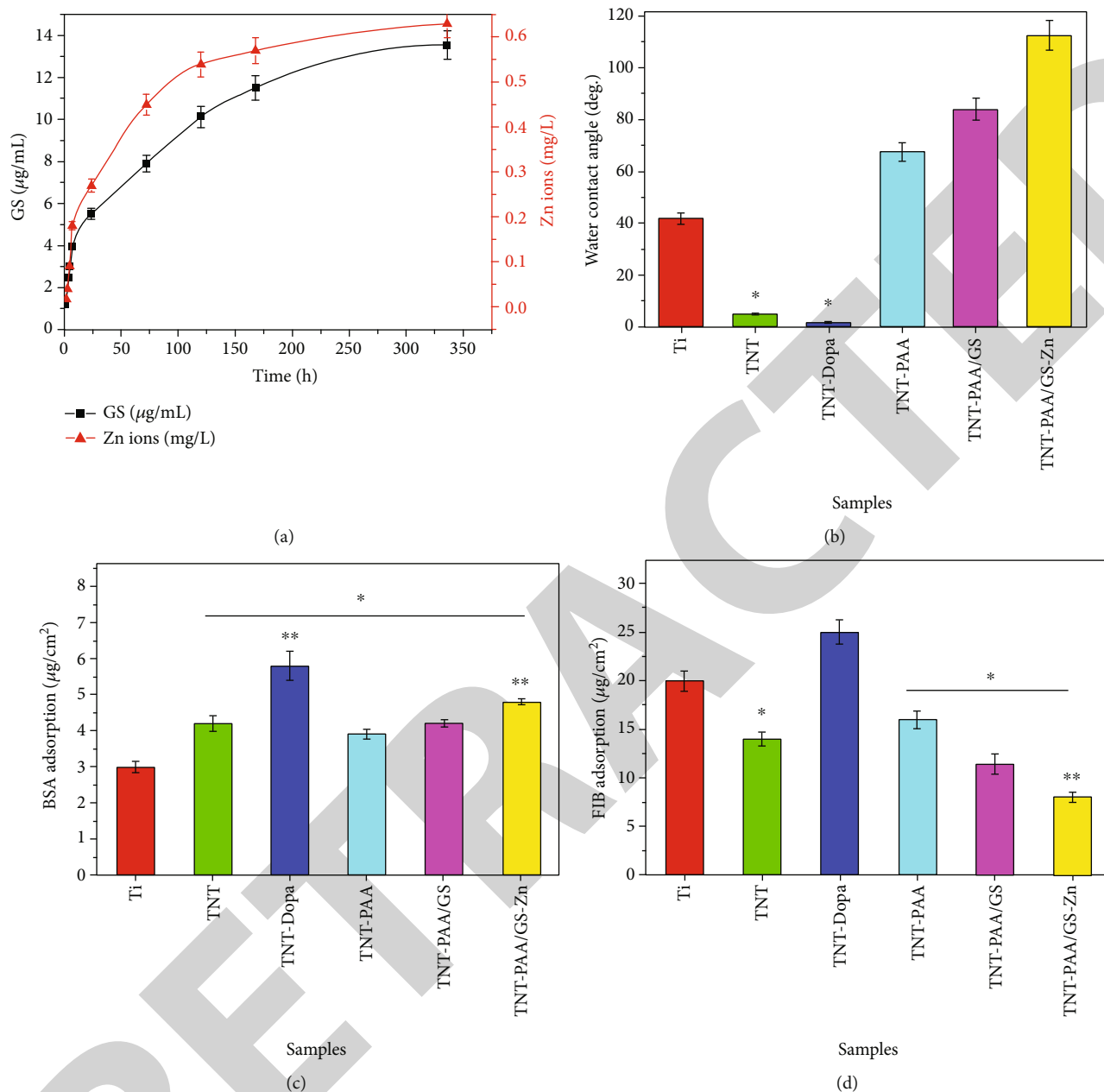
(a)

(b)

(c)

(d)

Figure 3: (a) GS and Zn^{2+} release profiles of TNT-PAA/GS-Zn. (b) The water contact angles of the different samples. (c, d) show BSA and fibrinogen adsorption of the different samples, respectively. Statistical differences are indicated by $^*p < 0.05$ compared with the Ti group and $^{**}p < 0.05$ compared with the Ti and TNT groups.

release in 14 days. After one day, the release rates of gentamicin and zinc ions became stable. After 14 days, the total concentration of zinc ion was 0.63 mg/L. It was reported that zinc ion concentration of 0.49-5.2 mg/L can promote cell viability, proliferation, adhesion, and migration; therefore, the released Zn^{2+} content was within the range of cell physiological concentration.

Biomaterials should have good surface properties to avoid adverse host reactions after contact with organisms [30], in which wettability is an important factor affecting interface biological reactions [31]. The surface hydrophilicity/hydrophobicity is closely related to the protein adsorption

and biocompatibility. Generally speaking, the good wettability is helpful to prevent the nonspecific protein adhesion and promote the cell adhesion and proliferation [32]. As can be seen from Figure 3(b), the water contact angle of the blank titanium decreased obviously after anodizing; it was considered that the introduction of a large amount of oxygen elements and the special nanoporous structure can contribute to the excellent hydrophilicity. Due to the introduction of hydrophilic amine groups after the immobilization of dopamine, TNT-Dopa still had excellent hydrophilicity. However, after the immobilization of PAA, the water contact angle increased significantly, which was mainly because the porous

structure on the surface was filled to some extent after the immobilization of PEI and PAA (as shown in Figure 1), which partially changed the surface morphology and made it difficult for water molecules to enter the interior of the nanotubes, so the contact angle increased. After GS loading, the surface porous structure was further filled, and thus, the water contact angle also increased although the hydrophilic carboxyl groups were introduced. Finally, because the positively charged zinc ions can chelate with the hydrophilic -COOH groups on the surface, combining with the further porous filling, the water contact angle increased further.

It is well known that protein adsorption is the first event when biomaterials contact blood, and it plays a decisive role in the blood compatibility [33]. Albumin and fibrinogen are the two main proteins in the blood. In general, albumin adsorption can reduce platelet adhesion. On the contrary, the adsorption of fibrinogen could increase the platelet adhesion and activation. Figures 3(c) and 3(d) show the adsorption concentrations of bovine serum albumin (BSA) and fibrinogen (Fib) on the different surfaces. As compared to the pristine titanium, the anodized titanium surface can enhance albumin adsorption, while the fibrinogen adsorption decreased to some degree, indicating that the nanotube array can selectively adsorb albumin. It was considered that the behaviors of protein adsorption were related to the surface wettability, surface morphologies, and surface charges [34]. The study showed that when the water contact angle is less than 110°, fibrinogen would preferentially be adsorbed on the hydrophobic surface [35]. At the same time, the superhydrophilic surface is obtained by anodization, which is beneficial to the adsorption of hydrophilic albumin; moreover, the anodized surface has negative charges due to the introduction of a large amount of hydroxyl groups, which is also beneficial to the adsorption of positively charged albumin. The polydopamine has very strong stickiness to lysine-rich proteins [36], so the content of BSA and fibrinogen adsorbed on TNT-Dopa surface increased significantly. It has been shown that the immobilization of polyacrylic acid on the surface can repel the nonspecific protein adsorption because of the hydration layer formed by PAA and the negatively charged character of PAA [37]. Therefore, after the immobilization of PAA on TNT-Dopa, both BSA and fibrinogen adsorption decreased significantly. However, it was worth noting that BSA adsorption returned to the level of titanium oxide nanotubes, while fibrinogen adsorption was slightly higher than that of TNT. Furthermore, after loading GS by the layer-by-layer technique, due to the further increase of hydrophobicity, the adsorption content of BSA did not change significantly, but the adsorption amount of fibrinogen decreased, indicating that with the increase of self-assembly layers, the introduction of a large number of PAA increased the content of negative charges on the surface, so that the negatively charged fibrinogen was not easily adsorbed on the PAA surface, resulting in the decreased fibrinogen adsorption. The zinc ions can chelate with the carboxyl group of PAA to reduce the surface hydrophilicity; at the same time, zinc ion loading reduced the content of negative charges on the surface, so BSA adsorption increased slightly, while the adsorption capacity of fibrinogen further decreased.

3.3. Blood Compatibility. Blood compatibility refers to the required response of blood to exogenous substances or materials, which generally refers to the compatibility between materials and various components of blood [38]. Generally speaking, blood compatibility includes three aspects: the interaction between materials and plasma proteins, the interaction between materials and blood cells, and the interaction between materials and coagulation factors.

Platelets are one of the main components of the human blood. Its main functions are clotting and hemostasis as well as repairing damaged blood vessels. The platelet adhesion to the biomaterial surface is a key event of coagulation. Platelet adhesion, aggregation, and activation will promote blood coagulation. Therefore, the biomaterials with good blood compatibility should have the role of maintaining normal platelet physiological function and can effectively prevent platelet adhesion, aggregation, and activation [39]. At the same time, the increase of cGMP released from platelets can inhibit platelet activation [40]. In this paper, the adhesion and aggregation of platelets were observed by SEM, and the platelet activation was evaluated by measuring the cGMP activities. The results are shown in Figures 4(a)–4(c). There were a large number of platelets adhered to the blank titanium surface, and the adhered platelets displayed the spread state and extended pseudopodia, indicating that the platelets on the titanium surface may have been activated; the results of cGMP further proved this point. After anodization, the number of platelets adhered to the surface was significantly reduced. On the one hand, the anodized TiO_2 nanotube arrays had excellent hydrophilic properties, which can reduce platelet adhesion and aggregation; on the other hand, the selective adsorption of albumin by the TiO_2 nanotube contributed to not only reduce platelet adhesion and aggregation but also promote the expression of cGMP (Figure 4(c)), leading to the improved blood compatibility. For TNT-Dopa, although its hydrophilicity was still excellent, compared with TNT, the number of platelets adhered to the surface was still significantly increased, while the expression of cGMP was also decreased, which could be due to the fact that the polydopamine coating had the ability of nonspecific protein adsorption which can significantly increase the fibrinogen adhesion to the surface so as to enhance platelet adhesion and activation. Compared with the blank titanium and TNT, the number of platelets on the TNT-PAA/GS surface decreased sharply, and the expression of cGMP also increased, indicating that the anticoagulation was enhanced. It was considered that PAA itself is a substance with good blood compatibility and can effectively reduce fibrinogen adsorption [41]. When zinc ions were loaded on the surface, the adsorption amount of fibrinogen further decreased, while the albumin adsorption increased, which not only reduced the adhesion and aggregation of platelets but also increased the cGMP release and inhibited platelet activation. On the other hand, zinc ions can make platelets produce more NO signals which can prevent platelet adhesion and aggregation by inhibiting the thromboxane A2 (TXA-2) receptor [42].
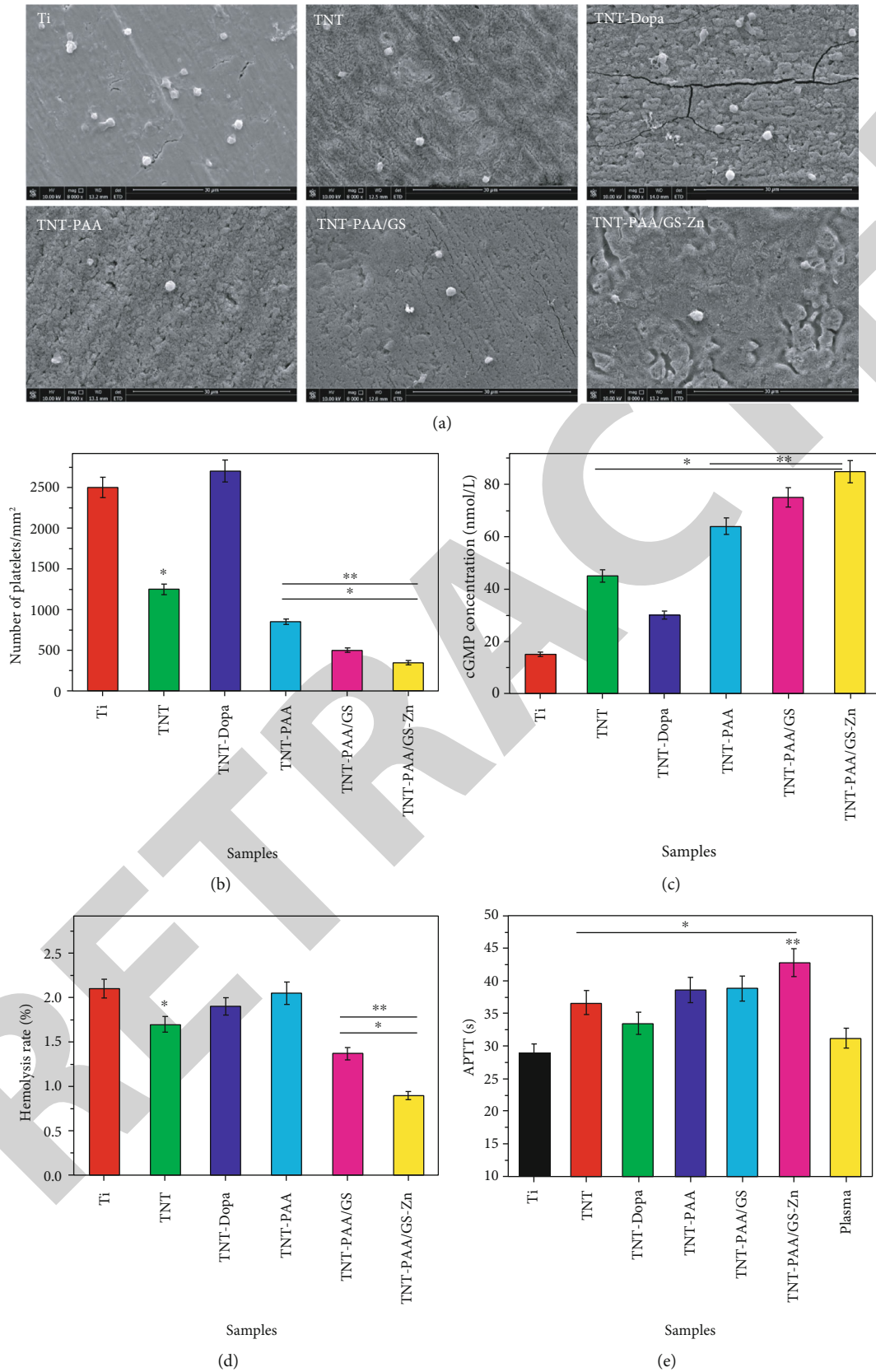
(a)

(b)

(c)

(d)

(e)

FIGURE 4: SEM images (a) and the number (b) of the platelets adhered on the different samples. (c–e) show the cGMP concentration of the attached platelets, hemolysis rate, and APTT of the different samples, respectively. Statistical differences are indicated by $^{*}p < 0.05$ compared with the Ti group and $^{**}p < 0.05$ compared with the Ti and TNT groups.
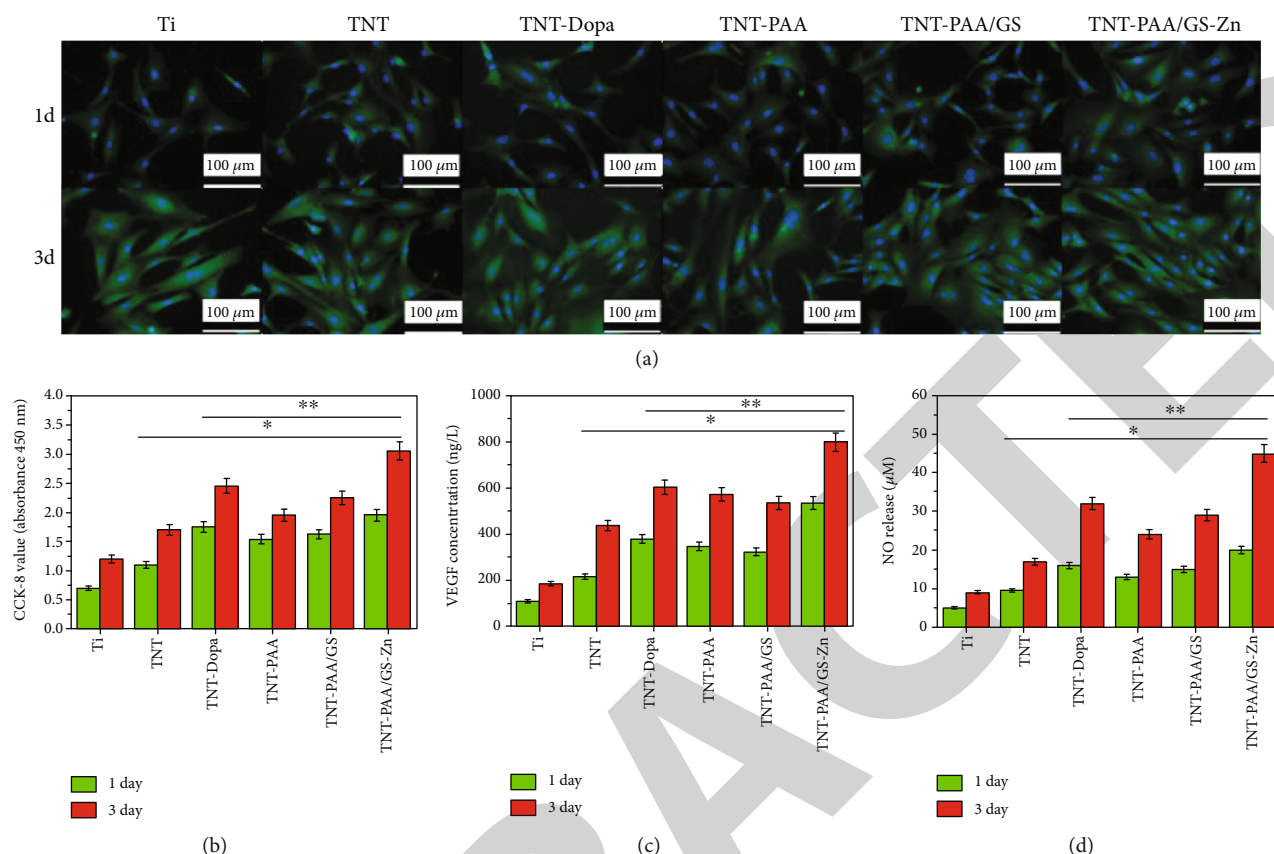
(a)

(b)

(c)

(d)

Figure 5: The fluorescent pictures of endothelial cells adhered to the surfaces of different samples (a). CCK-8 values (b), VEGF (c), and NO (d) activities of endothelial cells grown on the different sample surfaces for 1 and 3 days, respectively. Statistical significance of $p < 0.05$ is indicated by ∗ as compared with the Ti group and by ∗∗ as compared with the Ti and TNT groups.

Therefore, the loading of zinc ions on the surface further improved the blood compatibility.

The effects of the different materials on red blood cells were further studied. Hemolysis rate is one of the important methods to characterize the interaction between materials and red blood cells. According to the international ISO10993-4 standard, the hemolysis rate (HR) above 5% is not suitable to be used as a blood-contacting material. Figure 4(d) shows the hemolysis rates of the different samples. The hemolysis rates of all samples were less than 5%, indicating that none of them could cause severe hemolysis. The hemolysis rate of TiO$_2$ nanotubes was lower than that of pure titanium, but the hemolysis rate increased slightly after the preparation of polydopamine coating. When the composite film of PAA and GS was prepared and the zinc ion was loaded, the hemolysis rate further decreased significantly, indicating that PAA and zinc ions can improve the blood compatibility.

Generally speaking, when the biomaterial interacts with human blood, blood coagulation may happen. Blood coagulation is a complex chain process involving a series of stimulus responses in conjunction with coagulation factors and enzymes, whose intent is to stop blood fluxes when a vascular tissue injury occurs [43]. According to the difference of the initial pathway and participating factors, blood coagulation can be divided into two pathways: endogenous coagulation

and exogenous coagulation. Among them, the endogenous coagulation pathway is initiated by the activation of factor XII [44], and the activated partial thromboplastin time (APTT) is an important method reflecting the endogenous coagulation pathway, especially the activity of coagulation factor XII [45]. Figure 4(e) shows the APTTs of the different samples. It can be seen that the clotting time of blank titanium was shorter than that of normal plasma, indicating that it may promote blood coagulation to a certain extent. However, the clotting time of the anodized titanium was longer than that of normal plasma, suggesting that the surface of the TiO$_2$ nanotube had good anticoagulation performance. Although the clotting time decreased after dopamine surface modification, the clotting time was significantly prolonged after the immobilization of PAA and the loading of GS and Zn^{2+}, indicating that the subsequent surface modification improved the anticoagulant properties of the materials.

3.4. Endothelial Cell Growth Behaviors. Figures 5(a) and 5(b) show the fluorescent images, and the CCK-8 values of endothelial cells adhered to the different surfaces. It can be clearly seen that the number of cells that adhered to the surface of the blank titanium was less than that of other modified samples. After anodizing, the number of adherent cells on the surface increased, and the morphologies of adherent cells displayed the spread state; its proliferation was also improved
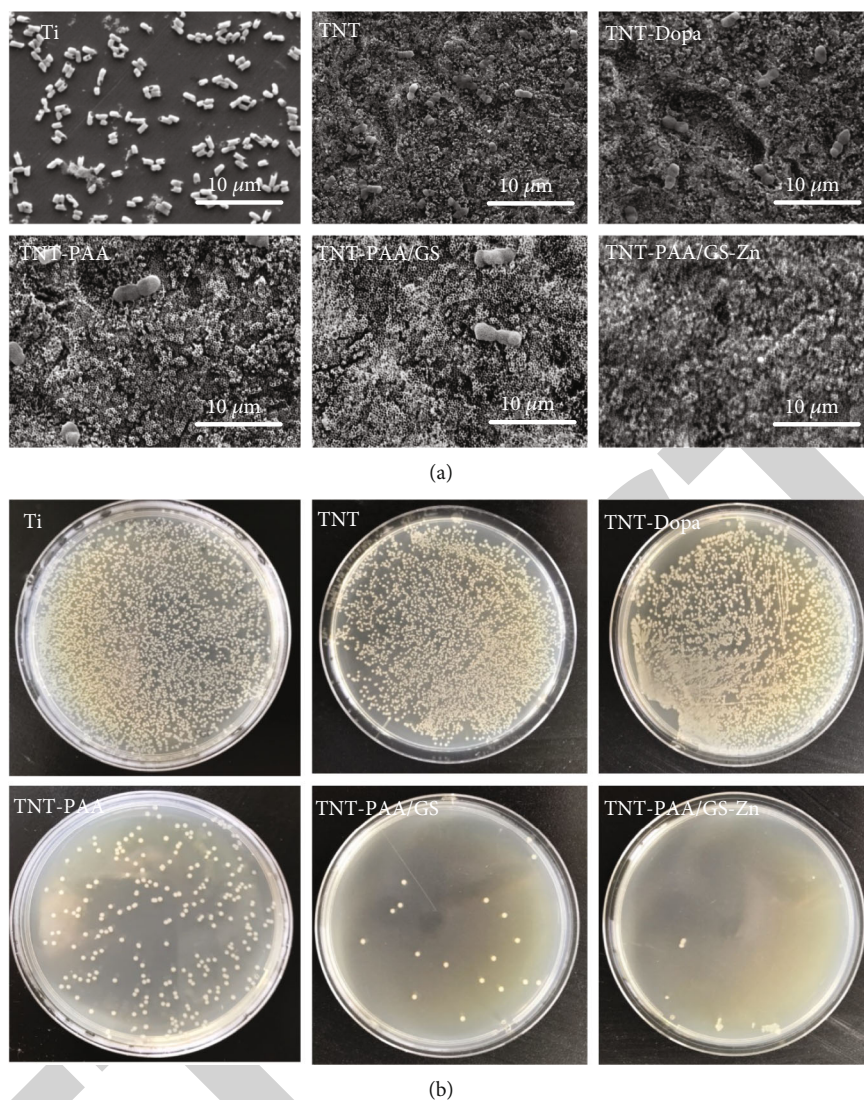
(a)

(b)

Figure 6: The bacterial adhesion (a) and antibacterial properties (b) of the different samples.

(Figure 5(b)). It can be concluded that the surface became more hydrophilic after anodizing, which can improve cell adhesion and proliferation on the surface through the exchange and adsorption of extracellular matrix proteins [46]; moreover, the special nanostructure also contributed to cell adhesion and spreading. The polydopamine coating on the surface can promote the adhesion and proliferation of endothelial cells [47]. Therefore, the number of endothelial cells adhered to TNT-Dopa increased significantly, and the proliferation performance was further improved. After the preparation of the first PAA layer on the PEI-modified TNT surface, due to the cytotoxicity of PEI and the hydrophobicity of PAA, the adhesion of cells to the surface was reduced, and the morphologies of cells did not spread well, so the proliferation of endothelial cells decreased slightly. When PAA and GS were deposited alternately for 10 times, the thickness of the coating increased, which eliminated the effect of PEI on cells. Therefore, the number of endothelial cells attached on the surface increased again, and the spreading and proliferation of endothelial cells were better than

those of TNT-Dopa. Zinc is an essential micronutrient for human health, and Zn^{2+} homeostasis in cells is essential for cell function and survival [48]. Zn^{2+} acts as the first or second messenger and is the signal pathway that triggers physiological functions. In our previous work, zinc ions were doped into TiO_2 nanotubes by the hydrothermal method. The results showed that the release of zinc ions not only increased the anticoagulant properties but also promoted the adhesion and proliferation of endothelial cells [49]. In this study, the zinc ions were loaded on the TNT surface by chelation with PAA. The results of Figure 5 showed that the release of zinc ions from the surface can significantly promote the adhesion and proliferation of the endothelial cells.

Furthermore, the function expression of endothelial cells was studied. Figure 5(c) shows the results of VEGF secretion of endothelial cells on the different samples. It can be seen that, compared with the blank titanium, anodization can promote the expression of VEGF in endothelial cells. When the polydopamine coating was prepared on the surface, due to the enhancement on cell adhesion and proliferation,

endothelial cells could express more VEGF. For TNT-PAA and TNT-PAA/GS, the amount of VEGF decreased slightly as compared to TNT-Dopa, but it was not significant. After zinc ion loading, the content of VEGF increased significantly, indicating that the release of zinc ions can upregulate the VEGF expression of the endothelial cells, which was conducive to maintaining the growth of endothelial cells and promoting the surface endothelialization of the implanted materials. Figure 5(d) shows the NO secretion of endothelial cells grown on the different samples. The NO content released by endothelial cells on the surface increased after anodizing. The NO content for TNT-Dopa was larger because the polydopamine coating can promote the growth of endothelial cells. After further preparation of the PAA film and alternating deposition of PAA and GS, the growth state of cells was slightly worse (Figure 5(a)). At the same time, the content of VEGF release could also indirectly affect the production of eNOS in endothelial cells, thus affecting the release of NO [50]; therefore, the NO content decreased slightly. However, it was worth noting that the loading zinc ions can significantly promote the activity of intracellular NO enzyme and promote the release of NO and thus enhance the NO expression of endothelial cells.

3.5. Antibacterial Activities. Bacterial adhesion is widespread in nature, and there are usually two antibacterial strategies: killing bacteria and reducing bacterial adhesion [51]. In this study, gentamicin and zinc ions were loaded into titanium oxide nanotubes to prevent infection. Gram-negative bacteria-*Escherichia coli* was used as a test strain to evaluate the antibacterial properties of the modified material surface. Figure 6(a) shows the SEM images of bacterial adhesion on the different sample surfaces. It can be seen that although titanium had good biocompatibility to endothelial cells, its antibacterial adhesion property was poor, and there were a large number of *Escherichia coli* adhering to the surface. In contrast, the property of nonspecific protein adsorption caused by the excellent hydrophilicity of the nanotubes and a small number of negative charges on the surface could contribute to inhibit the adhesion of negatively charged *Escherichia coli*. The same with the cell results, polydopamine coating could make *Escherichia coli* adhere to the surface easily; therefore, compared with the TNT sample, the adsorption of bacteria on TNT-Dopa increased. When PAA was prepared on the surface, the number of negative charges increased, which reduced the adhesion of *Escherichia coli* to the surface. Moreover, after the multilayer film of PAA and GS was prepared, the increased negative charges on the surface and the continuous GS release could further prevent the negatively charged *Escherichia coli* to stay on the surface. Due to the antibacterial and bactericidal activity of releasing zinc ions [52], there was almost no bacterial adhesion on TNT-PAA/GS-Zn. Figure 6(b) shows the antibacterial properties of the different samples, from which it can be seen that pure titanium, TiO$_2$ nanotubes, and dopamine coating had poor bactericidal properties. After further immobilization of PAA, the number of *Escherichia coli* colonies decreased significantly, indicating that the PAA coating had certain antibacterial properties. When the PAA and GS composite coating was prepared, the release of GS could effectively kill bacteria, so the number of observed colonies decreased significantly. Finally, the zinc ion can also inactivate the protein needed by bacteria and cause the condensation of DNA [53], so the antibacterial activity was further improved after Zn^{2+} loading.

4. Conclusion

In this paper, PAA/GS-Zn multifunctional bioactive coating was successfully prepared on the titanium surface with a nanostructure. The specific nanotube structure and the following functionalization significantly influenced the surface hydrophilicity, protein adsorption, blood compatibility, and endothelial cell growth behaviors of the materials. TiO$_2$ nanotubes had excellent hydrophilicity, but after the immobilization of PAA and loading of GS and zinc ions, the hydrophilicity became worse due to the decrease of the nanotube diameter. The superhydrophilic TiO$_2$ can selectively promote albumin adsorption, while the immobilization of PAA and the loading of GS and zinc ions can prevent the nonspecific protein adsorption. At the same time, combining the good blood compatibility and negative charged characteristics of PAA with the physiological activity of zinc ions, PAA/GS-Zn coating can not only significantly prevent platelet adhesion, aggregation, and activation but also reduce the hemolysis rate and increase the activated partial thromboplastin time, thus significantly improving the blood compatibility. In addition, the anodized nanotube array can promote endothelial cell adhesion and proliferation and upregulate expression of VEGF and NO. Although PAA/GS coating can promote cell adhesion and proliferation and upregulate NO expression, it cannot significantly promote the VEGF expression. Loading Zn^{2+} can not only significantly promote endothelial cell adhesion and proliferation but also upregulate the NO and VEGF expression. Finally, due to the continuous and slow release of GS and zinc ions, the surface-modified materials showed good antibacterial and germicidal efficacy to Escherichia coli.

Data Availability

The data used to support the findings of this study are included within the article.

Disclosure

This paper can be found as the presentation of the manuscript in Research Square (https://www.researchsquare.com/article/rs-50126/v1). Yuebin Lin and Li Zhang should be considered as co-first authors.

Conflicts of Interest

The authors declare that they have no known potential conflicts of interest.

Authors' Contributions

Yuebin Lin and Li Zhang contributed to the methodology, investigation, and writing—original draft. Ya Yang, Minhui Yang, and Qingxiang Hong contributed to the investigation and writing—original draft. Keming Chang and Juan Dai contributed to the cell experiments. Changjiang Pan contributed to the conceptualization, resources, supervision, and writing—review and editing. Yanchun Wei and Li Quan contributed to the blood compatibility experiments. Zhongmei Yang and Sen Liu contributed to the writing—review and editing. Yuebin Lin and Li Zhang contributed equally to this work.

Acknowledgments

References

[1] K. S. Lavery, C. Rhodes, A. McGraw, and M. J. Eppihimer, "Anti-thrombotic technologies for medical devices," *Advanced Drug Delivery Reviews*, vol. 112, pp. 2–11, 2017.

[2] R. Gbyli, A. Mercaldi, H. Sundaram, and K. A. Amoako, "Achieving totally local anticoagulation on blood contacting devices," *Advanced Materials Interfaces*, vol. 5, no. 4, 2018.

[3] P. Q. Nguyen, N. M. D. Courchesne, A. Duraj-Thatte, P. Praveschotinunt, and N. S. Joshi, "Engineered living materials: prospects and challenges for using biological systems to direct the assembly of smart materials," *Advanced Materials*, vol. 30, 2018.

[4] L. Bacakova, E. Filova, M. Parizek, T. Ruml, and V. Svorcik, "Modulation of cell adhesion, proliferation and differentiation on materials designed for body implants," *Biotechnology Advances*, vol. 29, no. 6, pp. 739–767, 2011.

[5] M. F. Maitz, M. C. L. Martins, N. Grabow et al., "The blood compatibility challenge. Part 4: Surface modification for hemocompatible materials: Passive and active approaches to guide blood- material interactions," *Acta Biomaterialia*, vol. 94, pp. 33–43, 2019.

[6] Y. Xiao, W. Wang, X. Tian et al., "A versatile surface bioengineering strategy based on mussel-inspired and bioclickable peptide mimic," *Research*, vol. 2020, pp. 1–12, 2020.

[7] J. Li, L. Chen, X. Zhang, and S. Guan, "Enhancing biocompatibility and corrosion resistance of biodegradable Mg-Zn-Y- Nd alloy by preparing PDA/HA coating for potential application of cardiovascular biomaterials," *Materials Science and Engineering: C*, vol. 109, p. 110607, 2020.

[8] A. E. Rodda, L. Meagher, D. R. Nisbet, and J. S. Forsythe, "Specific control of cell-material interactions: targeting cell receptors using ligand-functionalized polymer substrates," *Progress in Polymer Science*, vol. 39, no. 7, pp. 1312–1347, 2014.

[9] G. Pan, B. Guo, Y. Ma et al., "Dynamic introduction of cell adhesive factor via reversible multicovalent phenylboronic acid/cis-diol polymeric complexes," *Journal of the American Chemical Society*, vol. 136, no. 17, pp. 6203–6206, 2014.

[10] L. Cao, Y. Qu, C. Hu et al., "A universal and versatile approach for surface biofunctionalization: layer-by-layer assembly meets host–guest chemistry," *Advanced Materials Interfaces*, vol. 3, no. 18, 2016.

[11] X. Li, P. Gao, J. Tan et al., "Assembly of metal-phenolic/catecholamine networks for synergistically anti-inflammatory, antimicrobial, and anticoagulant coatings," *ACS Applied Materials & Interfaces*, vol. 10, no. 47, pp. 40844–40853, 2018.

[12] X. D. Wu, C. J. Liu, H. P. Chen, Y. F. Zhang, L. Li, and N. Tang, "Layer-by-layer deposition of hyaluronan and quercetin-loaded chitosan nanoparticles onto titanium for improving blood compatibility," *Coatings*, vol. 10, no. 3, p. 256, 2020.

[13] M. Kushwaha, J. M. Anderson, C. A. Bosworth et al., "A nitric oxide releasing, self assembled peptide amphiphile matrix that mimics native endothelium for coating implantable cardiovascular devices," *Biomaterials*, vol. 31, no. 7, pp. 1502–1508, 2010.

[14] I. Junkar, M. Kulkarni, M. Benčina et al., "Titanium dioxide nanotube arrays for cardiovascular stent applications," *ACS Omega*, vol. 5, no. 13, pp. 7280–7289, 2020.

[15] S. Minagar, C. C. Berndt, J. Wang, E. Ivanova, and C. Wen, "A review of the application of anodization for the fabrication of nanotubes on metal implant surfaces," *Acta Biomaterialia*, vol. 8, no. 8, pp. 2875–2888, 2012.

[16] K. Lee, A. Mazare, and P. Schmuki, "One-dimensional titanium dioxide nanomaterials: nanotubes," *Chemical Reviews*, vol. 114, no. 19, pp. 9385–9454, 2014.

[17] D. Khudhair, A. Bhatti, Y. Li et al., "Anodization parameters influencing the morphology and electrical properties of TiO_2 nanotubes for living cell interfacing and investigations," *Materials science & engineering C, Biomimetic and supramolecular systems*, vol. 59, pp. 1125–1142, 2016.

[18] S. Zhong, R. Luo, X. Wang et al., "Effects of polydopamine functionalized titanium dioxide nanotubes on endothelial cell and smooth muscle cell," *Colloids and Surfaces B: Biointerfaces*, vol. 116, pp. 553–560, 2014.

[19] A. Roguska, M. Pisarek, A. Belcarz et al., "Improvement of the bio-functional properties of TiO_2 nanotubes," *Applied Surface Science*, vol. 388, pp. 775–785, 2016.

[20] Z. Gong, Y. Hu, F. Gao et al., "Effects of diameters and crystals of titanium dioxide nanotube arrays on blood compatibility and endothelial cell behaviors," *Colloids and Surfaces B: Biointerfaces*, vol. 184, p. 110521, 2019.

[21] A. Krężel and W. Maret, "The biological inorganic chemistry of zinc ions," *Archives of Biochemistry and Biophysics*, vol. 611, pp. 3–19, 2016.

[22] P. D. Zalewski, J. F. Beltrame, A. A. Wawer, A. I. Abdo, and C. Murgia, "Roles for endothelial zinc homeostasis in vascular physiology and coronary artery disease," *Critical Reviews in Food Science and Nutrition*, vol. 59, no. 21, pp. 3511–3525, 2019.

[23] S. Choi, X. Liu, and Z. Pan, "Zinc deficiency and cellular oxidative stress: prognostic implications in cardiovascular diseases," *Acta Pharmacologica Sinica*, vol. 39, no. 7, pp. 1120–1132, 2018.

[24] X. Cai, G. J. Dai, S. Z. Tan, Y. Ouyang, Y. S. Ouyang, and Q. S. Shi, "Synergistic antibacterial zinc ions and cerium ions loaded α-zirconium phosphate," *Materials Letters*, vol. 67, no. 1, pp. 199–201, 2012.

[25] T. Alzahrani, A. P. Liappis, L. M. Baddour, and P. E. Karasik, "Statin use and the risk of cardiovascular implantable

Research Article

Surface Modification with NGF-Loaded Chitosan/Heparin Nanoparticles for Improving Biocompatibility of Cardiovascular Stent

Haixin Song [iD],[1] **Tao Wu** [iD],[1] **Xiaotian Yang,**[1] **Yangzheng Li,**[1] **Ye Ye,**[1] **Bo Li** [iD],[2] **Tao Liu,**[3] **Shihui Liu** [iD],[3] **and Jianhua Li** [iD][1]

[1]*Department of Rehabilitation, Sir Run Run Shaw Hospital, College of Medicine, Zhejiang University, Hangzhou, 310000 Zhejiang Province, China*
[2]*Department of Rehabilitation, Tongde Hospital of Zhejiang Province, Hangzhou, 310000 Zhejiang Province, China*
[3]*Medical College of Acu-Moxi and Rehabilitation, Guangzhou University of Chinese Medicine, Guangzhou, 510006 Guangdong Province, China*

Correspondence should be addressed to Bo Li; zj2010libo@163.com, Shihui Liu; liushihui@gzucm.edu.cn, and Jianhua Li; jianhua_li@zju.edu.cn

Late thrombosis and restenosis remain major challenges to the safety of drug-eluting stents. Biofunctional modification to endow the surface with selective anticoagulation and promote endothelium regeneration has become a hotpot recently. In this study, chitosan and heparin were found to form three-dimensional nanoparticles by spontaneous electrostatic interaction. Based on the specific binding properties between heparin and nerve growth factor (NGF), a new type of NGF-loaded heparin/chitosan nanoparticles was constructed for surface modification. The results of material characterization show that the nanoparticles are successfully immobilized on the surface of the material. In vitro blood compatibility and endothelial cell compatibility assay showed that the modified surface could selectively inhibit platelet adhesion and smooth muscle cell overproliferation, while accelerating endothelialization via promoting endothelial cell proliferation and enhancing endothelial progenitor cell mobilization.

1. Introduction

Percutaneous coronary intervention by using drug-eluting stent (DES) system is the main method for the treatment of cardiovascular diseases. Commonly, DES is mainly composed of metal stents, antiproliferative drugs (such as rapamycin and paclitaxel), and polymer coatings. However, due to the insufficient biocompatibility of polymers and the nonspecific effects of antiproliferative drugs, delayed endothelial healing and chronic inflammation may occur after stent implantation and raise the risk of late in-stent thrombus and restenosis [1]. In this regard, the researchers suggest that the biofunctional modification of the vascular stent surface may contribute to improve the biocompatibility and reduce the incidence of postoperative complications.

Vascular endothelium is the natural barrier between blood and vascular tissue, which mediated the metabolic exchange between blood and tissue and can synthesize a variety of bioactive substances to ensure the normal contraction and relaxation of blood vessels as well as inhibit blood coagulation and maintain the biological function of smooth muscle cells [2, 3]. Therefore, it is widely accepted that the rapid formation of a complete endothelium layer on stent surface will be an ideal way to reduce the risk of complications after implantation [4]. Since the discovery of endothelial progenitor cells (EPCs), the mechanism of regeneration and healing after vascular endothelium injury has been redefined as the combined action of EC proliferation and migration from the surrounding vascular tissue and EPC mobilization and homing from the bone marrow. The process of

endothelialization *in vivo* largely depends on the ordered synergistic effect of cytokines and extracellular matrix proteins on ECs and EPCs [5, 6]. Hence, various cytokines and adhesive proteins including VEGF [7], SDF-1 [8], laminin [9], collagen [10], and fibronectin [11] were incorporated into material surface to accelerate endothelialization. However, as bioactive macromolecules, proteins and cytokines have a short half-life *in vivo* and how to prevent the rapid inactivation of biological macromolecules *in vivo* continues to be problematic and needs to be solved urgently.

In recent years, multifunctional nanoparticle systems have shown great potential in controlling the release of biomolecules and regulating the behavior of vascular cells. Compared with other controlled release systems, the unique nanoeffect of the nanoparticle system greatly increases its drug loading capacity and can separate the active molecules from the surrounding environment to avoid rapid deactivation. In this regard, the researchers proposed to build biofunctional nanocoating with 3D structure on the surface of cardiovascular materials to enhance the biological activity and prolong the action duration of biomolecules, so as to achieve long-term and effective regulation of intravascular biological reactions [12]. Zhou et al. [13] covalently immobilized VEGF-loaded polycaprolactone (PCL) nanoparticles on acellular scaffolds and found that the nanocoating could significantly reduce the sudden release of biomolecules and promote the endothelialization of the material surface. Mohammadi et al. [14] introduced heparin/chitosan nanoparticles on the surface of anodized NiTi alloy and proved that the nanocoating can improve the surface blood compatibility and endothelial cell compatibility through controlled biomolecule release. In our previous study, a novel kind of heparin/poly-l-lysine nanoparticles was constructed for stent surface modification. We proved that this kind of nanocoating can effectively inhibit blood coagulation and reduce the occurrence of restenosis [15, 16]. However, some defects such as poor endothelial cell compatibility and significant cytotoxicity of high molecular weight poly-l-lysine continue to be resolved.

In this study, a new type of heparin/chitosan nanoparticles loaded with nerve growth factor (NGF) was designed for surface modification of cardiovascular materials. Chitosan (CHS) is a kind of natural polycationic polysaccharide, which has excellent antibacterial functions, promoting injury repair and reducing inflammatory reaction. In addition, CHS is also one of the most commonly used drug carriers due to its remarkable advantages such as biocompatibility, biodegradability, and easy chemical modification characteristics [17, 18]. NGF is an important neurotrophic factor, which plays an important role in maintaining the normal function of vascular endothelial tissue [19]. Studies have shown that NGF can promote the mobilization and homing of vascular endothelial progenitor cells (EPCs), showing the potential to accelerate the repair of vascular endothelial injury [20, 21]. NGF is also a heparin-binding protein; in this study, NGF was loaded into heparin/chitosan nanoparticles via the specific interaction between NGF and heparin to improve the cellular compatibility and accelerate endothelialization. According to a series of material charac-

TABLE 1: Size and zeta potential of prepared nanoparticles.

	Size (nm)	Zeta potential (mV)	PDI
CHS/Hep NPs	147.8 ± 6.7	-25.6 ± 1.7	0.107 ± 0.011
CHS/Hep@NGF NPs	133.4 ± 5.5	-25.4 ± 1.2	0.069 ± 0.008

terization, *in vitro* blood compatibility and cellular compatibility evaluation, this study has proved that the surface modification of nanoparticles can effectively improve the anticoagulant properties of materials and accelerate endothelium regeneration.

2. Materials and Methods

2.1. Materials and Reagents. 316L stainless steel (316L SS) was processed into round shape (Φ 10 mm, ~1.2 mm in thickness) and mirror polished. Dopamine (DA), toluidine blue O (TBO), and heparin (Hep) were purchased from Sigma-Aldrich. Chitosan (CHS, deacetylation $\geq$ 95%), rhodamine 123, and alcian blue were purchased from Shanghai Aladdin BioChem Technology Co., LTD.

2.2. CHS/Hep Nanocoating Construction. Firstly, a certain amount of CHS and Hep powder was dissolved in 0.1 M acetic acid/sodium acetate buffer (pH = 5), respectively. Then, equal volume of CHS was added dropwisely to the Hep solution (concentration ratio 1 mg/ml : 7.5 mg/ml) under magnetic stirring at room temperature to obtain the CHS/Hep nanoparticle suspension. For CHS/Hep@NGF nanoparticle preparation, 15 mg/ml Hep was firstly mixed with equal volume of 200 ng/ml NGF solution to obtain Hep@NGF mixture. The polydopamine coating was prepared on the surface of 316L SS (termed as SS-DA) according to the method described in our previous work [16]. After that, SS-DA was immersed in 0.5 ml CHS/Hep or CHS/Hep@NGF nanoparticle suspension and incubated at room temperature with gently shaking for 12 h to acquire the nanocoating (termed as SS-DA-NP or SS-DA-NP@NGF).

2.3. Size and Zeta Potential Assay. The mean size and particle dispersion index (PDI) as well as zeta potential of the prepared nanoparticles were determined by dynamic light scattering (DLS) using a ZETA-SIZER, MALVERN Nano-2S90 (Malvern Ltd., Malvern, UK).

2.4. FTIR and XPS Assay. Fourier transform infrared spectroscopy (FTIR) and X-ray photoelectron spectroscopy (XPS) were used to detect the alteration of the surface chemical structure and elemental composition during nanoparticle immobilization. The FTIR assay was performed on a Nicolet IS20 infrared spectrometer (Thermo, USA) using the model of attenuated total reflection. Infrared adsorption between 4000 and 650 cm^{-1} was recorded at room temperature. The XPS analysis was carried out by using VGESCALAB MK II spectrometer with a monochromatic Mg Ka X-ray source (1253.6 eV). The pressure of testing chamber was set as 8×10^{-8} Pa. The scale of binding energy was referenced by adjusting the C1s peak at 284.6 eV.
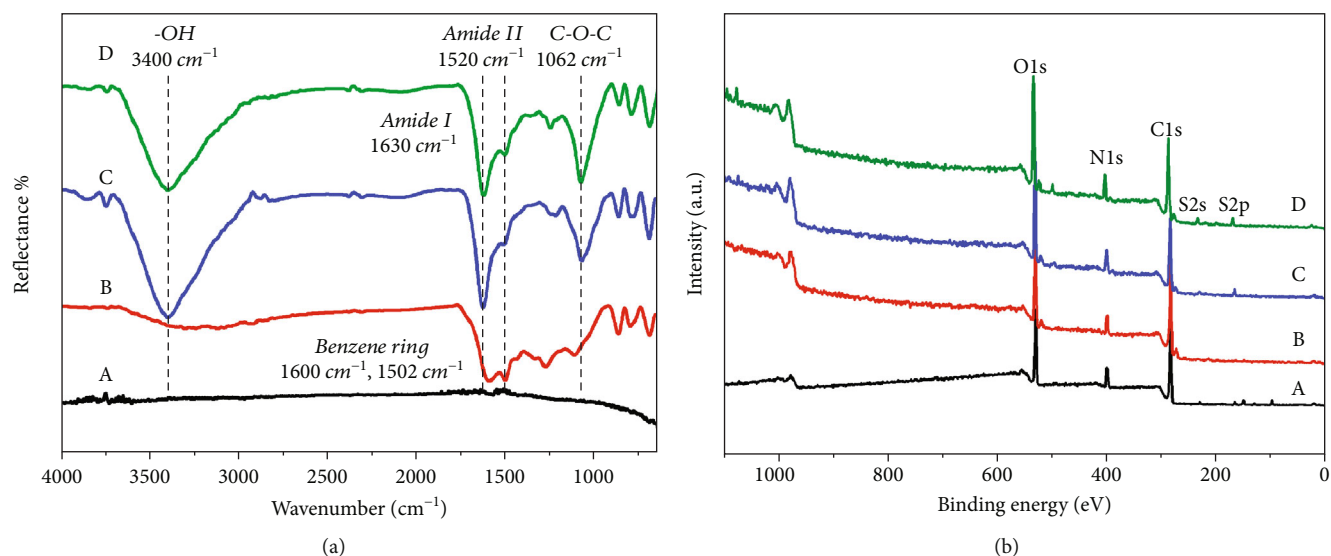
Figure 1: Surface chemical composition determined by (a) FTIR spectra and (b) XPS wide-scan spectra. (a)~(d) refer to 316L SS, SS-DA, SS-DA-NP, and SS-DA-NP@NGF, respectively.

2.5. AFM Assay. The alteration of surface topography after NP modification was determined by atom force microscopy (AFM) (CSPM 6000, Being Nano-Instruments, China) in tapping model at room temperature with subsequent image analysis using CSPM Imager software. Before AFM analysis, the samples were rinsed twice with UP water and the surface was carefully blown dry.

2.6. Water Contact Angle Assay. The hydrophilicity of the samples was determined by measuring the static water contact angle using a Krüss GmbH DSA100 Mk 2 goniometer at room temperature. A droplet of UP water was added to the dried surface, and then, the contact angle was calculated by a circle segment function of the DSA 1.8 software. At least three different sites were taken into measurement for each sample.

2.7. Quantitative Characterization of Hep and Amine Group. The density of exposed amine group and heparin was determined by acid orange II (AO II) and TBO assay, respectively. Detailed method was according to our previous study [16].

2.8. In Vitro Blood Compatibility Evaluation. Fresh whole blood from a healthy volunteer was anticoagulated with sodium citrate (3.8 wt.%) at 9 : 1 and centrifuged at 1500 rpm for 15 min to obtain platelet-rich plasma (PRP). Next, $50\,\mu$l PRP was added to each sample surface and incubated at 37°C for 2 h. Subsequently, the samples were rinsed gently with normal saline and used for morphology observation, lactate dehydrogenase (LDH) release, and P-selectin expression assay. Detailed method was according to our previous study [15].

2.9. In Vitro Cellular Compatibility Evaluation

2.9.1. EC and SMC Proliferation Assay. Endothelial cells (ECs) were isolated from a human umbilical vein and cul-

Table 2: Surface elemental composition determined by XPS.

Samples	C%	N%	O%	S%
316L SS	69.30	5.76	24.83	0.12
SS-DA	74.74	7.98	17.27	0
SS-DA-NP	65.78	9.68	23.44	1.11
SS-DA-NP@NGF	63.58	11.87	23.68	0.87

tured in DMEM/F12 medium containing 15% fetal bovine serum (FBS) and $20\,\mu$g/ml endothelial cell growth supplement (ECGS). Smooth muscle cells (SMCs) were isolated from a human umbilical artery and cultured in DMEM/F12 medium (high glucose) containing 10% FBS. Before cell seeding, the dopamine-coated samples were sterilized by autoclaving, and the subsequent nanocoating construction was carried out under sterile conditions.

For cell proliferation assay, ECs or SMCs were seeded on the surface of each sample at the density of 5×10^4 cells/cm^2 and incubated at 37°C under 5% CO_2 for 1 day and 3 days. At each time point, the supernatant was removed, and $500\,\mu$l fresh culture medium containing 10% CCK-8 reagent was added and incubated for 4 h. Then, $200\,\mu$l culture medium was transferred to a 96-well plate, and the absorbance was measured at 450 nm. The samples were gently rinsed with normal saline and fixed in 2.5% glutaraldehyde at room temperature for at least 6 h. Subsequently, $50\,\mu$l rhodamine 123 solution was added to the surface of each sample and incubated at room temperature for 30 min. Finally, the samples were thoroughly rinsed with normal saline and the morphology of adherent ECs was observed by inverted fluorescent microscopy.

2.9.2. EPC Mobilization and Homing. The mobilization and homing behavior of EPCs to the material surface induced by the nanoparticle coating was studied in vitro by transwell
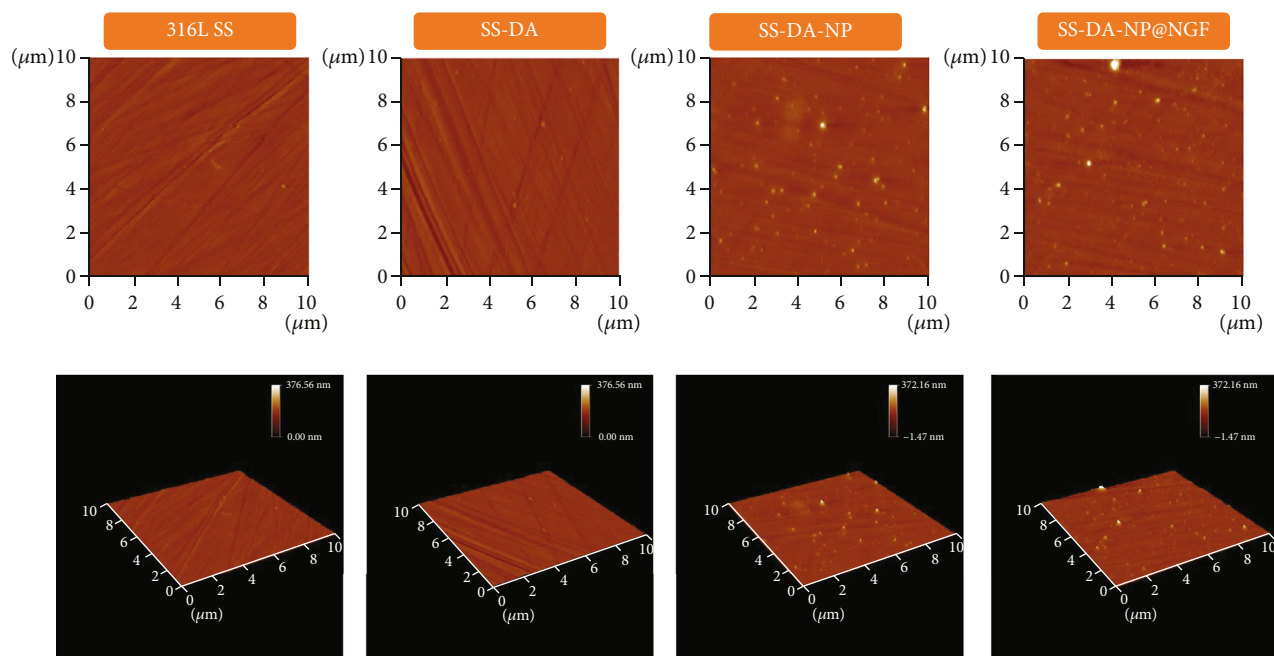
FIGURE 2: AFM images of CHS/Hep and CHS/Hep@NGF NP-modified surface.

chamber method described by Liu et al. [22]. In detail, 3 ml fresh medium (α-MEM medium containing 10% FBS) was added to a 6-well plate, and then, 2 ml EPC suspension with the density of 5×10^5 cells/ml was added to a 6-well Millipore transwell chamber with a bottom membrane pore diameter of 8 μm. After incubation at 37°C for 2 hours, the sterilized samples with a size of $2 \times 2\,cm^2$ were immersed in the medium of 6-well plate and cultured at 37°C for 24 hours. After that, the transwell chamber was rinsed gently with normal saline and then fixed at room temperature in 90% ethanol solution for 30 minutes. The cells in the upper layer of the chamber were wiped with a wet cotton swab, and the chamber was placed in 0.1% crystal violet solution and stained at room temperature for 15 minutes. The cell mobilization in the lower layer of the chamber was observed under an inverted microscope.

2.10. Statistical Analysis. All the biological experiments were performed at least three times. The statistical data was analyzed using SPSS 22.0 software. Statistical evaluation of the data was performed using one-way ANOVA. The probability value $p < 0.05$ was considered significant.

3. Results and Discussion

3.1. Size and Zeta Potential of NPs. As shown in Table 1, the average particle size of CHS/Hep@NGF (133.4 ± 5.5 nm) was slightly decreased compared with that of CHS/Hep (147.8 ± 6.7 nm), which indicate that the incorporation of NGF may enhance the compactness of nanoparticles. The absolute value of zeta potential of both CHS/Hep and CHS/Hep@NGF was greater than 20 mV, indicating that the particle system had adequate stability to avoid the settlement caused by particle agglomeration. Besides, the PDI

(particle dispersion index) of CHS/Hep and CHS/Hep@NGF was less than 0.2, indicating that the prepared nanoparticles have excellent size uniformity.

3.2. FTIR and XPS. In this paper, FTIR and XPS were used to detect the changes of chemical groups and element composition on material surface before and after the immobilization of NPs. As shown in Figure 1(a), the peak at 1600 cm^{-1} in the SS-DA spectrum represents the C=C bond of the benzene ring, and the peak at 1502 cm^{-1} represents the π bond of the benzene ring. New absorption peaks appeared in the infrared spectra of CHS/Hep NP-modified samples. Among them, the peaks at 1630 cm^{-1} and 1520 cm^{-1} refer to the stretching vibrations of amide I band and amide II band. These peaks mainly derived from the amides and amines in chitosan molecules. Besides, the vibration peak of C-O-C bond can be observed at 1062 cm^{-1}, which indicates the existence of heparin.

According to XPS result (Figure 1(b)), it was found that the absorption peak of S2s and S2p could be observed in the spectra of SS-DA-NP and SS-DA-NP@NGF, which demonstrated the existence of heparin. Elemental calculation results (Table 2) further proved the incorporation of NGF may significantly increase the content of N element, while the decrease of S element content may be related to the spatial shielding effect caused by the interaction between NGF and Hep. In summary, the above results show that CHS/Hep and CHS/Hep@NGF NPs are successfully immobilized on the surface of the material.

3.3. Morphology of NP-Modified Surface. The changes of surface morphology of different samples were detected by AFM. As shown in Figure 2, few numbers of particles could be observed on the surface of SS-DA, which may be produced

316L SS
58.9 ± 2.7°

SS-DA
67.5 ± 4.2°

SS-DA-NP
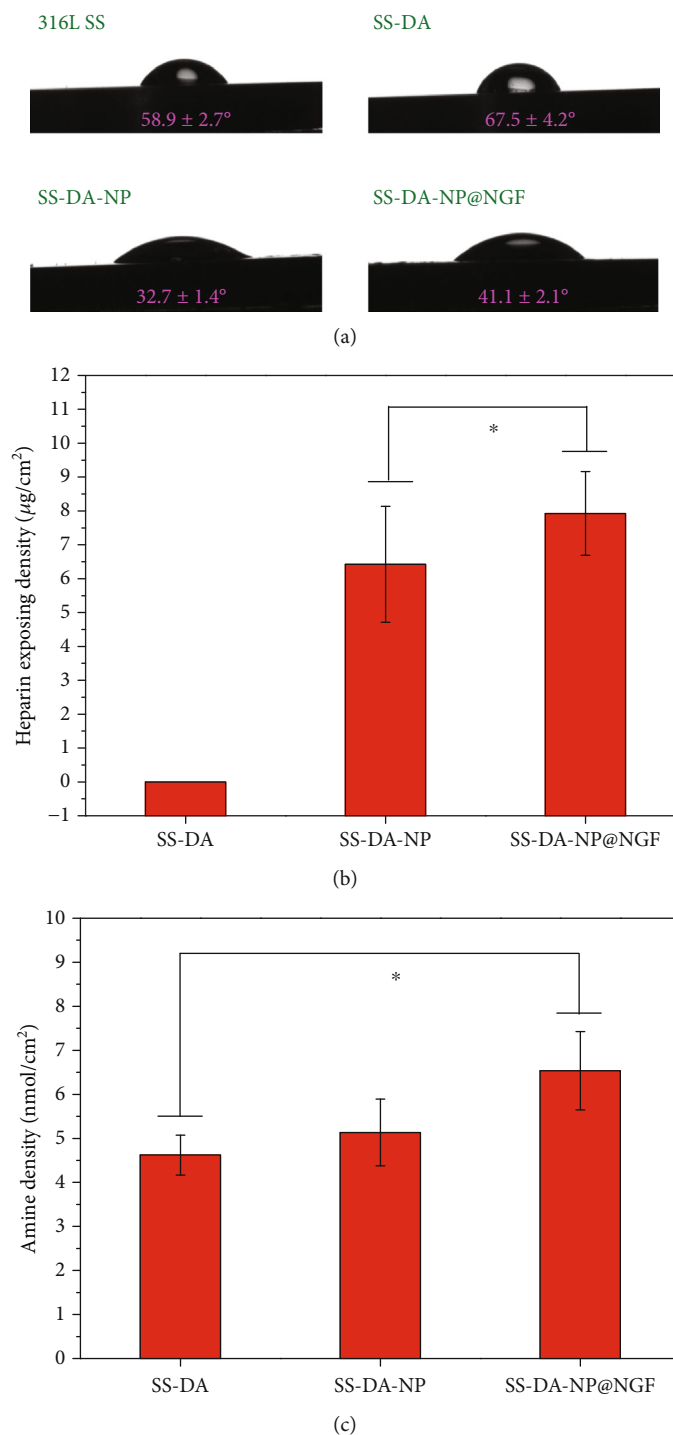32.7 ± 1.4°

SS-DA-NP@NGF
41.1 ± 2.1°

(a)

(b)

(c)

FIGURE 3: (a) Water contact angle of different sample surfaces. Quantitative characterization result of (b) heparin and (c) amine group exposing density (mean ± SD, $N = 6$, *$p < 0.05$ indicates significant difference).

during the polymerization of dopamine. A large number of nanoparticles appeared on the surface of the samples modified by CHS/Hep and CHS/Hep@NGF NPs, and the particle size was in the range of 100 to 200 nm, which was consistent with the results of particle size detection. In addition, the nanoparticles were uniformly distributed on the surface of the sample, with no obvious particle agglomeration found.

3.4. Surface Hydrophilicity Characterization Result. As shown in Figure 3(a), the water contact angle of SS-DA was obviously increased compared with that of 316L SS, which is mainly due to the hydrophobic structure of benzene ring in dopamine coating. The immobilization of CHS/Hep nanoparticles significantly improved the surface hydrophilicity, mainly due to the rich hydrophilic groups
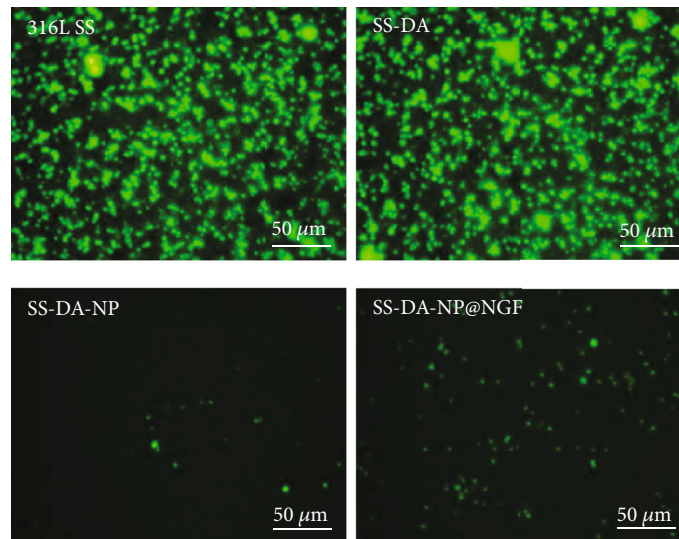
(a)
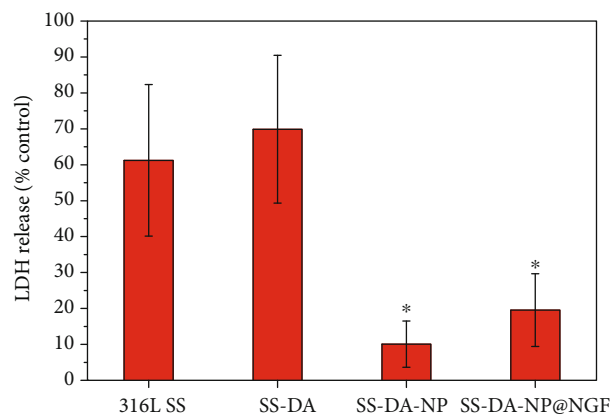
(b)
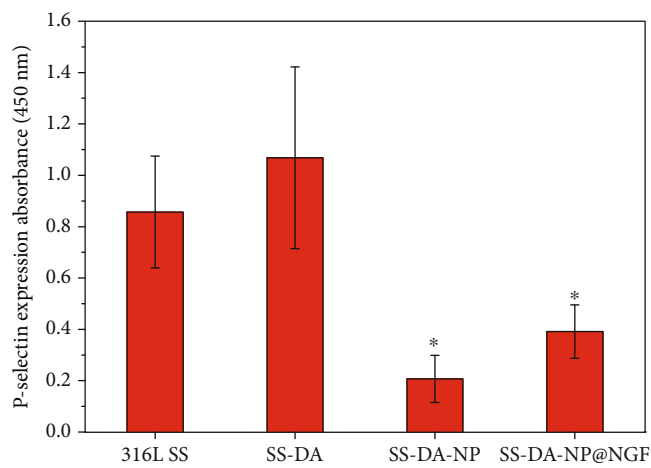
(c)

Figure 4: *In vitro* blood compatibility evaluation result. (a) Rhodamine 123 fluorescence staining of adherent platelets, (b) LDH release, and (c) P-selectin expression level of platelets adhered on different sample surfaces (mean ± SD, $n = 6$, *$p < 0.05$ indicates significant difference compared to 316L SS and SS-DA).

such as amino group, carboxyl group, hydroxyl group, and sulfonic acid group in chitosan and heparin molecules. The incorporat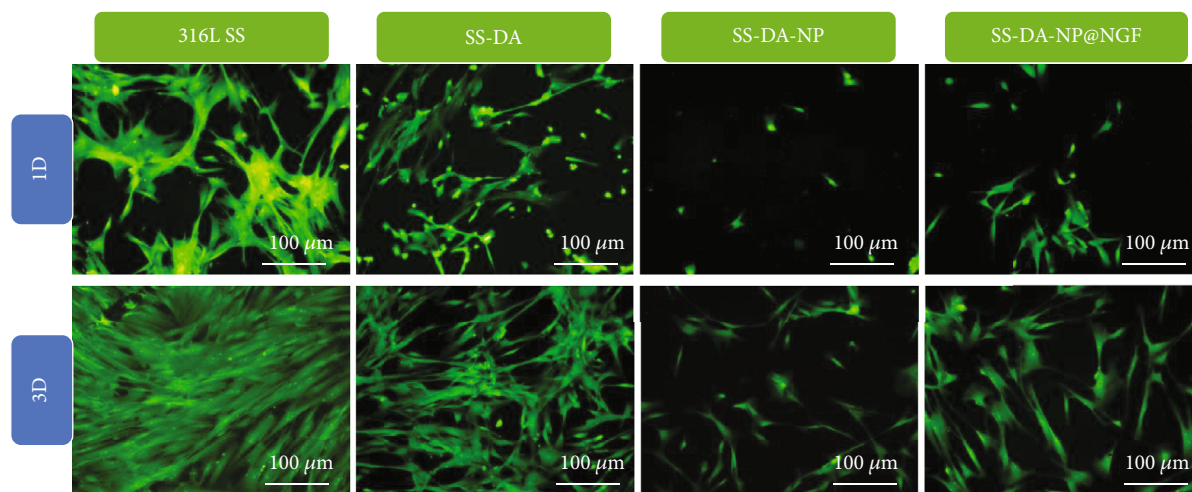ion of NGF into the nanoparticles slightly increased the water contact angle, which may be related to the exposure of hydrophobic group outside the protein structure.
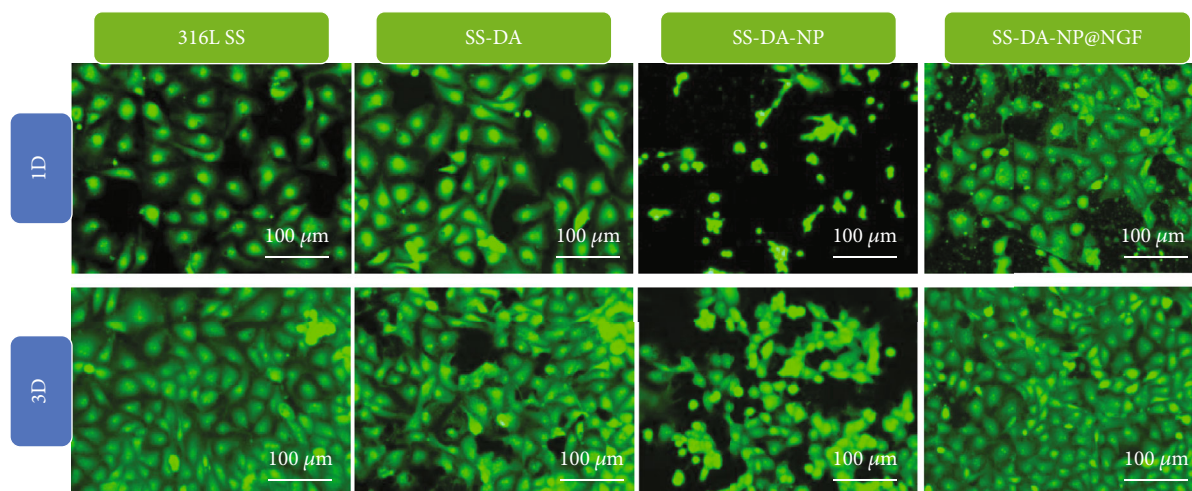
(a)
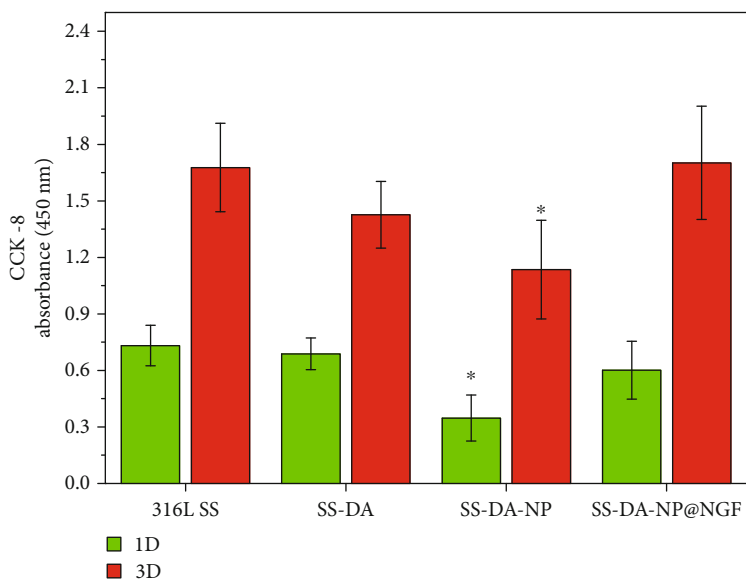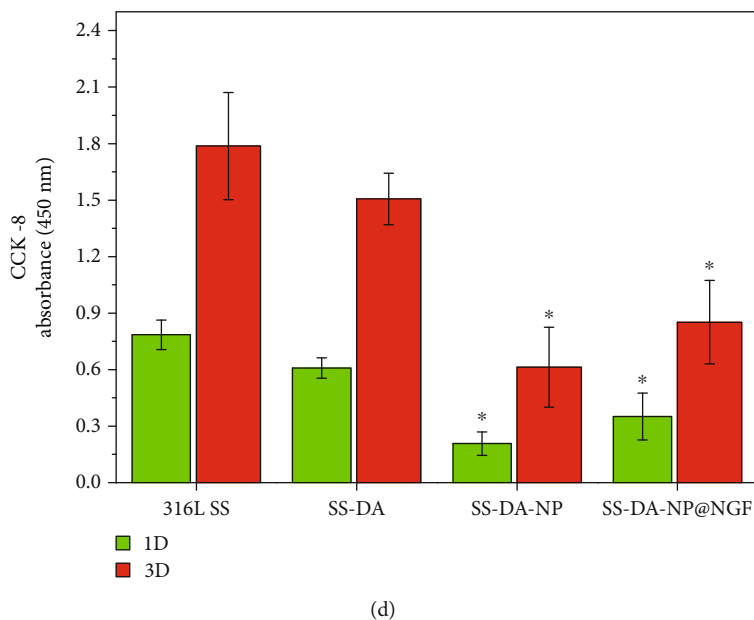

(b)

(c)

FIGURE 5: Continued.

(d)

Figure 5: Rhodamine 123 and DAPI fluorescence staining of adhered (a) ECs and (c) SMCs after culture of 1 day and 3 days. The proliferation activity of (b) ECs and (d) SMCs was detected by CCK-8 assay (mean ± SD, $n = 6$, $^*p < 0.05$ indicates significant difference compared to 316L SS and SS-DA).

The alteration of surface hydrophilicity may change the protein adsorption type and conformation and then affect its biocompatibility. In general, the surface with high hydrophobicity (water contact angle > 120°) may trigger irreversible adsorption of protein and destroy its conformation, while the surface with high hydrophilicity (water contact angle < 20°) will form water film on the surface, resulting in protein desorption [23]. In this study, the water contact angle of NP-modified surface was in the range of 40° to 60°, which may promote the adsorption of adhesive plasma proteins and thereby enhance cellular compatibility.

3.5. Quantitative Characterization of Heparin and Amine Group.
Figure 3(b) shows the quantitative characterization results of heparin on NP-modified surface, in which SS-DA was set as blank control. According to the calculation, the exposure density of heparin on SS-DA-NP is $6.4 \pm 1.7\,\mu g/cm^2$, while it slightly increased on SS-DA-NP@NGF-modified surface ($7.9 \pm 1.2\,\mu g/cm^2$). This may be attributed to the increase of amino group density after incorporation of NGF (Figure 3(c)), which may facilitate the covalent binding of nanoparticles to dopamine coating.

Heparin is a kind of negative-charged polysaccharide with superior anticoagulant property. According to previous study, heparin exposing density in the range of 3-7 $\mu g/cm^2$ may contribute to improving the blood compatibility of the material surface, prevent the occurrence of inflammatory reaction, and promote the healing of endothelium layer [15].

3.6. In Vitro Blood Compatibility Evaluation.
Figure 4(a) shows the fluorescence staining results of platelets adhering to the material surface for 2 hours in vitro. According to the results, a large amount of platelets was observed on the surface of 316L SS and SS-DA, and the adhered platelets were

aggregated seriously, indicating serious activation and poor blood compatibility. In contrast, the adhesion density of platelets on SS-DA-NP and SS-DA-NP@NGF surface was greatly decreased, and the adherent platelets mainly displayed round shape, with almost no deformation and pseudopodium, which indicates that the nanoparticle can effectively reduce the activation of platelets and improve the hemocompatibility. The results of LDH release (Figure 4(b)) and P-selectin expression (Figure 4(c)) further proved that the surface modified by CHS/Hep nanoparticles could significantly reduce the adhesion and activation of platelet ($^*p < 0.05$). Although the incorporation of NGF increased the platelet adhesion density to some extent, it still showed excellent anticoagulant properties compared with 316L SS and SS-DA.

3.7. In Vitro Cellular Compatibility Evaluation.
Figure 5(a) shows the fluorescence staining results of vascular endothelial cells cultured on different sample surfaces for a certain period of time. The results showed that after 1 and 3 days of culture, the adherent endothelial cells on the surface of 316L SS and SS-DA showed typical cobblestone morphology, indicating that the biological function of the cells was normal. However, on SS-DA-NP surface, ECs exhibit shrinkage or round-shaped morphology, which indicated poor cell adhesion and proliferation activity. In comparison, the morphology of endothelial cells on SS-DA-NP@NGF surface was normal, and the adhesion density was similar to that of 316L SS and SS-DA. CCK-8 result (Figure 5(b)) further proved that the cell proliferation activity on SS-DA-NP surface was significantly decreased, but shows no obvious alteration on SS-DA-NP@NGF surface.

Similar to that of ECs, the adhesion density and proliferation activity of SMCs on SS-DA-NP surface was
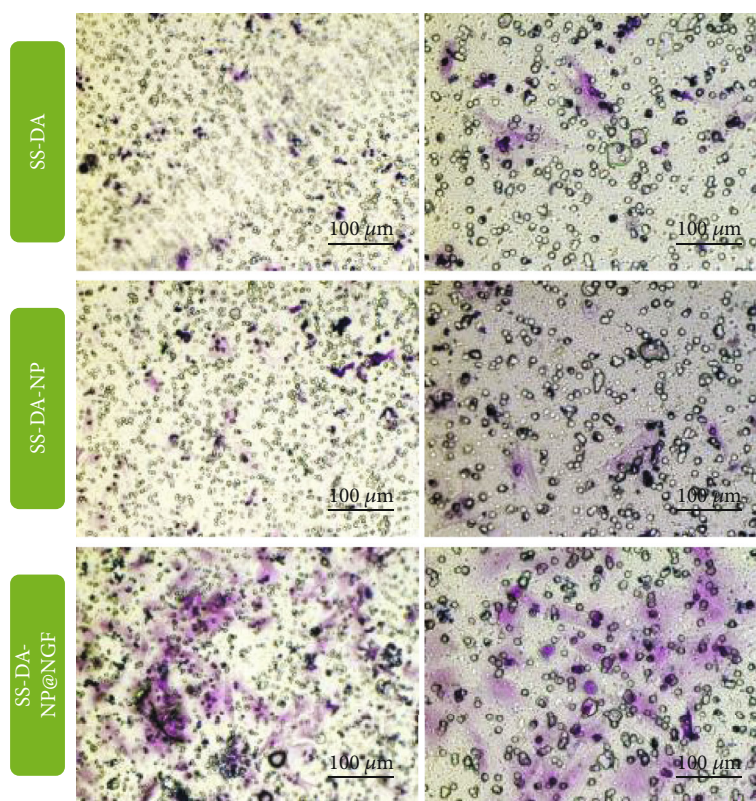
(a)
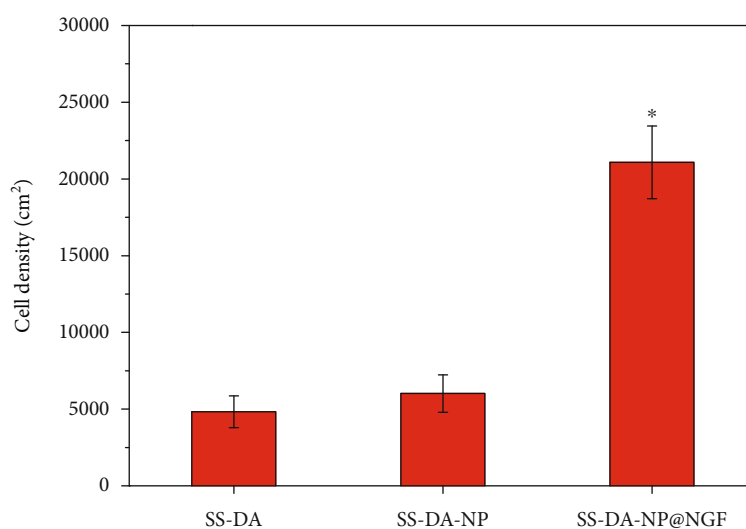
(b)

FIGURE 6: Mobilization and homing behavior of EPCs induced by nanocoating. (a) Crystal violet staining image of EPCs that mobilized to the bottom of the transwell chamber, and (b) cell counting result (mean ± SD, $n = 6$, $^*p < 0.05$ indicates significant difference compared to SS-DA and SS-DA-NP).

significantly decreased compared with that of 316L SS and SS-DA (Figures 5(c) and 5(d)). However, although the incorporation of NGF promotes the adhesion of the spreading of SMCs to some extent (Figure 5(c)), the proliferation activity was significantly lower ($^*p < 0.05$) compared with 316L SS and SS-DA (Figure 5(d)).

The results of in vitro cytocompatibility evaluation showed that the surface modified by CHS/Hep nanoparti-

cles was not conducive to the adhesion and growth of ECs and SMCs, which was mainly related to the inhibitory effect of heparin molecules on cell proliferation [24–26]. The introduction of NGF improved the adhesion and proliferation behavior of the two kinds of cells to some extent, but the enhancement extent was different for different cells. In general, the surface of SS-DA-NP@NGF showed the effect of selectively promoting the growth of

endothelial cells and inhibiting the proliferation of smooth muscle cells.

3.8. EPC Mobilization and Homing. As shown in Figure 6, SS-DA-NP@NGF has a significant chemotaxis effect on EPCs in the transwell chamber. After 24 hours of cell culture, the number of EPCs passing through the semipermeable bottom membrane to the bottom of the chamber was significantly higher than that in the SS-DA and SS-DA-NP control groups. The crystal violet staining results showed that the EPCs chemotactic by SS-DA-NP@NGF showed favorable proliferation morphology, and the cell spreading and covering area were also significantly higher than those in the control group. The results indicated that SS-DA-NP@NGF offers adequate capacity to induce the mobilization and homing of EPCs to the material surface.

In summary, since the discovery of EPCs, the mechanism of vascular endothelial injury healing has been redefined based on the migration of ECs from the surrounding vascular tissue and EPC homing at the injury site [27]. Although the surface modified by chitosan/heparin NPs shows excellent blood compatibility and the ability to inhibit the growth of smooth muscle cells, insufficient property in promoting the repair of endothelial injury continues to be problematic. NGF is a growth factor that has been reported to stimulate HUVEC proliferation and induce EPC mobilization and homing [21, 28, 29]. In this study, it was found that NGF-loaded NPs could effectively enhance the adhesion and proliferation activity of ECs on the sample surface and showed a strong chemotactic effect on vascular EPCs, indicating that the NGF-loaded nanocoating could selectively inhibit blood coagulation and intimal hyperplasia, while accelerating endothelial regeneration.

4. Conclusions

In this study, CHS/Hep@NGF NPs were successfully prepared by the electrostatic interaction among chitosan, heparin, and laminin and immobilized on the surface of dopamine-coated stainless steel. The results of material characterization showed that the NPs were uniformly immobilized on material surface. Biological evaluation results demonstrated that modified surface showed favorable capacity to inhibit platelet adhesion and activation and contributed to enhancing EC growth and preventing SMC overproliferation. This work has potential application for the design of polymer-free coronary artery stent coating.

Data Availability

The data used to support the findings of this study are available from the corresponding author upon request.

Conflicts of Interest

The authors declared that they have no conflicts of interest to this work.

Authors' Contributions

Haixin Song and Tao Wu contributed equally to this study.

Acknowledgments

References

[1] H. Jinnouchi, S. Torii, A. Sakamoto, F. D. Kolodgie, R. Virmani, and A. V. Finn, "Fully bioresorbable vascular scaffolds: lessons learned and future directions," *Nature Reviews Cardiology*, vol. 16, no. 5, pp. 286–304, 2019.

[2] J. A. Li, L. Chen, X. Q. Zhang, and S. K. Guan, "Enhancing biocompatibility and corrosion resistance of biodegradable Mg-Zn-Y- Nd alloy by preparing PDA/HA coating for potential application of cardiovascular biomaterials," *Materials Science and Engineering: C*, vol. 109, article 110607, 2020.

[3] H. M. Verheul and H. M. Pinedo, "Possible molecular mechanisms involved in the toxicity of angiogenesis inhibition," *Nature Reviews Cancer*, vol. 7, no. 6, pp. 475–485, 2007.

[4] T. Liu, S. Liu, K. Zhang, J. Y. Chen, and N. Huang, "Endothelialization of implanted cardiovascular biomaterial surfaces: the development from in vitro to in vivo," *Journal of Biomedical Materials Research Part A*, vol. 102, no. 10, pp. 3754–3772, 2014.

[5] S. L. Calzi, M. B. Neu, L. C. Shaw, J. L. Kielczewski, N. I. Moldovan, and M. B. Grant, "EPCs and pathological angiogenesis: when good cells go bad," *Microvascular Research*, vol. 79, no. 3, pp. 207–216, 2010.

[6] E. Iivanainen, V. M. Kahari, J. Heino, and K. Elenius, "Endothelial cell-matrix interactions," *Microscopy Research and Technique*, vol. 60, no. 1, pp. 13–22, 2003.

[7] L. L. Chiu and M. Radisic, "Scaffolds with covalently immobilized VEGF and angiopoietin-1 for vascularization of engineered tissues," *Biomaterials*, vol. 31, no. 2, pp. 226–241, 2010.

[8] G. De Visscher, L. Mesure, B. Meuris, A. Ivanova, and W. Flameng, "Improved endothelialization and reduced thrombosis by coating a synthetic vascular graft with fibronectin and stem cell homing factor SDF-1α," *Acta Biomaterialia*, vol. 8, no. 3, pp. 1330–1338, 2012.

[9] J. Wang, Y. Chen, T. Liu et al., "Covalent co-immobilization of heparin/laminin complex that with different concentration ratio on titanium surface for selectively direction of platelets and vascular cells behavior," *Applied Surface Science*, vol. 317, pp. 776–786, 2014.

[10] K. Zhang, J. A. Li, K. Deng, T. Liu, J. Y. Chen, and N. Huang, "The endothelialization and hemocompatibility of the functional multilayer on titanium surface constructed with type IV collagen and heparin," *Colloids and Surfaces. B, Biointerfaces*, vol. 108, pp. 295–304, 2013.

[11] C. J. Pan, Y. D. Hu, Y. Hou et al., "Corrosion resistance and biocompatibility of magnesium alloy modified by alkali heating treatment followed by the immobilization of poly (ethylene glycol), fibronectin and heparin," *Materials Science and Engineering: C*, vol. 70, Pt 1, pp. 438–449, 2017.

[12] P. Galvin, D. Thompson, K. B. Ryan et al., "Nanoparticle-based drug delivery: case studies for cancer and cardiovascular

applications," *Cellular and Molecular Life Sciences*, vol. 69, no. 3, pp. 389–404, 2012.

[13] J. L. Zhou, J. L. Ding, Z. G. Zhu et al., "Surface biofunctionalization of the decellularized porcine aortic valve with VEGF-loaded nanoparticles for accelerating endothelialization," *Materials Science and Engineering: C*, vol. 97, pp. 632–643, 2019.

[14] F. Mohammadi, N. Golafshan, M. Kharaziha, and A. Ashrafi, "Chitosan-heparin nanoparticle coating on anodized NiTi for improvement of blood compatibility and biocompatibility," *International Journal of Biological Macromolecules*, vol. 127, pp. 159–168, 2019.

[15] T. Liu, Y. Liu, Y. Chen et al., "Immobilization of heparin/poly-(L)-lysine nanoparticles on dopamine-coated surface to create a heparin density gradient for selective direction of platelet and vascular cells behavior," *Acta Biomaterialia*, vol. 10, no. 5, pp. 1940–1954, 2014.

[16] T. Liu, Z. Zeng, Y. Liu et al., "Surface modification with dopamine and heparin/poly-l-lysine nanoparticles provides a favorable release behavior for the healing of vascular stent lesions," *Applied Materials & Interfaces*, vol. 6, no. 11, pp. 8729–8743, 2014.

[17] B. Fonseca-Santos and M. Chorilli, "An overview of carboxymethyl derivatives of chitosan: their use as biomaterials and drug delivery systems," *Materials Science & Engineering. C, Materials for Biological Applications*, vol. 77, pp. 1349–1362, 2017.

[18] W. Wang, C. Xue, and X. Mao, "Chitosan: structural modification, biological activity and application," *International Journal of Biological Macromolecules*, vol. 164, pp. 4532–4546, 2020.

[19] J. D. Berglund and Z. S. Galis, "Designer blood vessels and therapeutic revascularization," *British Journal of Pharmacology*, vol. 140, no. 4, pp. 627–636, 2003.

[20] W. Zeng, W. Yuan, L. Li et al., "The promotion of endothelial progenitor cells recruitment by nerve growth factors in tissue-engineered blood vessels," *Biomaterials*, vol. 31, no. 7, pp. 1636–1645, 2010.

[21] C. S. Jadhao, A. D. Bhatwadekar, Y. Jiang, M. E. Boulton, J. J. Steinle, and M. B. Grant, "Nerve growth factor promotes endothelial progenitor cell-mediated angiogenic responses," *Investigative Ophthalmology & Visual Science*, vol. 53, no. 4, pp. 2030–2037, 2012.

[22] T. Liu, X. Wang, X. H. Tang et al., "Surface modification with ECM-inspired SDF-1α/laminin-loaded nanocoating for vascular wound healing," *ACS Applied Materials & Interfaces*, vol. 9, no. 36, pp. 30373–30386, 2017.

[23] E. Monchaux and P. Vermette, "Effects of surface properties and bioactivation of biomaterials on endothelial cells," *Frontiers in Bioscience (Scholar Edition)*, vol. S2, no. 1, pp. 239–255, 2010.

[24] D. Letourneur, B. L. Caleb, and J. J. Castellot Jr., "Heparin binding, internalization, and metabolism in vascular smooth muscle cells: I. Upregulation of heparin binding correlates with antiproliferative activity," *Journal of Cellular and Comparative Physiology*, vol. 165, no. 3, pp. 676–686, 1995.

[25] C. Ettelaie, D. Fountain, M. E. W. Collier, A. M. Elkeeb, Y. P. Xiao, and A. Maraveyas, "Low molecular weight heparin downregulates tissue factor expression and activity by modulating growth factor receptor-mediated induction of nuclear factor-κB," *Biochimica et Biophysica Acta*, vol. 1812, no. 12, pp. 1591–1600, 2011.

[26] L. Li, X. Rui, T. F. Liu, G. L. Xu, and S. Y. He, "Effect of heparin-derived oligosaccharide on vascular smooth muscle cell proliferation and the signal transduction mechanisms involved," *Cardiovascular Drugs and Therapy*, vol. 26, no. 6, pp. 479–488, 2012.

[27] M. Avci-Adali, G. Ziemer, and H. P. Wendel, "Induction of EPC homing on biofunctionalized vascular grafts for rapid in vivo self-endothelialization – a review of current strategies," *Biotechnology Advances*, vol. 28, no. 1, pp. 119–129, 2010.

[28] X. Yu, Y. Qi, T. Zhao et al., "NGF increases FGF2 expression and promotes endothelial cell migration and tube formation through PI3K/Akt and ERK/MAPK pathways in human chondrocytes," *Osteoarthritis and Cartilage*, vol. 27, no. 3, pp. 526–534, 2019.

[29] K. V. Moser, M. Reindl, I. Blasig, and C. Humpel, "Brain capillary endothelial cells proliferate in response to NGF, express NGF receptors and secrete NGF after inflammation," *Brain Research*, vol. 1017, no. 1-2, pp. 53–60, 2004.